Double crystal x-ray and gamma ray diffractometry

Gani, Siti Meriam Abdul

DOUBLE CRYSTAL X-RAY AND GAMMA RAY DIFFRACTOMETRY

by

Siti Meriam Abdul Gani, B.Sc.

A thesis submitted to the University of Durham in candidature for the Degree of Doctor of Philosophy

December 1982.

To my Parents

ABSTRACT

An introduction to the dynamical diffraction theory is given and its results are discussed in relation to double crystal diffractometry in the various arrangements. A review of the work using this technique is also given.

The micro-computer controlled diffractometers, the EGG and the COFFIN together with the interface system are described. The software written for the automatic control of the diffractometer is given in detail. The micro-computer controlled diffractometer has proved a great advantage in that it reduces tremendously the time of the experiment and made possible the experiment using γ-rays which otherwise is impossible to carry out due to its low intensity and high background.

Results are presented of a study of the damage introduced into silicon when cut with a diamond tool on a lathe. The depth of damage introduced is investigated by measuring rocking curves full width at half height maximum as the crystal was etched. The result obtained shows that the bulk of the surface damage introduced is confined to the first 5μm of the crystal which is completely removed after a further 100μm is removed and is independent of the tool type. Therefore diamond turning can replace the time consuming hand lapping process with a reduction in cost and would therefore be advantageous in the production of monochromators and mirrors of non-standard shapes and sizes.

Previous work using γ-ray energy is reviewed. The double crystal technique using gamma rays is potentially a powerful tool for the measurement of lattice tilts in thick

perfect single crystals. The narrow rocking curve (less than 0.5 arc seconds) and the long counting time (up to 6 minutes per point) necessitates the use of a micro-computer. Results are presented of experiments to establish the feasibility of the method.

The perfection of the triangular monochromator crystal used at the Protein Crystallography Station, Daresbury Laboratory was also investigated from rocking curve measurements. The effects of bending the triangular monochromator crystal on the FWHM and integrated reflecting power were studied and the measurement of curvature was made on the Lang camera. The 6-fold increase in the integrated intensity of an unpolished monochromator over a polished one could be a great advantage for protein crystallography experiments. This has yet to be tested at the Daresbury station.

Results are presented on the effect of a magnetic field parallel to the two fold axis on the double crystal rocking curves of hematite crystal which indicate a complex behaviour where multiple splitting occurs and is extremely unstable.

Double crystal topographs of Indium phosphide and gallium arsenide crystals indicate the usefulness of synchrotron radiation to crystal growers for a rapid and routine assessment of crystal perfection.

ACKNOWLEDGEMENTS

It is a pleasure for me to make the following acknowledgements.

I would like to thank Professor B.H. Bransden and Professor A.W. Wolfendale of the Physics Department for making available the facilities of the Physics Department of Durham University. I would also like to thank the Malaysian Government for the financial assistance and the University of Malaya for the award of a fellowship.

I am grateful to Dr. W.D. Corner, Head of the Solid State Physics Group for his guidance. In particular it is a pleasure for me to express my gratitude to Dr. B.K. Tanner for his constant guidance, encouragement and enthusiasm on all aspects of this work and without whom it would never have been completed.

I would like to thank the Director and staff of the Rutherford Laboratory who made it possible for me to use the facilities at the Neutron Division for the gamma ray work. My thanks also goes to the Director and staff of the SRS Daresbury Laboratory for the provision of the synchrotron radiation facilities at the Interferometry Station.

I would also like to thank Professor M. Hart who provided me with the silicon crystals and Dr. T.J.L. Jones for the germanium crystals used in the gamma ray experiments.

My thanks also goes to Dr. B.K. Bowen for the preparation of the diamond turned silicon, Dr. J.R. Helliwell who provided me with the monochromator crystals, Dr. B.K. Wanklyn who provided the hematite crystals and Dr. G.R. Jones and his colleagues for the indium phosphide and gallium

arsenide crystals.

My thanks again to Dr. D.K. Bowen and Dr. J.R. Helliwell for their valuable discussions and I am grateful to the past and present members of the group for their assistance and discussions, in particular Dr. G.F. Clark who helped me in the experiments.

My acknowledgement also goes to the technical assistance of Mr. K. Moulson the group technician, Mr. W. Leslie, Mr. T. Jackson, Mr. D. Jobling and Mr. J. Scott and their staffs in the Department's workshop and also Mr. M.W. Spalding for some of the photographs. I would also like to thank Mrs. M. Chipchase for typing this thesis.

Finally, I would like to thank my husband Zainol Abidin for his help and patience.

MEMORANDUM

I declare that the work has not been submitted for any other degree. This thesis is my original work, except where indicated by reference to other work.

Part of this thesis has been published.

" Double crystal gamma ray diffractometry" :
S. Meriam Abdul Gani, G.F. Clark and B.K. Tanner;
Inst. Phys. Conf. Ser. No. 60 : Section 5,
pp 259. Paper presented at Micros. Semicond. Mater.
Confer., Oxford, 1981.

CONTENTS

CHAPTER 1

DYNAMICAL DIFFRACTION THEORY

1.1 Introduction

A perfect crystal will produce a strong diffracted beam if the reflecting plane of lattice parameter d is set to reflect an incident monochromatic beam of wavelength λ at the Bragg angle θ_B. That is

$$2d \sin \theta_B = \lambda \qquad 1.1$$

If an imperfection exists in the crystal the lattice parameter around that region varies and therefore the Bragg relation is not satisfied simultaneously in the perfect and imperfect regions. As a result the intensity of the diffracted beam is non-uniform and a photographic film placed to record the intensity will display a different image contrast.

There are generally two diffraction theories which can be used to account for the intensity distribution in X-ray diffraction : the kinematical theory and the dynamical theory. The more general of the two theories, the dynamical theory will be discussed in detail in this chapter as in the limit of small crystals, the results approach that of the kinematical theory.

In the kinematical diffraction theory the scattering from each volume element is treated as being independent of that from other volume elements except for the incoherent power losses in reaching and leaving the volume. In simple terms the amplitude of the scattered waves is assumed to be small compared to that of the incident wave. This assumption

is justified if the crystal is small (of less than 1 micron in diameter) and in large highly deformed crystals where the mosaic structure acts as individual diffracting units. The kinematical diffraction theory may be found in many text books on solid state physics.

For large perfect single crystals the amplitude of the diffracted beam is no longer small compared to that of the incident beam and thus the dynamical diffraction theory which takes account of all the interactions within the crystals must be used. The original theoretical work was done by Darwin (1914), Ewald (1958, 1916 and 1917) and von Laue (1931). The theory has also been summarized and extended by Compton and Allison (1934), Zachariasen (1945), James (1948), von Laue (1952) and Pinsker (1978). Excellent reviews of the theory has also been published by Batterman and Cole (1964), Authier (1970) and Hart (1980). The treatment here follows that of Tanner (1976).

1.2 Fundamental Equations of the Dynamical Theory in Perfect Crystals

In obtaining the fundamental equations of dynamical theory, the solution of Maxwell's equations in a periodic medium must be matched to the plane wave solutions outside the medium.

The Laue equation relates the diffracted beam wavevector $\underline{K}_g$ to the incident beam wavevector $\underline{K}_o$ in reciprocal space via a reciprocal lattice vector $\underline{g}$:

$$\underline{K}_g = \underline{K}_o + \underline{g} \qquad 1.2$$

The solution of Maxwell's equation for the electric displacement vector $\underline{D}$ should be of the form

$$\underline{D} = \sum_g D_g \exp(-2\pi i \underline{K}_g . \underline{r}_i) \exp(i\omega t) \qquad 1.3$$

This Bloch wave, as it is called, describes a wavefield consisting of an infinite number of plane waves with wavevector $\underline{K}_g$ and reflects the periodicity of the crystal lattice.
If the electrical conductivity and the magnetic permeability are assumed to be zero and unity respectively then Maxwell's equation reduces to

$$\text{curl curl } \underline{D} = \frac{-(1 + \chi)}{c^2} \frac{\partial^2 \underline{D}}{\partial t^2} \qquad 1.4$$

As the electrical susceptibility χ is a continuous periodic function it can be expanded as a Fourier series over all the reciprocal lattice vectors

$$\chi = \sum_h \chi_h \exp(-2\pi i \, \underline{h} . \underline{r}) \qquad 1.5$$

χ_h is related to the structure factor F_h by

$$\chi_h = \frac{-r_e \lambda^2 F_h}{\pi V_c} \qquad 1.6$$

where r_e is the classical electron radius and V_c is the volume of the unit cell. The structure factor is related to the atomic scattering factor f_i by

$$F_h = \sum_{\substack{\text{unit} \\ \text{cell}}} f_i \exp(2\pi i \, \underline{h} . \underline{r}) \qquad 1.7$$

where $\underline{r}_i$ is the position vector in real space of the ith atom with respect to origin.

Since χ is small in the X-ray region that is of the order of 10^{-5} it can be expanded as a power series. Thus equation 1.4 can be written as

$$\text{curl curl } (1 - \chi)\underline{D} = -\frac{1}{c^2}\frac{\partial^2 \underline{D}}{\partial t^2} \qquad 1.8$$

On substitution of equations 1.3 and 1.5 in 1.8, and after some manipulation, the following relation is obtained:

$$\sum_h \{\chi_{g-h}(\underline{K}_g.\underline{D}_h)\underline{K}_g - \chi_{g-h}(\underline{K}_g.\underline{K}_g)\underline{D}_h\} = \{k^2-(\underline{K}_g.\underline{K}_g)\}\underline{D}_g \qquad 1.9$$

k is a vacuum wavevector and is equal to ω/c. In X-ray diffraction usually only two wavevectors have significant amplitude, that is the refracted vector $\underline{K}_o$ and the Bragg reflected vector $\underline{K}_g$. Therefore equation 1.9 reduces to

$$\chi_g(\underline{K}_g.\underline{D}_o)\underline{K}_g - \chi_g(\underline{K}_g.\underline{K}_g)\underline{D}_o + \chi_o(\underline{K}_g.\underline{D}_g)\underline{K}_g - \chi_o(\underline{K}_g.\underline{K}_g)\underline{D}_g = (k^2-\underline{K}_g.\underline{K}_g)\underline{D}_g \qquad 1.10a$$

$$\chi_{\bar{g}}(\underline{K}_o.\underline{D}_g)\underline{K}_o - \chi_{\bar{g}}(\underline{K}_o.\underline{K}_o)\underline{D}_g + \chi_o(\underline{K}_o.\underline{D}_o)\underline{K}_o - \chi_o(\underline{K}_o.\underline{K}_o)\underline{D}_o = (k^2-\underline{K}_o.\underline{K}_o)\underline{D}_o \qquad 1.10b$$

Taking the scalar product of equation 1.10a with $\underline{D}_g$ and equation 1.10b with $\underline{D}_o$, equation 1.10a and 1.10b reduces to

$$k^2C\chi_{\bar{g}}D_g + \{k^2(1 + \chi_o) - \underline{K}_o.\underline{K}_o\}D_o = 0 \qquad 1.11a$$

$$\{k^2(1 + \chi o) - \underline{K}_g.\underline{K}_g\}D_g + k^2C\chi_g D_o = 0 \qquad 1.11b$$

C is the polarization factor where

$$C = \underline{D}_o.\underline{D}_g = 1 \text{ for } \sigma \text{ polarisation}$$
$$= \cos 2\theta_B \text{ for } \pi \text{ polarization}$$

For non trivial solution of equations 1.11a and 1.11b the determinant must be zero

$$\begin{vmatrix} k^2 C\chi_{\bar{g}} & k^2(1+\chi_o) - \underline{K}_o.\underline{K}_o \\ k^2(1+\chi_o) - \underline{K}_g.\underline{K}_g & k^2 C\chi_g \end{vmatrix} = 0 \qquad 1.12$$

Therefore $\alpha_o\alpha_g = \frac{1}{4} k^2 C^2 \chi_g \chi_{\bar{g}}$ 1.13

where $\alpha_o = \frac{1}{2k} \{\underline{K}_o.\underline{K}_o - k^2(1+\chi_o)\}$ 1.14a

and $\alpha_g = \frac{1}{2k} \{\underline{K}_g.\underline{K}_g - k^2(1+\chi_o)\}$ 1.14b

Define the amplitude ratio $R = D_g/D_o$. From equations 1.11 and 1.13

$$R = \frac{D_g}{D_o} = \frac{2\alpha_o}{C\chi_{\bar{g}}k} = \frac{C\chi_g k}{2\alpha_g} \qquad 1.15$$

Thus $$R^2 = \frac{\alpha_o\chi_g}{\alpha_g\chi_{\bar{g}}} \qquad 1.16$$

1.2.1 The Dispersion Surface

The dispersion equation 1.13 links the incident and diffracted wavevectors in the crystal. Figure 1.1 shows a section of spheres of radius k and $k(1 + \chi_o/2)$ with centres O and G where $\vec{OG}$ is the reciprocal lattice vector $\underline{g}$. The Laue point L is the intersection of the spheres and X-rays will only be diffracted close to the Laue point that is when the Laue equation 1.2 is nearly satisfied. Away from the Laue point $\underline{D}_g = 0$ and from equation 1.11a.

$$|\underline{K}_o| = k(1 + \chi_o/2) \qquad 1.17$$

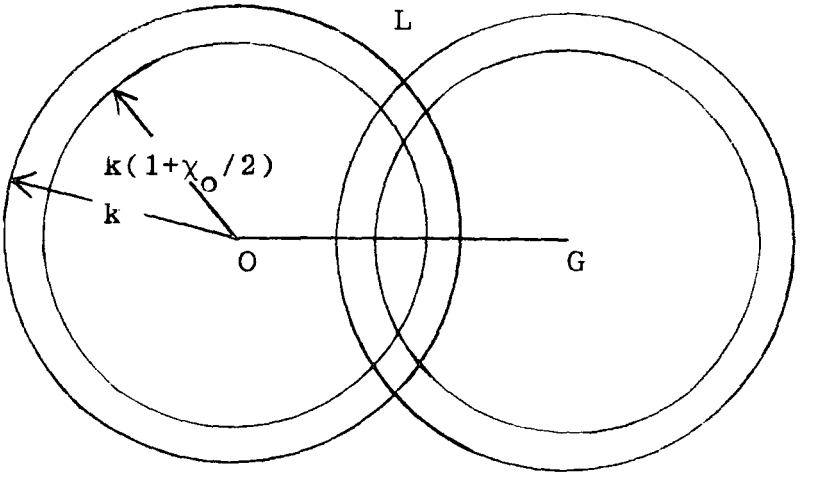

Fig. 1.1 Spheres in reciprocal space about the lattice point O and G. L is the Laue point.

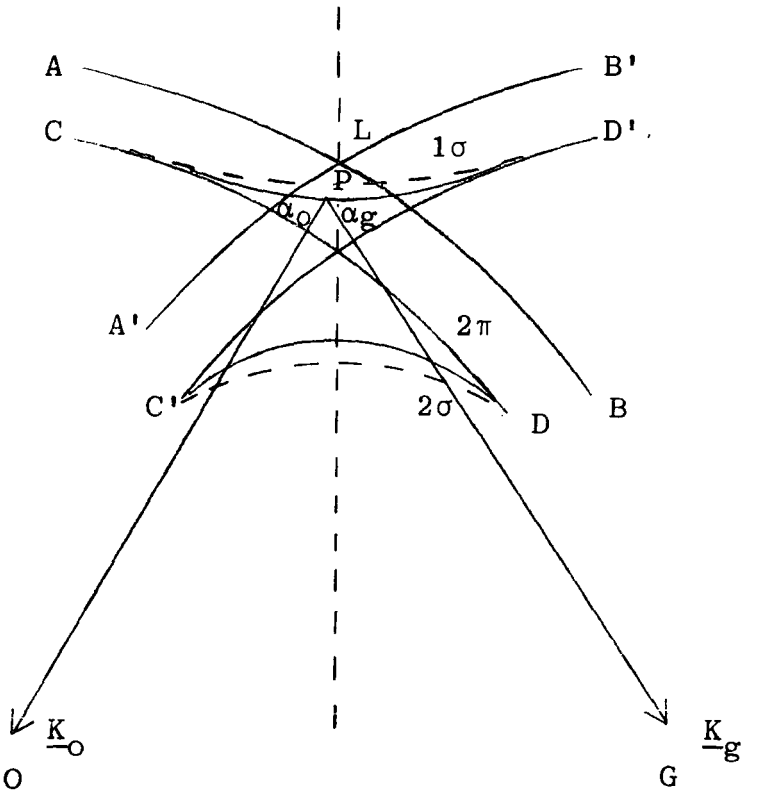

Fig. 1.2 The magnified view of the region about L which is the diepersion surface construction.

that is the wavevector inside the crytal is equal to the wavevector in vacuum corrected for refractive index and is represented by a sphere of radius $k(1 + \chi_o/2)$ (Figure 1.1). Since χ_o is small $|\underline{K}_o| = k$. The loci of the tails of wavevectors during Bragg reflection does not lie on the sphere in the region of the Laue point and this loci given by the dispersion equation 1.13 is known as a dispersion surface.

Figure 1.2 is the expanded view of the region close to the Laue point L. AB and A'B' are the traces of the segments of spheres of radius k, CD and C'D' are those of radius $k(1 + \chi_o/2)$ with centres at O and G respectively. For a point P on the dispersion surface α_o and α_g are the respective perpendicular distances from point P to CD and C'D'. As the radius of the sphere is large compared to the Laue region, the segments of the spheres are approximated to planes and thus the dispersion surface is the equation of a hyperboloid of revolution about axis OG with CD and C'D' as asymptotes. There are four branches of the dispersion surface. The upper branch is denoted as branch 1 and the lower is branch 2. Each branch has two polarization state σ and π.

1.2.2. Boundary Conditions.

A plane wave incident outside a crystal has to satisfy certain boundary conditions on the field vector and wavevector in order to propagate across the crystal. The condition which relates to the amplitude matching requires the tangential component of E and H to be continuous across the boundary. As the refractive index of the crystal in the X-ray region

is close to unity the reflection amplitude or the refraction effect is negligible provided that the glancing angle of incidence is not close to the critical angle of total external reflection. Therefore to a good approximation the field vector is continuous across the crystal surface and the electric displacement vectors are equal on either side of the boundary. For an electric displacement amplitude $\underline{D}_i$ outside the crystal

$$\underline{D}_i = \underline{D}_{o_1} + \underline{D}_{o_2} \qquad 1.18a$$

$$0 = \underline{D}_{g_1} + \underline{D}_{g_2} \qquad 1.18b$$

Also at the crystal surface the waves inside and outside the crystal must have the same phase velocity parallel to the crystal surface implying that only the vector normal to the crystal surface contributes to the difference in wavevector inside and outside the crystal, that is

$$\underline{K}_{o_i} - \underline{k}_e = \underline{K}_{g_i} - \underline{k}_e = \delta\hat{n} \qquad 1.19$$

where $\hat{n}$ is a unit vector normal to the surface and i = 1 or 2 depending on the branch of the dispersion surface as shown in Figures 1.3a and 1.3b for the transmission and reflection geometry. The tie points excited inside the crystal by an external wave are at the intersection of the vector normal to the crystal surface drawn from the tip of the wavevector $\underline{k}_e$ and the dispersion surface. For the transmission geometry (Laue case) the tie points are on opposite branches of the dispersion surface but for the reflection geometry (Bragg case) the tie points lie on the

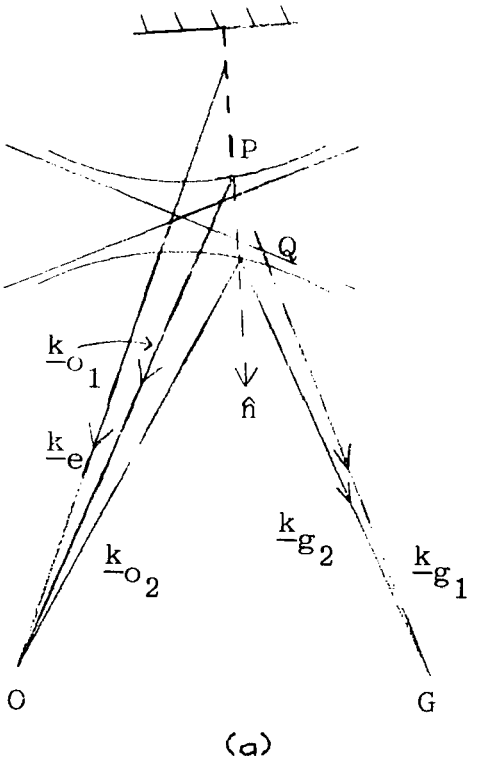

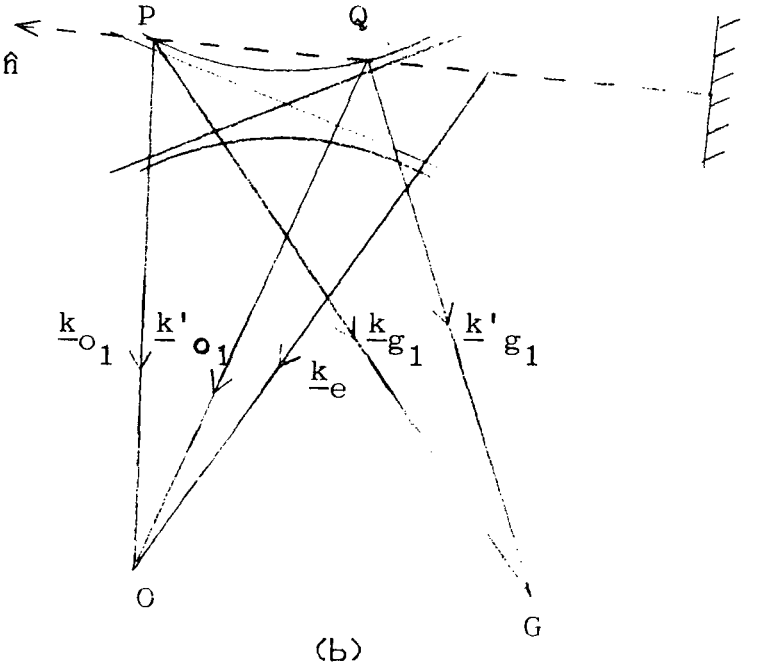

Fig. 1.3 Geometrical representation of the boundary conditions.
(a) Laue, transmission geometry.
(b) Bragg, reflection geometry.

same branch.

1.2.3 Energy Flow

The direction of energy flow in the crystal is described in terms of the Poynting vector $\underline{P}$ for the total wavefield and represents the energy flowing across a unit area in a unit time.

$$\underline{P} = \underline{E} \times \underline{H} \qquad 1.19$$

The average value over the unit cell and time is given by

$$\underline{P} = I_o \hat{s}_o + I_g \hat{s}_g \qquad 1.20$$

where $\hat{s}_o$ and $\hat{s}_g$ are unit vectors parallel to the incident and reflected direction and I_o and I_g are the refracted and diffracted beam respectively (Figure 1.4). The propagation of any wavefield in the direction perpendicular and parallel to the reflecting plane are given by

$$\underline{P}.\hat{u} = P \sin \Delta = I_o \hat{s}_o.\hat{u} + I_g \hat{s}_g.\hat{u} = (I_g - I_o)\sin \theta_B \qquad 1.21$$

$$\underline{P}.\hat{v} = P \cos \Delta = I_o \hat{s}_o.\hat{v} + I_g \hat{s}_g.\hat{v} = (I_g + I_o)\cos \theta_B \qquad 1.22$$

$\hat{u}$ and $\hat{v}$ are unit vectors perpendicular and parallel to the reflecting plane and Δ is the angle between the propagation direction of the wavefield and the Bragg planes. From equations 1.21 and 1.22

$$\tan \Delta = \tan \theta_B \frac{(I_g/I_o - 1)}{(I_g/I_o + 1)} = \tan \theta_B \frac{(R^2 - 1)}{(R^2 + 1)} \qquad 1.23$$

The equation of the dispersion surface in the coordinate system Ox, Oz (Figure 1.5) is

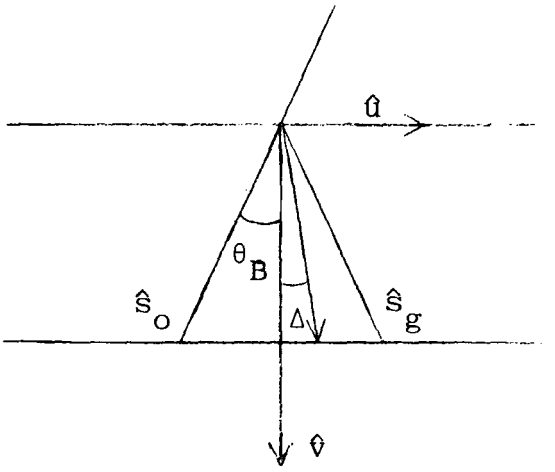

Fig. 1.4 The Bormann fan showing the direction of energy flow.

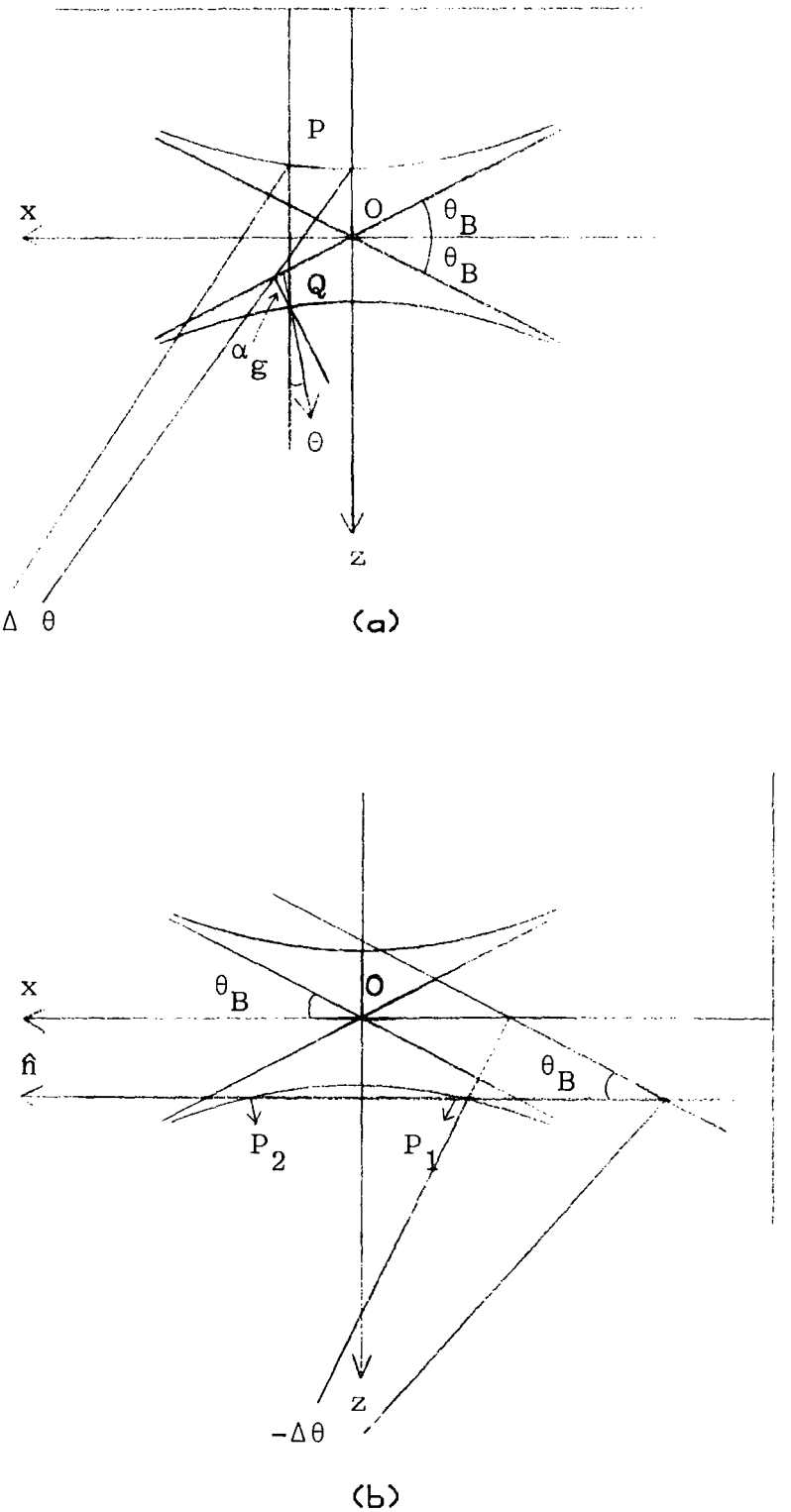

Fig. 1.5 Dispersion surface construction with the co-ordinate system x and z.
(a) Laue geometry.
(b) Bragg geometry.

$$z^2 = \frac{1}{4}\Lambda_o^2 + x^2\tan^2\theta_B \qquad 1.24$$

Λ_o is the diameter of the dispersion surface. If θ is the angle between Oz and the normal to the dispersion surface then

$$\tan\theta = \frac{dz}{dx} = \frac{x\tan^2\theta_B}{z} \qquad 1.25$$

The deviation parameter η determines the deviation of the tie points from the exact Bragg position and is defined as

$$\eta = \frac{2x\tan\theta_B}{\Lambda_o} \qquad 1.26$$

The angular deviation from the exact Bragg angle $\Delta\theta$ is

$$\Delta\theta = \frac{x\sec\theta_B}{k} \qquad 1.27$$

$\Delta\theta$ is negative when the angle of incidence is less than the Bragg angle. From equations 1.26 and 1.27

$$\eta = \frac{2\sin\theta_B k\Delta\theta}{\Lambda_o} \qquad 1.28$$

Substituting equation 1.26 in 1.24

$$z = \pm\frac{\Lambda_o(1+\eta^2)^{\frac{1}{2}}}{2} \qquad 1.29$$

The perpendicular distance from the tie point to the sphere about G is

$$\alpha_g\sec\theta_B = z - x\tan\theta_B \qquad 1.30$$

From equation 1.24, 1.26 and 1.30

$$(\alpha_g\sec\theta_B)^2 + \Lambda_o\eta\alpha_g\sec\theta_B - \frac{1}{4}\Lambda_o^2 = 0 \qquad 1.31$$

Solving the quadratic equation 1.31

$$\alpha_g \sec\theta_B = -\tfrac{1}{2}\Lambda_o\{-\eta \pm (1 + \eta^2)^{\frac{1}{2}}\} \qquad 1.32$$

The amplitude ratio in terms of the deviation parameter is given by

$$R = \eta \pm (1 + \eta^2)^{\frac{1}{2}} \qquad 1.33$$

The positive sign corresponds to branch 1 and the lower sign to branch 2. At the centre of the dispersion surface $\alpha_o = \alpha_g$ and therefore the diameter of the dispersion surface is

$$\Lambda_o = 2\alpha_o \sec\theta_B = 2\alpha_g \sec\theta_B \qquad 1.34$$

Therefore $$\Lambda_o^2 = \sec^2\theta_B k^2 C^2 \chi_g \chi_{\bar{g}} \qquad 1.35$$

From equations 1.25, 1.26, 1.29 and 1.33

$$\tan\Theta = \tan\theta_B \frac{(R^2 - 1)}{(R^2 + 1)} \qquad 1.36$$

Comparing equations 1.36 and 1.23

$$\Delta = \Theta \qquad 1.37$$

The result of equation 1.37 implies that the Poynting vector has the same direction as the normal to the dispersion surface. If the tie point P is near C the direction of energy flow is normal to the sphere CD in the direction of $\hat{s}_o$ and if P is near D' the energy flow is in the direction of $\hat{s}_g$. At the Brillouin zone boundary or the exact Bragg condition the energy flow is along the Bragg planes in the direction $(\hat{s}_o + \hat{s}_g)$.

1.3 Results of the Dynamical Theory

There have been many experiments carried out to demonstrate the validity of dynamical theory. The following section is a discussion of a few of the important results.

1.3.1 The Bormann Effect

The Bormann effect was first observed by Bormann in calcite single crystals (Bormann 1941, 1950) but most of the quantitative investigation was carried out using germanium crystals as it can be obtained in a highly perfect state. These investigations can be found in articles by Bormann and Hilderbrandt (1959), Hunter (1959), Battermann (1962), Okkerse (1962) and Penning (1966).

The Bormann effect experiment can be schematically represented by Figures 1.6 and 1.7. A perfect crystal cut in the form of a parallel-sided slab with the diffracting plane perpendicular to the slab surface was rotated about an axis parallel to the diffracting plane. As absorption is mainly due to photoelectric processes at X-ray wavelengths, the transmitted intensity at $\theta \neq \theta_B$ is given by $I_o \exp(-\mu_o t)$. If the thickness of the crystal slab t is small such that the product of the absorption coefficient μ_o and t is $\mu_o t \ll 1$ the transmitted intensity profile is as shown in the upper curve of Figure 1.6c, where a dip in the profile was obtained as expected. For $\mu_o t \gg 1$ a peak was observed in the profile at the angular position θ_B when the Bragg relation is satisfied. This phenomenon is known as anomalous transmission or the Bormann effect. As shown in Figure 1.7b three spots

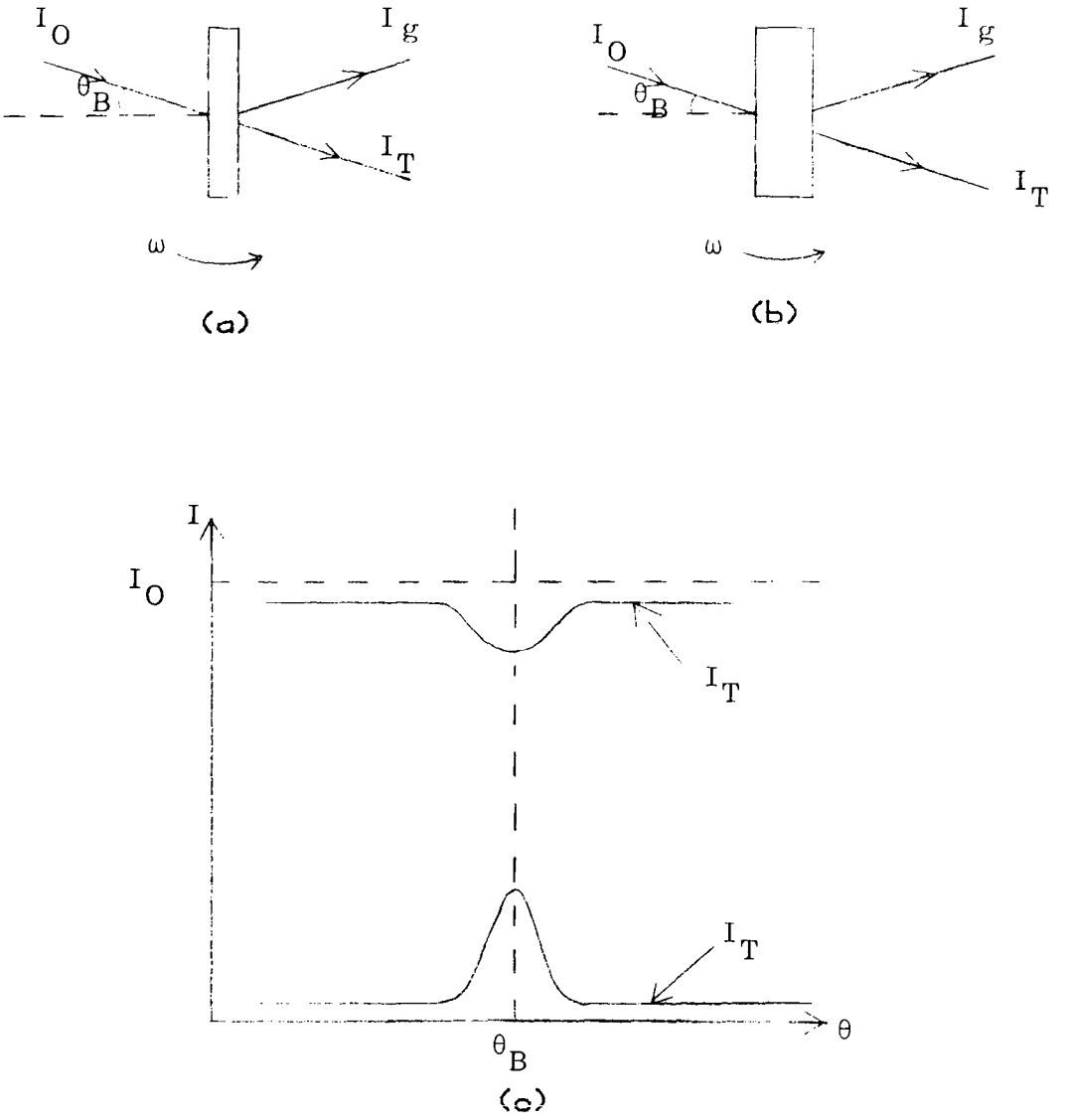

Fig. 1.6 The Bormann effect.
(a) Laue diffraction in thin crystal, $t \ll 1$.
(b) Laue diffraction in thick crystal, $t > 10$.
(c) Transmitted intensity for thin crystal (upper curve) and thick crystal (lower curve).

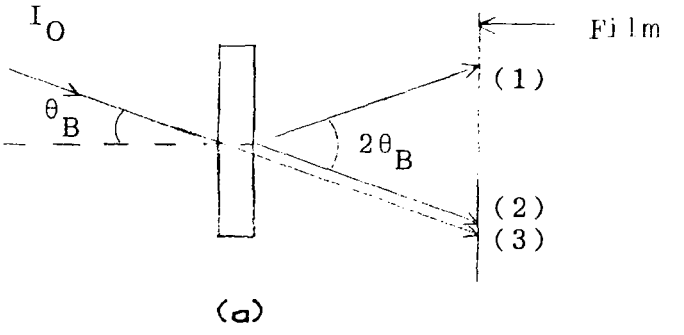

(a)

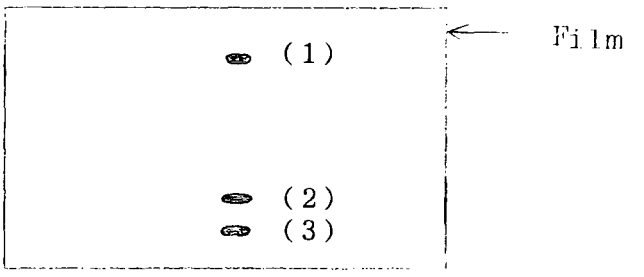

(b)

Fig. 1.7 (a) Ray diagram corresponding to the spots obtain on the film.

(b) Spots obtain on a film. Spot 1 correspond to the diffracted beam. Spot 2 is at an angular position 2 from spot 1. Spot 3 is in line with the incident beam.

were obtained on a photographic film placed parallel to the crystal surface to intercept the beam emerging from the crystal. Spot 1 was due to the diffracted beam, spot 2 is at a distance corresponding to an angular position $2\theta_B$ from spot 1 and of about the same darkness as spot 1. Spot 3 is in line with the incident beam. The separation of spots 2 and 3 is proportional to the crystal thickness. From Figure 1.7a the beam for spots 1 and 2 must be from a point opposite to the point when the incident beam hits the crystal surface which implies that the radiation travels along the atomic planes. This property of anomalous transmission is a diffraction phenomenon, a feature of a perfectly periodic lattice and imperfections tend to reduce or eliminate the effect. Anomalous transmission has been used to image dislocations directly (Bormann, Hartwig, Irmler 1958) and a statistical theory relating the transmission to the small size defect concentration have been developed by Dederichs (1970) and applied to silicon (Patel 1973) and aluminium (Nost, Larson and Young 1972).

The total field in the crystal in terms of intensity is given by

$$I_g = D^2 = D_o^2\{1 + R^2 + 2RC \cos(2\pi \underline{g}.\underline{r})\} \qquad 1.38$$

A maximum intensity occurs when $\underline{g}.\underline{r} = n$ and a minimum intensity when $\underline{g}.\underline{r} = (2n + 1)/2$ where n is an integer. Therefore the nodes of the standing wave coincide with the atomic planes where photoelectric absorption is significant. The sign of R determines whether the maximum or minimum occurs at the atomic planes. When R is negative (branch 1) the wave has a

minimum at the atomic planes and vice versa when R is positive. For example in the 200 reflection in NaCℓ as the structure factor is positive χ_g is negative and thus R is negative. Therefore it is expected that the wavefield has a minimum at the atomic plane on branch 2 and a maximum at the atomic plane of branch 1 but experimentally it is not the case as shown in Figure 1.8. Similarly the peak in the bottom curve of Figure 1.6c is due to the elimination of the normal photoelectric absorption and the dip in the top curve occurs as the crystal is thin and little absorption was taking place.

1.3.2 Pendellosung Fringes

The phenomenon where interference effect occurs between two Bloch waves is termed Pendellosung. This effect is due to the difference in wavevector of the tie points associated with the Bloch waves. The intensity distribution of the diffracted and transmitted beam shows a periodic variation with crystal thickness. For a symmetric Laue case the boundary conditions given by equation 1.18 must be satisfied.

$$1 = D_{o_1} + D_{o_2} \qquad 1.39a$$

$$0 = D_{g_1} + D_{g_2} \qquad 1.39b$$

From equation 1.33 the amplitude ratio is given by

$$R_i = D_{g_i}/D_{o_i} = \eta \pm (1+\eta^2)^{\frac{1}{2}} \qquad 1.40$$

Defining β as

$$\eta = \cos\beta \qquad 1.41$$

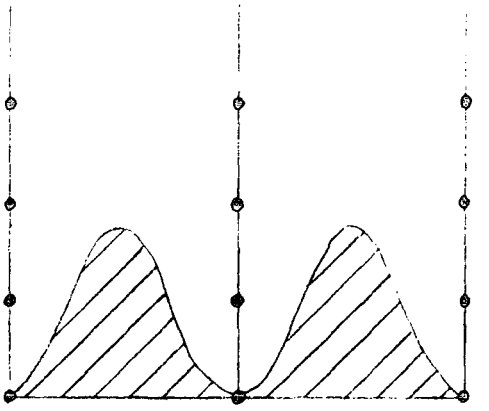

BRANCH 1

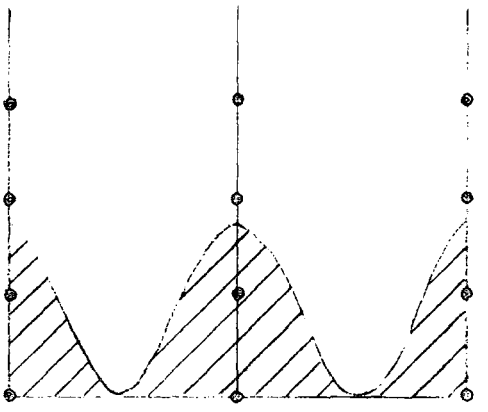

BRANCH 2

Fig. 1.8 Intensity of two wavefields at the exact Bragg condition in the 200 reflection of NaCl.

From equations 1.39 and 1.40

$$D_{o_1} = \cos^2\beta/2 \qquad D_{o_2} = \sin^2\beta/2 \qquad 1.42$$

$$D_{g_1} = -\sin\beta/2\ \cos\beta/2 \qquad D_{g_2} = \sin\beta/2\ \cos\beta/2$$

The amplitudes of the transmitted and diffracted beams emerging from the opposite surface at depth t are

$$D_o^e = D_{o_1}(t) + D_{o_2}(t) \qquad 1.43a$$

$$D_{g_i}(t) = D_{g_1}(t) + D_{g_2}(t) \qquad 1.43b$$

where

$$D_{o_i}(t) = D_{o_i} \exp(-2\pi i t \underline{K}_{o_i} . \hat{n}) \qquad 1.44a$$

$$D_{g_i}(t) = D_{g_i} \exp(-2\pi i t \underline{K}_{g_i} . \hat{n}) \qquad 1.44b$$

The intensity of the diffracted beam I_g is given by

$$I_g = D_g^{e*} D_g^e = D_{g_1}^2 + D_{g_2}^2 + 2D_{g_1} D_{g_2} \cos 2\pi t(K_{g_2} - K_{g_1}).\hat{n}$$

$$= \tfrac{1}{2} \sin^2\beta\{1 - \cos 2\pi t(K_{g_2} - K_{g_1}).\hat{n}\} \qquad 1.45$$

From Figures 1.3 and 1.5

$$(K_{g_1} - K_{g_2}).\hat{n} = 2z = \Lambda_o(1 + \eta^2)^{\frac{1}{2}} \qquad 1.46$$

$$\therefore \quad I_g = \frac{\sin^2[\pi\Lambda_o t(1+\eta^2)^{\frac{1}{2}}]}{1 + \eta^2} \qquad 1.47$$

Similarly the intensity of the transmitted beam I_o is

$$I_o = 1 - \frac{\sin^2[(\pi\Lambda_o t(1+\eta^2)^{\frac{1}{2}}]}{1 + \eta^2} \qquad 1.48$$

Equations 1.47 and 1.48 demonstrate the periodic behaviour of the diffracted and transmitted beam as a function of crystal thickness and their intensity are complementary with period $\{\Lambda_o(1 + \eta^2)^{\frac{1}{2}}\}^{-1}$. At the exact Bragg condition $\eta = o$ and the period has its maximum value of Λ_o^{-1} which is called the extinction distance ξ_g and is equal to the reciprocal of the dispersion surface diameter

$$\xi_g = \Lambda_o^{-1} = \frac{\pi V_c \cos\theta_B}{r_e \lambda C (F_g F_{\bar{g}})^{\frac{1}{2}}} \qquad 1.49$$

Away from the Bragg condition the effective extinction distance is

$$\xi_g' = \xi_g / (1 + \eta^2)^{\frac{1}{2}} \qquad 1.50$$

which decreases to zero as $\eta \to \infty$ implying that interference does not occur as only one wave is excited in the crystal.

Malgrange and Authier (1965) observed Pendellosung fringes from wedge-shaped crystal with complementary contrast in the diffracted and transmitted beam using a double crystal arrangement (Figure 1.9). Using a slit a pseudo plane wave was selected from the Borrmann fan which then excited just two tie points in the second crystal.

Pendellosung fringes have also been observed in Bragg geometry by Batterman and Hilderbrandt (1968) where they used an asymmetrically cut first crystal to increase the effective width of the incident beam and therefore approach the plane wave condition. Similar fringes have also been observed by Nakayama, Hashizume and Kohra (1970). Measurements of structure amplitudes have also been made using Pendellosung fringes (Kato and Lang 1959, Hattori et al. 1965, Kato and

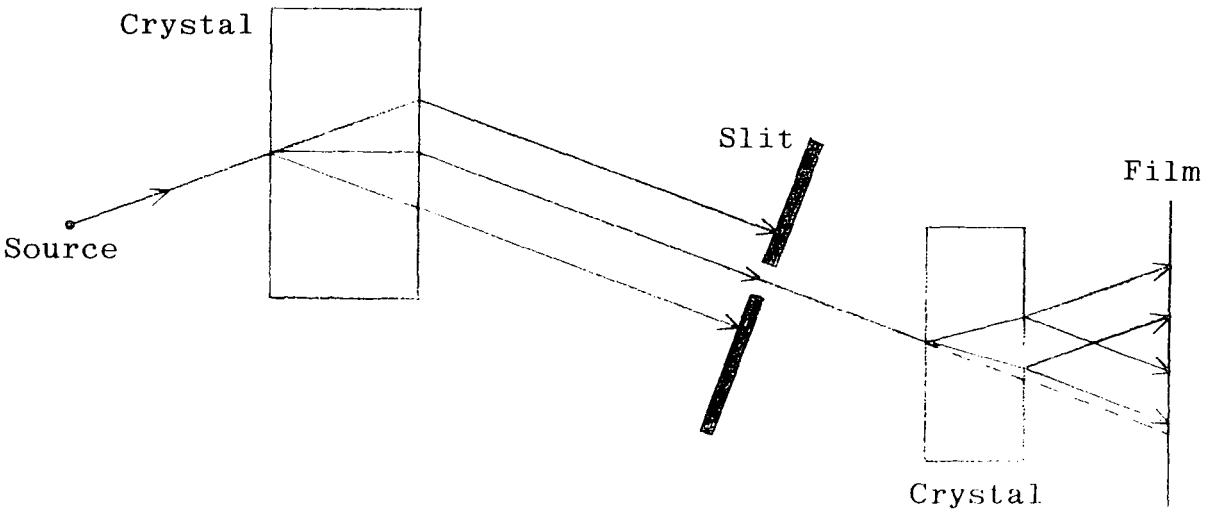

Fig. 1.9 Schematic diagram of the double crystal arrangement used by Authier and co-workers to obtain a pseudo-plane wave in the second crystal.

Tanemura 1967, Hart and Milne 1969 and Tanemura and Kato 1972).

1.3.3 Reflection Profiles

In the non-dispersive double crystal arrangement it was shown (Compton and Allison 1934, James 1948) that the variation of the doubly diffracted intensity $I(\beta)$ as the second crystal is rotated is given by the convolution of the reflection profiles $R_1(\theta)$ and $R_2(\theta)$ of the two crystals.

$$I(\beta) \int_{-\infty}^{\infty} R_1(\theta) R_2(\theta-\beta) d\beta \qquad 1.51$$

The reflection profile obtained characterizes the crystal in terms of rocking curve width and the integrated reflectivity. The single crystal reflection profile must be considered first before the convolution can be done. The detailed derivation from the equation of the dispersion surface with boundary conditions for the Laue and Bragg geometry was done by Zachariasen (1945) and Pinsker (1978).

Using the method used by Zachariasen the dispersion equation can be written, for the normal polarization state, as

$$(2\delta_o - \chi_o)(\frac{2}{b}\delta_o - \chi_o + \alpha) = \chi_g \chi_{\bar{g}} \qquad 1.52$$

and in terms of the amplitude ratio x as

$$x^2 + x\left|(1-b)\frac{\chi_o}{\chi_{\bar{g}}} + \frac{b}{\chi_{\bar{g}}}\alpha\right| - b\frac{\chi_g}{\chi_{\bar{g}}} = 0 \qquad 1.53$$

where $K_o^2 = k_o^2(1 + 2\delta_o)$

$$b = \frac{\gamma_o}{\gamma_g}$$

$$\alpha = 2(\theta_B - \theta)\sin 2\theta_B$$

γ_o and γ_g are the direction cosines of the incident and diffracted beams respectively.

The solutions of the quadratic equations 1.52 and 1.53 are

$$\delta_o = \frac{1}{2}\left[\chi_o - z \pm \sqrt{q + z^2}\right] \qquad 1.54$$

$$x = \frac{-z \pm \sqrt{q + z^2}}{\chi_{\bar{g}}}$$

where $$z = \frac{1-b}{2}\chi_o + \frac{b}{2}\alpha$$

and $$q = b\chi_g\chi_{\bar{g}}$$

As there are two possible values of δ_o and x, there are two internal incident waves and two diffracted waves. The general form of the incident beam inside the crystal is

$$\exp(i\omega t - i2\pi\underline{k}_e.\underline{r})[D_{o_1}\exp(-i\psi_1 t) + D_{o_2}\exp(-i\psi_2 t)] \qquad 1.56$$

and the diffracted beam is

$$\exp[i\omega t - i2\pi(\underline{k}_e + \underline{K}_g).\underline{r}]\,[x_1 D_{o_1}\exp(-i\psi_1 t) + x_2 D_{o_2}\exp(-i\psi_2 t)] \qquad 1.57$$

where $$\psi_1 = \frac{2\pi k_o \delta_{o_1}}{\gamma_o}$$

$$\psi_2 = \frac{2\pi k_o \delta_{o_2}}{\gamma_o}$$

$$t = \underline{n}.\underline{r}$$

1.3.3.a The Laue Case

Figure 1.10a shows the direction of the incident and diffracted waves. The amplitudes of the incident wave at the surface $\underline{n}.\underline{r} = 0$ are given by equations

$$D_{o_1} + D_{o_2} = D_i \qquad 1.58a$$

$$x_1 D_{o_1} + x_2 D_{o_2} = 0 \qquad 1.58b$$

From equations 1.58a and 1.58b

$$D_{o_1} = \frac{x_2}{x_2 - x_1} D_i \qquad 1.59$$

$$D_{o_2} = -\frac{x_1}{x_2 - x_1} D_i \qquad 1.60$$

If I_T and I_g are the intensities of the transmitted and diffracted beam and $t = t_o$ is the thickness of the crystal then using equations 1.56, 1.57 and 1.60

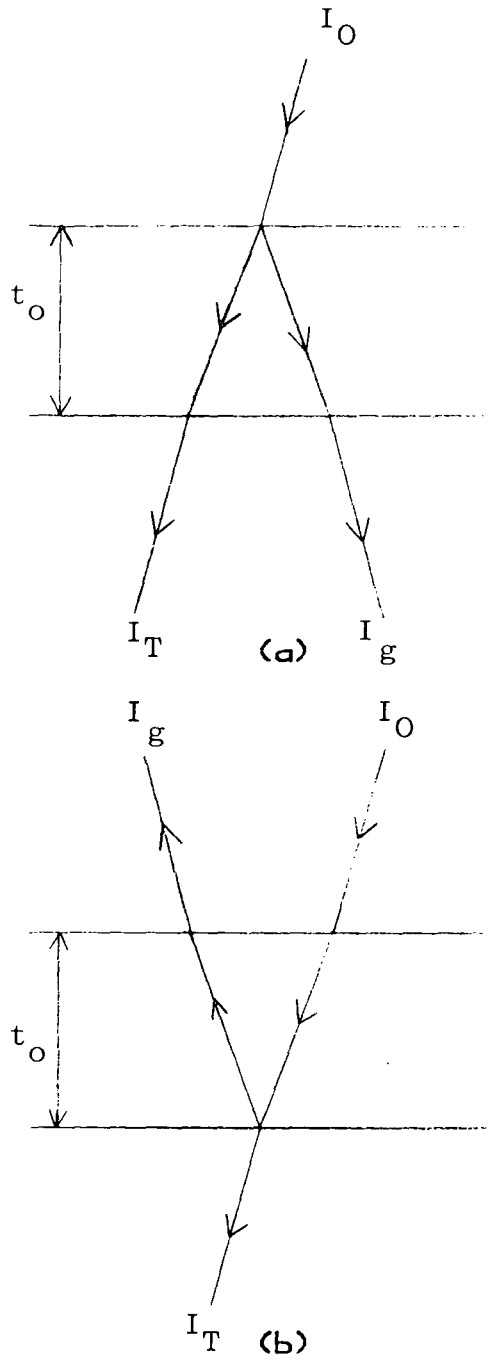

Fig. 1.10 Incident, transmitted and diffrracted beam directions in
(a) Laue case.
(b) Bragg case.

$$\frac{I_g}{I_o} = \left| \frac{x_1 x_2 (c_1 - c_2)}{x_2 - x_1} \right|^2 \qquad 1.61$$

$$\frac{I_T}{I_o} = \left| \frac{x_2 c_1 - x_1 c_2}{x_2 - x_1} \right|^2 \qquad 1.62$$

where $c_1 = \exp(-i\psi_1 t_o)$

$c_2 = \exp(-i\psi_2 t_o)$

Equation 1.61 can be written as

$$\frac{I_g}{I_o} = b^2 \, |\chi_g|^2 \, e^{-\mu_o t} \, \frac{\sin^2(av) + \sinh^2(a\omega)}{|q + z^2|} \qquad 1.63$$

where $v + i\omega \equiv \sqrt{q + z^2}$

$$a \equiv \frac{\pi k_o t_o}{\gamma_o}$$

and $$t \equiv \frac{1}{2}\left(\frac{1}{\gamma_o} + \frac{1}{\gamma_g} \right) t_o$$

The symmetric Laue case with zero absorption will be discussed in detail in section 6.4. The reflection curve is given by

$$R = \frac{\sin^2\left[\frac{\pi t_o}{\xi_g} \sqrt{1 + y^2} \right]}{1 + y^2} \qquad 1.64$$

(c.f. with equation 1.47)

From the equation it can be seen that the oscillation that occurs is a function of the crystal thickness and the extinction distance ξ_g. Figures 1.11a and 1.11b are examples of the reflection profiles for t_o/ξ_g equal to 5.16 and 5.66. As the Pendellosung distance is normally in the range of 1 to 100 μm, small variations in crystal thickness result in the average reflection curve as shown by the smooth curve in Figure 1.11 and is given by

$$R = \frac{1}{2(1 + y^2)} \qquad 1.65$$

When absorption is taking place the susceptibility is complex that is

$$\chi = \chi' + i\chi'' \qquad 1.66$$

χ' and χ'' are real and can be expanded as a Fourier series. Therefore the refractive index is

$$n = 1 + \tfrac{1}{2}\chi_o' + i\tfrac{1}{2}\chi_o'' \qquad 1.67$$

The imaginary part of equation 1.67 is related to the linear absorption coefficient μ_o

$$\mu_o = \frac{-2\pi}{\lambda}\chi_o'' \qquad 1.68$$

In the symmetric Laue case when $|\kappa| << 1$ equation 1.63 can be written as

$$\frac{I_g}{I_o} \approx e^{-\mu_o t/\gamma_o} \frac{\sin^2[A\sqrt{1 + y^2}]}{1 + y^2} + \frac{\sinh^2\left[\frac{\kappa A}{\sqrt{1 + y^2}}\right]}{1 + y^2} \qquad 1.69$$

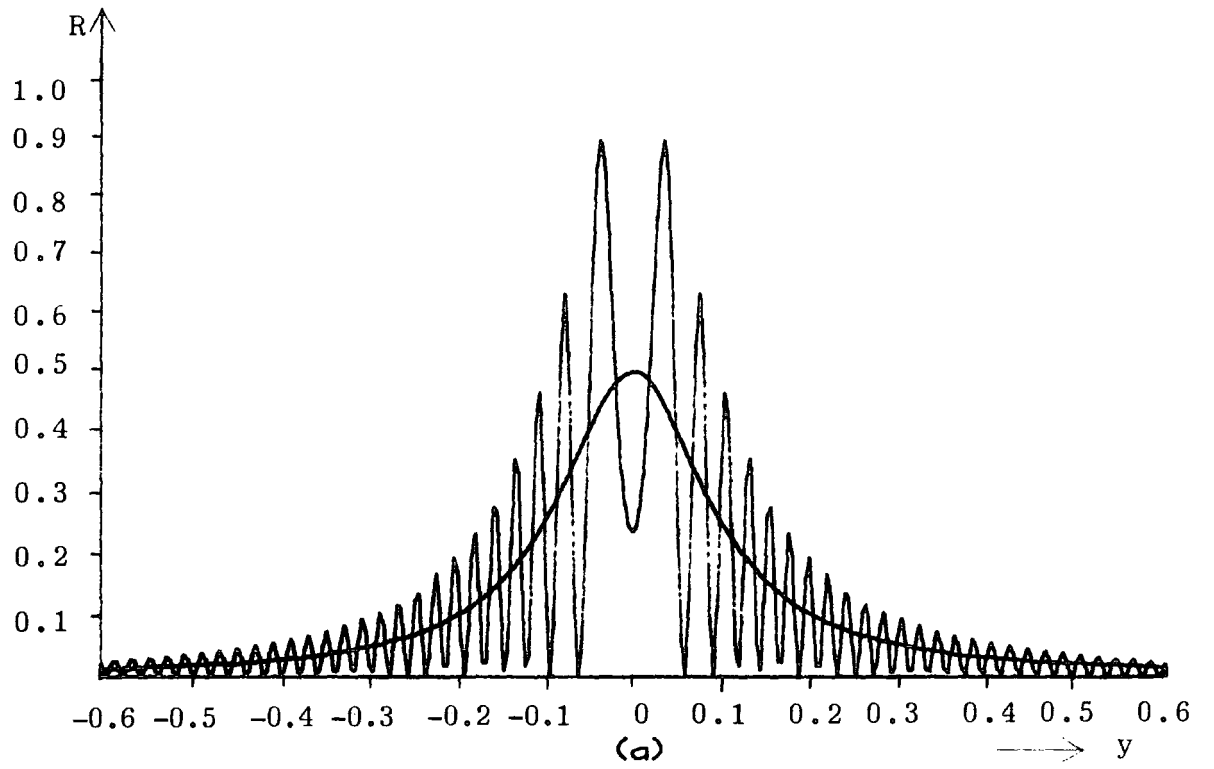

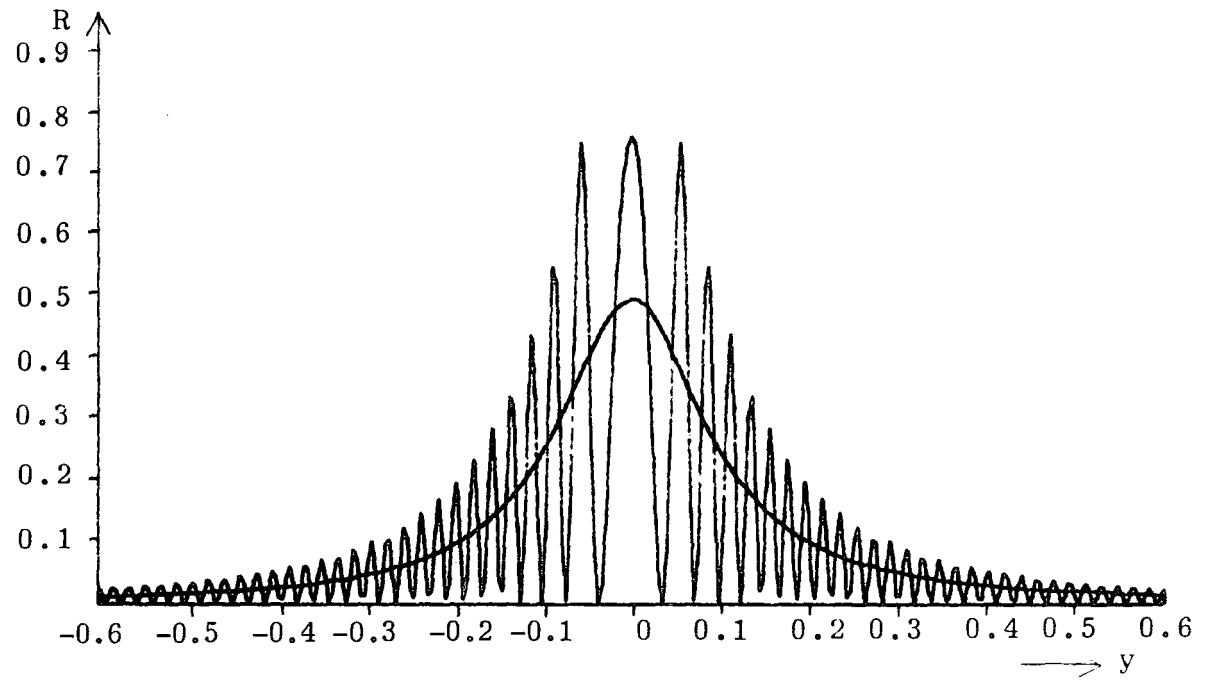

Fig. 1.11 Zero absorption plane wave reflection curves in the Laue case
(a) t/ξ_g=5.16
(b) t/ξ_g=5.66

where $$y = \frac{\frac{1-b}{2}\chi_o' + \frac{b}{2}\alpha}{K\,|\chi_g'|\sqrt{|b|}}$$

$$g = \frac{\frac{1-b}{2}\chi_o''}{K\,|\chi_g'|\sqrt{|b|}}$$

$$A = \pi k_o K\,|\chi_g'|\,\frac{t_o}{\sqrt{|\gamma_o\gamma_g|}}$$

$$\kappa \quad \frac{\chi_g''}{\chi_g'}$$

1.3.3.b The Bragg Case

As the diffracted beam emerges through the boundary $\underline{n}.\underline{r} = 0$ in the Bragg geometry (Figure 1.10b) b is negative. Therefore the boundary conditions are

$$D_{o_1} + D_{o_2} = D_i \qquad 1.70a$$

$$c_1x_1D_{o_1} + c_2x_2D_{o_2} = 0 \qquad 1.70b$$

Equations 1.70a and 1.70b give

$$D_{o_1} = \frac{c_2x_2}{c_2x_2 - c_1x_1} D_i \qquad 1.71$$

$$D_{o_2} = \frac{c_1x_1}{c_2x_2 - c_1x_1} Di \qquad 1.72$$

From equations 1.57, 1.71 and 1.72

$$\frac{I_g}{I_o} = \left| \frac{x_1 x_2 (c_1 - c_2)}{c_2 x_2 - c_1 x_1} \right|^2 \qquad 1.73$$

$$\frac{I_T}{I_o} = \left| \frac{c_1 c_2 (x_2 - x_1)}{c_2 x_2 - c_1 x_1} \right|^2 \qquad 1.74$$

In the simplified case of zero absorption and symmetrical reflection of thick crystals the reflection curve is

$$R = [1 - \sqrt{1 - y^{-2}}] \quad |y| > 1 \qquad 1.75$$

and the diffraction pattern is shown in Figure 1.12. The range of total reflection is given by

$$\Delta\theta_{\frac{1}{2}} = \frac{2}{g\xi_g} \qquad 1.76$$

Absorption cause the curve to become asymmetric as shown in Figure 1.13. The corresponding reflection curve for an absorbing thick crystal is

$$R = L - \sqrt{L^2 - (1 + 4\kappa^2)} \qquad 1.77$$

where $L \equiv \left| \sqrt{(-1+y^2-g^2)^2 + 4(gy-\kappa)^2} \right| + y^2 + g^2$

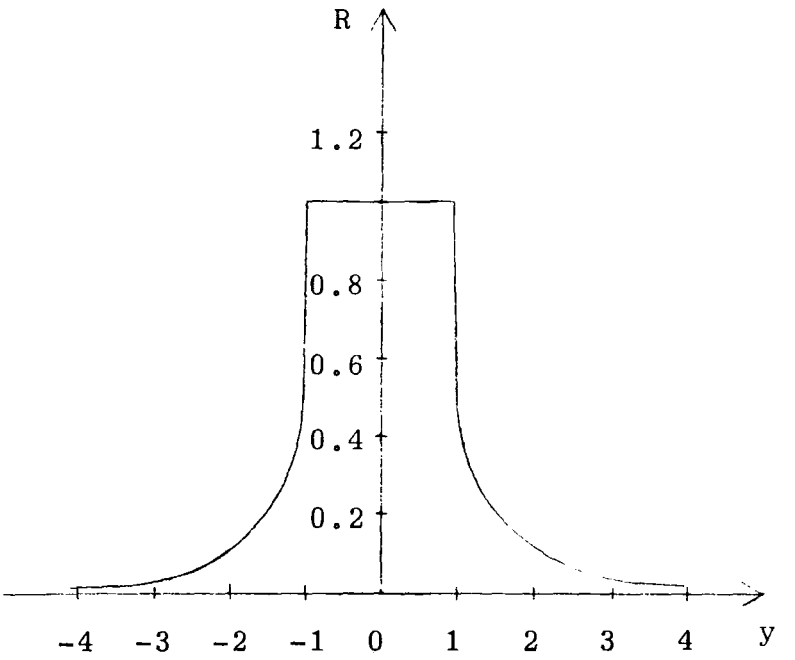

Fig. 1.12 Perfect crystal reflection curve with zero absorption in the Bragg case.

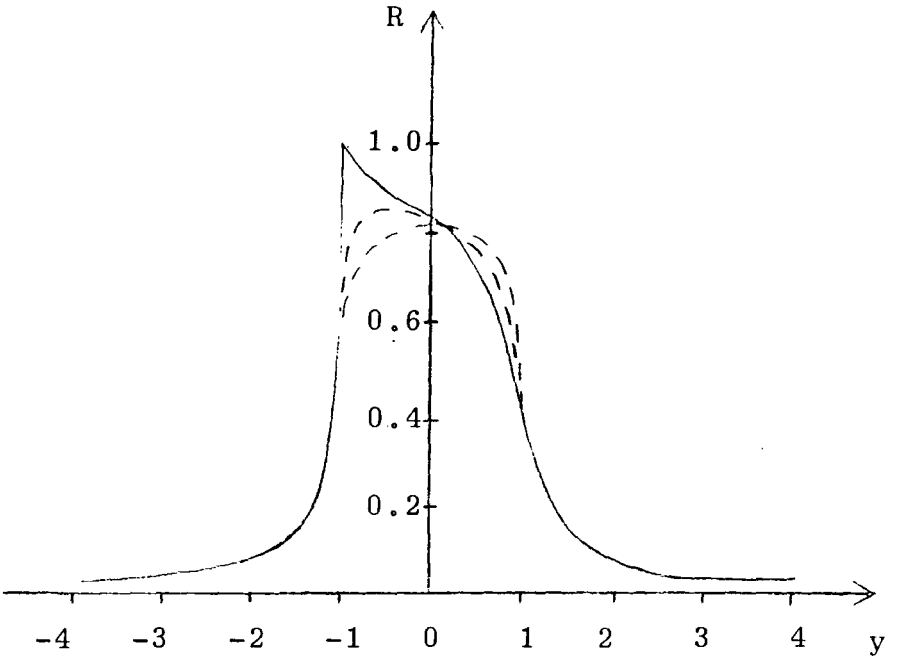

Fig. 1.13 Reflection curve of a thick absorbing crystal in the Bragg case.

CHAPTER 2

DOUBLE CRYSTAL DIFFRACTOMETRY

2.1 X-ray Diffraction Topography

X-ray diffraction topography is used primarily to study the distribution of individual dislocations in crystals. This method is non-destructive in nature and particularly useful for relatively perfect crystals. The imperfections may be regarded as a perturbations of the perfect crystal lattice which gives rise to local changes in diffracted X-ray intensities. The integrated intensity diffracted by a crystal orientated near the Bragg angle and the angular width of the Bragg peak in a rocking curve are strongly dependent on crystal perfection.

X-ray diffraction topography includes a variety of different techniques with varying geometry and resolution. Three commonly used techniques are the Berg-Barrett technique, the Lang technique and the double crystal technique. It is the transmission technique initiated by Lang (1958) which is most extensively used and which stimulated the growth of topography.

The schematic diagram of the technique is shown in Figure 2.1a. This technique is sensitive to both orientation and extinction contrast, with orientation sensitivity approximately equal to 5×10^{-4} radian. Here the beam from the X-ray tube is collimated by the slit system S_1 and passes through the crystal C which is orientated to satisfy the Bragg condition $2d \sin \theta_B = n\lambda$. The diffracted beam emerges at the

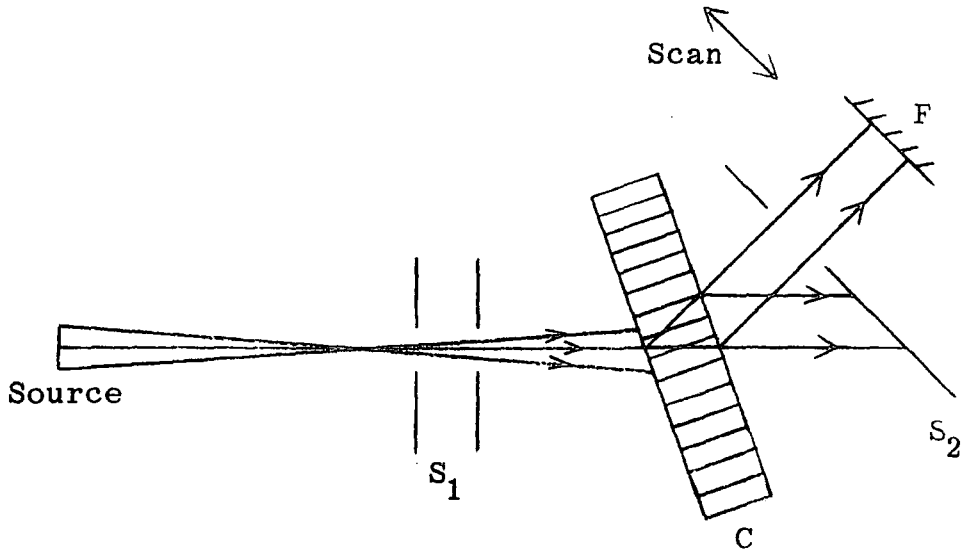

(a)

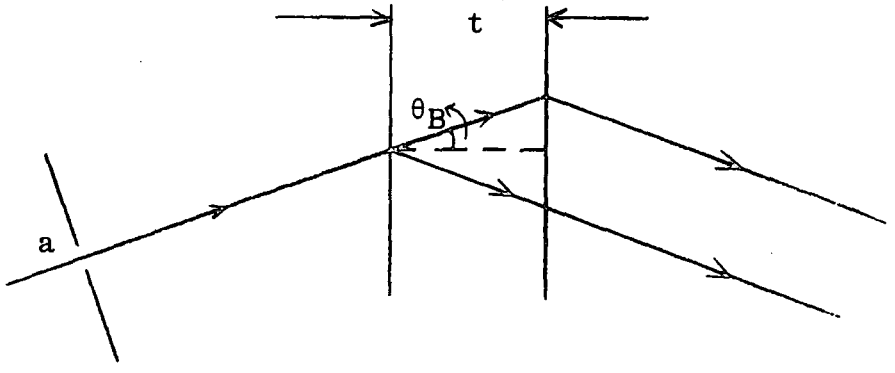

(b)

Fig. 2.1 (a) Lang's transmission technique. Section topographs correspond to the stationary situation, projection topographs are taken by scanning the crystal and film across the beam.
(b) The Bormann fan.

rear of the specimen, passes through the slit S_2 and is recorded on the photographic film F. The slit S_2 is used to remove the direct beam and the collimation is adjusted such that only diffraction from the $K\alpha_1$ line is possible at one crystal setting. $K\alpha_1$ is chosen due to its greater intensity, about twice the intensity of the $K\alpha_2$ line. If the incident beam is narrow compared with the base of the Bormann fan (Figure 2.1b), that is $a < 2t\sin\theta_B$ where t is the thickness of the crystal, a is the width of slit S_1 which defines the incident beam and θ_B is the Bragg angle, a section topograph is obtained which corresponds to the stationary situation. A projection topograph (Lang 1959) is obtained by translating the crystal and film together across the diffracted beam. Therefore the projection topograph is equivalent to the superposition of many section topographs. The maximum imperfection density at which individual imperfections are resolved is much lower in projection topographs but the projection topograph gives a picture of the overall distribution of imperfections in the crystal.

The Berg-Barrett method was first developed by Berg (1931) and later improved by Barrett (1945). The essential features of the reflection and transmission geometry are shown schematically in Figures 2.2a and 2.2b respectively. Using an extended source the single crystal is set to diffract the characteristic radiation from a chosen set of lattice planes. The position of the crystal is not critical due to the extended source used. Bragg reflections can still be detected within an angular range of 1^{o} and a wide rocking

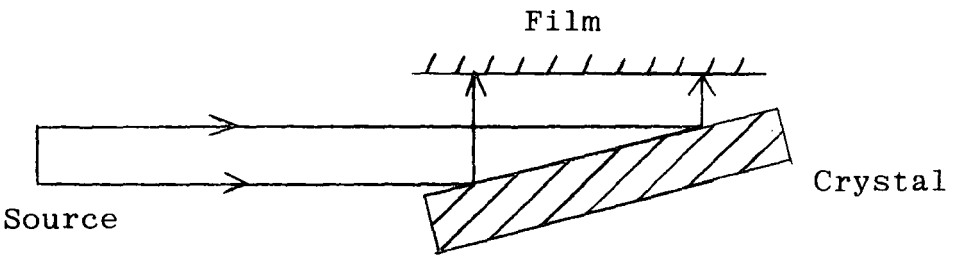

(a)

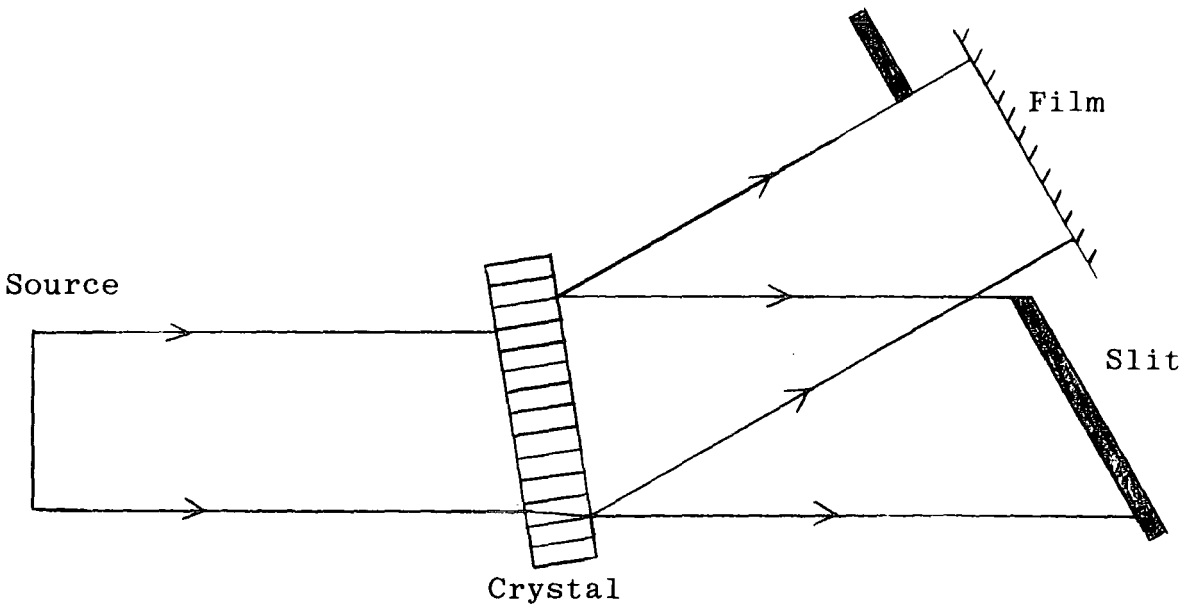

(b)

Fig. 2.2 (a) Berg-Barrett reflection geometry.
(b) Berg-Barrett transmission geometry.

curve is obtained. Conventionally the photographic plate is placed very close, (a few mm), to the specimen crystal to obtain high resolution as well as eliminating the double images due to the closely spaced $K\alpha_1$ and $K\alpha_2$ doublet.

The next technique which is becoming increasingly important is the double crystal method. X-ray double crystal topography was first performed independently by Bond and Andrus (1952) in a study of the surface of natural quartz, and Bonse and Kappler (1958) in detecting the strain fields of individual dislocations in germanium crystals. Although single crystal topography appears to be sensitive to slow variations of strain of the order of 1 part in 10^5, in actual situations it is insensitive to slow variations of lattice parameter. This is due to the large angular divergence of the incident beam as a result of which the diffracted intensity is equal to the integrated intensity. Double crystal topography has become increasingly important due to the availability of good nearly perfect single crystals.

2.2 Principle of Double Crystal Diffractometry

As the name implies double crystal topography and diffractometry utilizes two successive Bragg reflections. The schematic diagram of the arrangement is shown in Figure 2.3a for the symmetric (+,-) parallel setting. X-rays from target T are reflected at the Bragg angle by the reference crystal A to the specimen crystal B which is also orientated at the Bragg angle. The diffracted beam from the specimen is detected by a counter or recorded on the photographic

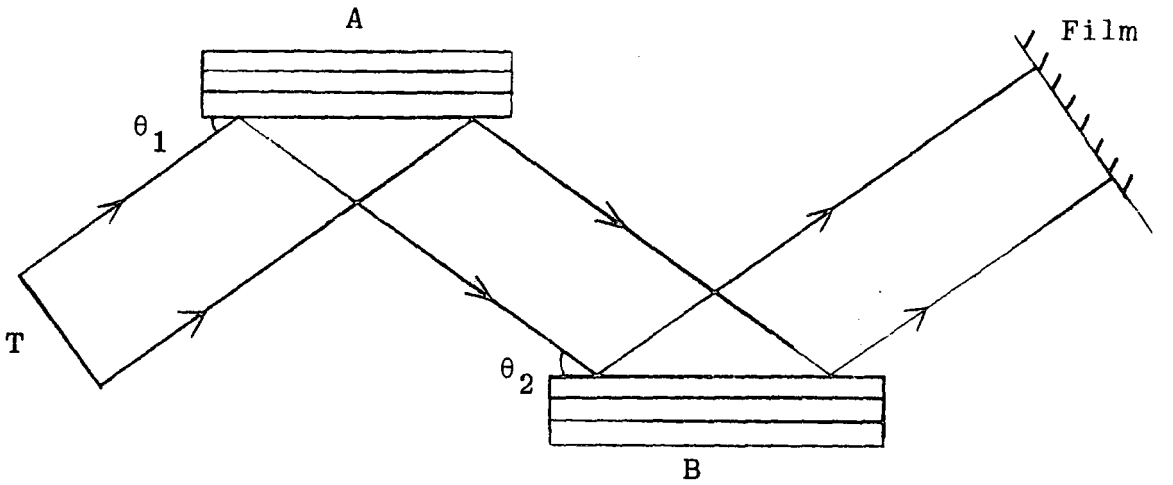

(a)

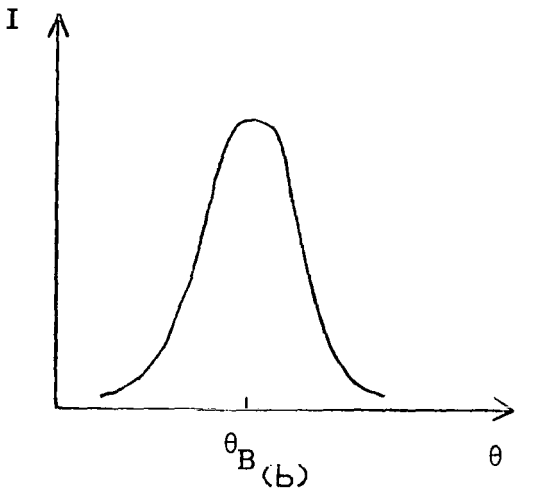

Fig. 2.3 (a) (+, −) parallel setting for the double crystal technique.

(b) rocking curve obtained when one of the crystals is rotated about the goniometer axis. The flank of the rocking curve is approximately linear.

emulsion. Alternatively a rocking curve can be recorded using an X-Y recorder by connecting the output of the detector to the Y-terminal and a signal proportional to the angular rotation of one of the crystals to the X-terminal. The term rocking curve refers to the variation in intensity as one crystal is rotated about an axis parallel to the goniometer axis (Figure 2.3b). The following is a quantitative analysis of the intensity reflected from crystal B as it is rotated through its reflecting range for the general case (Compton and Allison 1934, James 1948).

The horizontal divergence α of an incident beam is the angle made with its projection in a vertical plane containing the incident beam and the vertical divergence ϕ is the angle made with its projection on a horizontal plane containing the incident beam. Thus an incident beam may be characterized by three quantities (λ,α,ϕ) where λ is the wavelength.

Referring to Figures 2.4a, 2.4b and 2.5, the central beam XO in a horizontal plane is incident on the reference crystal A at a glancing angle θ (λ_o, n_A) where $\alpha = \phi = 0$ and λ_o is a characteristic wavelength in the incident beam corresponding to the centre of the spectrum or an absorption edge. This is referred to as the central ray, that is a ray passing through the centre of the slit system. If MO is the ray which defines a horizontal divergence α, the glancing angle of ray MO with the reference crystal is $\theta(\lambda_o, n_A) \pm \alpha$. α is given a positive value if the glancing angle of ray MO

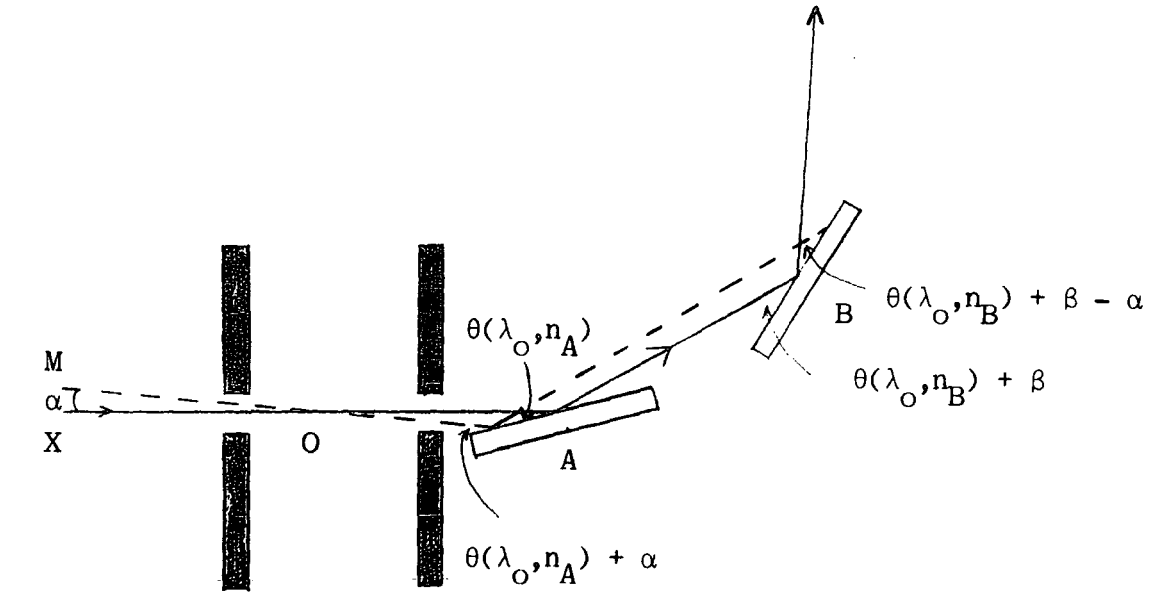

(a)

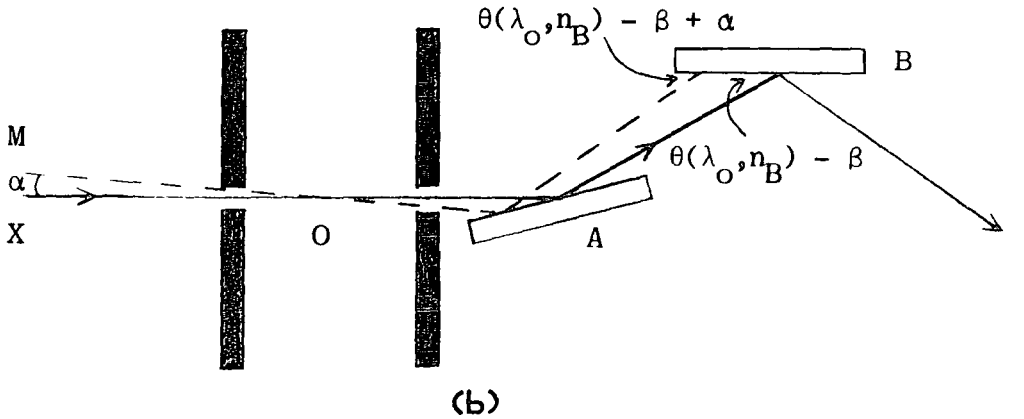

(b)

Fig. 2.4 (a) the (+, +) arrangement in the double crystal technique.
(b) the (+, −) arrangement in the double crystal technique.

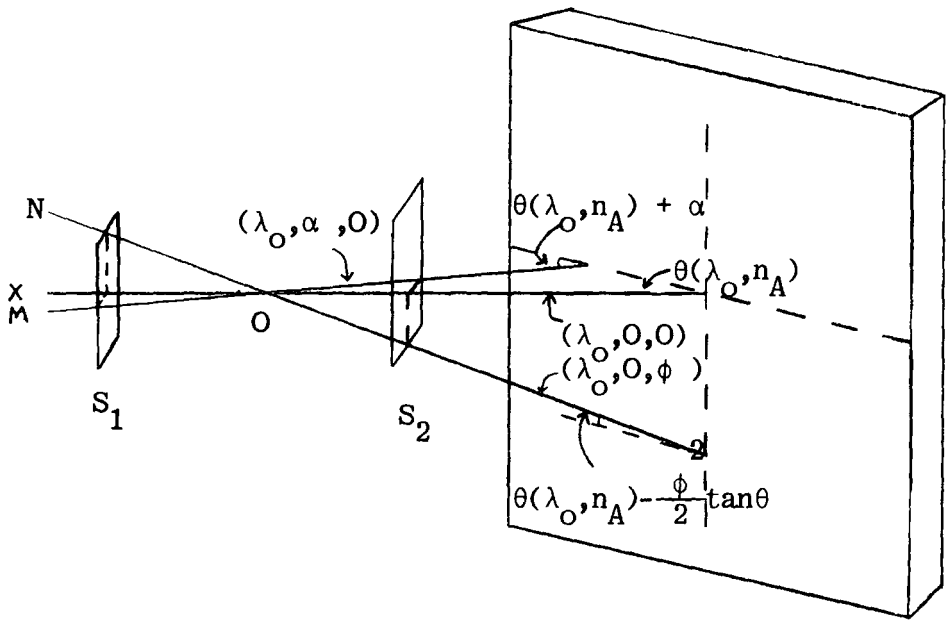

Fig. 2.5 The glancing angle made by the rays $(\lambda_o,\alpha,0)$ and $(\lambda_o,0,\phi)$ when the glancing angle of the central ray is $\theta(\lambda_o,n_A)$.

is greater than that of the central ray. In Figure 2.4a, 2.4b and 2.5 α is positive. If NO defines the vertical divergence ϕ and is small the glancing angle of the central ray is reduced by $\frac{1}{2}\phi^2 \tan\theta(\lambda_o, n_A)$. Therefore the glancing angle of any ray (λ,α,ϕ) on crystal A can be written as

$$\theta(\lambda_o, n_A) + \alpha - \tfrac{1}{2}\phi^2\tan\theta(\lambda_o, n_A) \qquad 2.1$$

$$\text{But } \theta(\lambda,n_A) = \theta(\lambda_o, n_A) + (\lambda-\lambda_o)\frac{\partial}{\partial\lambda_o}\theta(\lambda_o,n_A) \qquad 2.2$$

where $\theta(\lambda, n_A)$ is the reference angle corresponding to λ in the n_Ath order with $\alpha = \phi = 0$. Thus the deviation of the glancing angle as given by equation 2.1 from the reference angle as given by equation 2.2 is

$$\alpha - \tfrac{1}{2}\phi^2\tan\theta(\lambda_o, n_A) - (\lambda-\lambda_o)\frac{\partial}{\partial\lambda_o}\theta(\lambda_o, n_A) \qquad 2.3$$

The reflected intensity of ray (λ,α,ϕ) from crystal A will be very small if crystal A has a diffraction pattern approaching that of a perfect crystal with a deviation given by equation 2.3 of a few seconds of arc.

The intensity profile obtained when the specimen crystal B is rotated about the Bragg angle is a function of the angle of rotation β. The glancing angle made by ray (λ,α,ϕ) on crystal B after reflection from cyrstal A depends on the type of arrangement the diffractometer is operating. The two types of arrangement are shown in Figures 2.4a and 2.4b. Let the crystal B be placed at an angular deviation β from the position in which the glancing angle of the central ray is $\theta(\lambda_o, n_B)$. In the (+,+) setting the glancing angle made by the central ray is therefore $\theta(\lambda_o, n_B) + \beta$. Using a

similar argument the glancing angle made by the ray (λ,α,ϕ) is therefore

$$\theta(\lambda_o,\ n_B)+\beta-\alpha-\tfrac{1}{2}\phi^2\tan\theta(\lambda_o,n_B) \qquad 2.4$$

and its deviation from the angle $\theta(\lambda_o,n_B)$ is

$$\beta-\alpha-\tfrac{1}{2}\phi^2\tan\theta(\lambda_o,\ n_B)\ -\ (\lambda-\lambda_o)\ \frac{\partial}{\partial\lambda_o}\ \theta(\lambda_o,\ n_B) \qquad 2.5$$

In the (+,-) mode the glancing angle made by the central ray is $\theta(\lambda_o,\ n_B)-\beta$. The glancing angle of ray (λ,α,ϕ) is then

$$\theta(\lambda_o,\ n_B)-\beta\ +\ \alpha-\tfrac{1}{2}\phi^2\tan\theta(\lambda_o,n_B) \qquad 2.6$$

and the deviation from $\theta(\lambda,\ n_B)$ is

$$-\beta+\alpha-\tfrac{1}{2}\phi^2\tan\theta(\lambda_o,\ n_B)\ -\ (\lambda-\lambda_o)\ \frac{\partial}{\partial\lambda_o}\ \theta(\lambda_o,\ n_B) \qquad 2.7$$

In general the deviation of the glancing angle of the ray (λ,α,ϕ) on B from the ray $\theta(\lambda,\ n_B)$ is

$$\pm\beta\mp\alpha-\tfrac{1}{2}\phi^2\tan\theta(\lambda_o,n_B)\ -\ (\lambda-\lambda_o)\frac{\partial}{\partial\lambda_o}\theta(\lambda_o,\ n_B) \qquad 2.8$$

when the angular deviation of crystal B from the central ray $\theta(\lambda_o,\ n_B)$ is β. The upper sign is for the (+,+) setting and the lower sign is for the (+,-) setting.

To obtain the reflecting power from cyrstal B the power incident on A and reflected from cyrstal A has to be considered first. An element of the incident beam on A has a wavelength range between λ and $\lambda + d\lambda$ with a horizontal divergence between α and $\alpha + d\alpha$ and a vertical divergence in the range ϕ and $\phi + d\phi$. The power from this element of the incident beam can be written as

$$G(\alpha,\phi)J(\lambda-\lambda_o)d\alpha d\phi d\lambda$$

where J is the energy distribution of the incident spectrum and the function G is a term which takes care of the geometry of the instrument; that is the shape of the slits aperture, the distribution of intensity in the source etc.

The power reflected from crystal A when this element is incident on it is dependent on the deviation of the glancing angle on A given by equation 2.3 from the angle $\theta(\lambda, n_A)$. This is given by the single crystal diffraction function C and is a function of the deviation given by equation 2.3. Therefore the power in the elementary beam after reflection from crystal A is given by

$$G(\alpha,\phi)J(\lambda-\lambda_o)C_A[\alpha-\tfrac{1}{2}\phi^2\tan\theta(\lambda_o,n_A)-(\lambda-\lambda_o)\frac{\partial}{\partial\lambda_o}\theta(\lambda_o,n_A)]\,d\alpha d\lambda d\phi \qquad 2.9$$

Similarly the power reflected from crystal B is dependent on the deviation of the glancing angle on B from angle $\theta(\lambda, n_B)$ given by equation 2.8

$$G(\alpha,\phi)J(\lambda-\lambda_o)C_A[\alpha-\tfrac{1}{2}\phi^2\tan\theta(\lambda_o,n_A)-(\lambda-\lambda_o)\frac{\partial}{\partial\lambda_o}\theta(\lambda_o,n_A)]$$
$$\text{X } C_B[\pm\beta\mp\alpha-\tfrac{1}{2}\phi^2\tan\theta(\lambda_o,n_B)-(\lambda-\lambda_o)\frac{\lambda}{\partial\lambda_o}\theta(\lambda_o,n_B)]d\alpha d\lambda d\phi \qquad 2.10$$

The total intensity reflected from crystal B is obtained by integrating equation 2.10

$$P'(\beta) = \int_{-\phi_m}^{\phi_m}\int_{\lambda_{min}}^{\lambda_{max}}\int_{-\alpha_m}^{\alpha_m} G(\alpha,\phi)J(\lambda-\lambda_o)$$
$$C_A[\alpha-\tfrac{1}{2}\phi^2\tan\theta(\lambda_o,n_A)-(\lambda-\lambda_o)\frac{\partial}{\partial\lambda_o}\theta(\lambda_o,n_A)]$$
$$C_B[\pm\beta\mp\alpha-\tfrac{1}{2}\phi^2\tan\theta(\lambda_o,n_B)-(\lambda-\lambda_o)\frac{\partial}{\partial\lambda_o}\theta(\lambda_o,n_A)]d\alpha d\lambda d\phi \qquad 2.11$$

2.3 Dispersion for the Double Crystal Arrangement

The dispersion of the double crystal arrangement can be deduced from equation 2.11 by considering the limiting case in which the diffraction pattern of the two crystals are so narrow that no appreciable contribution to the function $P'(\beta)$ occurs except when the argument of both the C functions are zero, that is

$$\alpha - \tfrac{1}{2}\phi^2 \tan\theta(\lambda_o, n_A) - (\lambda - \lambda_o)\frac{\partial}{\partial \lambda_o}\theta(\lambda_o, n_A) = 0 \qquad 2.12$$

$$\pm\beta \mp \alpha - \tfrac{1}{2}\phi^2 \tan\theta(\lambda_o, n_B) - (\lambda - \lambda_o)\frac{\partial}{\partial \lambda_o}\theta(\lambda_o, n_B) = 0 \qquad 2.13$$

Eliminating α from equations 2.12 and 2.13 gives

$$\beta - \tfrac{1}{2}\phi^2\left[\tan(\lambda_o, n_A) \pm \tan\theta(\lambda_o, n_B)\right] - (\lambda - \lambda_o)\left[\frac{\partial\theta(\lambda_o, n_A)}{\partial\lambda_o} \pm \frac{\partial\theta(\lambda_o, n_B)}{\partial\lambda_o}\right] = 0 \qquad 2.14$$

Define $$D = \frac{\partial\theta(\lambda_o, n_A)}{\partial\lambda_o} \pm \frac{\partial\theta(\lambda_o, n_B)}{\partial\lambda_o} \qquad 2.15$$

where the upper sign is for (+,+) setting and the lower sign is for the (+,-) setting.

Differentiating Bragg's Law, $2d\sin\theta = n\lambda$ 2.16

gives $$2d\cos\theta\, d\theta = n\, d\lambda, \qquad 2.17$$

or

$$\frac{d\theta}{d\lambda} = \frac{n}{2d\cos\theta} \qquad 2.18$$

From equations 2.16 and 2.17

$$\frac{\tan\theta}{d\theta} = \frac{\lambda}{d\lambda}$$

or $$\frac{d\theta}{d\lambda} = \frac{\tan\theta}{\lambda} \qquad 2.19$$

Substituting equations 2.18 and 2.19 in equation 2.15 gives

$$D = \frac{n_A}{2d_1\cos\theta(\lambda_o, n_A)} \pm \frac{n_B}{2d_2\cos\theta(\lambda_o, n_B)} \qquad 2.20$$

or $$D = \frac{1}{\lambda_o}\left[\tan\theta(\lambda_o, n_A) \pm \tan\theta(\lambda_o, n_B)\right] \qquad 2.21$$

Substituting equations 2.20 and 2.21 in 2.14 yields

$$\beta - \tfrac{1}{2}\phi^2 D\lambda_o - (\lambda - \lambda_o)D = 0$$

or $$\beta = \tfrac{1}{2}D\lambda_o\phi^2 + D(\lambda - \lambda_o) \qquad 2.22$$

The dispersion of the double crystal arrangement when crystal B is rotated is defined as $\frac{d\beta}{d\lambda}$ and therefore from equation 2.22 is

$$\text{Dispersion} = \frac{d\beta}{d\lambda} = D \qquad 2.23$$

It is clearly seen from equation 2.23 that for the (+,-) parallel arrangement where the specimen and reference crystals are of the same substance and the same Bragg reflection are used, the dispersion will be equal to zero.

2.4 The (+,-) Parallel Setting

As derived in Section 2.3, the dispersion for the (+,-) parallel setting is zero. As the lattice constant and the diffracting planes are identical for both crystals, it is reasonable to assume that $C_A = C_B = C$ and $\theta(\lambda_o, n_A) = \theta$. Then equation 2.11 simplifies to

$$P'(\beta) = \int_{-\phi_m}^{\phi_m} \int_{\lambda_{min}}^{\lambda_{max}} \int_{-\alpha_m}^{\alpha_m} G(\alpha,\phi) J(\lambda-\lambda_o) C[\alpha - \tfrac{1}{2}\phi^2 \tan\theta - (\lambda-\lambda_o)(\partial\theta/\partial\lambda_o)] \; C[\alpha-\beta-\tfrac{1}{2}\phi^2\tan\theta-(\lambda-\lambda_o)(\partial\theta/\partial\lambda_o)]\, d\alpha\, d\lambda\, d\phi \qquad 2.24$$

For a perfect crystal, C is negligible except in the region where the argument of C is nearly zero and is of the order of a few seconds of arc. The function $G(\alpha,\phi)$ which is a property of the geometry of the instrument can be considered as a product of two functions, that is

$$G(\alpha,\phi) = G_1(\alpha)\, G_2(\phi) \qquad 2.25$$

where G_1 and G_2 are finite in the range of the maximum horizontal and vertical divergence of the incident beam respectively which is several minutes of arc wide. The term $\frac{1}{2}\phi^2\tan\theta$ is very small in most cases compared to the diffraction pattern width. Therefore from equation 2.24 α is approximately equal to $(\partial\theta/\partial\lambda_o)(\lambda-\lambda_o)$ for the first C function to be appreciable. Considering the argument of the second C function that is

$$\alpha-\beta-\tfrac{1}{2}\phi^2\tan\theta - (\lambda-\lambda_o)(\partial\theta/\partial\lambda_o)$$

If β is large, the value of $\alpha-(\partial\theta/\partial\lambda)(\lambda-\lambda_o)$ must be sufficiently large to have the argument small enough for the second C function to be appreciable. However, the first C function is then small if $\alpha-(\partial\theta/\partial\lambda)(\lambda-\lambda_o)$ is large and therefore the whole integral of equation 2.24 is negligible. Thus β must be small in order that both C functions are appreciable. This implies that in the (+,-) parallel arrangement the rocking curve width is very narrow and is of the order of the single crystal diffraction pattern.

Since α is close to the value $(\partial\theta/\partial\lambda_o)(\lambda-\lambda_o)$ the function $G_1(\alpha)$ can be written as

$$G_1(\alpha) = G[(\lambda-\lambda_o)(\partial\theta/\partial\lambda_o)] \qquad 2.26$$

Therefore the limit of the integral of equation 2.24 with respect to α can be extended to $\pm\infty$ as $2\alpha_m$ is of the order of minutes of arc and the integral is only appreciable for α of the order of a few arc seconds; that is if α approaches $\pm\alpha_m$, G_1 will approach zero and the contribution to $P'(\beta)$ is insignificant.

Then using the theorem where a function F is finite and continuous and a is a constant

$$\int_{-\infty}^{\infty} F(\alpha)d\alpha = \int_{-\infty}^{\infty} F(\alpha-a)d\alpha \qquad 2.27$$

Let $$\frac{2\delta\ell}{\sin 2\theta_B} = \alpha - \frac{\phi}{2}^2\tan\theta - \frac{\partial\theta}{\partial\Lambda}(\lambda-\lambda_o)$$

where ℓ is a variable, δ is the refractive index of the medium and θ_B is the Bragg angle. The argument of C is measured in

angular units of $2\delta/\sin 2\theta_B$ radians. Therefore equation 2.24 can be written as

$$P'(\beta) = \frac{2\delta}{\sin 2\theta_B} \int_{\lambda_o-(\partial\lambda_o/\partial\theta)\alpha_m}^{\lambda+(\partial\lambda_o/\partial\theta)\alpha_m} \int_{-\phi_m}^{\phi_m} G_1\left[\frac{\partial\theta}{\partial\lambda_o}(\lambda-\lambda_o)\right] G_2(\phi)\, d\phi\, d\lambda$$

$$\int_{-\infty}^{\infty} C(\ell)(\ell-\beta)\, d\ell \qquad 2.28$$

or $$P'(\beta) = K \int_{-\infty}^{\infty} C(\ell)C(\ell-\beta)\, d\ell \qquad 2.29$$

where the constant K is proportional to the power of the beam incident on crystal A. The normalised rocking curve $P(\beta)$ where

$$P(\beta) = \frac{P'(\beta)}{K \int_{-\infty}^{\infty} I'(\ell)\, d\ell} \qquad 2.30$$

is the ratio of the power reflected from crystal B to that incident on crystal B. The power incident on crystal B is obtained by integration of equation 2.9. For an unpolarized radiation $P(\beta)$ is written as a sum of two components, the σ polarization state and the π polarization state

$$P(\beta) = \frac{\int_{-\infty}^{\infty} I_\sigma(\ell) I_\sigma(\ell-\beta)\, d\ell + \int_{-\infty}^{\infty} I_\pi(\ell) I_\pi(\ell-\beta)\, d\ell}{\int_{-\infty}^{\infty} I_\sigma(\ell)\, d\ell + \int_{-\infty}^{\infty} I_\pi(\ell)\, d\ell} \qquad 2.31$$

where $C(\ell) = I(\ell)$ is the function for a perfect crystal. I_σ is the

component where the electric vector is perpendicular to the plane of incidence (the vertical plane) and I_π is the component where it lies in a plane parallel to the plane of incidence (the horizontal plane). The function I is the Darwin curve if absorption is negligible and if absorption is significant the Prinz curve is used.

The double crystal integrated reflecting power or the coefficient of reflection R is the area under the curve $P(\beta)$ if β is in radians.

$$R = \int_{-\infty}^{\infty} P(\beta)d\beta$$

$$R = \frac{2\delta}{\sin 2\theta_B} \frac{\int_{-\infty}^{\infty}\int_{-\infty}^{\infty} I_\sigma(\ell)I_\sigma(\ell-\beta)d\ell d\beta + \int_{-\infty}^{\infty}\int_{-\infty}^{\infty} I_\pi(\ell)I_\pi(\ell-\beta)d\ell d\beta}{\int_{-\infty}^{\infty} I_\sigma(\ell)d\ell + \int_{-\infty}^{\infty} I_\pi(\ell)d\ell} \qquad 2.32$$

where ℓ and β are measured in units of $2\delta/\sin 2\theta_B$.

Let $\gamma = \ell-\beta$, $d\gamma = -d\beta$. Then

$$\int_{-\infty}^{\infty}\int_{-\infty}^{\infty} I_\sigma(\ell)I_\sigma(\ell-\beta)d\ell d\beta = \int_{-\infty}^{\infty}\int_{-\infty}^{\infty} I_\sigma(\ell)I_\sigma(\gamma)d\ell(-d\gamma)$$

$$= \int_{-\infty}^{\infty}\int_{-\infty}^{\infty} I_\sigma(\ell)I_\sigma(\gamma)d\ell d\gamma$$

$$= \left[\int_{-\infty}^{\infty} I(\ell)d\ell\right]^2$$

$$\therefore R = \frac{2\delta}{\sin 2\theta_B} \frac{\left[\int_{-\infty}^{\infty} I_\sigma(\ell)d\ell\right]^2 + \left[\int_{-\infty}^{\infty} I_\pi(\ell)d\ell\right]^2}{\int_{-\infty}^{\infty} I_\sigma(\ell)d\ell + \int_{-\infty}^{\infty} I_\pi(\ell)d\ell} \qquad 2.33$$

For the Darwin approximation $\int_{\infty}^{\infty} I_\pi{}^D(\ell)d\ell = \cos 2\theta_B \int_{-\infty}^{\infty} I_\sigma{}^D(\ell)d\ell$

$$R = \frac{2\delta}{\sin 2\theta_B} \frac{1 + \cos^2 2\theta_B}{1 + \cos 2\theta_B} \int_{-\infty}^{\infty} I_\sigma^D(\ell)d\ell$$

$$= \frac{2(1 + \cos^2 2\theta_B)}{(1 + \cos 2\theta_B)^2} R_c \qquad 2.34$$

where R_c is the single crystal coefficient of reflection. The percent reflection P(O) is the ratio of the maximum value of $P(\beta)$ to that incident on B.

2.5 Du Mond Diagram

In the double crystal arrangement the X-rays diffracted successively by the two crystals can be easily understood by reference to the Du Mond diagram (Du Mond 1937). The following is a discussion of the three different geometries for the symmetric case that is the non-dispersive (+,-) parallel setting, the (+,-) non-parallel setting and the (+,+) setting.

2.5.1 The (+,-) parallel setting

In the (+,-) parallel setting a diffracted beam can only be detected if the diffracting planes of both crystals are exactly parallel. Essentially this requires that the two crystals are of the same material in which the same order of reflection is used.

The Du Mond diagram in Figure 2.6a is a graphical representation of Bragg's law where the curves B_1 and B_2 represent the respective diffraction conditions for the reference and specimen crystals. The width ω of each curve is the angular spread of the beam diffracted from each crystal.

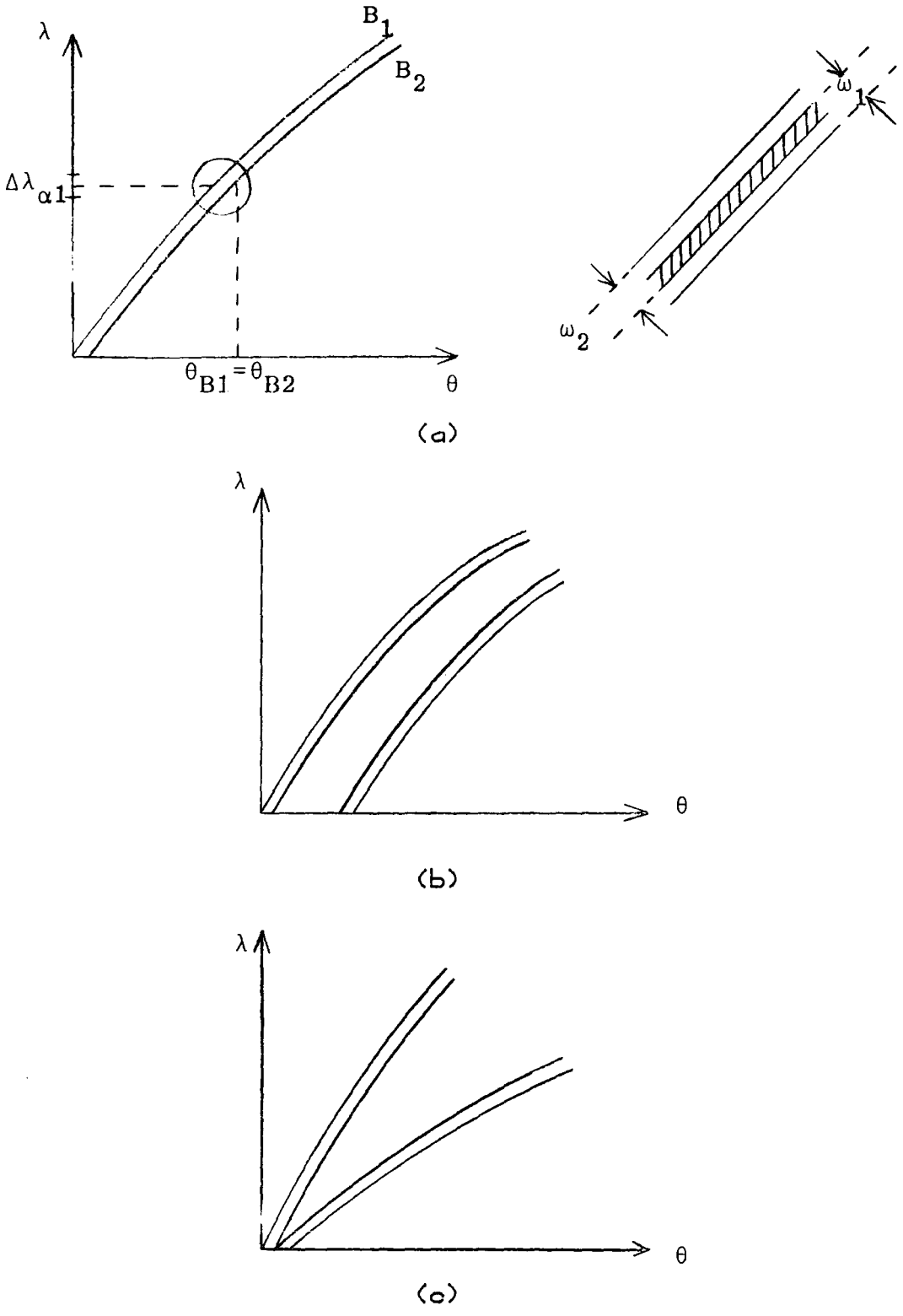

Fig. 2.6 (a) Du Mond diagram for two perfect crystals in the (+,−) parallel setting.

(b) Du Mond diagram corresponding to local rotation of the lattice in the second crystal.

(c) Du Mond diagram corresponding to local dilation in the second crystal.

As the diffracting planes are parallel and equispaced the two curve bands overlap for all values of (λ,θ) satisfying the Bragg condition unless limited by a slit system. This overlapping region as shown by the expanded view in Figure 2.6a also represents the X-ray diffracted simultaneously from the two crystals which corresponds to the perfect crystal reflecting range convoluted with that of the second crystal and is very narrow, maybe as low as 0.1 arc second.

As explained by the Du Mond diagrams in Figures 2.6b and c the (+,-) parallel setting is very sensitive to local misorientation and distortion of the order of a few arc seconds. The curve bands are misplaced and no overlapping occurs for any wavelength resulting in no diffracted intensity recorded.

2.5.2 The (+,-) non-parallel setting

In the (+,-) non-parallel arrangement (Figure 2.7a) the lattice constant and or the diffracting planes of both crystals are different and when Bragg condition is satisfied by both crystals their planes are not parallel. The intersection of the curves B_1 and B_2 as shown by the Du Mond diagram in Figure 2.7b represent the exact Bragg condition $2d\sin\theta_B = \lambda$ where X-rays are diffracted simultaneously from both crystals. This is indicated by the shaded region in the expanded view of the intersection of B_1 and B_2 (Figure 2.7c). The shaded region will move along the curve B_1 if there is local distortion, that is change in orientation and spacing of the diffracting planes. The intensity from the distorted region is still

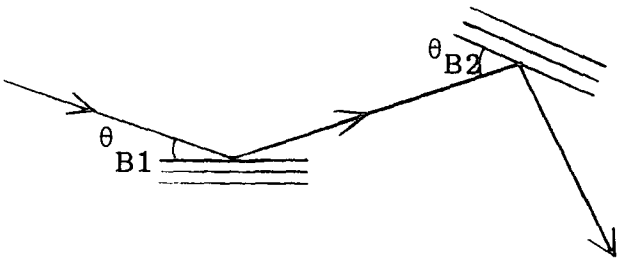

(a)

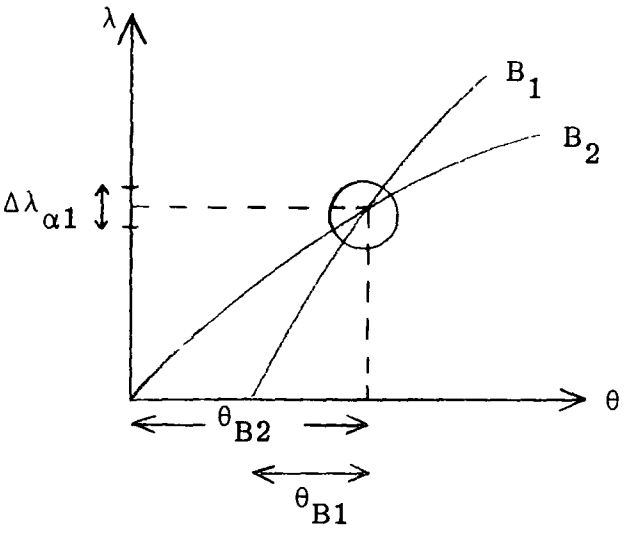

(b)

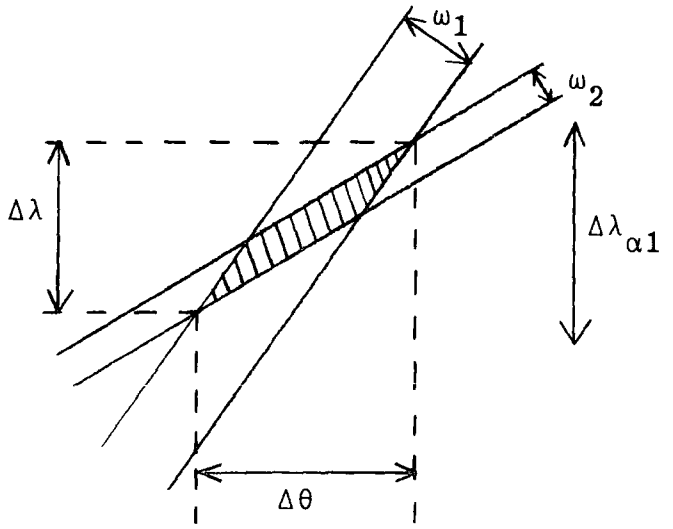

(c)

Fig. 2.7 (a) (+, −) non-parallel arrangement.
(b) Correeponding Du Mond diagram.
(c) Exploded view of the intereeotion of the ourve B_1 and B_2.

strong if it is within the natural line width $\Delta\lambda_{\alpha_1}$ of the characteristic line. Thus the angular range at which diffraction can take place is of the order of a few minutes of arc.

The wavelength spread $\Delta\lambda$ is approximately given by (Kohra et al. 1970).

$$\Delta\lambda = \frac{\lambda(\omega_1 + \omega_2)}{|\tan\theta_{B_1} - \tan\theta_{B_2}|}$$

and the angular spread is given by

$$\Delta\theta = \frac{\omega_1 \tan\theta_{B_1} + \omega_2 \tan\theta_{B_2}}{|\tan\theta_{B_1} - \tan\theta_{B_2}|}$$

where the subscripts 1 and 2 refer to the reference and sample crystal respectively, ω is the angular spread of the beam diffracted from the crystal and θ is the Bragg angle. Although this setting is non-dispersive in wavelength it is angular dispersive and the images formed by different wavelengths are formed at different positions on the photographic plate. Lattice parameter variation of 1 part in 10^5 can still be detected if a highly perfect reference crystal is used whose d is nearly equal to that of the sample crystal.

2.5.3 The (+,+) setting

The main difference between the arrangements of the (+,+) setting and the dispersive and non-dispersive (+,-) settings is that the incident beam on the reference crystal and the diffracted beam from the sample crystal in the (+,+)

setting (Figure 2.8a) are on the same side of the beam passing between the two crystals, while they lie on opposite sides in the other two settings. Therefore the lattice constant for the reference and sample crystals can either be different or identical. The corresponding Du Mond diagram is shown in Figures 2.8b and c. Similar to the (+,-) non-parallel setting it is angular dispersive, thus a range of wavelengths diffract at any setting and large misorientation can be tolerated without loss in intensity if the range of wavelength diffracted is within the natural line width of the characteristic radiation. Using the same notation as in the (+,-) non-parallel setting, the wavelength spread $\Delta\lambda$ and the angular spread $\Delta\theta$ are given by

$$\Delta\lambda = \frac{\lambda(\omega_1 + \omega_2)}{\tan\theta_{B_1} + \tan\theta_{B_2}}$$

and

$$\Delta\theta \quad \frac{\omega_1 \tan\theta_{B_1} + \omega_2 \tan\theta_{B_2}}{\tan\theta_{B_1} + \tan\theta_{B_2}}$$

This setting has been studied and developed by Kohra and co-workers (Kohra, Hashizume and Yoshimura, 1970; Nakayama, Hashizume, Miyoshi, Kikuta and Kohra, 1973).

2.6 Effect of Lattice Tilt on Rocking Curve Full Width at Half Height Maximum.

The rocking curve FWHM is a minimum if the diffracting planes of the reference and sample crystal are exactly parallel in the case of the (+,-) parallel setting or the angle the diffracting planes made with the vertical is zero for the

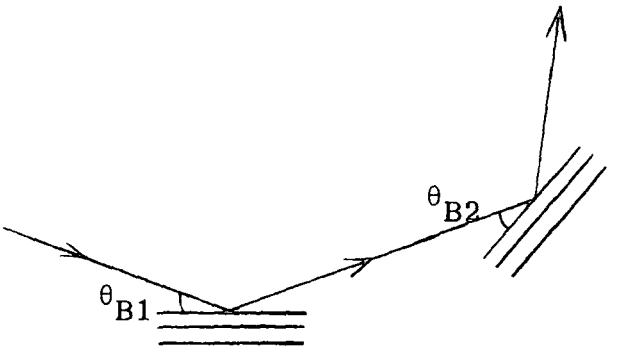

(a)

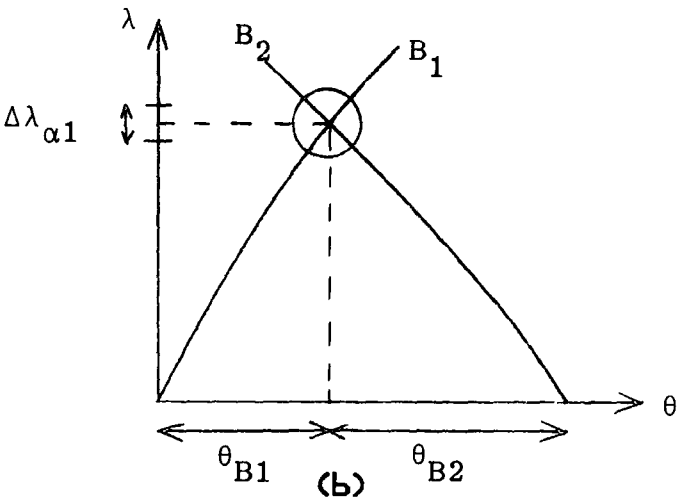

(b)

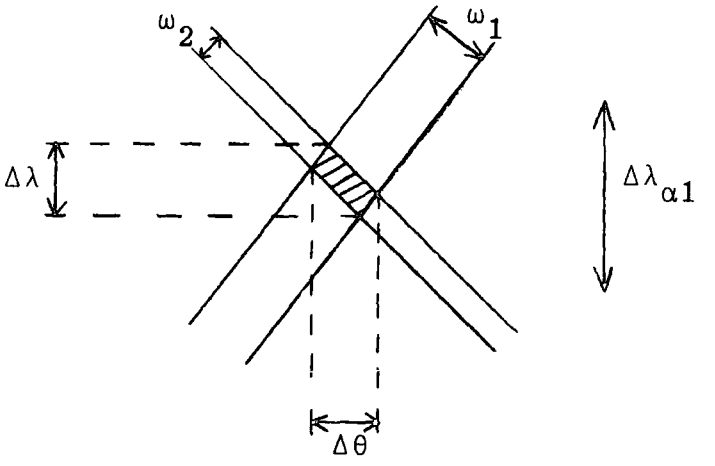

(c)

Fig. 2.8 (a) (+, +) setting.
(b) Correesponding Du Mond diagram.
(c) Exploded view of the intereection of ourve B_1 and B_2.

(+,+) setting.

It is easiest to obtain the relationship between broadening of rocking curve with lattice tilt by using vector equations (Schwarzchild 1928). Referring to Figure 2.9, AB and CD are the reflecting planes of the first and second crystal respectively. The z-axis which is perpendicular to both the x and y-axes is perpendicular to the plane of Figure 2.9 and coming out of the paper. The unit vectors $\underline{r}$ and $\underline{R}$ are in the direction of the incident beam and the first reflected beam respectively. The vectors $\underline{n}_1$ and $\underline{n}_2$ are unit vectors perpendicular to the reflecting surfaces. The Bragg angle for the first reflection is θ_1 and is the angle between AB and the x-axis. The corresponding Bragg angle for the reflection from the second crystal is equal to θ_2 and is the angle between EF and CD. ω is the angle between the horizontal projection of $\underline{r}$ and the x-axis and ε is the angle between the horizontal projection of $\underline{R}$ and EF. The angles ψ, δ_1 and δ_2 are the angles between $\underline{r}$, $\underline{n}_1$ and $\underline{n}_2$ and its horizontal projection respectively.

The following equations 2.35, 2.36 and 2.37 satisfy the Bragg condition for reflection from the first and second crystal where p_1 and p_2 are the order for the first and second reflection respectively, λ is the wavelength and d is the lattice constant.

$$\underline{r}.\underline{n}_1 = rn_1 \cos (90 + \theta_1) = -\sin \theta_1$$

$$\underline{r}.\underline{n}_1 = -\sin \theta_1 = -\frac{p_1\lambda}{2d} \qquad 2.35$$

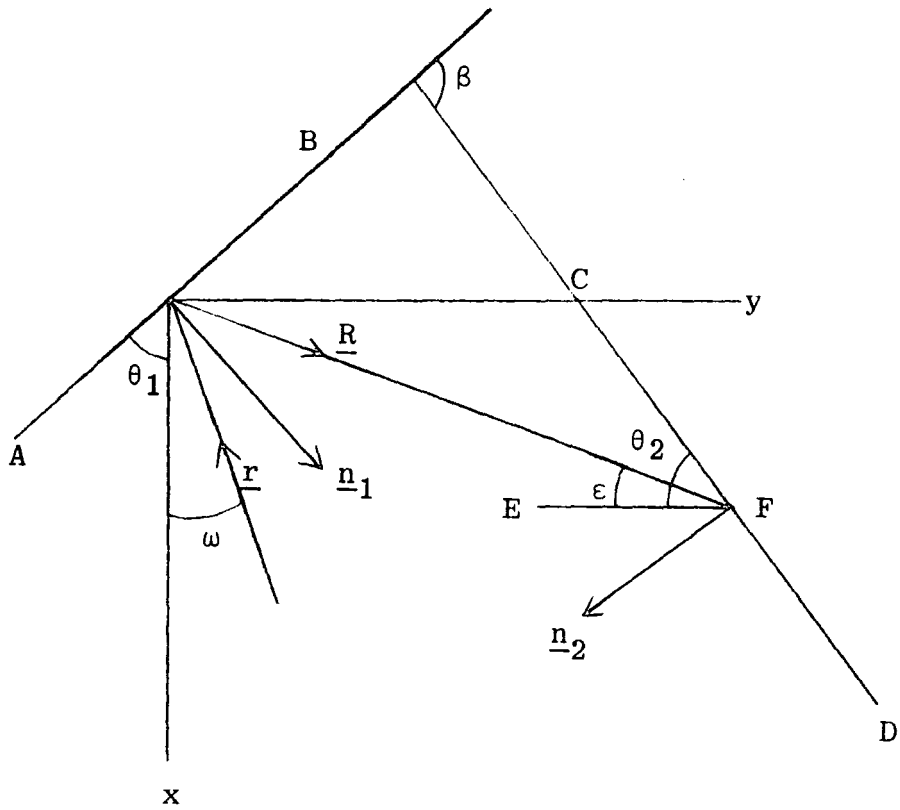

Fig. 2.9 Traces on the xy plane of two Bragg reflectors at an angle β. $\underline{n}_1$ and $\underline{n}_2$ are unit vectors perpendicular to the reflecting surfaces. $\underline{r}$ and $\underline{R}$ are unit vectors in the direction of incidence and first reflection respectively.

$$\underline{R}.\underline{n}_1 = Rn_1 \cos (90 - \theta_1) = \sin \theta_1$$

$$\therefore \underline{r}.\underline{n}_1 = -\underline{R}.\underline{n}_1 \qquad 2.36$$

$$\underline{r} \times \underline{n}_1 = rn_1 \sin (90 + \theta_1) = \cos \theta_1$$

$$\underline{R} \times \underline{n}_1 = Rn_1 \sin (90 - \theta_1) = \cos \theta_1$$

$$\therefore \underline{r} \times \underline{n}_1 = \underline{R} \times \underline{n}_1 \qquad 2.37$$

$$\underline{R}.\underline{n}_2 = Rn_2 \cos (90 + \theta_2) = -\sin \theta_2$$

$$\underline{R}.\underline{n}_2 = -\sin \theta_2 = \frac{-p_2\lambda}{2d} = \frac{p_2}{p_1} \underline{r}.\underline{n}_1 \qquad 2.38$$

Taking the cross product of $\underline{n}_1$ with equation 2.37 and substituting equation 2.36 gives

$$\underline{R} = \underline{r} - 2\underline{r} \cdot \underline{n}_1 \underline{n}_1 \qquad 2.39$$

Taking the dot product of $\underline{n}_2$ with equation 2.39 and substituting equation 2.38 gives

$$p_1\underline{r} \cdot \underline{n}_2 - 2p_1 \underline{r} \cdot \underline{n}_1 \underline{n}_1 \cdot \underline{n}_2 = p_2 \underline{r} \cdot \underline{n}_1 \qquad 2.40$$

Equations 2.35 and 2.40 are the vector equations for the condition of double reflection. Rewriting equations 2.35 and 2.40 in terms of the direction coordinates and neglecting the second order powers of θ_1 and θ_2, yields

$$r_x = -\cos \psi \cos \omega$$
$$r_y = -\cos \psi \sin \omega$$
$$r_z = -\sin \psi \qquad 2.41$$

$$n_{1x} = \cos \delta_1 \cos (90 - \theta_1) = \sin \theta_1$$
$$n_{1y} = \cos \delta_1 \sin (90 - \theta_1) = \cos \theta_1$$
$$n_{1z} = \sin \delta_1 \qquad 2.42$$

$$n_{2x} = \cos\delta_2 \sin(180 - \theta_1 - \beta) = \sin(\theta_1 + \beta)$$
$$n_{2y} = -\cos\delta_2 \cos(180 - \theta_1 - \beta) = \cos(\theta_1 + \beta) \qquad 2.43$$
$$n_{2z} = \sin\delta_2 = \delta_2$$

Substituting equations 2.41, 2.42 and 2.43 in equation 2.40 results in

$$p_1\underline{r}.\underline{n}_2 = p_1[-\cos\psi\cos\omega\sin(\theta_1+\beta) - \cos\psi\sin\omega\cos(\theta_1+\beta) - \delta_2\sin\psi]$$
$$= -p_1\{\cos\psi[\cos\omega\sin(\theta_1+\beta) + \sin\omega\cos(\theta_1+\beta)] + \delta_2\sin\psi\}$$
$$= -p_1[\cos\psi\sin(\omega+\theta_1+\beta) + \delta_2\sin\psi]$$
$$2p_1\underline{r}.\underline{n}_1\underline{n}_1.\underline{n}_2 = 2p_1(-\sin\theta_1)[\sin\theta_1\sin(\theta_1+\beta)+\cos\theta_1\cos(\theta_1+\beta)+\delta_1\delta_2]$$
$$= -2p_1\sin\theta_1\cos(\beta+\delta_1\delta_2)$$

However,

$$p_2\underline{r}\cdot\underline{n}_1 = -p_2\sin\theta_1$$

$$\therefore -p_1[\cos\psi\sin(\omega+\theta_1+\beta)+\delta_2\sin\psi]+2p_1\sin\theta_1\cos(\beta+\delta_1\delta_2) = p_2\sin\delta_1$$

or,

$$p_1\cos\psi\sin(\omega+\theta_1+\beta)+p_1\delta_2\sin\psi-2p_1\sin\theta_1\cos(\beta+\delta_1\delta_2) = p_2\sin\theta_1 \qquad 2.44$$

Substituting equations 2.41 and 2.42 in equation 2.35 gives

$$-\cos\psi\cos\omega\sin\theta_1-\cos\psi\sin\omega\cos\theta_1-\delta_1\sin\psi = -\sin\theta_1$$
$$\cos\psi\sin(\omega + \theta_1) = \sin\theta_1 - \delta_1\sin\psi \qquad 2.45$$

On squaring equation 2.45 we obtain

$$\cos^2\psi \sin^2(\omega + \theta_1) = (\sin\theta_1 - \delta_1\sin\psi)^2$$

$$\cos^2\psi[1-\cos^2(\omega+\theta_1)] = \sin^2\theta_1 - 2\delta_1\sin\theta_1\sin\psi + \delta_1{}^2\sin^2\psi$$

$$\cos^2\psi \cos^2(\omega + \delta_1) = \cos^2\psi + 2\delta_1\sin\theta_1\sin\psi - \sin^2\theta_1$$

$$\cos\psi\cos(\omega + \theta_1) = (\cos^2\psi + 2\delta_1\sin\theta_1\sin\psi - \sin^2\theta_1)^{\frac{1}{2}}$$

2.46

Substituting equations 2.45 and 2.46 in equation 2.44 and noting the identity $\sin(\omega+\theta_1+\beta) = \sin\beta\cos(\omega+\theta_1)+\cos\beta\sin(\omega+\theta_1)$ yields,

$$p_1\sin\beta(\cos^2\psi+2\delta_1\sin\theta_1\sin\psi-\sin^2\theta_1)^{\frac{1}{2}}+p_1\cos\beta(\sin\theta_1-\delta_1\sin\psi)$$

$$+ p_1\delta_2\sin\psi - 2p_1\sin\delta_1\cos\beta = p_2\sin\delta_1$$

From equations 2.38 and 2.35 we have

$$\sin\theta_2 = -\frac{p_2}{p_1}\sin\theta_1$$

$$\therefore \sin\beta(\cos^2\psi+2\delta_1\sin\theta_1\sin\psi-\sin^2\delta)^{\frac{1}{2}}-\cos\beta(\sin\theta_1+\delta_1\sin\psi)$$

$$= \sin\theta_2 - \delta_2\sin\psi \qquad 2.47$$

Introducing angles γ and η such that

$$\sin\beta\cos\gamma - \cos\beta\sin\gamma = \sin\eta \qquad 2.48$$

and comparing equations 2.47 and 2.48 leads to

$$\cos\gamma = (\cos^2\psi + 2\delta_1\sin\theta_1\sin\psi - \sin^2\theta)^{\frac{1}{2}} \qquad 2.49$$

$$\sin\gamma = \sin\theta_1 + \delta_1\sin\psi \qquad 2.50$$

$$\sin\eta = \sin\theta_2 - \delta_2\sin\psi \qquad 2.51$$

Consider the right angled triangle ABC

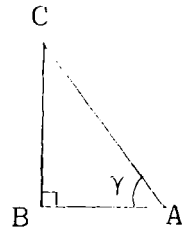

and using equations 2.49 and 2.50.

$$AC^2 = AB^2 + BC^2$$

$$1 = \cos^2\psi+2\delta_1\sin\theta_1\sin\psi-\sin^2\theta_1+(\sin\theta_1+\delta_1\sin\psi)^2$$

$$1 = \cos^2\psi+2\delta_1\sin\theta_1\sin\psi-\sin^2\theta_1+\sin^2\theta_1+2\delta_1\sin\psi\sin\theta_1 + \delta_1^2\sin^2\psi \qquad 2.52a$$

Neglecting third order powers of ψ and second order power of δ simplifies these expressions to

$$1 = \cos^2\psi + 4\delta_1 \sin\theta_1 \sin\psi + \delta_1^2 \sin^2\psi$$

$$1 = (1 - \psi^2 + 4\delta_1 \psi\sin\theta_1)$$

$$\psi(4\delta_1 \sin\theta_1 - \psi) = 0$$

$$\psi = 4\delta_1 \sin\theta_1 \qquad 2.52b$$

Using equation 2.52, equations 2.50 and 2.57 can be rewritten as

$$\sin\gamma = \sin\theta_1+\delta_1\sin\psi - 2\sin^2\theta_1\delta_1\psi+\tfrac{1}{2}\sin\theta_1\psi^2$$

$$\gamma = \sin^{-1}(\sin\theta_1+\delta_1\psi - 2\sin^2\theta_1\delta_1\psi+ \tfrac{1}{2}\sin\theta_1\psi^2) \qquad 2.53$$

$$\sin\eta = \sin\theta_2-\delta_2\sin\psi - 2\sin\theta_1\sin\theta_2\delta_1\psi+\tfrac{1}{2}\sin\theta_2\psi^2$$

$$\eta = \sin^{-1}(\sin\theta_2-\delta_2\psi- 2\sin\theta_1\sin\theta_2\delta_1\psi+\tfrac{1}{2}\sin\theta_2\psi^2) \qquad 2.54$$

Equations 2.53 and 2.54 can be expanded by Taylor's theorem about $\sin\theta_1$ and $\sin\theta_2$ respectively.

Taylor's theorem states that

$$f(z) = f(a) + \frac{(z-a)}{1!}f'(a) + \frac{(z-a)^2}{2!}f''(a) + \ldots..$$

Write equation 2.53 as

$$f(z) = \sin^{-1} z$$

where $z = \sin\theta_1 + \delta_1\psi - 2\sin^2\theta_1\delta_1\psi + \frac{1}{2}\sin\theta_1\psi^2$

and $a = \sin\theta_1$

$\therefore f(a) = \sin^{-1}(\sin\theta_1) = \theta_1$

Similarly, $f'(z) = \dfrac{1}{(1 - z)^{\frac{1}{2}}}$

$$f'(a) = \frac{1}{(1 - \sin^2\theta_1)^{\frac{1}{2}}} = \frac{1}{\cos\theta_1}$$

$$f(z) = \theta_1 + \frac{\sin\theta_1 + \delta_1\psi - 2\sin^2\theta_1\delta_1\psi + \frac{1}{2}\sin\theta_1\psi^2 - \sin\theta_1}{\cos\theta_1}$$

$$= \theta_1 + \tan\theta_1 + \frac{\delta_1\psi}{\cos\theta_1} - 2\sin\theta_1\tan\theta_1\delta_1\psi + \frac{1}{2}\tan\theta_1\psi^2 - \tan\theta_1$$

Defining γ as

$$\gamma = \theta_1 + \frac{\delta_1\psi}{\cos\theta_1} - 2\sin\theta_1\tan\theta_1\delta_1\psi + \frac{1}{2}\tan\theta_1\psi^2 \qquad 2.55$$

and η as

$$\eta = \theta_2 - \frac{\delta_2\psi}{\cos\theta_2} - 2\sin\theta_1\tan\theta_2\delta_1\psi + \frac{1}{2}\tan\theta_2\psi^2 \qquad 2.56$$

From equation 2.48 reduce to

$$\sin(\beta - \gamma) = \sin\eta \qquad 2.57$$

Equation 2.57 yields two solutions

$$\beta - \eta - \gamma = 0 \qquad 2.58$$

and

$$\beta - \pi + \eta - \gamma = 0 \qquad 2.59$$

Substituting equations 2.55 and 2.56 in equations 2.58 and 2.59 we obtain

$$M\psi^2 + R\psi = \Delta \qquad 2.60$$

where $\Delta = \beta - [\theta_1 + \frac{\pi}{2} \pm (\theta_2 - \frac{\pi}{2})]$ represents the angular deviation of the position of the second crystal from the position for reflection of a horizontal ray entering along the x-axis,

$$R = \delta_1/\cos\theta_1 + \delta_2/\cos\theta_2 - 2\sin\theta_1(\tan\theta_1 \pm \tan\theta_2)\delta_1 \qquad \text{or}$$

$R \overset{\sim}{\sim} \delta_1^2 + \delta_2^2$ is the sum or difference of the angles of inclination of the crystals to the vertical and $M = \frac{1}{2}(\tan\theta_1 \pm \tan\theta_2)$.

The upper signs are for the (+,+) setting and the lower signs are for the (+,-) setting.

Taking the special case for the (+,-) parallel setting where $\theta_1 = \theta_2$

$$\Delta = \beta - \pi$$

$$M = 0$$

Therefore equation 2.60 becomes

$$R\psi = \Delta \qquad 2.61$$

The angle ψ is limited by the vertical divergence ϕ_v of the source.

Therefore from equation 2.61 the fractional change in the angle of diffraction $\Delta\theta_B/\theta_B$ is given by

$$\frac{\Delta\theta_B}{\theta_B} = \frac{\phi_v\phi_c}{\theta_B} \qquad 2.62$$

where $\Delta\theta_B = \Delta$

and $\phi_c = R$ is the angle of misalignment.

2.7 Strain Theory of Contrast at a Dislocation in Double Crystal Topographs

Bonse (1962) derived a simple geometrical relation for diffraction contrast observed at dislocation for the double crystal technique. The strained region around a dislocation is treated as a macroscopic region in which Bragg's law $2d\sin\theta_B = n\lambda$ is the only necessary diffraction equation. Changes in lattice spacing ∂d or orientation $\partial\theta_B$ due to the strain field of the dislocation will shift the Bragg angle θ_B for the strained region by an amount $\Delta\theta_B$ where

$$\Delta\theta_B = \partial\theta_B + \tan\theta_B \frac{\partial d}{d}$$

The first term is the contribution of the component of local lattice rotation with respect to the goniometer axis and the second term is the contribution of local changes in interplanar spacing of the diffracting planes. Diffraction contrast can arise when local distortion produces a sufficient Bragg angle change $\Delta\theta_B$ to change the diffracted intensity.

As the flank of the rocking curve in the (+,-) parallel setting is very steep, it can be approximated to be linear as shown in Figure 2.3b. Therefore the slope of the flank of the rocking curve can be related to the change in intensity ΔI caused by distortion $\Delta\theta_B$ by the relation below

$$\Delta I = K(\partial\theta_B + \tan\theta_B \frac{\partial d}{d})$$

where K is the slope of the flank of the rocking curve. This simple geometrical theory seems to be in quite reasonable agreement with experiment in the (+,-) parallel setting.

More complex dynamical diffraction effects have been observed in the dispersive (+,-) non-parallel setting (Jones et al. 1981).

2.8 Asymmetric Reflection

Asymmetric reflection is another important feature of double crystal diffractometry. It has the property of increasing or decreasing the spatial width of the X-rays diffracted by the first crystal depending on the asymmetry factor b which is defined as

$$b = \frac{\sin\theta_o}{\sin\theta_h} = \frac{\sin(\theta_B - \alpha)}{\sin(\theta_B + \alpha)} \qquad 2.63$$

θ_o is the angle between the incident beam and the crystal surface. θ_h is the angle made by the diffracted beam with the crystal surface. θ_B is the Bragg angle and α is the inclination of the diffracting plane to the crystal surface. α is defined as positive when $\theta_o < \theta_B$ and negative if $\theta_o > \theta_B$. Therefore in the later case $b > 1$ (Figure 2.10a) and $b < 1$ in the former case (Figure 2.10b).

According to dynamical theory (Laue 1960, Kohra 1962) the angular width of the incident and diffracted beam ω_o and ω_h for a selective reflection in the asymmetric case is given by

$$\omega_o = \sqrt{\frac{\sin\theta_h}{\sin\theta_o}}\ \omega_s = \omega_s \sqrt{b} \qquad 2.64$$

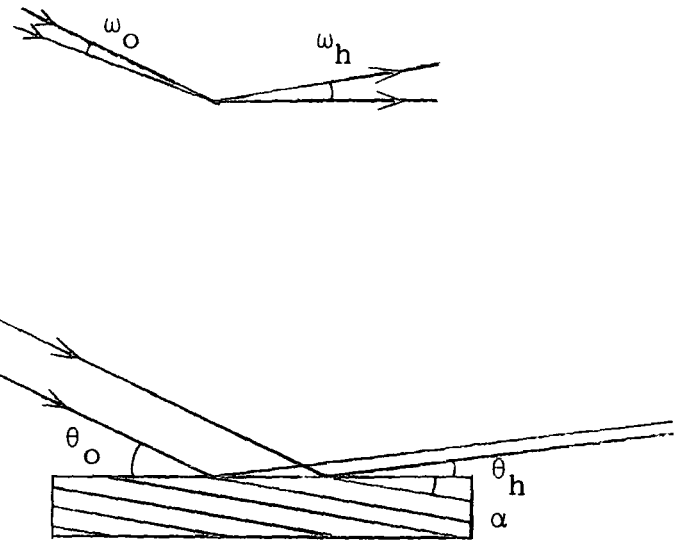

(a)

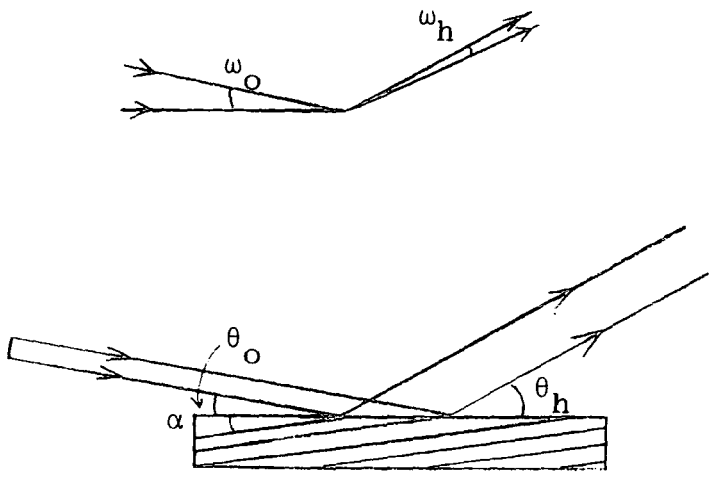

(b)

Fig. 2.10 Geometry and angular width of the incident and diffracted beam for an asymmetric reflection when
(a) b>1
(b) b<1

and $$\omega_h = \sqrt{\frac{\sin\theta_o}{\sin\theta_h}}\ \omega_s = \omega_s \sqrt{b} \qquad 2.65$$

ω_s is the angular range in the symmetric case.

From equations 2.64 and 2.65

$$\omega_h = b\omega_o \qquad 2.66$$

Asymmetric reflections have been used by many workers to produce a beam of extremely narrow width (b>1) for precise measurement of diffraction curves in the (+,-) parallel arrangement. (Kohra 1962, Kohra et al. 1968, Kikuta et al. 1970, Kikuta 1971 and Matsushita et al. 1971). The intensity of the beam diffracted from the specimen crystal is greater as the angular spread of the incident beam on the specimen is stronger by a factor $\sqrt{b}$. The asymmetric reflection where b<1 enables large areas of the samples to be photographed (Kohra et al. 1970, Jones et al. 1981).

2.9 Review of Previous Work on Double Crystal Diffractometry

The usual method to determine the lattice parameter is to measure the angle at Bragg reflection and using the known value of X-ray wavelength, the interplanar spacing of the Bragg plane is calculated using the Bragg equation $2d\sin\theta = \lambda$ corrected for refraction effect. Due to the precision in which the X-rays wavelength is known this method only gives an accuracy of 1 part in 10^5. A higher accuracy can be achieved if a relative measurement is made (Bearden et al. 1964, Bond 1960 and Baker et al. 1966, 1967). By

differentiating Bragg equation we obtain

$$\frac{\partial d}{d} = \frac{\partial \lambda}{\lambda} - \cot \theta \, \partial\theta$$

The precision of this method is limited by the width of the dispersed single reflection profile. Typical value of $\partial\lambda/\lambda$ is 3×10^{-4} and as the reflection profile is rarely symmetrical this method provides relative values of lattice parameter with error less than a few parts in 10^7 even if $\cot\theta$ is small.

Hart (1969) achieved a higher accuracy of 1 part in 10^9 by using the non-dispersive double crystal arrangement and the dispersion of the source. Absolute values of wavelength are avoided. Referring to Figure 2.11 for the experimental set-up, the reference crystal A was set at the Bragg reflection and rocking curve was recorded as the sample crystal B is rotated. The rocking curves from the $(h\bar{h})$ reflection (path from source 2 to detector 2) and the $(\bar{h}h)$ reflection (path from source 1 to detector 1) are recorded simultaneously. The detectors record the peak intensity simultaneously at the sample setting $\beta = 0$ where the Bragg planes of both crystals are parallel if both crystals have the same lattice parameter. When the two crystals have different lattice parameters d_A and d_B the peak intensity occurs at different angular setting of β. For an angular separation $\Delta\beta$

$$\Delta\beta = 2(\theta_A - \theta_B) = 2\Delta\theta$$

Differentiating Bragg law gives,

$$\frac{\Delta\theta}{\tan\theta} = \frac{\Delta d}{d}$$

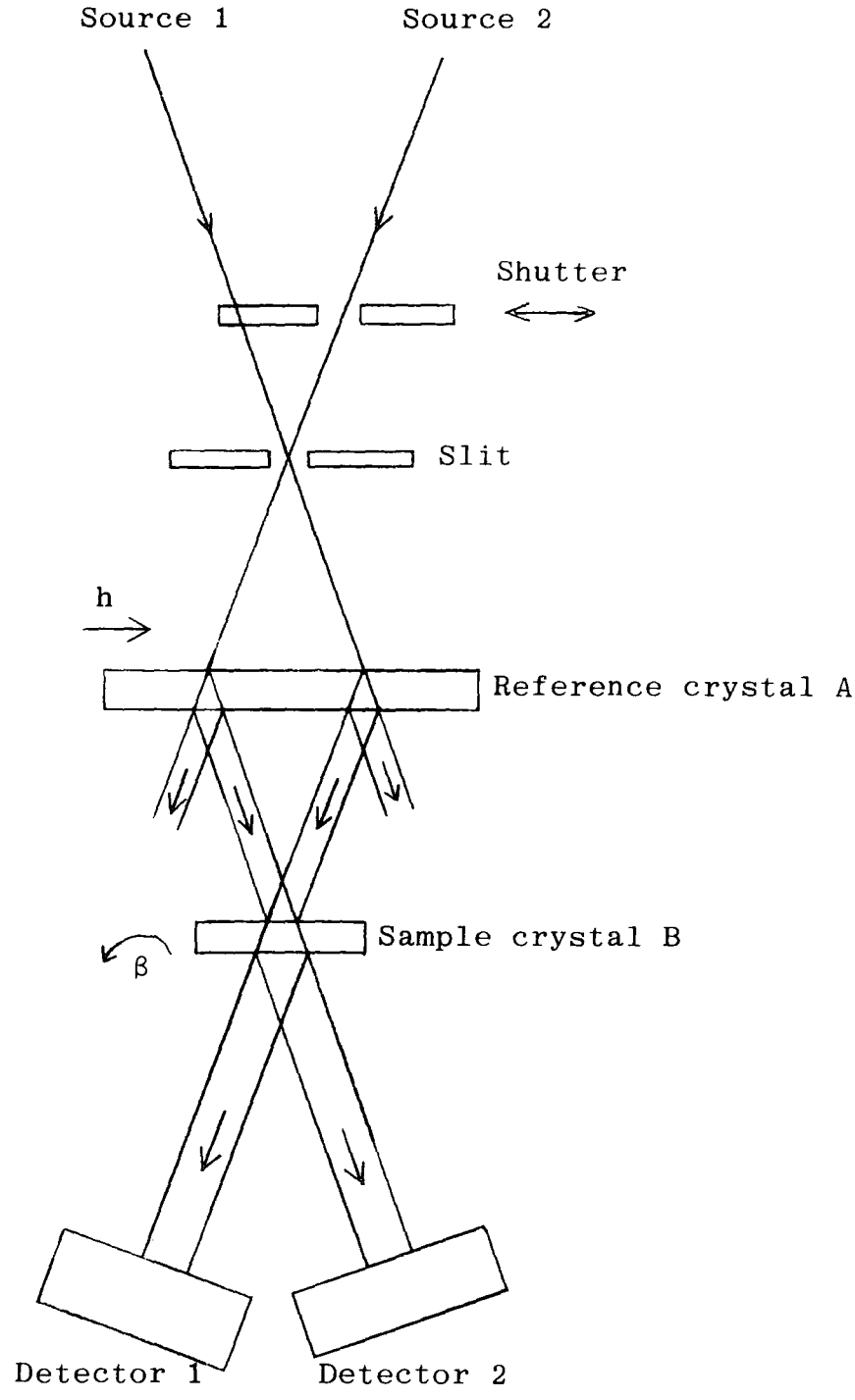

Fig. 2.11 Hart's experimental set up for the measurement of lattice parameter using multiple Bragg reflection.

If Δd is small, $\Delta\beta = 2 \frac{\Delta d}{d} \tan\theta$

As the FWHM of the rocking curve is narrow, typically 10^{-6} radians the equality of Bragg angle can be detected to within 10^{-9} radian if the peak centroid can be measured within 0.1% on a symmetric curve. This implies that the equality of the lattice parameter can be detected with uncertainties of one part in 10^9. The same method was used to compare the lattice parameter of the 800 reflection of germanium and the 355 reflection of silicon, (Baker and Hart 1975).

Larson (1974) modified Hart's technique and measured the lattice parameter changes in neutron irradiated copper. He used the reflection geometry and one X-ray source instead of transmission geometry and two sources as used by Hart (Figure 2.12). A monolithic U-shape monochromator with two upright diffracting wafers was fixed on a rigid base at the first diffractometer axis to Bragg reflect the two beams from the single source. The doubly and triply reflected rocking curve was recorded simultaneously and $\Delta\beta$ measured. Baker et al. (1976) used Larson's method to measure lattice parameter variation of dislocation free gallium arsenide and also doped samples where 1-20 ppm variation in composition is present. This method is particularly useful for the study of semiconductor materials such as silicon (Baker et al. 1968, Yeh et al. 1969, North et al. 1974) and gallium arsenide (Baker et al. 1976).

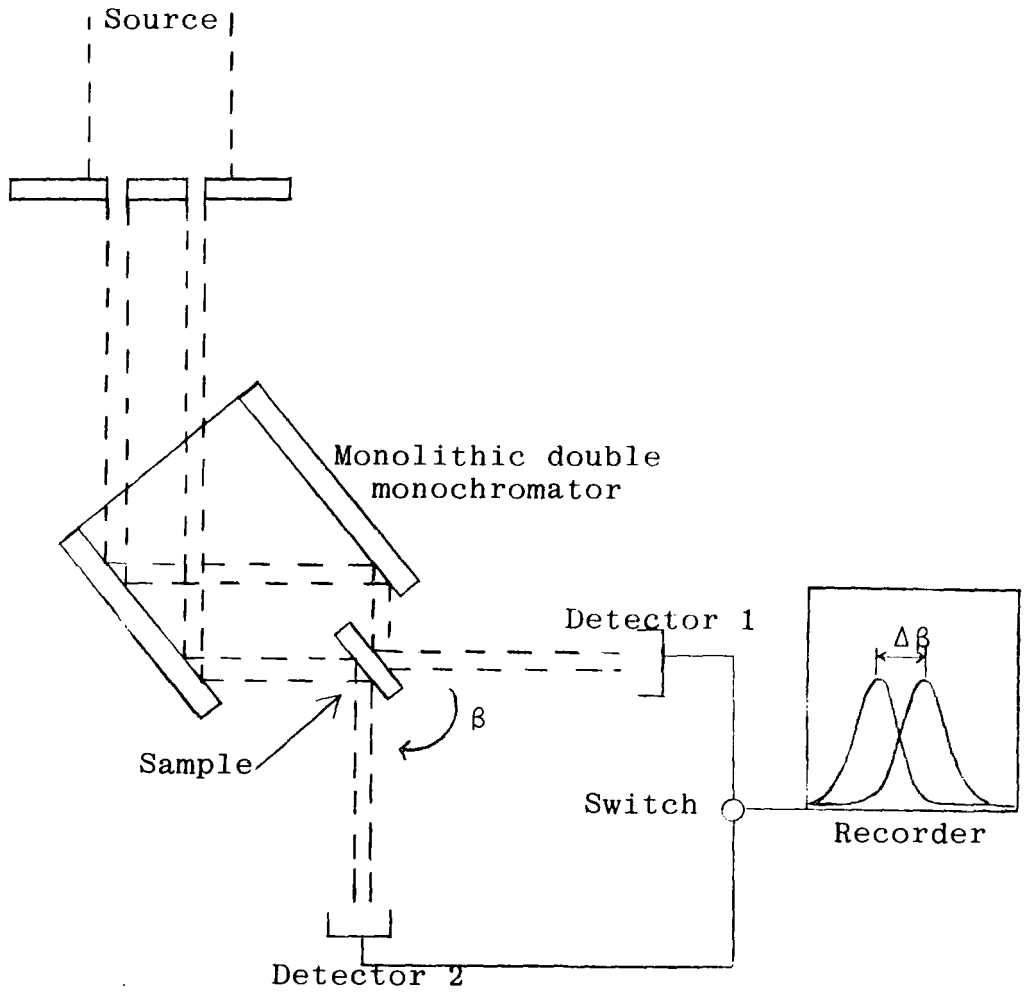

Fig. 2.12 Larson's experimental set up for the measurement of lattice parameter changes in neutron irradiated copper.

Another commonly used method to measure variations in lattice parameter and orientation is to record rocking curves for two azimuthal angles for each position of the crystal where in the second position the sample is rotated by 180^{O} around the surface normal(Kikuta and Kohra 1966, Yoshimura et al. 1979, Bonse and Hartmann 1981). They obtain

$$\Delta\theta_{ik} = (\Delta R^{O}_{ik} + \Delta R_{ik}{}^{180})/2$$

$$\Delta\alpha_{ik} = (\Delta R^{O}_{ik} - \Delta R_{ik}{}^{180})/2$$

where ΔR_{ik} is the difference for the angular position of the peak intensity for region i and k of the crystal and α_i is the angle made by the horizontal component of the normal of the diffracting plane to the surface normal for region i. Therefore from the above equation and $\Delta d_{ik}/d_i = -\cot\theta_i \Delta\theta_{ik}$, the local variations in orientation $\Delta\alpha_{ik}$ and spacing Δd_{ik} can be obtained.

Another important application of double crystal diffractometry is for measurement of the lattice parameter difference between a substrate and epitaxial layer for materials such as garnet which is used for bubble memory devices (Hart and Lloyd 1975). The matching of the two lattices from the substrate and epilayer is very important. An imperfect matching may result in the formation of elastic strain and plastic deformation which may result in device failure. Similar experiments have also been carried out for materials such as aluminium-substituted gallium arsenide on a gallium arsenide substrate (Estop et al. 1976) which is an important

material in infra-red laser diodes; and epitaxial layer of ternary and quaternary III-V semiconductor compounds on binary substrates, for example (GaIn)As and (GaIn)(As,P) layers on InP substrate (Halliwell 1981). With the increasing use of computer controlled diffractometers measurements can be made quickly and the technique is potentially very useful at an industrial level.

Double and multiple crystal diffractometry is also used to study crystal perfection by topographic methods. The pioneers for this technique (Bond and Andrus 1952, Bonse and Kappler 1958) used topography to study the structural imperfection of quartz crystals and individual dislocations in germanium single crystals respectively. As the method has a higher strain sensitivity it gives a more detailed information compared to single crystal topography. An asymmetric reflection can be used for the first crystal to provide a spatially narrow beam and high resolution X-ray section topographs can be achieved (Mai Zhen-Hong, Mardix and Lang 1980). A number of workers have used the highly sensitive (+,-) arrangement to study small strains, for example, (Hart 1968, Kohra et al. 1970, Stacy et al. 1974, Hashizume et al. 1975, Yoshimura and Kohra 1976, Jones et al. 1981).

Studies on magnetic materials have also been carried out using double crystal diffractometry (Miyaka 1949, Hulubei 1952, Merz 1960, Ridou and Rousseau 1980). The magnetostriction will give rise to changes in the X-ray diffraction from a crystal undergoing magnetization. A

diffraction peak will shift due to the change in lattice parameter and an increase in integrated intensity due to strain. From the measurement of the angular difference of the peaks position of two domains from a rocking curve the magnitude of the magnetostriction can be calculated (Jones and Tanner 1980).

The availability of synchrotron radiation sources have boosted the application of double crystal diffractometry where the first crystal acts as a monochromator. Such a system is essential as the synchrotron radiation spectrum is continuous and many experiments require a monochromatic beam. The main advantage in use of synchrotron radiation for topography is the fast exposure time for double crystal topographs of the order of a couple of minutes compared to several hours (typically 18 hours) when using a conventional X-ray source.

CHAPTER 3

INSTRUMENTS AND INTERFACE

3.1 Introduction

Two axis instruments have not been used as widely as single axis instruments and this may be partly due to the non-availability of these instruments commercially. Owing to the high sensitivity and the availability of perfect single crystals, this technique is becoming increasingly important. Most of the double crystal diffractometers in existence were built by the individuals who use them (Knowles 1959; Bearden and Henins 1965; Bradler and Polcarova 1972; Sauvage 1978; Ohama, Sakashita and Okazaki 1979; Yoshimura et al. 1979; Mai, Mardix and Lang 1980; Bonse and Hartmann 1981 etc.) for various purposes.

The double crystal spectrometer built by Knowles (1959) was used for the measurement of γ-ray energies resulting from neutron capture where the relative angle between the reflecting planes was measured by an optical system. The design of Ohama et al. (1979) is a high angle double crystal diffractometer (HADOX) used for measuring the temperature dependence of lattice constant and can obtain an accuracy of 1 part in 10^7. The double crystal camera which had been built and installed at LURE-DCl in 1978 is used for topographic studies (Sauvage 1978). Both axes are driven by piezoelectric translators and an accuracy better than 0.1 arc second is claimed. However it is not monolithic and the stability is probably not as high as this figure.

The three double crystal diffractometers used for experiments described in this thesis were originally designed by Hart (1980) some twenty years ago. References to similar instruments can be found (Jones et al. 1981, Halliwell 1981) but a full description has not been published. A version similar to the EGG is now available commercially (Bede Scientific Instruments, Durham). Another double crystal diffractometer is also available commercially from Rigaku. It is the scanning type and although it can take large samples it is not a high precision instrument. Two instruments based on the same monolithic principle (Hart 1980) with an axis separation of 300 mm have been installed at the Synchrotron Radiation Source at Daresbury (Bowen et al. 1982). One is mainly used for interferometric studies and the other for real time experiments where a magnetic field of up to 1 Tesla can be applied to the material under study or a cryostat containing the sample can be placed on either diffractometer axis.

3.2 The EGG

The EGG was constructed at the departmental workshop in Durham and as already stated, the design of the diffractometer is similar to the one built by Professor Hart and now at King's College, London.

3.2.1 The Main Body

The main body of the camera was cast as a single piece of gun metal. The casting was about 10 mm thick and 114 mm

high. The hollow interior provides space for the construction of the mechanisms which control the angular rotation of the goniometers. The length of the camera is about 320 mm with the goniometer axes a distance 150 mm apart and the width of the camera at the two axis is different, the width at the second axis being larger. This design arises because it is usually desirable that the second axis has a greater sensitivity than the first. As the body was cut as a single piece, the sleeves which support the spindles of the goniometer axes can be accurately machined to be exactly coincident with the horizontal axis of the casting. The spindles and sleeves are made from stainless steel and rotate on two O-ring loaded ball journal bearings.

4-phase Impex IDO4 $7\frac{1}{2}^{O}$ stepping motors are fixed on brackets on each side of the outside of the casting. The motors control the rotation of the goniometers through a folded lever system as shown in Figure 3.1, driving the micrometer via a 100:1 gear-box. The output shaft of the gear-box is coupled to the micrometer via a thin brass bellows. Alignment of the input shaft of the gear-box and stepper motor is very critical. Even slight misalignment between them will significantly affect the smoothness of the rotation of the IDO4 motors which although inexpensive have a poor torque output. One step of the motor corresponds to 0.74 arc second on the first axis and 0.55 arc second on the second axis. Two pairs of microswitches are used, one pair for each goniometer fixed between the protruding circular brass plate attached to the bellows on the side nearer the micrometer. When the circular plate is in contact

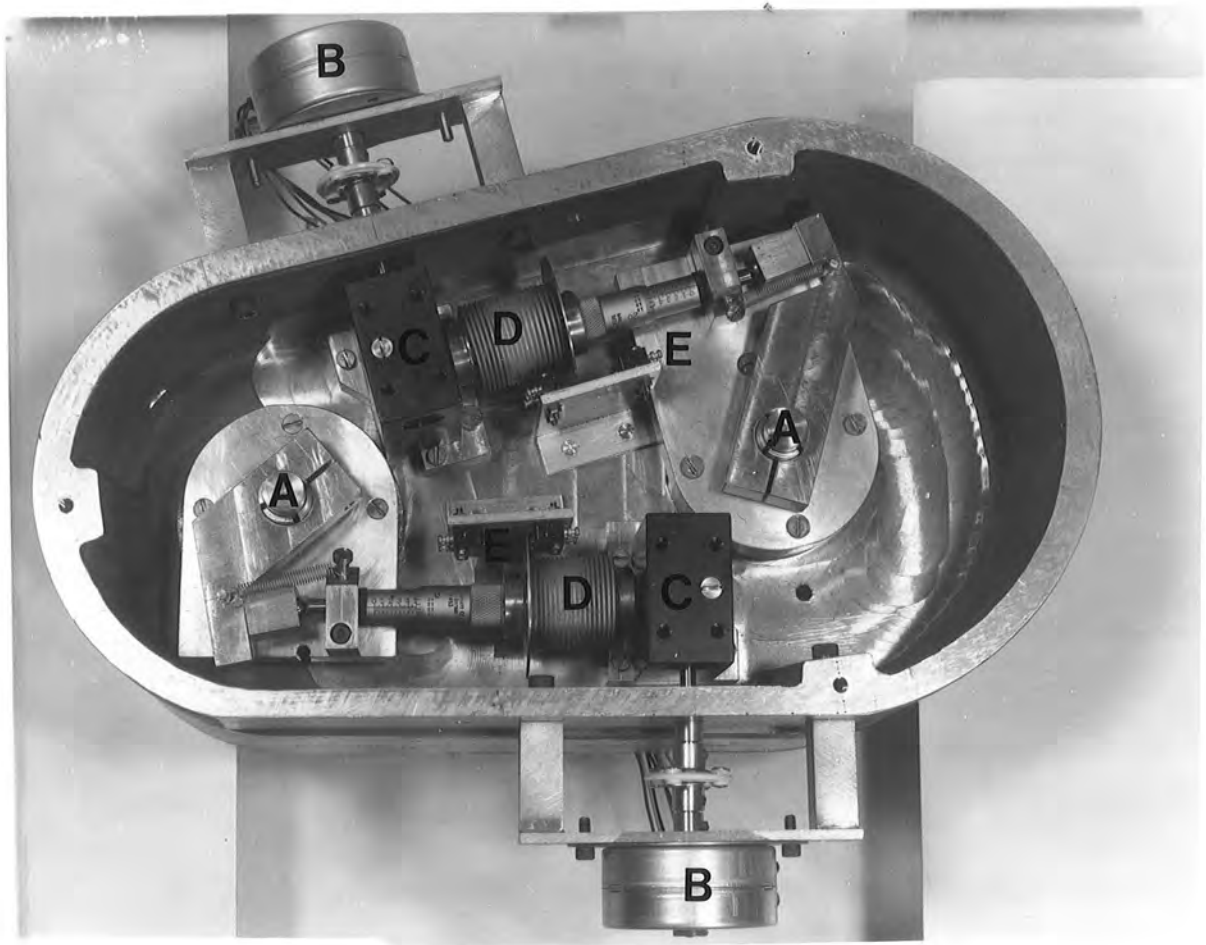

Fig. 3.1 Photograph of the underside of the EGG.

A - Goniometer axis
B - Stepper motor
C - Gear-box
D - Brass bellows
E - Microswitch

with the microswitch, the drive circuit is broken and the motor stops. The same is for the other microswitch which limits the movement of the micrometer in the opposite direction. This is to prevent dangerous overrunning of the micrometer tracks. A disadvantage is that although the motor is stopped the computer still sends pulses to the drive module and absolute positioning is lost. The motor must then be driven manually back into the safe working region. The total range of rotation for both goniometers is about 15^{o}.

The bottom hollow part of the casting is covered with a 6 mm thick steel plate and together with the goniometers were mounted on a graduated rotary milling table 70 mm high with its axis of rotation concentric with the first goniometer axis. The whole camera can therefore be rotated simultaneously and this made easy alignment between both goniometer and the X-ray beam. The table is driven by rotating the shaft manually.

The detector support assembly is mounted on a large ball journal bearing fixed on the outside of the casting concentric with the second goniometer axis and is positioned manually. An arm is attached to the assembly to support the detector and a plate holder.

3.2.2 The Goniometer

The goniometers was made from two L-shaped aluminium pieces and were attached together using pre-loaded bearings. Each L-piece was machined as a single piece to maintain the stability of the goniometer. The photograph of the goniometers together with the whole experimental

set-up is shown in Figure 3.2. The spindle of the goniometer was fixed at the bottom of the outer L-piece and a good fit was made between the spindle and the supporting sleeve so that the whole goniometer is extremely stable. This is very important since slight wobbling of the goniometer will affect the sensitivity if a rocking curve of a few seconds of arc is to be obtained. The position of the sample holder was constructed at the base of the inner L-piece with its axis coincident with the axis of the spindle. A micrometer fixed at the top of the outer L-piece is in contact with a ball-bearing fixed at the inner L-piece. An elastic spring retains the two L-pieces. Thus the inner L-piece is movable in a vertical plane parallel to the goniometer axis and thus controls the tilt angle ϕ which is necessary for optimum results. The micrometer was coupled to the output shaft of a 50:1 gear-box via a brass bellows. The stepping motor which was coupled to the input shaft of the gear-box will control the movement of the micrometer which will slag or stretch the spring and thus changing the tilt angle ϕ. A bracket was attached to the outer L-piece to support the gear-box and motor. One motor step is equivalent to a tilt angle of 0.25 arc second.

3.3 The COFFIN

The COFFIN is a bigger version of the EGG and has the same principle design with axes rotated by levers pushed by stepper motor driven micrometers via gear-boxes. The diffractometer was initially made for magnetostriction measurements up to a field of 1 Tesla (Jones and Tanner, 1980).

A - Goniometer
B - Diffractometer
C - Crystals
D - Detector
E - Micro-computer
F - Harwell 2000 pulse amplifier

Fig. 3.2 Photograph of the goniometers and the whole experimental set-up in the (+, -) parallel arrangement.

Figure 3.3 is a photograph of the underside of the diffractometer.

An unusual feature of the diffractometer is that the crystals can be mounted below the instrument as the large bearings permit use of a wide collet and through this a Helium gas flow cryostat can be inserted. For γ-ray work this feature was modified so that the crystals were mounted in the usual manner, that is above the flat surface of the instrument and can take the same goniometers as used with the EGG. It has a larger axis separation of 825 mm which has proved very suitable for γ-ray work. The first axis has a 20:1 gear-box and a 46 mm lever resulting in an angular rotation of 0.93 arc second per motor step. The second axis with a 90:1 gear-box and a lever length of 292 mm has a step angle of 0.1 arc second.

During this work, modification was made on the second axis for the measurement of very narrow rocking curves less than 0.1 arc second. A longer lever (573 mm) was used and together with a higher ratio gear-box of 312.5:1, the angle per step was reduced to 0.012 arc second.

3.4 Micro-Computer Control System

Before the widespread use of microprocessors, automation was only restricted to large scale experiments due to the large capital involved. At present more and more small scale experiments are being interfaced to micro-computers with consequent great advantage of an on-line control and data processing system.

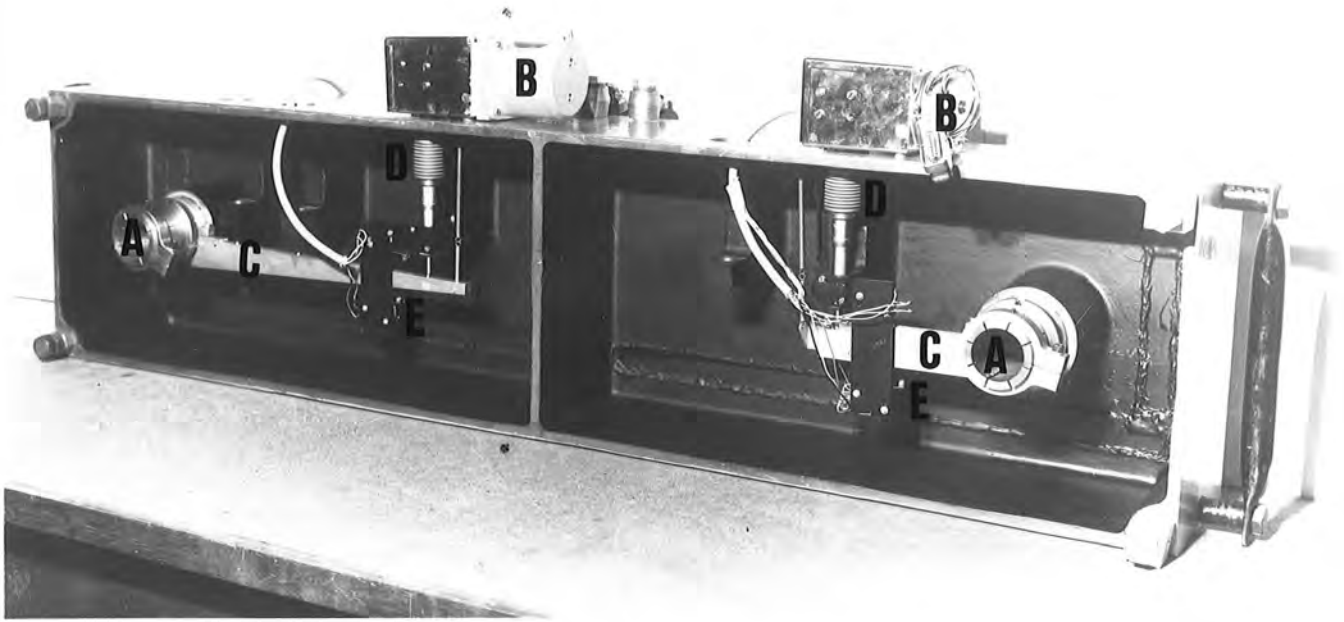

A - Goniometer axis
B - Stepper motors
C - Levers
D - Brass bellows
E - Microswitch

Fig. 3.3 Photograph of the underside of the COFFIN.

The micro-computer used to control the diffractometer described below is the Commodore System P.E.T. and the 'MINICAM' interface system designed by Rodrigues and Siddons (1979) and available from Besselec, Isleworth, Middlesex. This systen can also be used for any other similar based experiments. The 32K byte PET is used preferentially although the 8K is sufficient for some of the control programs written.

The PET system can be divided into four main building blocks. These are the (a) Central Processing Unit, (b) Storage or Memory, (c) Input and (d) Output. The 6502 microprocessor which is the main component of the CPU circuitry controls the operation of the screen, keyboard, cassettes and other additional peripherals. The high level language used is BASIC, stored in ROM, which is easy to learn and use even if one does not have any previous knowledge of programming languages. BASIC includes the function PEEK and POKE used for memory inspection and modification. This is essential to provide extra commands and functions as well as fast execution speed in the form of subroutines written for the specific requirement of the experiments. The subroutines are stored in a 1K byte EPROM on the bus interface board and are available whenever required. The subroutines are linked to the main BASIC program by the function SYS(X) and USR(X).

3.4.1 The Interface Rack System and the Power Supply Unit

The rack system used is the standard 19 inch subrack system. The 43-way gold-plated edge connectors which are bused together accepts standard size cards used for plug in modules. Table 3.1 shows the function of each terminal of the bus. The power supply unit and the interface board are built behind a 5 inch aluminium panel which carries the mains power inlet, switch, fuse and indicator light. The circuit diagram in Figure 3.4 is the power supply unit which provides nominally + 15V at 4A and -15V at 1A. The unregulated supply is fused and the regulated supply is current limited. The total load should not exceed 100VA. Two of the four ground terminals are for the unregulated supply, one for the regulated supply and the fourth is used for analog devices.

3.4.2 The Interface Board

The main component of the interface module is the 6522 versatile interface adaptor. Each device consists of two 8-bit bi-directional lines which is programmed as either input or output, 4 control lines, an 8-bit shift register and 2 programmable 16-bit timers. The two devices provide parallel control lines and 16 bi-directional data lines. One is mainly concerned with data movement and the others with interface control (Figure 3.5). Eight of the lines (lines 30-38) are connected to two chip decoder (Figure 3.6) which are treated as an 8-bit address. A total of 255 addresses can be allocated to one system.

Table 3.1 Function of each terminal of the MINICAM interface bus.

Pin No.	Function
1	Reset 1
2	Analog ground
3	+5V regulated
4	OV logic ground
5	Gate 1 (in parallel with Gate 2, pin 39)
6	Reserved for future MINICAM extensions
7	
8	-15V nominal
9	Strobe
10	Motor supply +15V nominal
11	
12	Motor supply OV
13	
14	L.S.B.
.	
.	16 data lines
.	
.	
29	M.S.B.
30	L.S.B.
.	
.	7 address lines
.	
.	
36	N.M.S.B.
37	Polarizing key
38	M.S.B. address line
39	Gate 2
40	not allocated
41	Interrupt request
42	Handshake
43	Reset 2

Notes:
1. Reset 1 and 2, Gate 1 and 2, pairs connected in parallel.
2. OV lines connected together at main reservoir capacitor only.

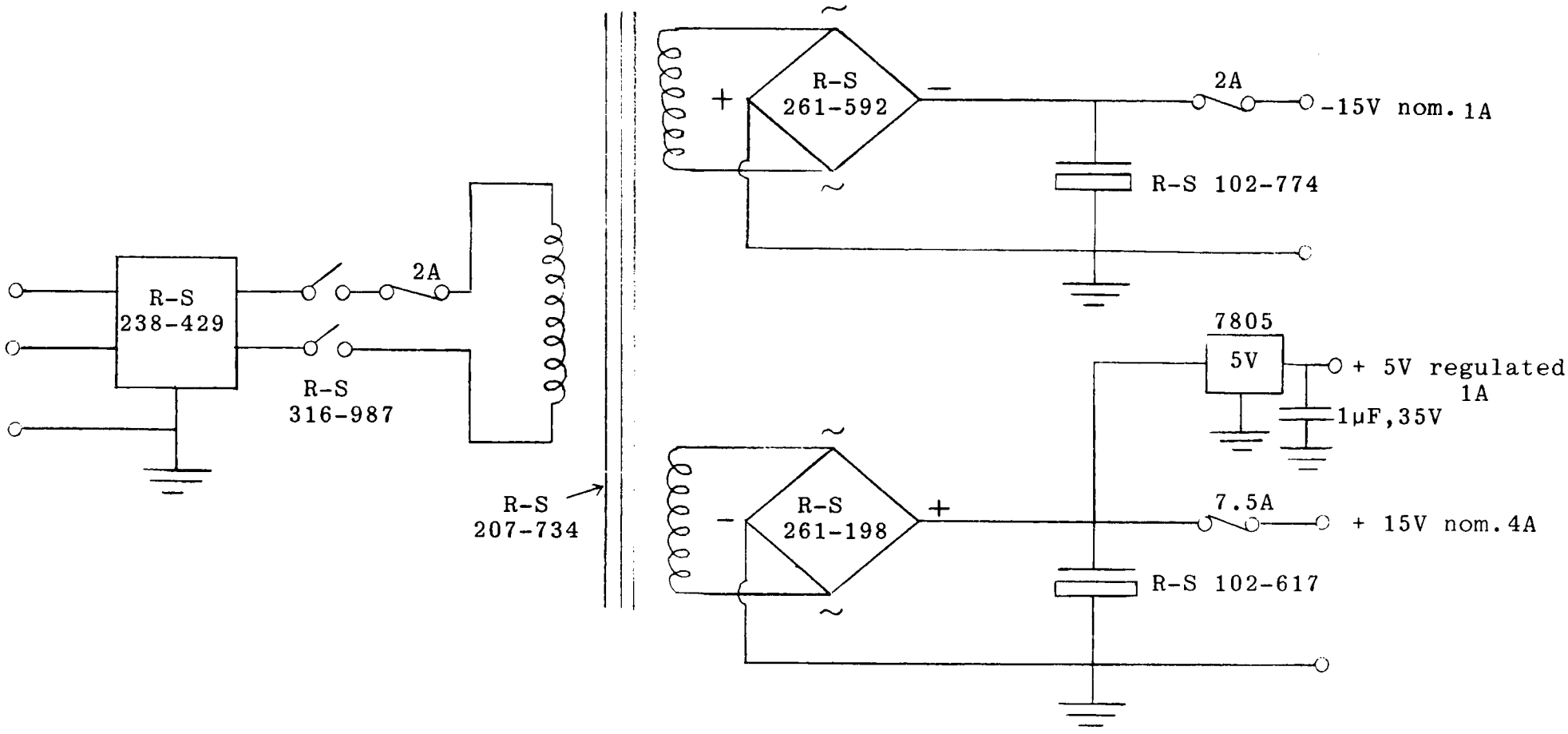

Fig. 3.4 The power supply unit for the MINICAM interface.

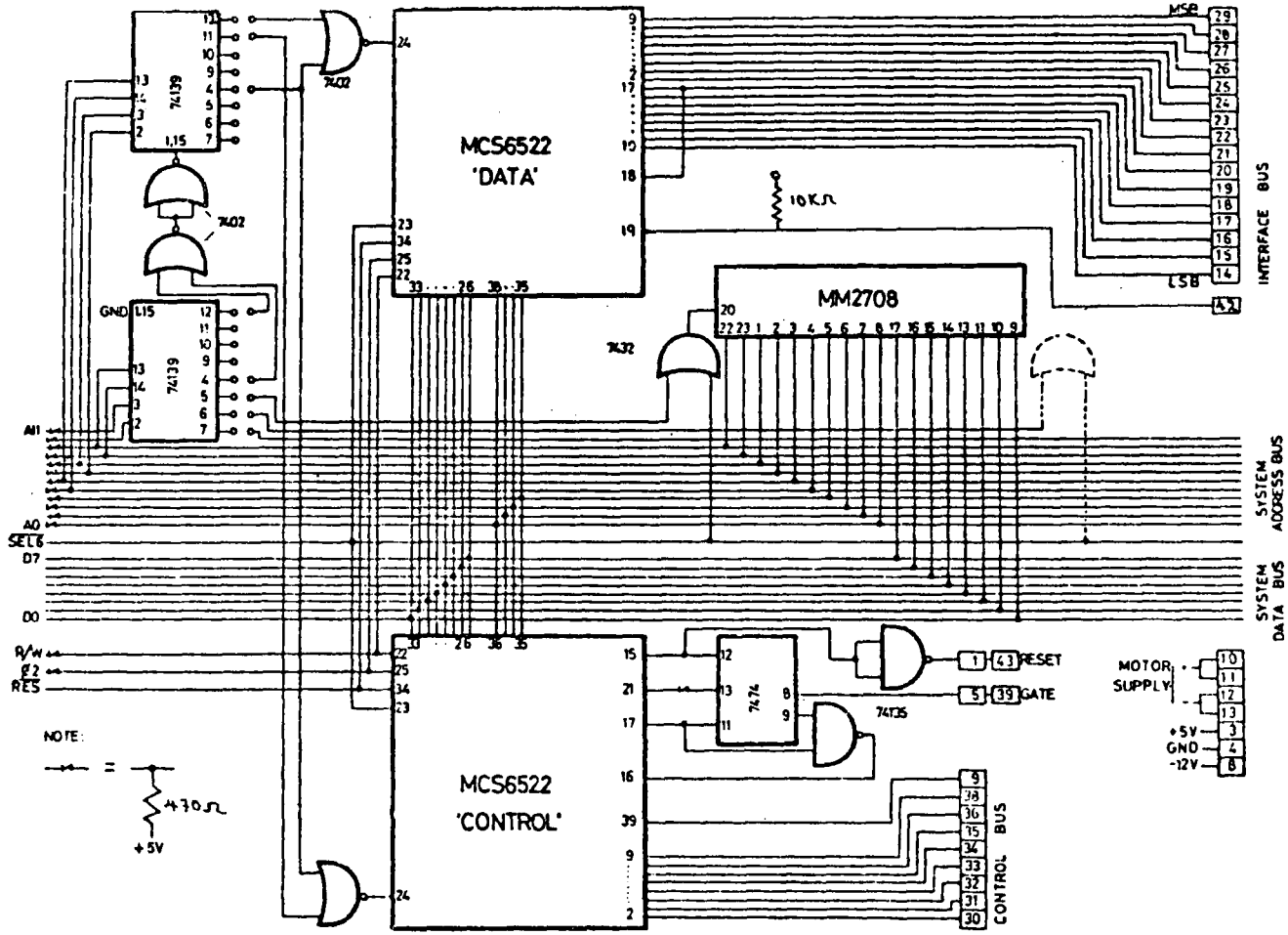

Fig. 3.5 The circuit diagram of the interface board for the MINICAM interface system.

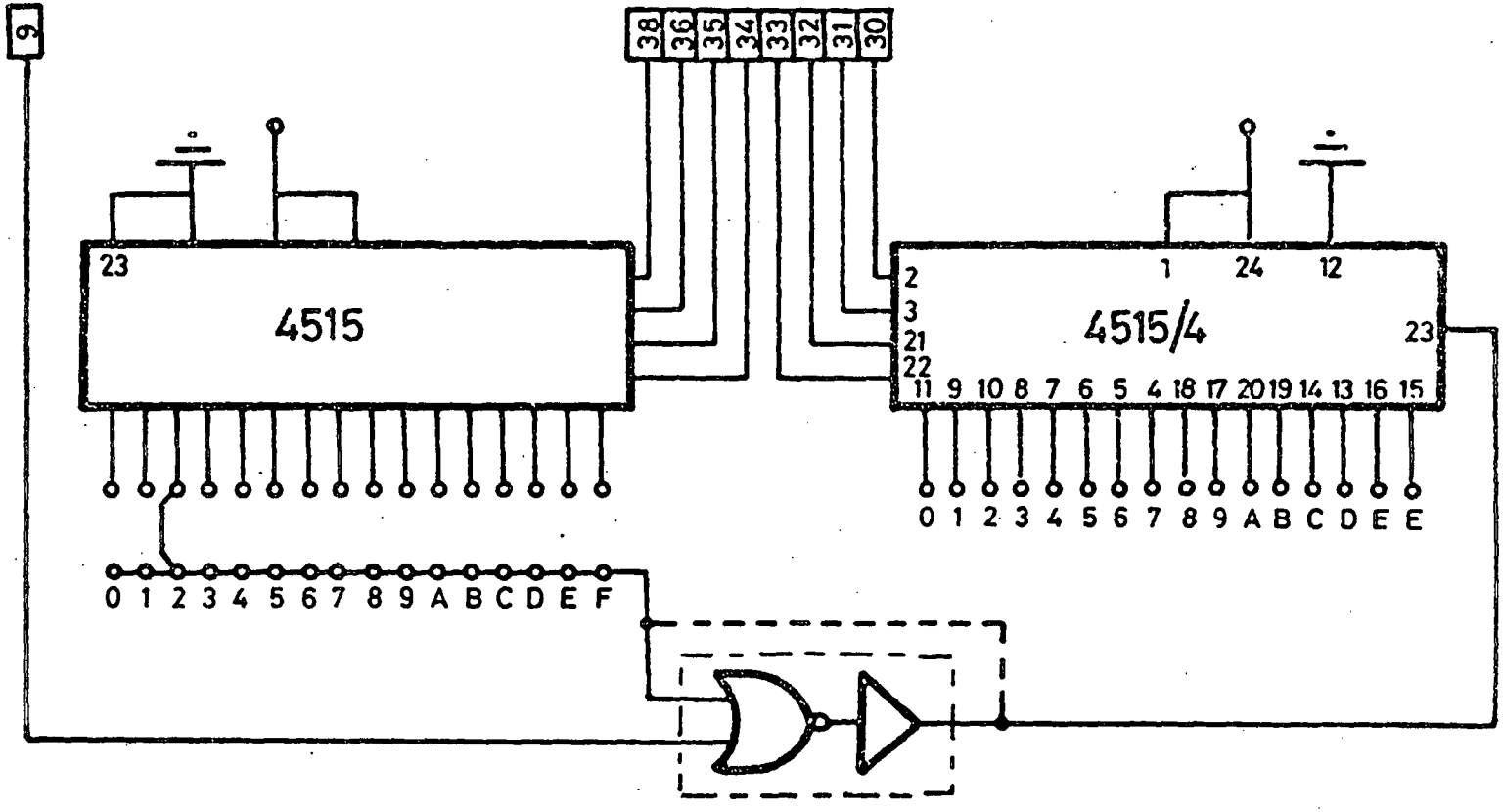

Fig. 3.6 The circuit diagram for the interface address decoder.

The PET memory expansion port used for the interface provides access to the buffered and decoded input/output lines from the 6502 microprocessor. The interface appears as 32 bytes of memory and occupies block 9 of the PET memory map. The different function within the 6522's are controlled and examined by writing to and reading from these 32 locations. Table 3.2 shows the functions of the 16 registers in one 6522. The DATA 6522 is unrestricted by external hardware except a link between pins 17 and 18 used for stepper motor timing. The four Register Select lines RSO-RS3 are connected to the computer address lines to allow the computer to select the internal 6522 register which is to be accessed. The other 7 bits are connected to two 74LS139 and other NAND gates (7402) which act as the decoder for the PET address lines.

The CONTROL 6522 is more restricted to external hardware. PB5, 6 and 7 and the IRQ output are solely used to provide a highly repeatable monostable for counting purposes. The first PAO-7 drives the address lines of the interface bus and CA2 is used as the strobe line. The 8 bi-directional data lines (DO-D7) are used to transfer data between the 6522 and the computer. The direction of data transfers between the 6522 and the computer is controlled by the READ/WRITE line (R/W). If R/W is low or 'O' data will be transferred out of the computer into the selected 6522 register (write operation) and if R/W is high or '1' and the chip is selected, data will be transferred out of the 6522 (read operation). The RESET input ($\overline{RES}$) clears all internal registers to logic 'O' which places all peripheral interface

Table 3.2 Function of the 16 registers of one 6522.

ADDRESS	MNEMONIC	FUNCTION	USE IN 'CONTROL' CHIP	USE IN 'DATA' CHIP
0	ORB	Output register B	bit 5 resets counters (PB5=0) and starts count time (PB5=1) Bit 7 = 1 on count finished	Data in/out, low byte
1	ORA(H)	Output register A, with handshake	Outputs addresses	Data in/out, high byte
2	DDRB	Data direction register B	Sets bit 6 as input (to timer two) other bits as outputs.	Set to 255 for Data Out or 0 for Data In
3	DDRA	Data direction register A	Set to 255 to allow address output	Set to 255 to Data Out or 0 for Data In
4	T1C-L	Timer One counter lower byte	Set to 60	together determine
5	T1C-H	Timer One counter higher byte	Set to 195 together with T1C-L =60, gives 0.1s clock on PB7	step motor speed
6	T1L-L	Timer One latch lower byte	-	-
7	T1L-H	Timer One latch higher byte	-	-
8	T2L-L	Timer Two latch lower byte	together determine count	-
9	T2C-H	Timer Two counter higher byte	period (in multiples of 0.1s)	-
10	SR	Shift register	-	divide step motor speed by 8
11	ACR	Auxilliary control register	-	
12	PCR	Peripheral control register		
13	IFR	Interrupt flag register	bit 7 detects 'count finished'	
14	IER	Interrupt enable register	enables timer 2 interrupt ('time out' for counters)	enables SR interrupt ('time out' for stepper motors)
15	ORA(NH)	Output register A no handshake	Output addresses without latch pulse	Data in/out, high byte, no handshake.

lines in the input state, disables the timers, shift register etc. and disables interupts from the chip. The 7474 and the NAND gates are used as a synchronizing circuit in counting circuits to provide an accurate gating signal. A RESET line and the GATE function is used to clear all counters before each counting period to avoid spurious data being collected. The connections of the 1K byte EPROM, MM2708 which contains the subroutines is also shown in Figure 3.5. The interface board can accommodate up to 3 EPROMS if needed.

3.4.2 The Stepper Motor Module

The stepper motor module (Figure 3.7) provides the right signal level to drive the unipolar Impex stepping motor type 9904-112-04101 which requires 350 mA per phase. The binary up/down counter IC type 40193 is used. The inputs (pin 4 and 5) are each connected to the output of a three input NOR gate (1a and 1b). One input from each NOR gate is always at logic 'O' if the manual control is not used and the second input is also at logic 'O' if the interlock is made which is necessary for the motor to step. The motor will rotate in a clockwise direction if the step pulses are sent to the up input and anticlockwise if sent to the down input. Therefore each motor drive will have two addresses, one for each direction of rotation. The two outputs of the up/down counter are connected to a network of a two input exclusive OR gate and the outputs (A, B, C and D) from the gate network are each connected to identical circuits comprising transistors, resistors, diode and capacitor one of which is

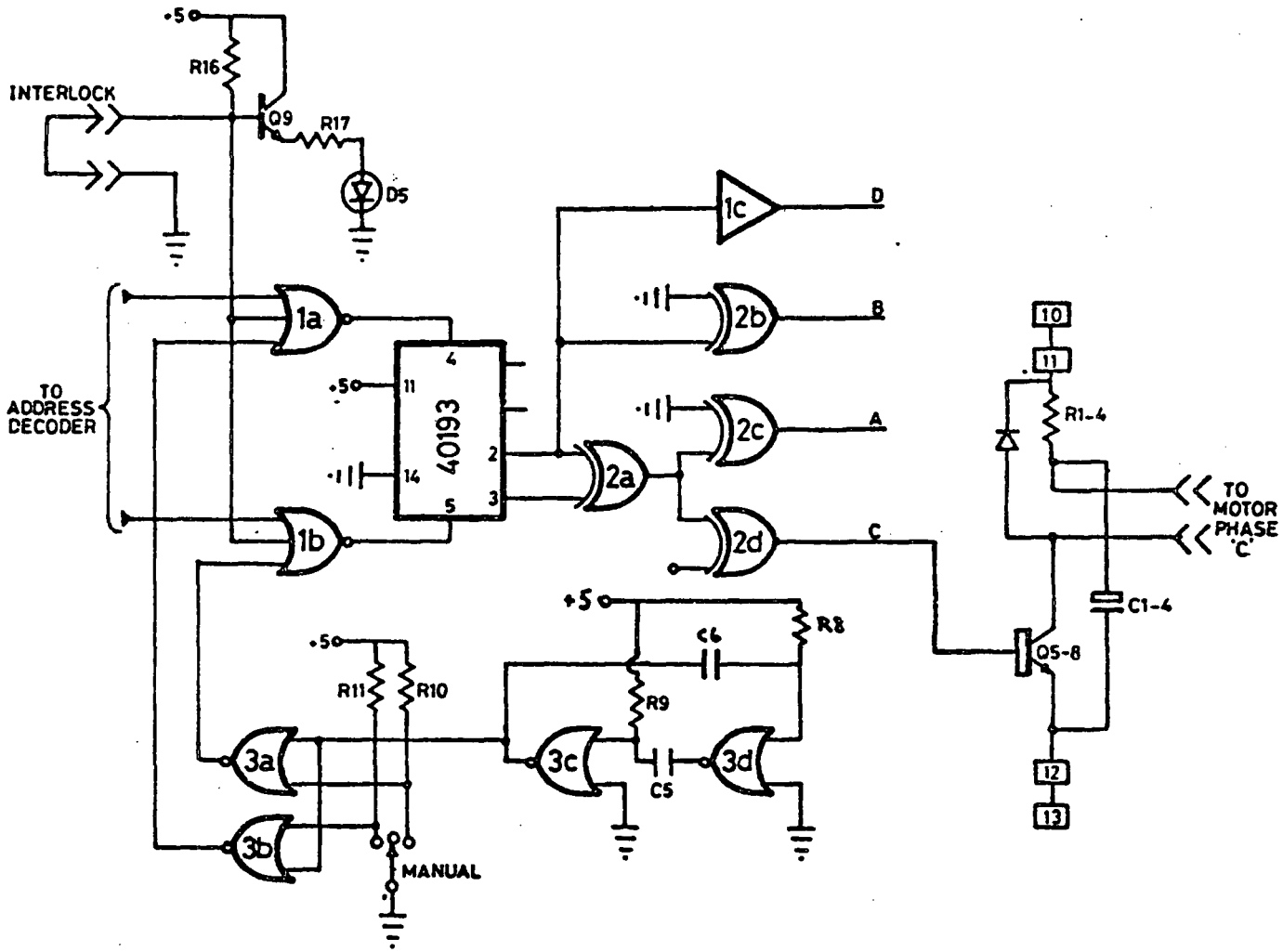

Fig. 3.7 The 4-phase stepper motor circuit used with the MINICAM interface for the computer control system.

also shown. A special routine in the EPROM can be called to facilitate programmed use of the module.

The module can drive stepper motors which takes current up to 500 mA by changing the values of the resistor R_{1-4} and can also drive the motors manually. A switch is provided on the front panel to select the direction of rotation of the motor. The resistor R_9 and capacitor C_5 determine the speed of the motor in the manual mode. For convenience the value of R_9 is chosen to be 330 KΩ and C_5 is 0.047μF so that the time between motor steps of 7½ degrees is approximately 0.016 sec (= RC) that is about 62 steps per second. In the manual mode the first input of the NOR gate (1a, 1b) which are connected to the address decoder will be at logic 'O' and the third input will oscillate between logic 'O' and logic '1' thus providing the step pulses to the inputs of the up/down counter. When the interlock is broken the indicator light (D5) on the front panel illuminates. It is this facility which is used in connection with the interlock terminal to the microswitch system in the diffractometer to inhibit all motion if the limit switch breaks which corresponds to the interlock system being in open circuit and thus the motor stops stepping.

Access to the stepper motor routine is via USR(1). For example,

```
20 A% = 32 : N% = 100 : T% = 1 : A = USR(1)
```

This program causes the motor with address 32 to advance 100 steps with time proportional to T% between each step.

3.4.4 The Dual 16-bit Scalar or Pulse Counter

The C-MOS integrated circuit type 4502 which is a Strobed Hex inverter/buffer and a dual 4-bit binary up counter type 4520 form the main components of the dual 16-bit binary counter module. Each counter comprises two 4520's connected in cascade and three 4502's. Figure 3.8 shows the connections between them.

The dual 4-bit output of the 4502's (pins 3,4,5,6 and pins 11,12,13,14) are each connected to the inputs of the 4520's (pins 1,3,6,10,13,15). This corresponds to the first input of the NOR gates which make up the buffer. The second input of the NOR gates are earthed. This is the inhibit terminal (pin 12). Therefore the outputs (pins 2,5,7,9,11,14) are connected to the data to form a 16-bit pulse counter. The disable tri-state output of the 4502's (pin 4) are connected to the address decoder so that when the correct address is output onto the control bus the output of the counter is placed on the data bus. The gate signal from the interface bus (terminal 39) is connected to the clock input (pin 1) of one of the 4520's which enable the counter. This signal is controlled by an accurately repeatable timer governed by PET's system clock. The RESET (terminal 43) connection is also made with the 4520's (pins 7,15) so that the counter is reset before each period. Since Reset 1 and 2 and Gate 1 and 2 on the control bus are connected in parallel, all the counters are cleared together. Therefore it is not possible to acquire data for different periods in different counters. The counters will accept T.T.L. level positive

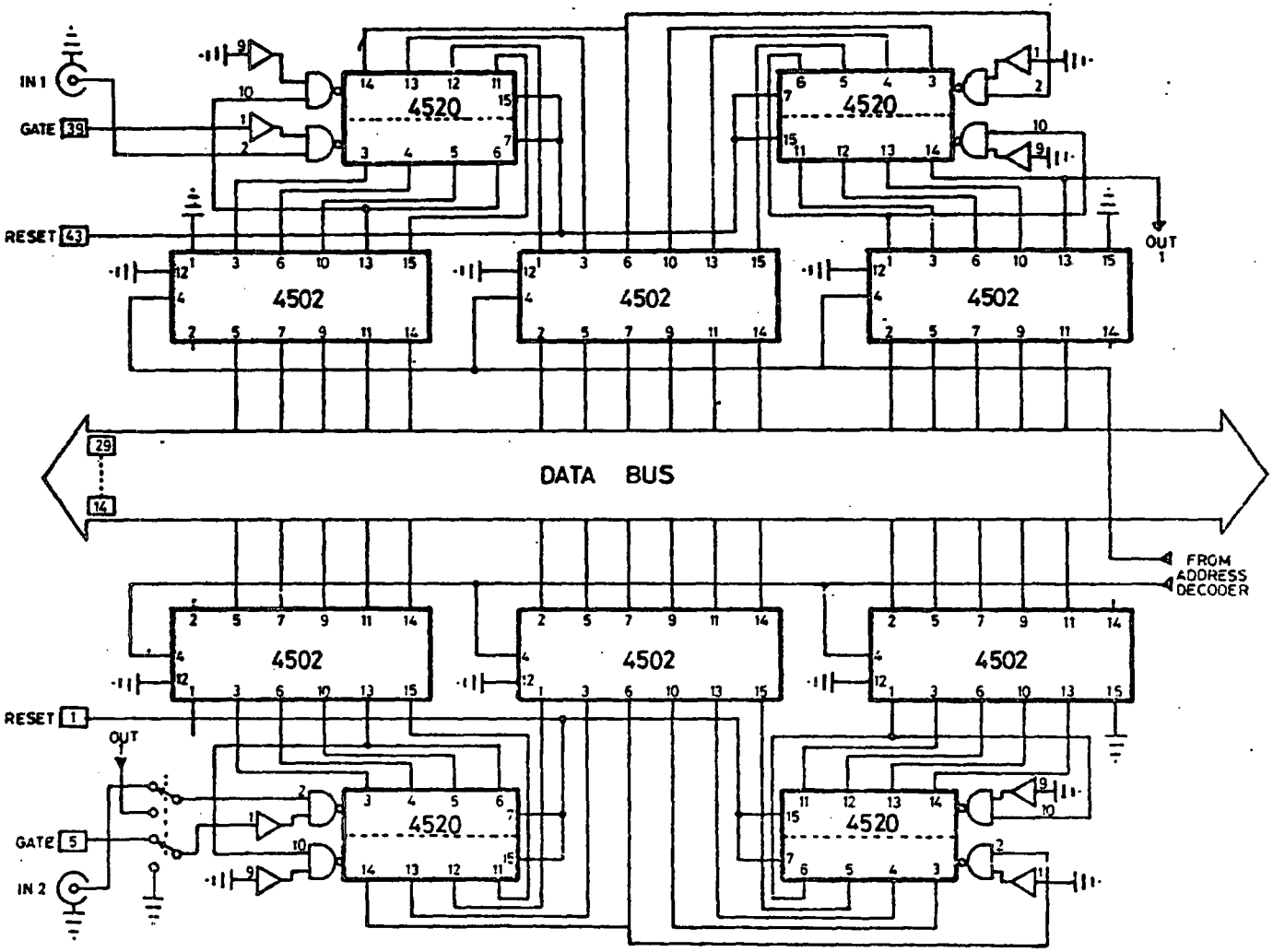

Fig. 3.8 The dual 16-bit binary counter used with the MINICAM interface.

going pulses of minimum duration 1μs and was made compatible with the output from our amplifier system which is greater than 5V by incorporation of a Hex Buffer type 4050 in the circuit since it has a high-to-low level voltage conversion. The output from the amplifier is fed to the buffer's input and its output is then connected to the enable terminal (pin 2) of the 4520.

A subroutine in the EPROM provides a routine which provides variable time intervals in units of 100 ms. The software first clears the counters, opens the gate for the programmed period, closes the gate and returns the value in the currently addressed counter. For example,

```
30  A% = 48 : T% = 10 : A = USR(2)
```

This program causes the counter with address 48 to count in intervals of 1 sec and the value is assigned to the variable A.

3.4.5 The Dual Digital-to-Analog Converter

The dual 12-bit D-A converter module provides two independent output voltages and is usually used here with an X-Y recorder. The module consists of 2 AD565 chips, 2 address decoders and 3 IC chips type 4508 (Figure 3.9). The AD565 is a fast 12-bit digital-to-analog converter with a stable voltage reference on a single monolithic chip. It uses 12 precision, high speed bipolar current steering switches, control amplifier, laser trimmed thin film resistor network and buried Zener diode reference to provide a very

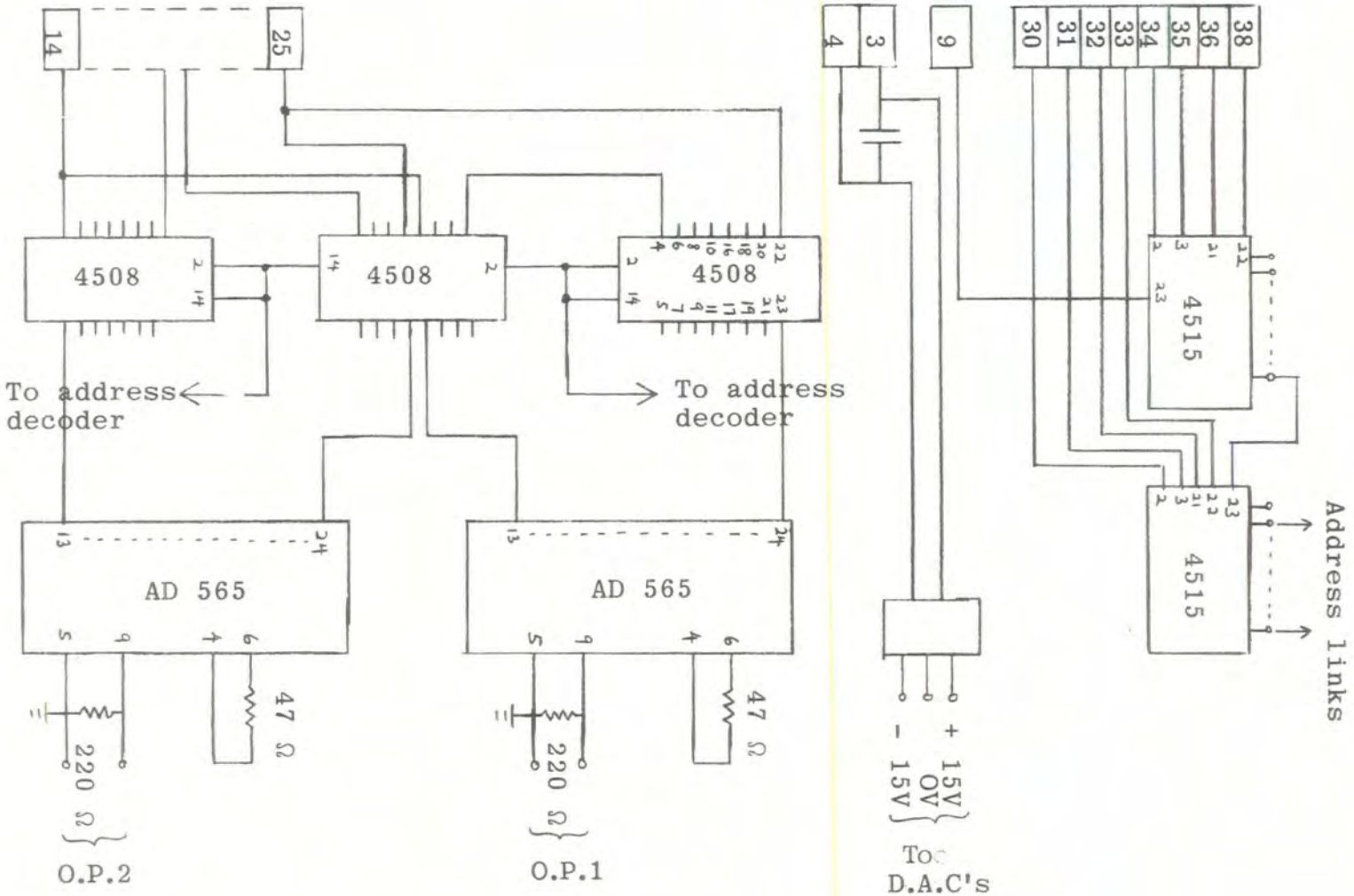

Fig. 3.9 The dual digital to analog converter used with the MINICAM interface.

fast, high accuracy analogue output current.

The digital input passed to either DAC must be in the range 0 to 4095 which corresponds to a maximum output voltage of 0.4V ± 5%. Values outside the range 0-4095 will cause the module to 'wrapped around'. Access to the converter is via USR(4). For example,

```
40  A% = 16: N% = 10: A = URS(4)
```

This causes the converter with address 16 to output the number in N% on the data bus and a single strobe pulse on the strobe line.

3.5 Manual Control System

The diffractometer was initially controlled manually before the time saving computer control system was installed. Figure 3.10 is the circuit diagram for the whole manual control system built by the author. The pulse generator provides square pulses and was fed into the stepper motor drivers. The drivers in turn generate sequential pulses suitable for driving the stepper motors which control the angular rotation of the goniometers. The counters register the motor steps. The microswitches incorporated in the diffractometer limit the range of the goniometers' angular rotation. The counter can also be used as an external counter by changing the selecting switch on the front panel. Appendix 1 shows the lay-out of the system.

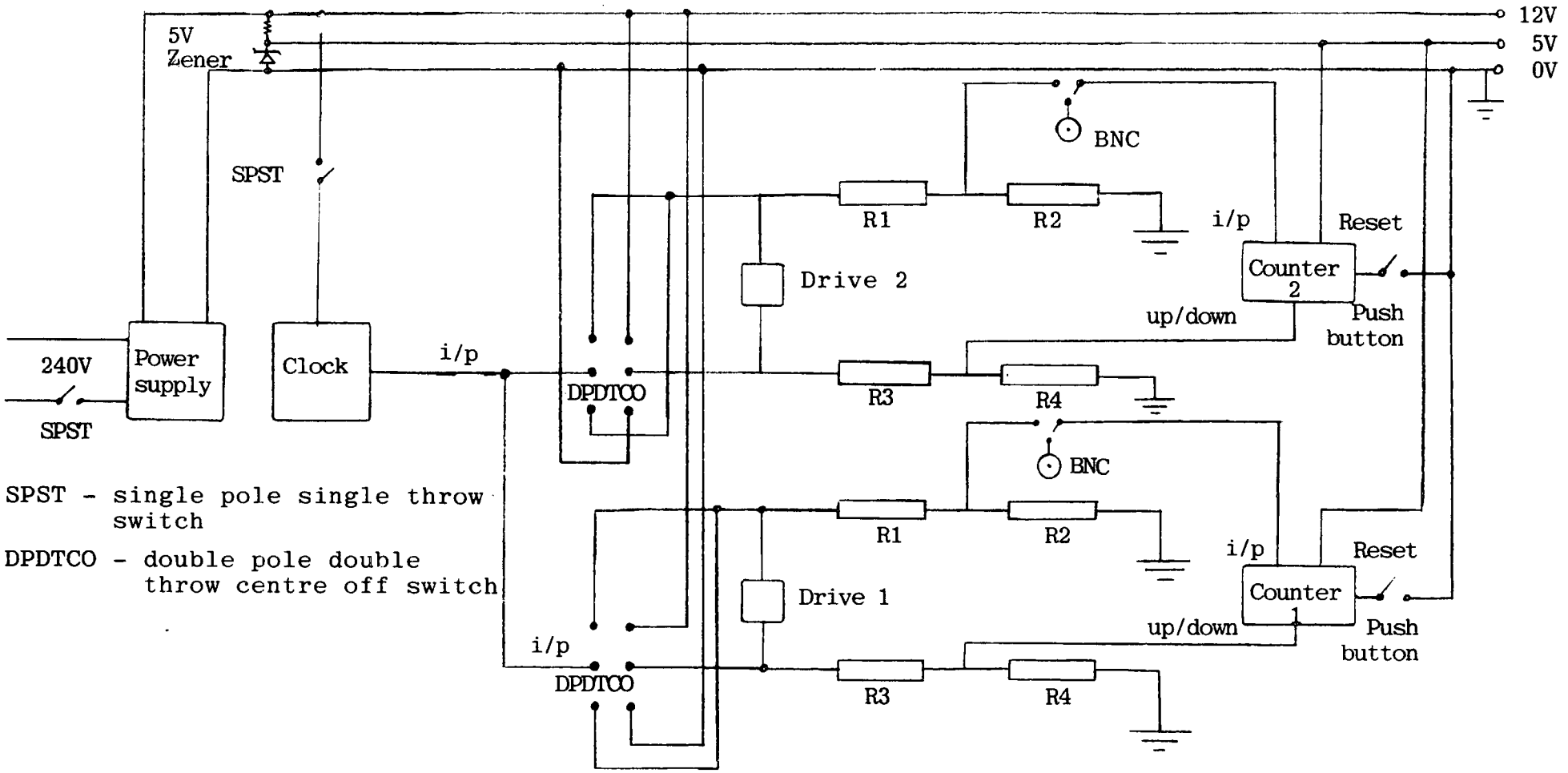

Fig. 3.10 The circuit diagram of the manual control system.

3.5.1 The Rack System and Power Supply Unit

The modules for the manual control system were also built in a standard 19 inch sub-rack system. It consists of a power supply module, a pulse generating module, a dual stepper motor module, a module to reduce the 12V supply to 5V and a dual counter module. 24-way module connectors with gold-plated silver contacts were used for this system. Its non-reversible plugs and sockets are particularly suitable for this plug-in module system.

The power supply unit has an adjustable voltage between 4 and 12V at 1A (RS951-253). The presettable voltage is adjusted by an integral preset control and short circuit protection is incorporated. The dimensions of the unit are 160 mm x 100 mm x 57 mm. The input voltage is between 216-260 V a.c. in the frequency range 50-400 Hz. In this particular application the output voltage is adjusted to 12V and a 5V supply is obtained by using a 5V zener diode. The unit was built in a 5 inch panel which carries the main power inlet, a switch and an indicator light.

3.5.2 The Pulse Generator

The pulse generator makes use of the 555 timer as a multivibrator. Figure 3.11a is the circuit used for the generation of pulses.

The pulse generating circuit can be divided into 3 sections as shown in Figure 3.11a (a) the unijunction transistor 2N2646, (b) the npn transistor BC107 and (c) the 555 timer. Referring to the left most part of Figure 3.11a which consists

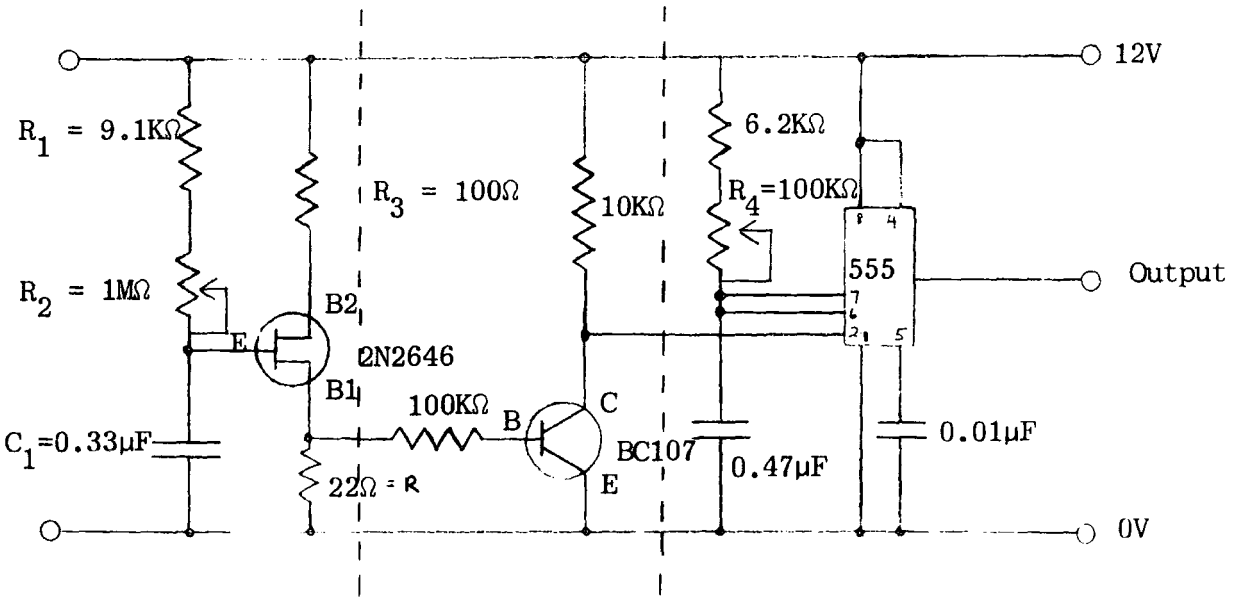

(a)

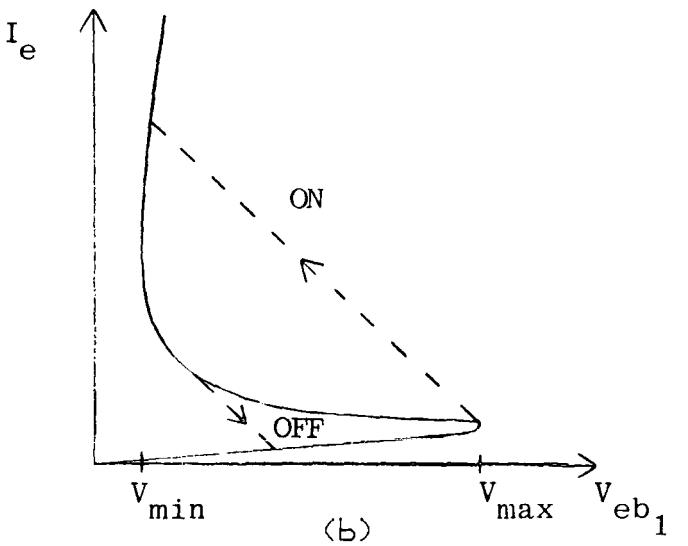

(b)

Fig. 3.11 (a) The pulse generating circuit for the manual control system.

(b) The ON-OFF state of the unijunction transistor 2N2646.

of the 2N2646; suppose the capacitor is in a discharged state initially. When a voltage is applied, the capacitor C_1 charges through the resistor R_1 and R_2 towards the supply voltage. The voltage V_e at the emitter and base 1 reaches the threshold maximum corresponding to the rapid transition to a very high emitter current. The unijunction transistor will then trigger to the on-state. A low-voltage state is attained by using a suitable resistor R_3 to prevent the device from burning out. When the transition has occurred V_{eb_1} is small and the capacitor then discharges through R. Therefore V_e falls and the transistor triggers to the off state. These two states, the ON and OFF states are indicated in Figure 3.11b. The charge discharge cycle will repeat continuously and the pulse repetition frequency can be varied by adjusting the variable resistor R_2.

The output pulse produced at the base 1 of the transistor is fed into the base of BC107 before it triggers the 555 timer. The transistor acts as a switch. The ON-state corresponds to the emitter junction being in the forward bias such that the base cirrent I_b is large enough to drive the transistor into its saturated condition where the collector cirrent I_c is at its maximum value and V_{ce} is small. In this particular case the transistor switch is used as a squaring or limiting circuit where a squared-off output signal is produced which is fed to the timer. Signal inversion occurs between the input and output of the transistor as shown by the table on the next page.

Input Signal	Transistor State	Output Signal
High	ON	Low
Low	OFF	High

The square-off signal triggers the timer or more appropriately the flip-flop circuit (bistable multivibrator) in the chip. To understand how the timer works consider the bistable multivibrator in Figure 3.12. R_{c1} and R_{c2} are equal but due to the random thermal fluctuation I_{b1} and I_{b2} are not equal. Suppose I_{b2} drops slightly from $I_b = I_c/h_{fe}$, this implies that I_{c2} becomes less and the voltage V_{c2} on the collector T_2 rises. As a result I_{b1} and I_{c1} increase causing the voltage V_{c1} on the collector T_1 to decrease. The reduction of V_{c1} cause I_{b2} to drop further. If this continues, due to the positive feedback, T_1 will ultimately be in an ON state and T_2 in an OFF state. This final state is completely stable unless an external triggering pulse is applied. In this case it is the squared off output pulse from the collector of transistor BC107. Therefore transistors T_1 and T_2 of the flip flop circuit will be in an ON and OFF state alternately at a rate 1/T depending on the value of the resistor R_2. The width of the output pulse is dependent on the resistor R_4.

This module was built in a 2 inch panel which carries a switch, a push button and a control knob to vary the frequency of the pulse generated. The push button is used to produce a single strobe pulse and is controlled manually.

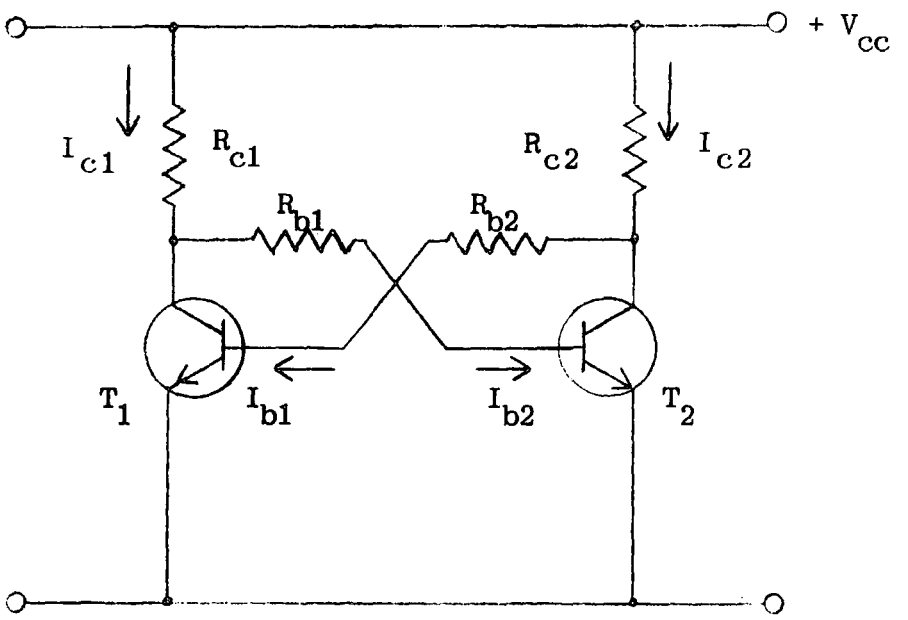

Fig. 3.12 The flip-flop circuit (bistable multivibrator).

3.5.3 The Dual Stepper Motor Driver

The integrated circuit SAA 1027 is used to drive the four phase unipolar stepper motor which controls the rotation of the goniometers. It changes a train of input pulses from the pulse generator to a sequential output pulse which provides the required pulse pattern for driving the stepper motor. The schematic diagram of the drive circuit is shown in Figure 3.13.

The dual stepper motor driver was built in a 2 inch panel which carries two double pole double throw centre off switches and a push button. The switches control the direction of rotation of each of the stepper motors. The stepper motor driver is powered from the 12V supply rail. The circuit consists of four output stages, a logic part and three input stages. The logic part is driven by three input stages: a triggering input T, an input R which change the switching sequence of the logic part so that the motor can rotate clockwise or counter clockwise and a set input S to set the four output stages. The triggering input receives the pulses from the pulse generator which signals the motor to step. Triggering only occurs when T goes from LOW to HIGH. When the triggering level is LOW V_T is between O to 4.5V and I_T is about 1μA, when it is HIGH V_T is between 7.5 to 12V and I_T is typically 30μA. The input R is connected either to OV or 12V by means of the selecting switch on the front panel and the direction of rotation is clockwise when V_R is low and vice versa when V_R is high. The three inputs are compatible with high noise immunity logic to ensure proper operation even in noisy environments.

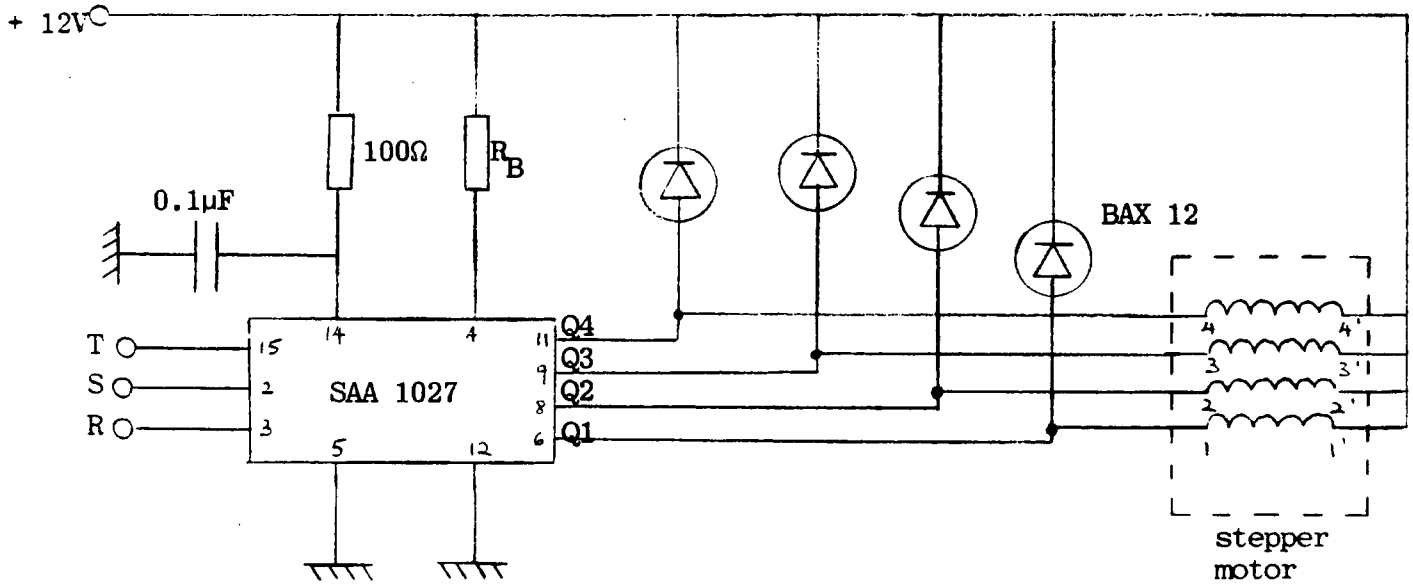

Fig. 3.13 The stepper motor driver for the manual control system.

The four output stages are connected to each of the 4 terminals of the stepper motor while the other four terminals are maintained at 12V. The output stages can supply 350mA in each phase. Integrated diodes BAX12 are connected across the motor windings to dissipate stored energy in the motor coils and to protect the output Q from transient spikes when they are switched on. Since the SAA1027 and the motor are connected to the same power supply, a RC network is used in the supply line of the logic part to prevent the logic sequence from being disabled by transient spikes, caused by the switching of the motor coils.

3.5.4 The Dual Counter System

The counter system uses the count display integrated circuit ZN1040E. The device is contained in a 28 pin dual-in-line package which requires a voltage supply of 5 volts and consumes an internal current of 90mA. The counter is capable of counting pulses up to 5MHz and driving directly 7-segment L.E.D. common anode or cathode displays with minimum external components. Other features of the ZN1040E includes 4 digit counter, up/down synchronous counting, separate memory latches, anticipatory carry/borrow output, counter cascading by direct connections, separate B.C.D. outputs as well as segment outputs, blanking including mark/space intensity control, automatic zero suppression which can cater for a decimal point, self scanning oscillator for synchronization, switch on reset which clears all counters, Schmitt input on count, inhibit and clear and lamp test facility. Only a few of the facilities are required for the

counter constructed. The minimum voltage for input logic 1 is 2V and the maximum voltage for input logic 0 is 0.8 volts.

The display board (RS 434-239) consists of two printed circuit boards, one accepts the ZN1040E and the other the display bezel which can accommodate the four common anode 7-segment L.E.D. All the facilities of the ZN1040E are brought to a 24-way gold plated edge plug. Both boards are interconnected by ribbon cables. This dual counter module was built on a 5 inch panel which carries a pair of display bezels and a pair of push buttons for resetting the counter. The input of the counter is conencted to the input of the stepper motor drive via the 24-way plug and socket and hence the counter displays the number of steps the motor moves. The up/down terminal is connected to the selecting switch of the stepper motor module which determine the direction of rotation of the motor. When the motor is rotating clockwise, the selecting switch is at logic 1 and the counter will count up or increase in counts and vice versa if the selecting switch is at logic 0. Therefore this keeps track the position of the goniometer.

The input of the counter and the up/down terminal only accepts voltages of not more than 5 volts. The output of the pulse generator which is fed into the stepper motor driver and thus the counter is greater than 5 volts and logic 1 also corresponds to a voltage of 12 volts for the selecting switch. Therefore before these voltages are fed to the counter input and the up/down terminal they are fed to a simple resistor network as shown in Figure 3.10 to drop the voltage to the

appropriate values before feeding it to the counter. This simple resistor circuit was built as another 2 inch module in which the front panel carries two single pole double throw centre off switches and two BNC sockets. The switches are used to select whether the counter is used for counting the motor steps or used as an external counter by an input through the external BNC sockets.

3.6 The Detecting System

The detector used for this system is a scintillation counter. The operation is based on three basic principles: (a) the ability of X-rays to cause certain substance to fluoresce and emit visible light, (b) the photoelectric emission of electrons when visible light is incident on a photosensitive surface and (c) the emission of secondary electrons by certain surface when primary electrons impinge on them. The amount of light emitted is proportional to the X-ray intensity and as the light emitted is very small a photo-multiplier tube is used so that a measurable current output is obtained.

The basic design of the counter is shown in Figure 3.14. The photomultiplier tube is highly evacuated and the semi-transparent photocathode is deposited on the inside surface of the tube window, whilst the scintillator is placed in contact with the outside surface using an optical grease. The major length of the tube consist of a series of metal electrodes called dynodes. Each dynode is maintained at a potential of about 100 volts higher than the preceding one. The scintillator used is a sodium iodide crystal activated

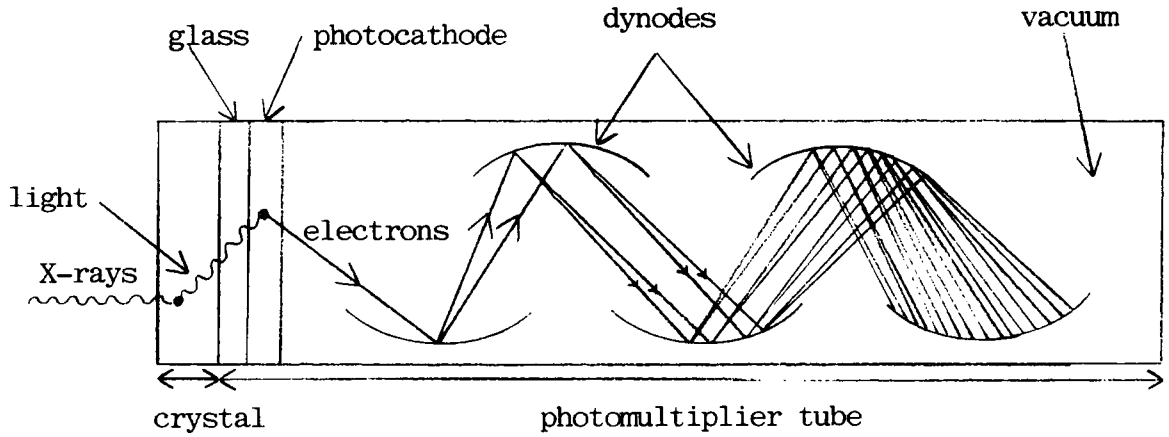

Fig. 3.14 Basic features of a scintillation counter.

with a small amount of thallium and emits light under X-ray bombardment (Rank Precision Instruments Type P1035). The light photons will pass through the tube window to the photocathode which in turn emits primary electrons with kinetic energy E given by

$$E = h\nu + \phi$$

where $h\nu$ is the energy of the light photon emitted by a quantum of X-rays and ϕ is the work function of the photocathode. The liberated electrons are then accelerated by the electric potential towards the first dynode whose surface is chosen such that for each incident electron, 5 or more secondary electrons are emitted. The electrons liberated from the first dynode are drawn towards a similar dynode by the electric field. The process continues and the total number of electrons leaving the last dynode depends on the number of dynodes used. If 10 dynodes are used the multiplication factor will be 5^{10} or about 10^7 or ten million times the original emission at the photocathode. The final emission is then led off by a collecting electrode, the anode, to be further amplified by a Harwell 2000 pulse amplifier. Figure 3.14 also shows the stages of multiplication for only one electron from the photocathode assuming that the gain of each dynode is 2. It is obvious that even a weak source of light may be detected by the photomultiplier. The whole process takes place in less than a microsecond so that a scintillation counter can operate at rates as high as 10^5 counts per second without losses. The main disadvantage of the counter is its relatively high background count of about 5 cps due

to electrons produced by thermionic emission from the photocathode even when no X-rays quanta are incident on the counter.

3.6.1 Photomultiplier Tube Dynode Chain Design

The basic function of the dynode chain is to provide the potential difference to accelerate and amplify the electrons emitted from its surface. The voltages for the dynodes are obtained from resistors in series across a high voltage source. The values of the resistors depend on the tube specification as well as the application. Therefore the choice of a photomultiplier tube and the dynode chain circuit is an important factor for good performance of the tube for the particular application desired.

The first important point to note is that the voltage between the cathode and the first dynode V_{k-d_1} must be adequate to ensure proportionality between the cathode current and the cathode illumination. It is desirable that the first stage gain is high and this is very much dependent on the voltage V_{k-d_1}. The recommended value is usually given in the specification of the tube. The intermediate stages usually operate satisfactorily from uniformly distributed voltage covering a wide range of 20 to 300V subject to not exceeding the maximum ratings of the photomultiplier. The voltage applied to the final dynode is more critical because of the high current flowing from them. For pulsed application the last three stages must be decoupled to suitable capacitors. Figure 3.15 shows the dynode chain circuit for the photomultiplier used, that is EM1 9524B. The tube is 30 mm

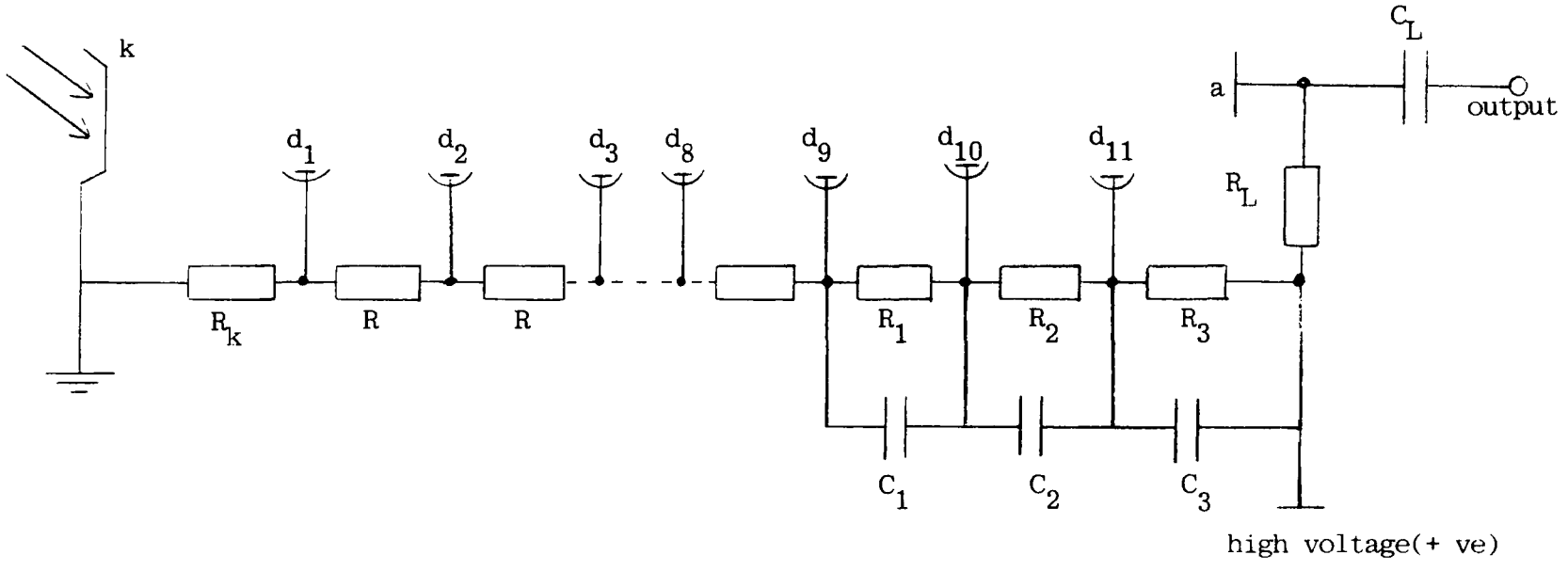

Fig. 3.15 Eleven stages dynode chain design.

in diameter having 11 box and grid dynodes with highly stable CsSb surfaces. The gain is typically 4 x 10^6 at 1000 volts and has the advantage of low current and a rugged design which are suitable for portable instruments and applications where available power is limited. The recommended cathode to first dynode chain voltage is 150V, and use of a Zener diode across this stage is preferable. The present tube is operated at 1 kV. The intermediate stages are maintained at 70V and the last three stages is at approximatdly 150V.

The values of the resistors $R_k = R_1 = R_2 = R_3 = 680$ kΩ, ¼W and $R = R_L = 330$ kΩ, ¼W. The decoupling capacitors C_1, C_2, C_3 and C_L are 1nF (750 V d.c.).

CHAPTER 4

SOFTWARE FOR CAMERA CONTROL

4.1 General Purpose Routine

The control program (Appendix 2) for the double crystal diffractometer is based on a combination of the three USR functions described in Chapter 3. The program is divided into eight routines which perform the various functions for the two axes and goniometers. Each routine is selected by inputting the string variables: RS, CO, SC, GN, FI, PL, FL and AU. A GOSUB statement (lines 260-330) is then executed depending on which routine was chosen. At the beginning of each routine the necessary variables are input. The routines also keep track of the axis and goniometer position in number of motor steps and display them and other necessary information before a RETURN command is encountered. Most of the eight routines can be interrupted by pressing any key, except the STOP key on the keyboard and a RETURN command is encountered.

4.1.1 The Reset, Count, Scan and Goniometer Tilt Routines

Figure 4.1 is the flow-chart for the control program. When the RUN command is executed to start the program the axis is chosen. The RESET routine or RS (lines 1000-1030 of program) allows the user to change to the other axis.

Fig. 4.1 The flow-chart for the control program of the double crystal diffractometer.

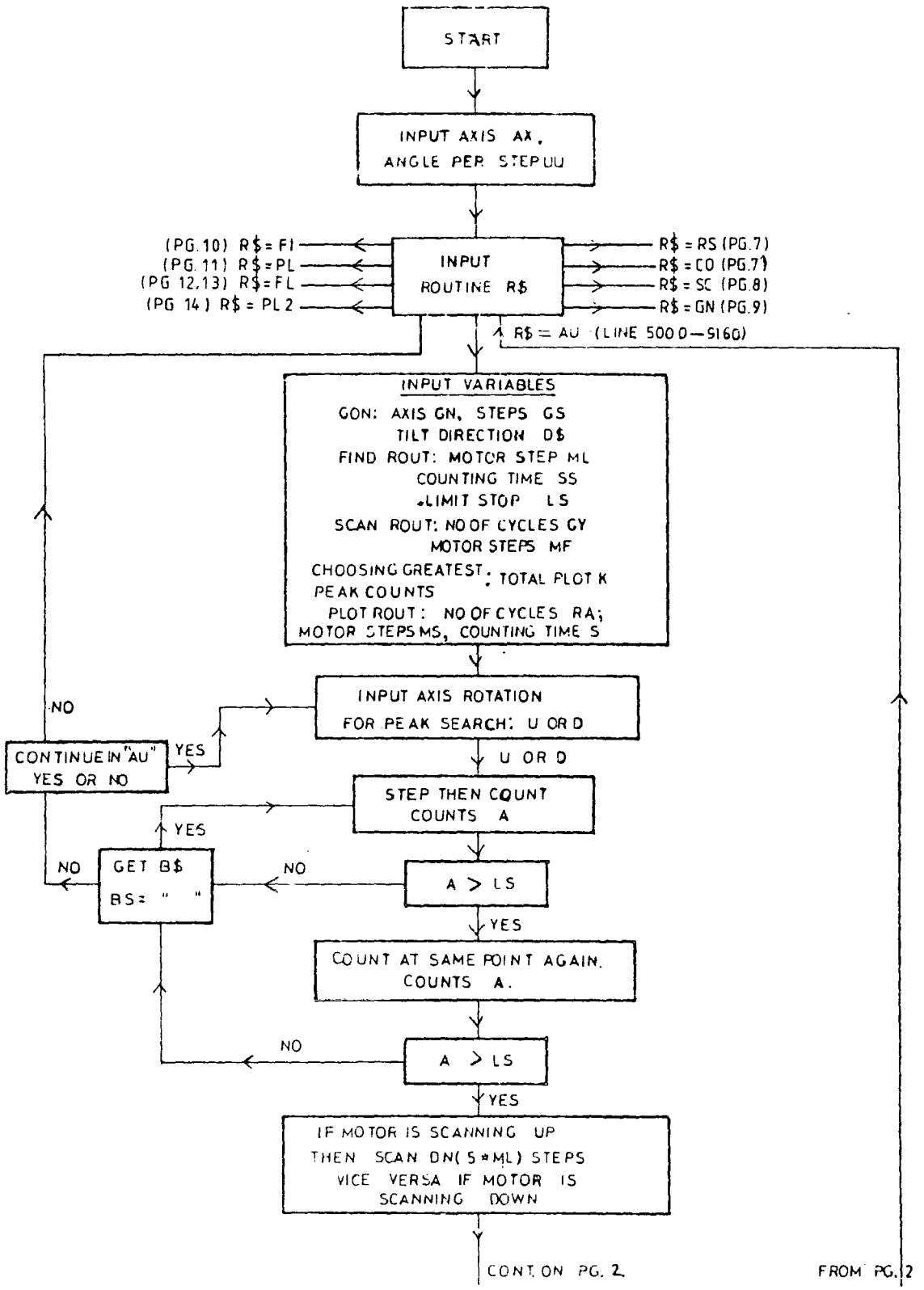

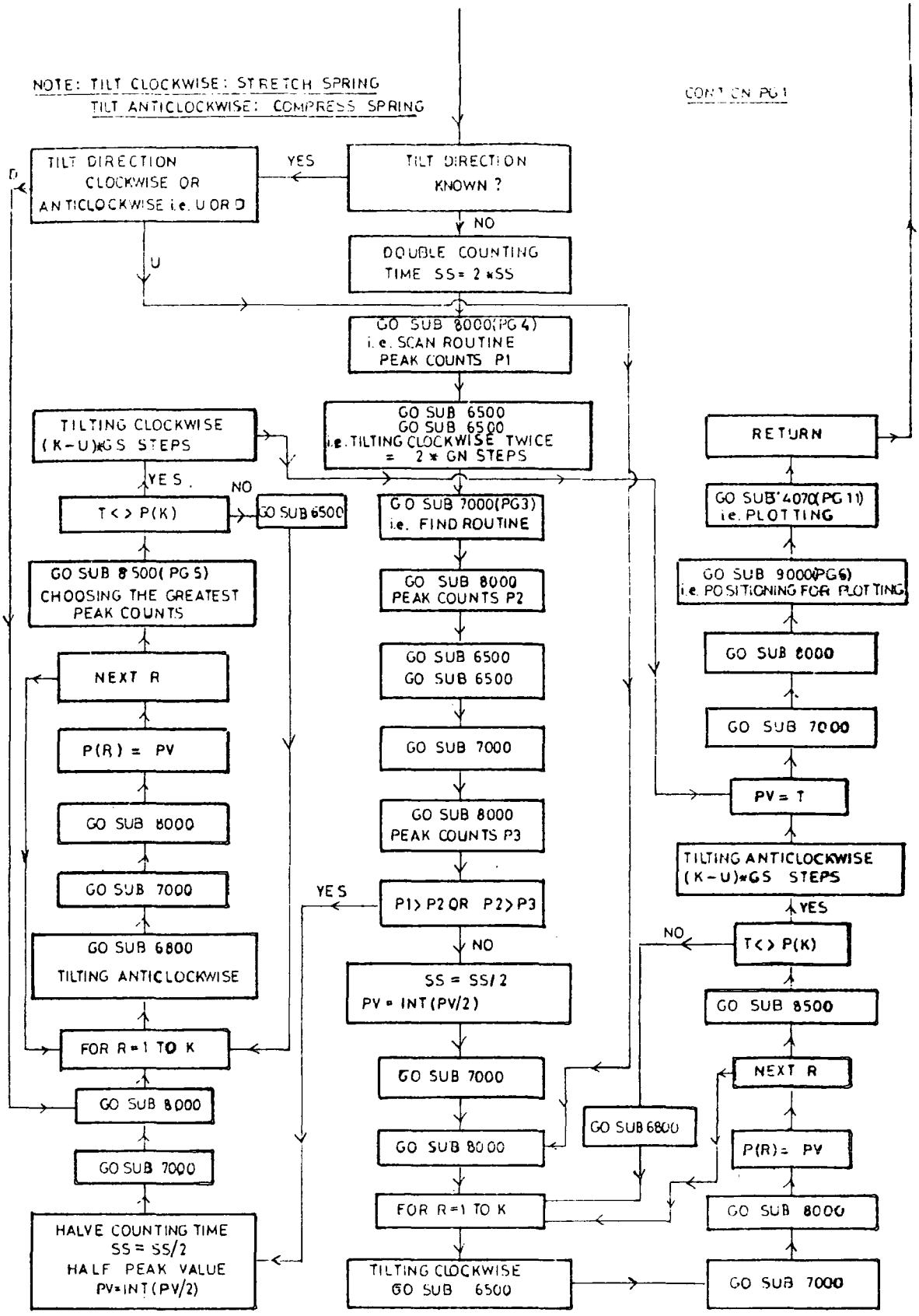
NOTE: TILT CLOCKWISE: STRETCH SPRING
TILT ANTICLOCKWISE: COMPRESS SPRING
CONT ON PG 1
TILT DIRECTION KNOWN ?
YES
NO
TILT DIRECTION CLOCKWISE OR ANTICLOCKWISE i.e. U OR D
D
U
DOUBLE COUNTING TIME SS= 2*SS
GO SUB 8000(PG 4) i.e. SCAN ROUTINE PEAK COUNTS P1
GO SUB 6500 GO SUB 6500 i.e. TILTING CLOCKWISE TWICE = 2 * GN STEPS
TILTING CLOCKWISE (K-U)*GS STEPS
YES
NO
T<> P(K)
GO SUB 6500
GO SUB 7000(PG3) i.e. FIND ROUTINE
GO SUB 8500(PG 5) CHOOSING THE GREATEST PEAK COUNTS
GO SUB 8000 PEAK COUNTS P2
NEXT R
GO SUB 6500 GO SUB 6500
P(R) = PV
GO SUB 7000
GO SUB 8000
GO SUB 8000 PEAK COUNTS P3
GO SUB 7000
YES
P1> P2 OR P2> P3
GO SUB 6800 TILTING ANTICLOCKWISE
NO
SS = SS/2 PV = INT(PV/2)
FOR R=1 TO K
GO SUB 7000
GO SUB 8000
GO SUB 8000
GO SUB 7000
GO SUB 6800
FOR R=1 TO K
HALVE COUNTING TIME SS = SS/2 HALF PEAK VALUE PV=INT(PV/2)
TILTING CLOCKWISE GO SUB 6500
RETURN
GO SUB 4070(PG 11) i.e. PLOTTING
GO SUB 9000(PG6) i.e. POSITIONING FOR PLOTTING
GO SUB 8000
GO SUB 7000
PV = T
TILTING ANTICLOCKWISE (K-U)*GS STEPS
YES
NO
T<> P(K)
GO SUB 8500
NEXT R
P(R)= PV
GO SUB 8000
GO SUB 7000

LINE 7000 — 7240

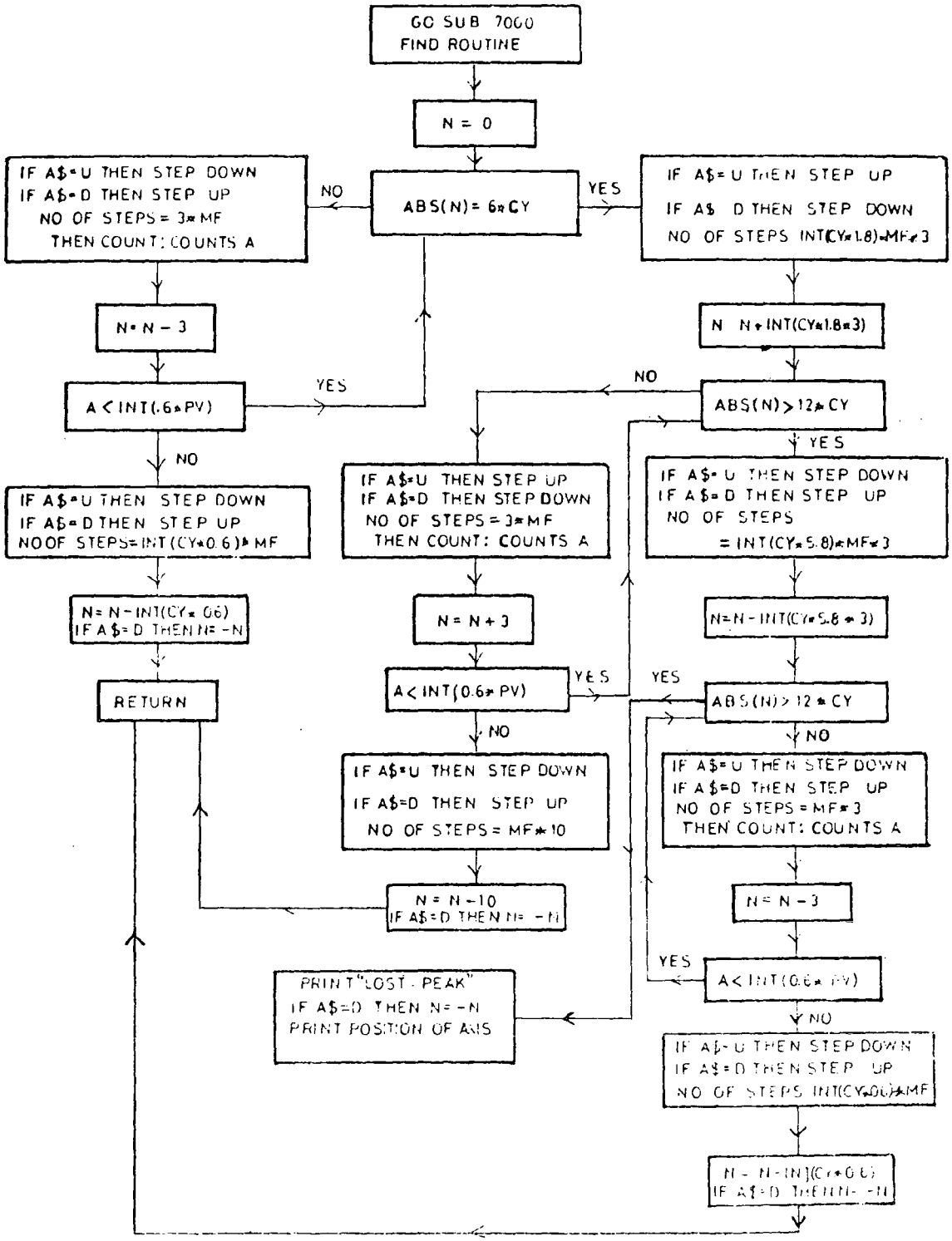

LINE 8000 – 8240

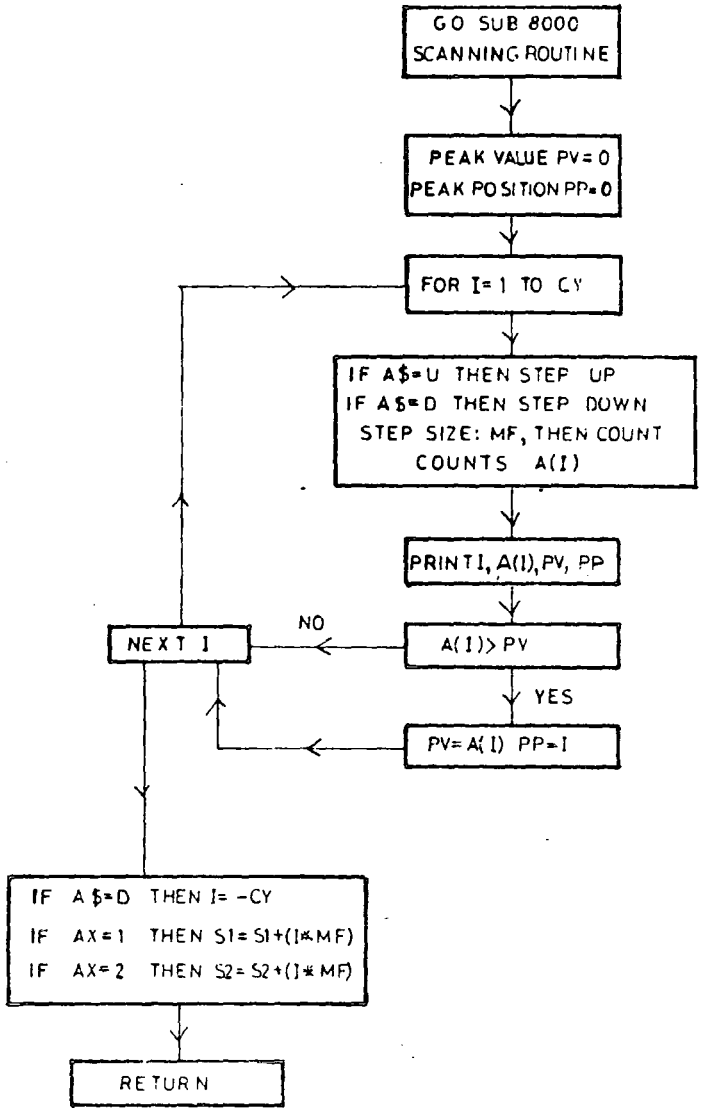

LINE 8500—8580

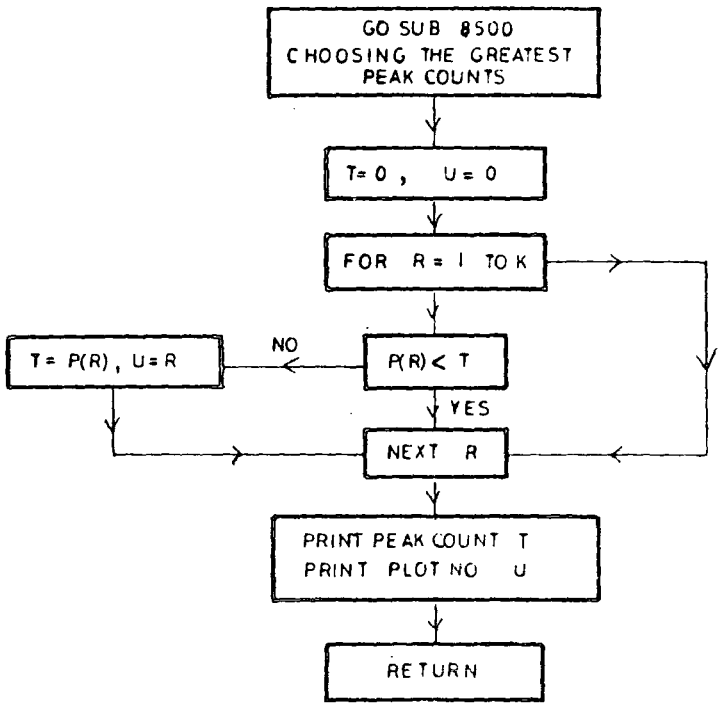

LINE 9000 — 9160

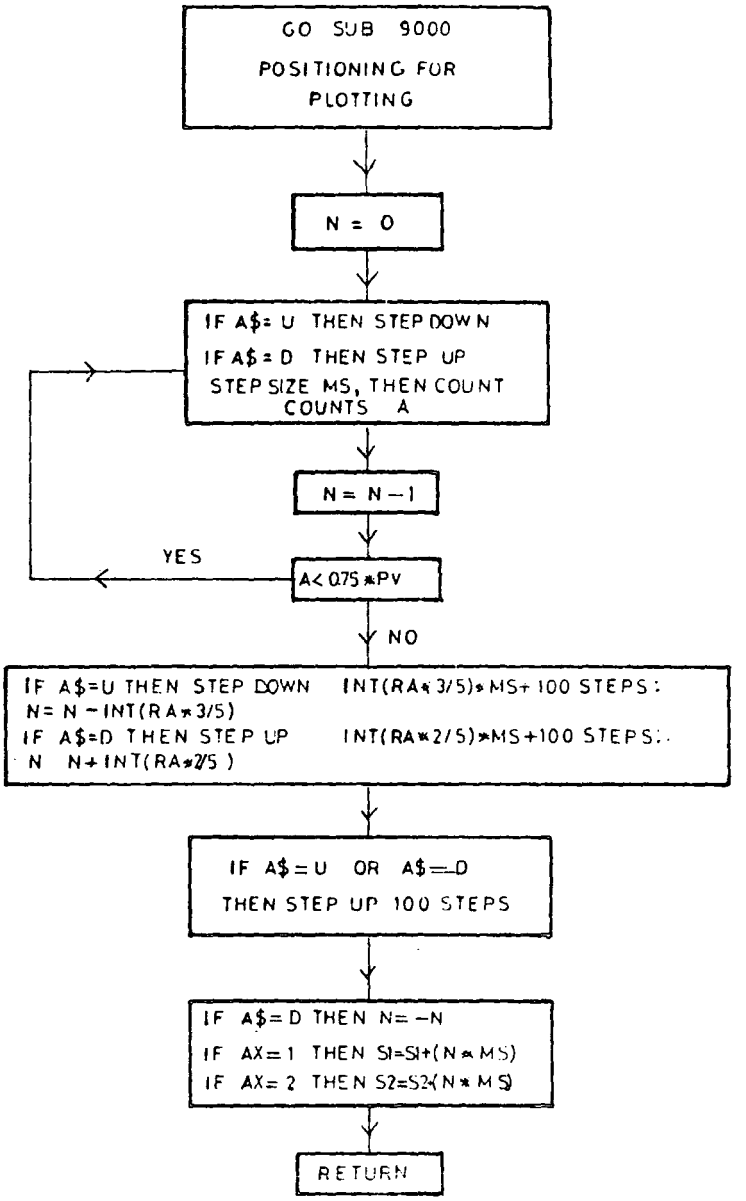

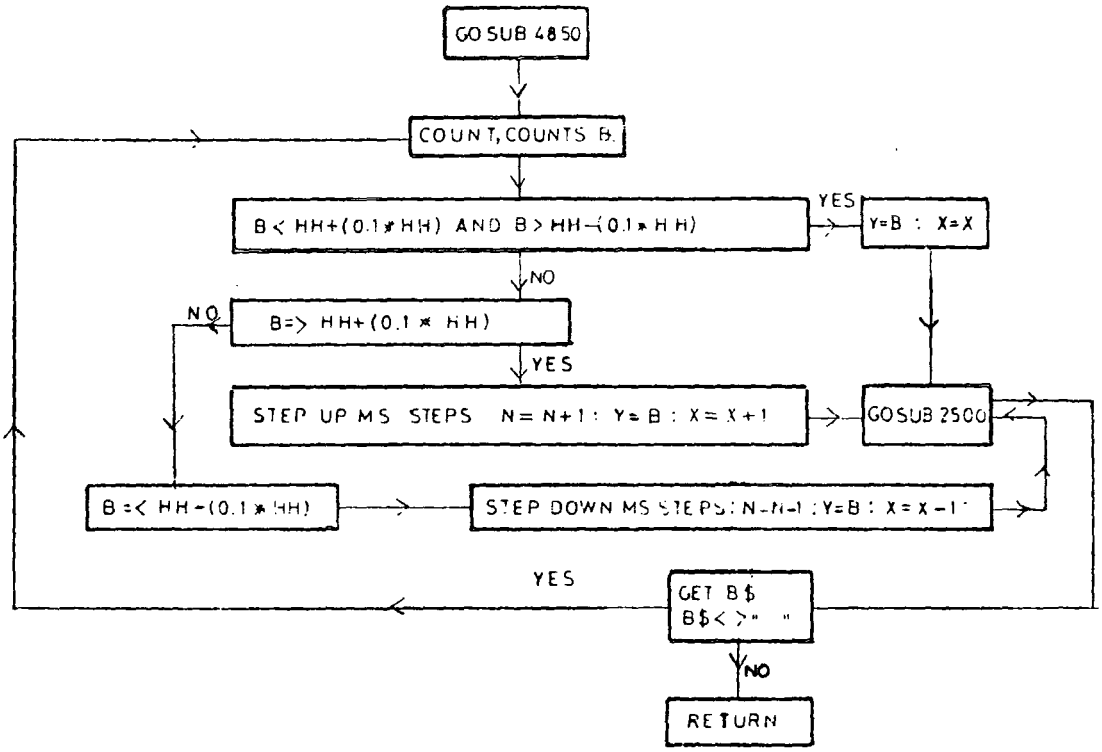
GO SUB 4850
COUNT, COUNTS B.
B < HH+(0.1*HH) AND B > HH-(0.1*HH)
YES
Y=B : X=X
NO
NO
B=> HH+(0.1 * HH)
YES
STEP UP MS STEPS N= N+1 : Y= B : X= X+1
GOSUB 2500
B =< HH-(0.1*HH)
STEP DOWN MS STEPS: N=N-1 : Y=B : X= X-1
YES
GET B$
B$< >" "
NO
RETURN

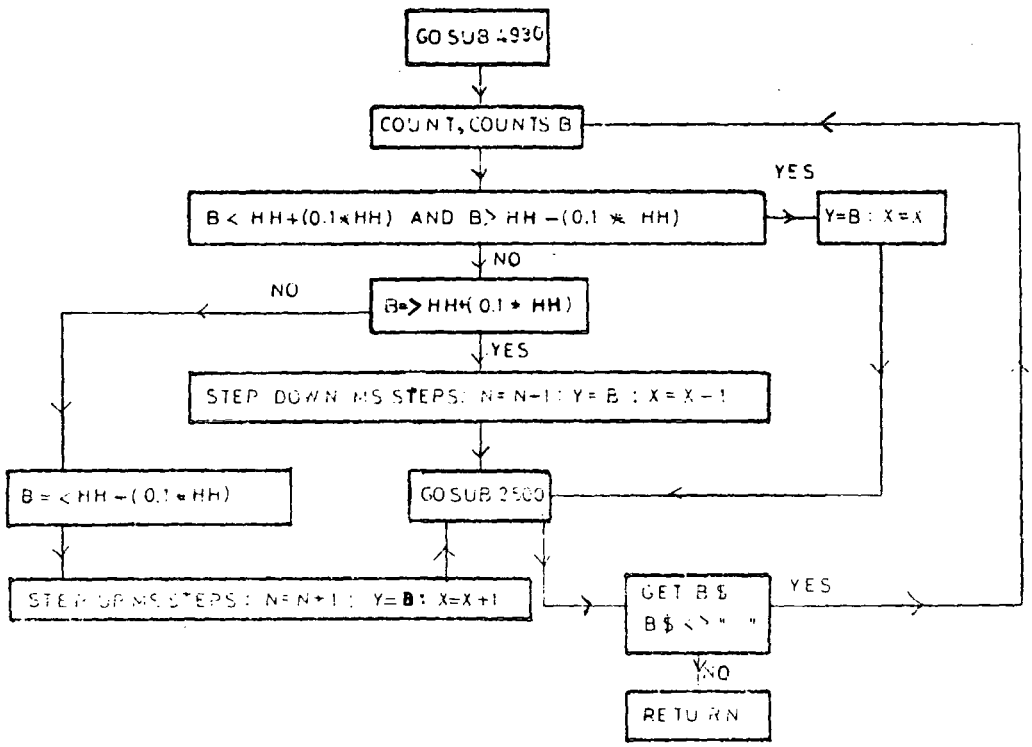
GO SUB 4930
COUNT, COUNTS B
YES
B < HH+(0.1*HH) AND B> HH-(0.1 * HH)
Y=B : X=X
NO
NO
B=> HHH(0.1 * HH)
YES
STEP DOWN MS STEPS: N= N-1 : Y= B : X= X-1
B = < HH-(0.1*HH)
GOSUB 2500
STEP UP MS STEPS : N=N+1 : Y=B: X=X+1
GET B$
B$ <>" "
YES
NO
RETURN

LINE 2000-2260

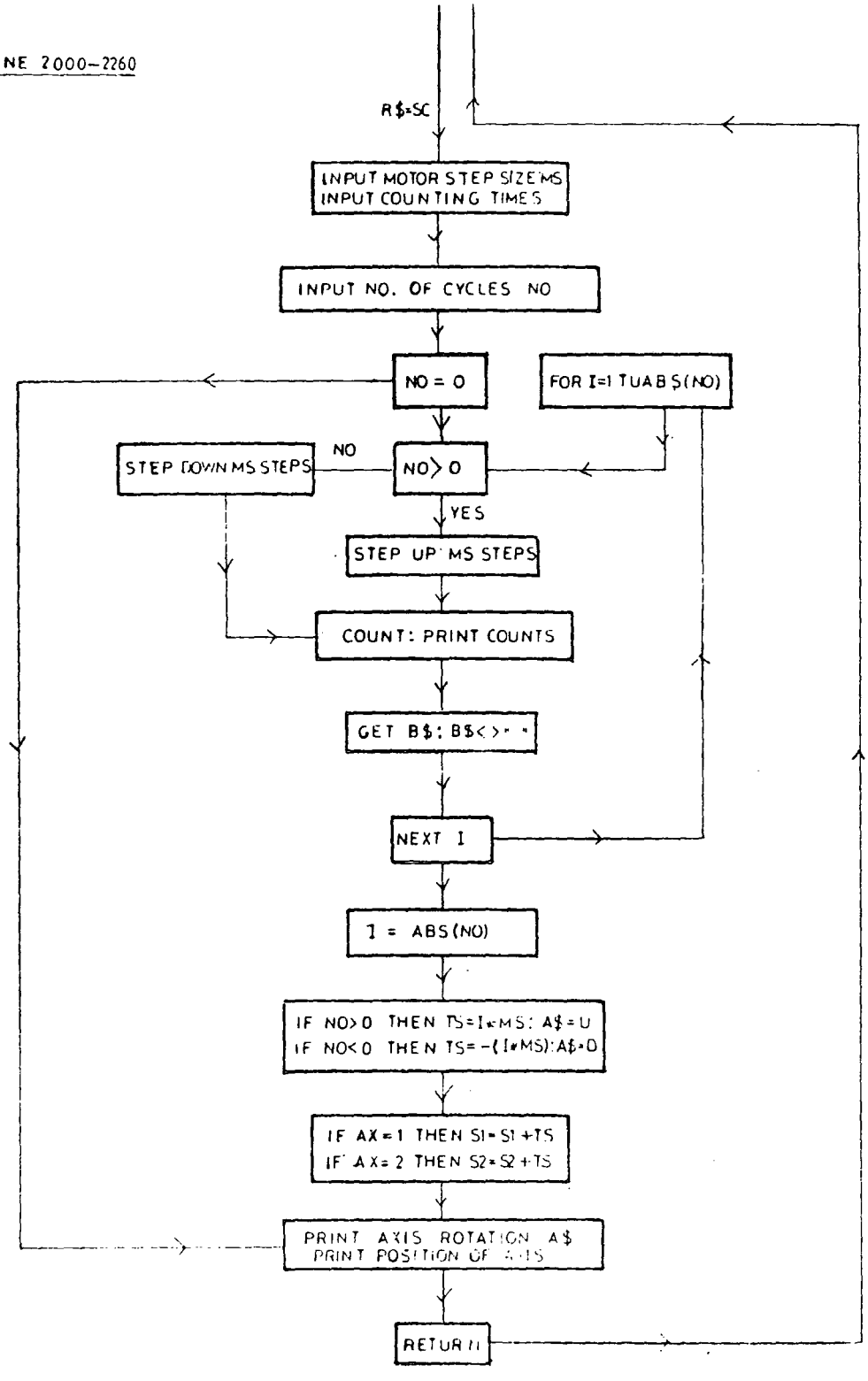

LINE 3000-3150

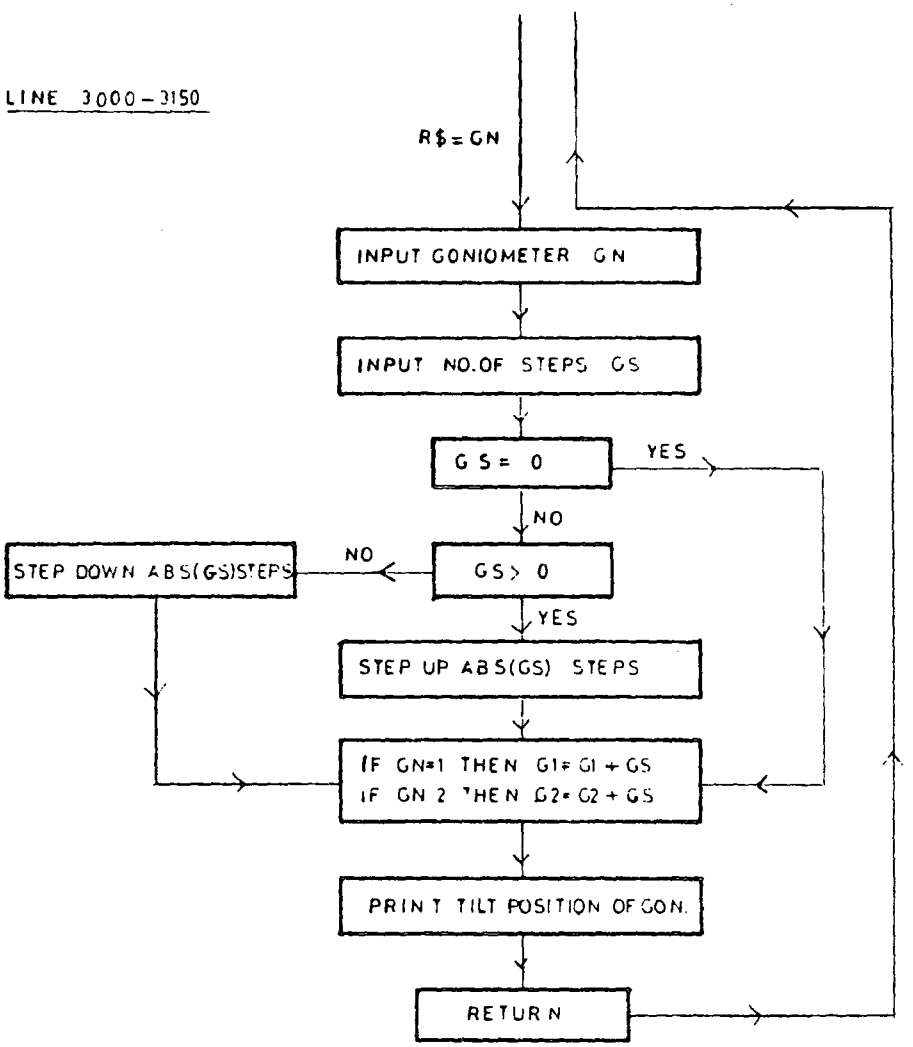

LINES 3500-3930

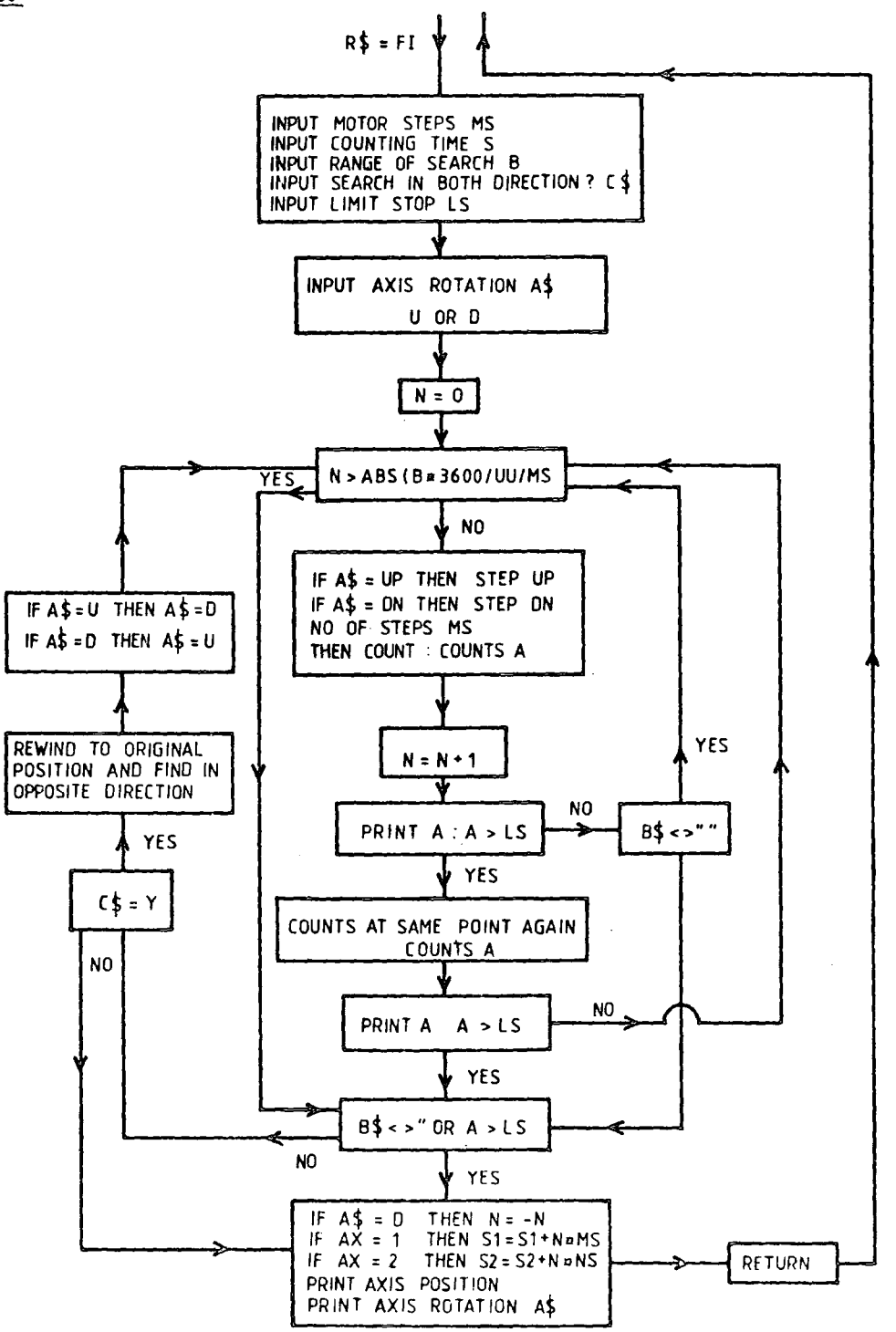

LINE 4000-4360

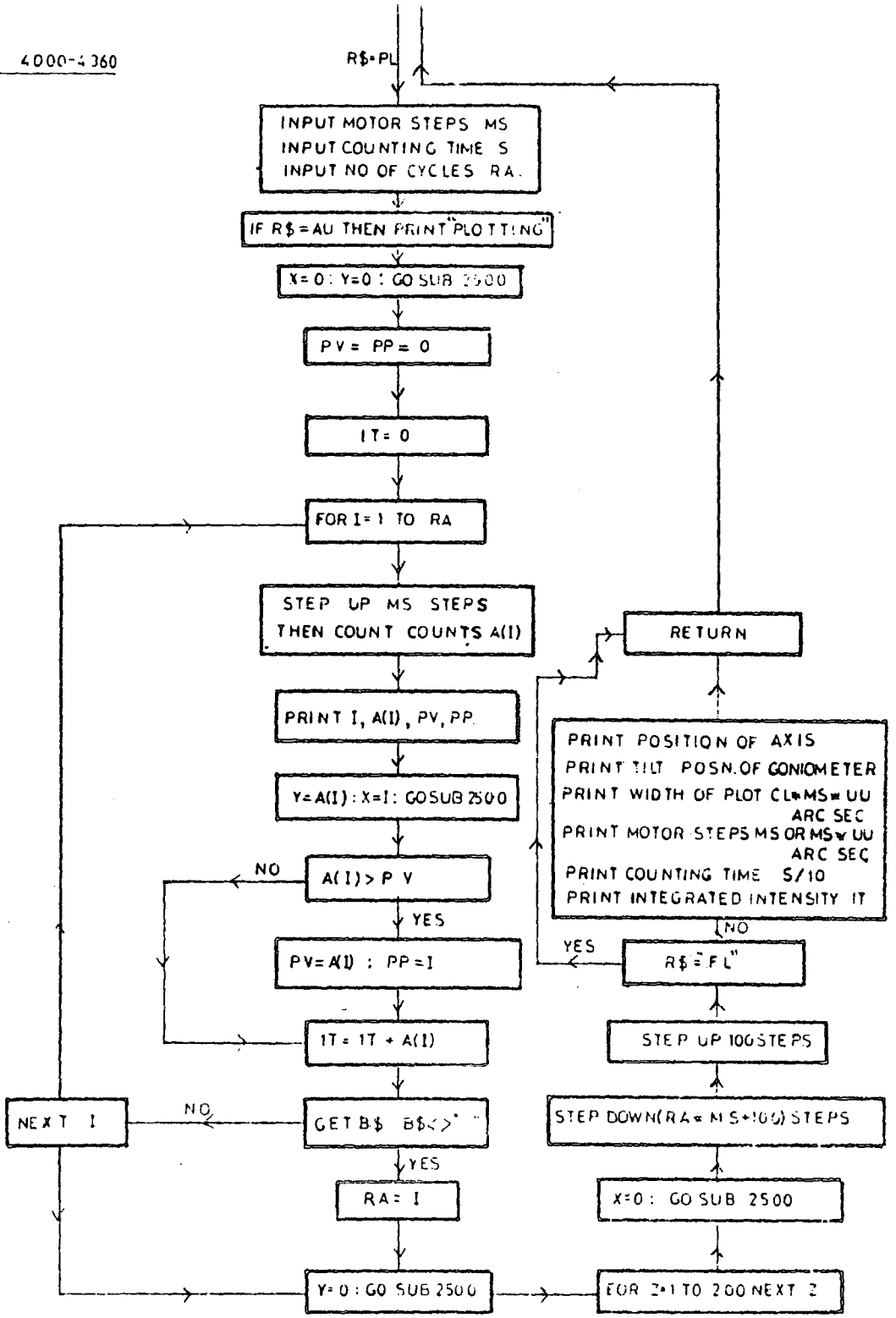

LINE 4500–4995

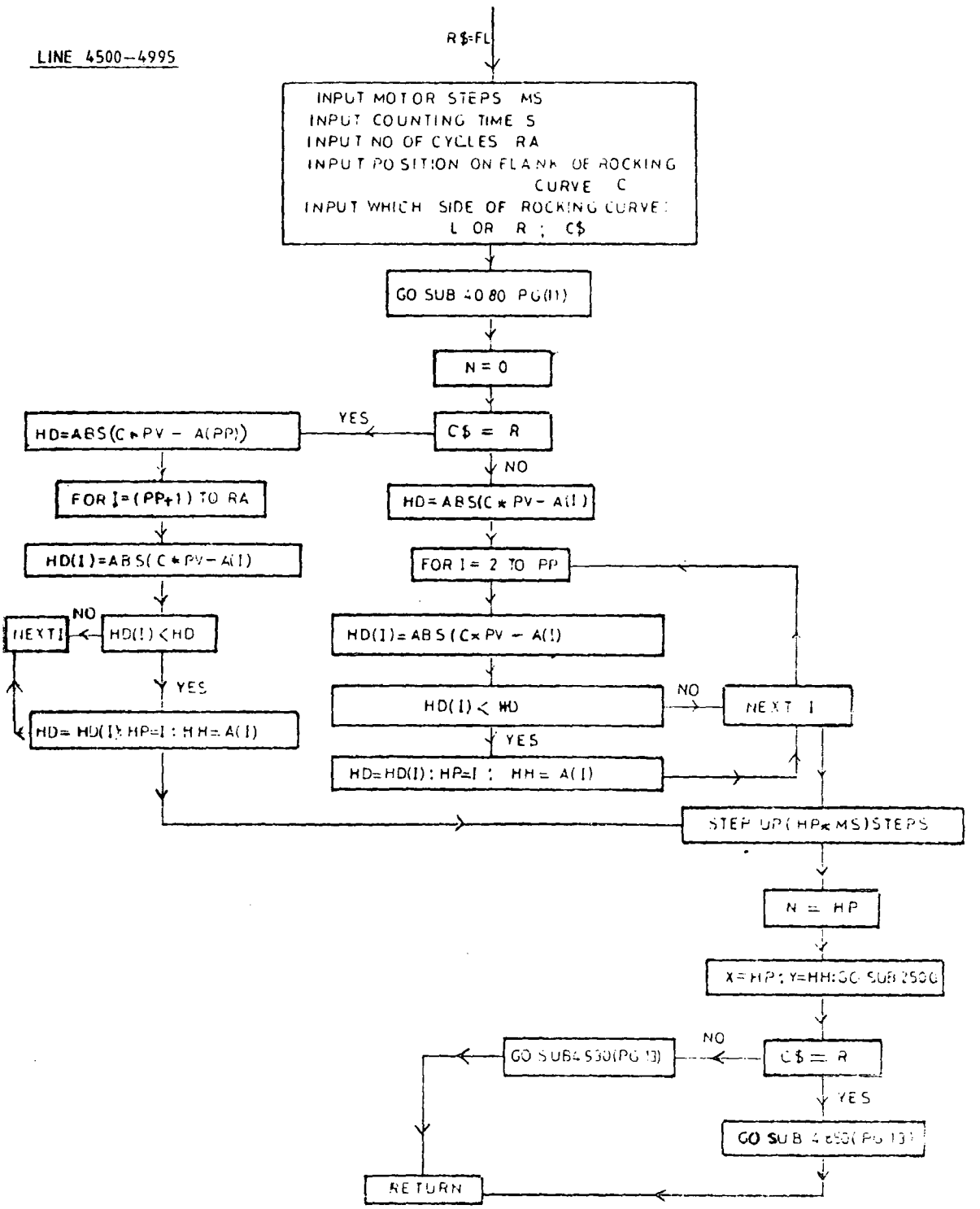

LINE 1000-1030

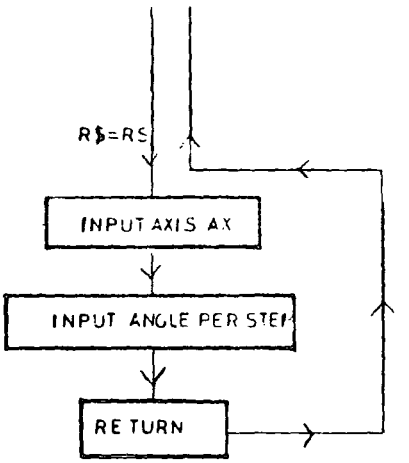

LINE 1500-1550

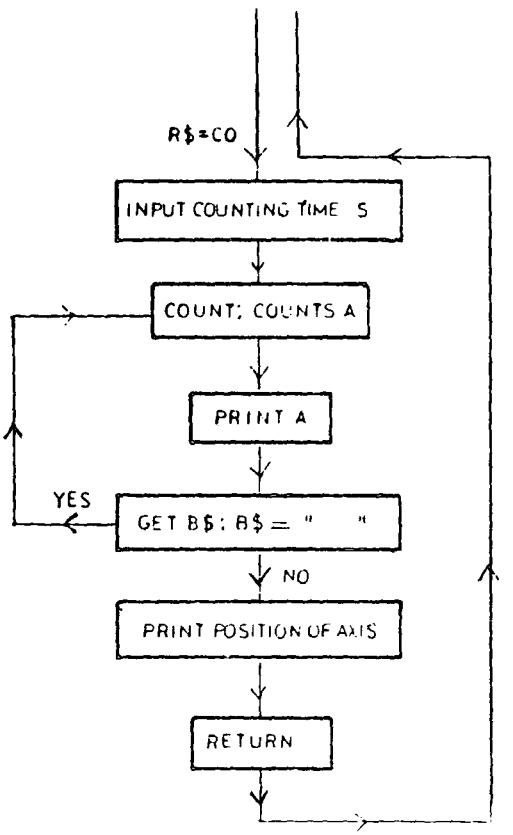

The flow-chart for the separation of layer and substrate.

LINE 9500 - 10170

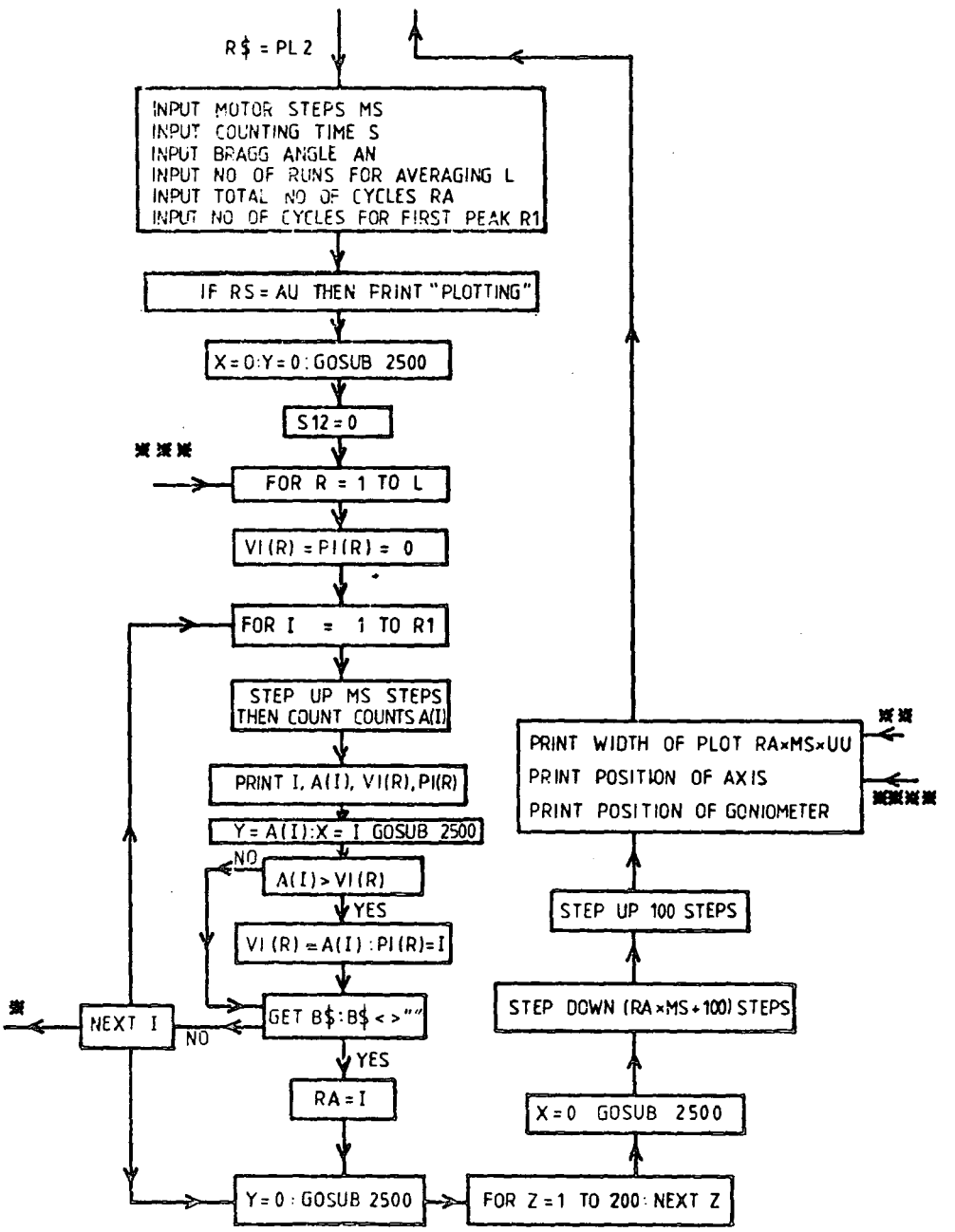

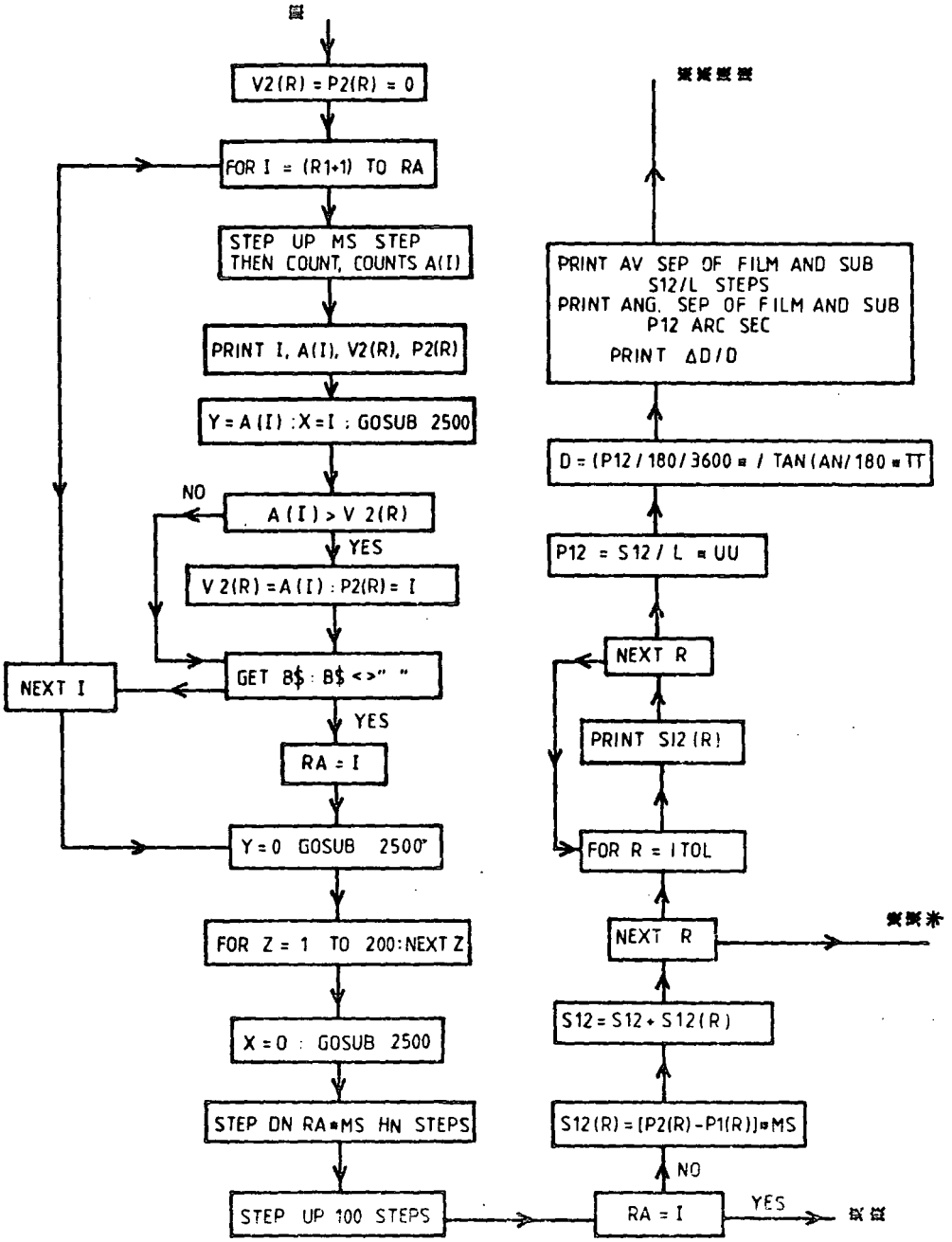
V2(R) = P2(R) = 0
FOR I = (R1+1) TO RA
STEP UP MS STEP
THEN COUNT, COUNTS A(I)
PRINT I, A(I), V2(R), P2(R)
Y = A(I) : X = I : GOSUB 2500
NO
A(I) > V 2(R)
YES
V 2(R) = A(I) : P2(R) = I
NEXT I
GET B$: B$ <>" "
YES
RA = I
Y = 0 GOSUB 2500"
FOR Z = 1 TO 200:NEXT Z
X = 0 : GOSUB 2500
STEP DN RA*MS HN STEPS
STEP UP 100 STEPS
RA = I
NO
S12(R) = [P2(R) - P1(R)]*MS
S12 = S12 + S12(R)
NEXT R
FOR R = 1 TOL
PRINT S12(R)
NEXT R
P12 = S12 / L * UU
D = (P12 / 180 / 3600 * / TAN(AN/180 * TT
PRINT AV SEP OF FILM AND SUB
S12/L STEPS
PRINT ANG. SEP OF FILM AND SUB
P12 ARC SEC
PRINT ΔD/D
YES

The second routine is the COUNT routine or CO (lines 1500 - 1550). It sets the counter to count repeatedly for a predetermined period and display the numbers on the screen. A different routine can be chosen by depressing a key.

The SCAN routine or SC (lines 2000 - 2260) allows the user to scan through an angle in a particular direction determined by the motor step size MS and the number of cycles NO in a scan-count mode. The scan-count mode is repeated for the number of cycles NO. A positive value of NO causes the axis to rotate in a clockwise direction and vice versa if NO is negative. The routine keeps track of the axis position and can be interrupted in the usual way.

In order to narrow up the rocking curve the GN routine (lines 3000 - 3150) is used. It tilts the goniometer so as to make the diffracting planes of both crystals parallel. Similarly the direction of rotation is determined by the sign of the step size.

4.1.2 The Find Routine

The FIND routine or FI (lines 3500 - 3930) is a very useful routine. It sets the computer to locate the Bragg peak automatically. The parameters set initially are the step angle MS, the counting interval S, the range in degrees and the direction for the search to take place if not both, and the limit stop LS. The choice of the limit stop depends very much on the step angle for the scan and the theoretical full width at half height maximum (FWHM) of the rocking curve.

The Bragg peak cannot be detected if a high limit stop and a step angle much greater than the FWHM are chosen. The best compromise is a step angle two to three times the value of the expected FWHM and a limit stop twice the background count. Sometimes due to fluctuations in the X-ray generator a high count is obtained although it is not the peak position. The routine checks this by recounting at the same position when the count exceeds the limit stop. Only if it exceeds the limit stop again will the routine branch to the RETURN command. The routine also branches to the RETURN command if the peak is not found within the specified range for a one way search. If the search is set for both directions, the motor rewinds back to the position before the search starts after taking care of the motor backlash and searches in the opposite direction.

4.1.3 The Plotting Routine

The plotting routine or PL (lines 4000 - 4360) is used to obtain a hard copy of the rocking curve. To avoid confusion as to whether the plot is in increasing or decreasing angle the routine plots only in one direction. The subroutine SUB 2500 (lines 2500 - 2530) is used to activate the dual digital to analogue converter which is connected to the X and Y terminal of the pen recorder. After each scan-count mode the cycle number, the count for the cycle, the maximum count so far obtained and the corresponding cycle number are displayed on the screen. The axis scans back to its starting position at the end of the plot or when the routine is interrupted after taking care of the motor backlash (lines

4250 - 4260). The width of the plot and the integrated intensity are evaluated and displayed on the screen together with the goniometer and axis position, the motor step size and counting time.

4.1.4 The Flank Routine

When a topograph of the sample is required the FLANK routine or FL (lines 4500 - 4995) is used. The routine plots out the rocking curve and sets itself at the chosen position on the flank. It also takes care of the drift due to long exposure time to ensure that the same part of the sample is exposed. The detail of the routine is easily understood with the aid of the flow-chart (Figure 4.1). The motor step size MS, counting interval S, number of cycles RA and the position on the flank of the rocking curve are input at the beginning of the routine. The count for each cycle of the plot are stored in the memory. For example; a topograph is to be taken on the left flank of the rocking curve at a position 0.7 times the peak intensity PV. The difference of each count between cycle 1 to PP and (0.7 x PV) is evaluated. PP is the peak position. The count which gives the smallest difference is the required position and suppose this position corresponds to cycle HP with a count HH. Similarly if the topograph to be taken is on the right flank of the rocking curve the routine locates a point between cycle (PP + 1) and RA. The axis then scans to position HP and the scaler counts repeatedly at the same point.

To take care of the drift the count B is each time

compared to the value HH. If B is equal to or greater than HH + (0.1 x HH) the motor scan MS steps in an anticlockwise direction and vice versa if B is equal to or less than HH -(0.1 x HH) but if B lies between HH -(0.1 x HH) and HH + (0.1 x HH) the axis will remain at the same point. For a topograph on the right flank of the rocking curve the axis scan clockwise if B is greater or equal to HH + (0.1 x HH) and anticlockwise if B is equal to or less than HH - (0.1 x HH).

4.1.5 The Automatic Routine

When the Bragg peak is located the usual procedure is to adjust the tilt of the sample crystal parallel to the reference crystal. The last subroutine AU (line 5000 - 9160) is a totally automatic set-up routine which locates the peak, determines the goniometer tilt direction if not known, finds the best tilt position before plotting out the rocking curve. The AU routine consists of seven subroutines. The subroutine SUB 8000 (lines 8000 - 8240) is the scan routine. It locates the peak position and value. The rotation angle for the axis is chosen such that an accurate peak position and value are obtained. The next important subroutine is SUB 7000 (line 7000 - 7740). This routine is essential since the peak position shifts when the goniometer is tilted. An axis scan in both directions is performed if necessary to locate the peak position. The angular rotation is three times that of the scan routine so as to locate the peak position quickly.

As in all the other routines the necessary parameters

are input at the beginning of the routine. Since the best tilt position is determined by the peak count, a reasonable counting time is chosen to reduce statistical fluctuation. When the peak is located the tilt direction is determined. The counting time for the scan in this case is doubled to be absolutely certain that a correct tilt direction is obtained. Using subroutine SUB 8000 the peak is located and is assigned to a variable P1. The goniometer is tilted through twice the angle specified in a clockwise direction using the sub-routine SUB 6500 (lines 6500 - 6550). The subroutine SUB 7000 then locates the peak followed by subroutine SUB 8000 which locates the peak value and position again. The peak value is assigned to the variable P2. The procedure is repeated and another peak value P3 is obtained. If P1 > P2 or P2 > P3 then the tilt direction should be anticlockwise and if P1 < P2 or P2 < P3 the tilt direction is clockwise, that is the same direction as it was already tilting. The next step is to tilt in the chosen direction to find the best tilt position. This is done by comparing the peak value for several scans at various tilt positions. The number of scan was initially chosen and five is an adequate figure. The peak value for each of these five scans is assigned to the variable P(R) where R = 1 to 5. The subroutine SUB 8500 (lines 8500 - 8580) then compares P(1) to P(5) to find the greatest value and the goniometer tilts back to the position which corresponds to the value. If the value is P(5), the goniometer tilts in the same direction again and this group of five scans will include the last tilt position of the previous

group. The subroutine SUB 8500 is used again to find the greatest value. When the best tilt position has been found the peak is located and the subroutine SUB 9000 (lines 9000 - 9160) positions the axis for plotting.

4.2 Substrate and Epilayer Routine

The next program is similar to that of the general case except for a slight modification to include the routine PL2 (lines 9500 - 10170) for finding the angular separation of two peaks as in the case of a substrate and epilayer (Appendix 2).

Initially a rough value of the peak separation of the layer and substrate is measured from the rocking curve. This value is necessary because the plotting routine for the two peaks case is divided into two sections. The first section locates the peak position for the first peak and the second locates the second peak position. Therefore the first cycle is carefully chosen so as not to include the second peak. The routine is repeated to obtain the average value of the peaks separation and $\Delta d/d$ evaluated from the relation

$$\Delta d/d = \Delta\theta/\tan\theta$$

where Δd = lattice mismatch for the layer and substrate and

$\Delta\theta$ = angular separation of layer and substrate.

Figure 4.2 is an example of the double crystal rocking curve obtained from a pair of garnet crystals in the (+,-) parallel mode using the automatic routine. Both crystals are produced by Bell Laboratories. The reference crystal on the first axis is a gadolinium gallium garnet (GGG) and

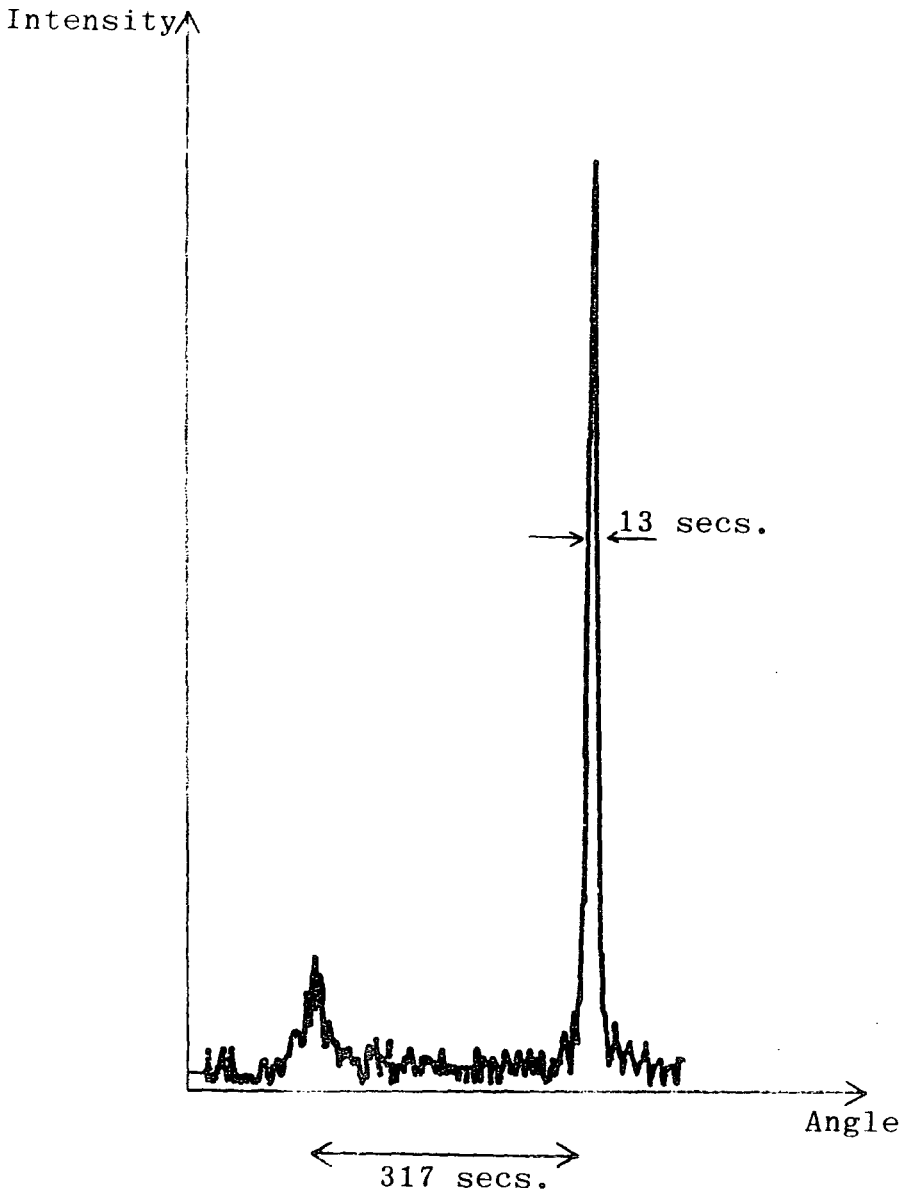

Fig. 4.2 888 double crystal rocking curve in the (+, −) parallel mode. The reference crystal was a garnet crystal (GGG) and the sample crystal has an epilayer on a GGG substrate.

the sample crystal has an epilayer on a GGG substrate. The FWHM of the main peak (substrate) is about 13 arc seconds for the 888 reflection using $K\alpha_1$ copper radiation. The average separation of the peak for the substrate and epilayer is about 317 ± 5 arc seconds and therefore the fractional change of the lattice spacing $\Delta d/d$ at the epilayer and substrate boundary is about 9.0×10^{-4} ± 2%. The peak intensity of the substrate is about 6 times the peak intensity of the epilayer.

Rocking curves for another two garnet crystals with epilayers were also obtained by placing the crystal in turn on the second axis. Their corresponding rocking curves are shown in Figures 4.3 and 4.4. $\Delta d/d$ was found to be 9.1×10^{-4} ± 0.2% for the sample from Plessey and 6.0×10^{-3} ± 0.6% for the sample from Philips.

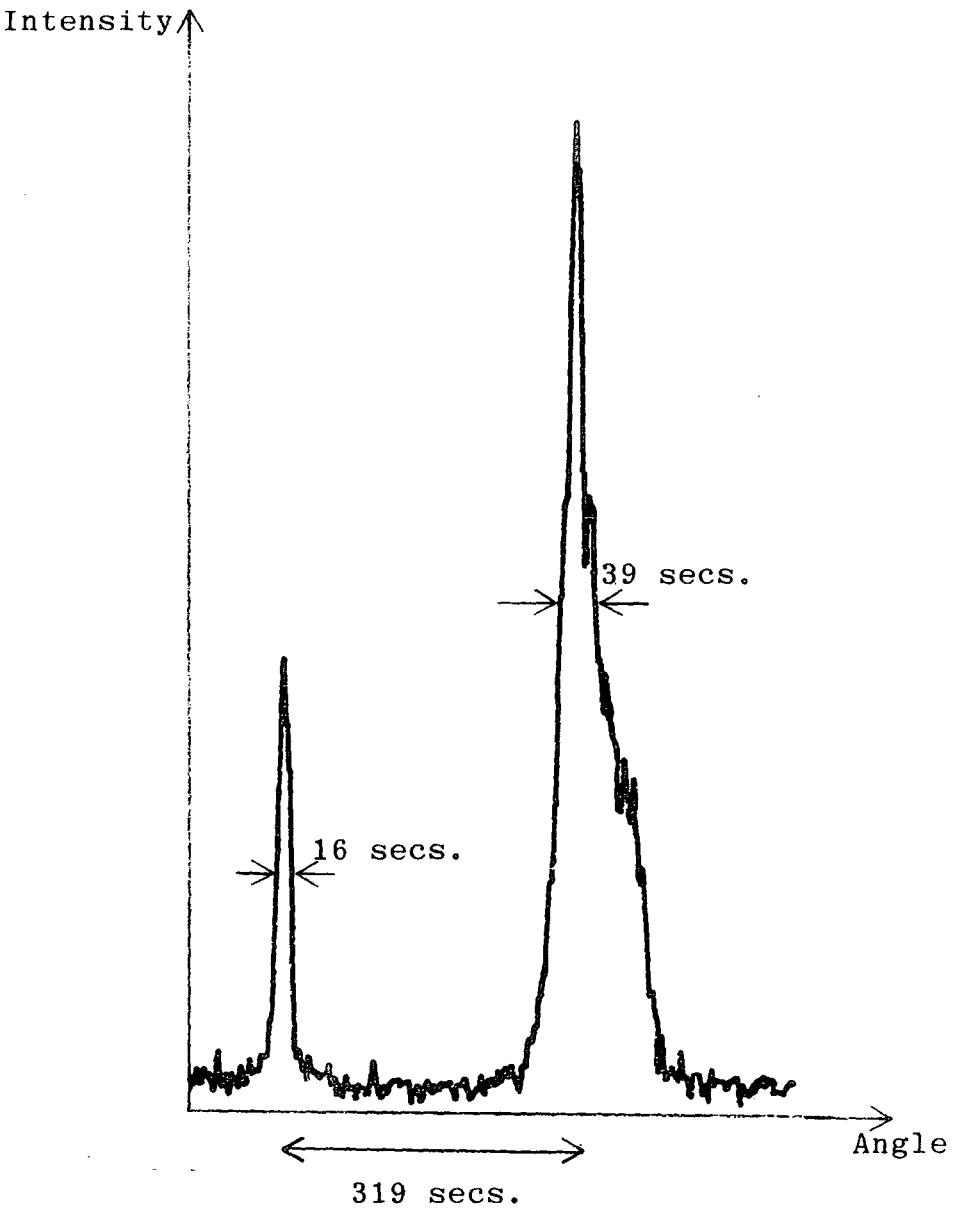

Fig. 4.3 888 double crystal rocking curve from a pair of garnet crystals (GGG) from Plessey using Cu radiation. The second crystal has an epilayer on a GGG substrate.

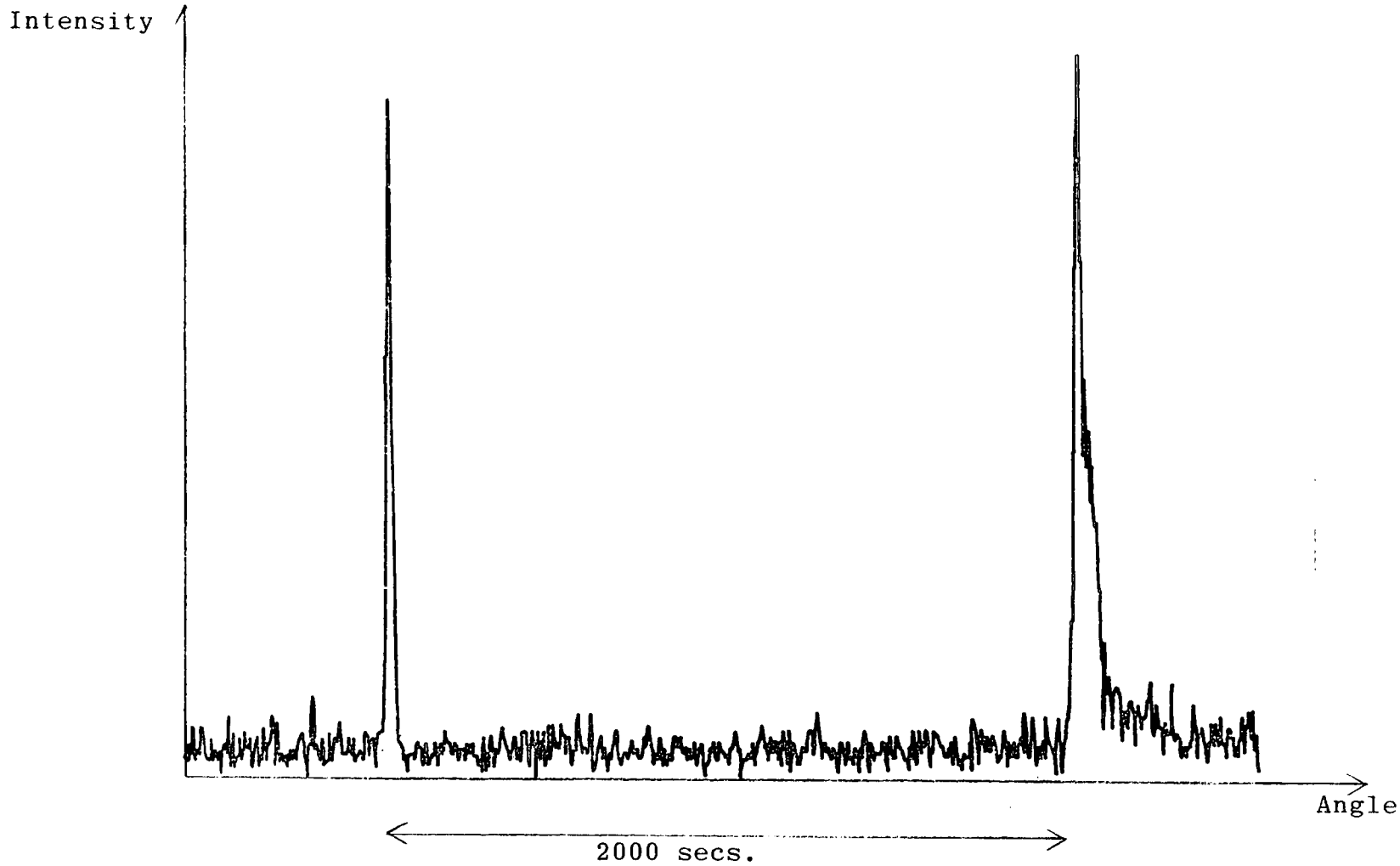

Fig. 4.4 888 double crystal rocking curve from a pair of garnet crystals (GGG) from Philips using Cu radiation. The second crystal has an epilayer on a GGG substrate.

CHAPTER 5

DIAMOND TURNED SILICON

5.1 Introduction

Monochromators and mirrors are now commonly used as a beam conditioner in X-ray experiments especially at Synchrotron Radiation Sources. It is vital that the monochromator surface is flat, smooth and free from surface damage. This is to ensure that an even distribution of the reflected beam is obtained without loss in intensity due to scattering. Therefore the choice of material for monochromator is important.

A brittle material is desirable so as to minimize surface damage during its preparation. It should be chemically inert so that it will not deteriorate in atmosphere, will tolerate beam heating and mechanically strong for easy handling. Germanium and silicon single crystals have so far satisfied this criteria and combined with the availability of perfect germanium and silicon crystals, due to the semiconductor industry, are commonly used as monochromators. Silicon or germanium is chosen depending on the intensity of the diffracted beam required, funds available and wavelength required.

The present method of producing these monochromators is by diamond sawing and hand lapping with diamond abrasive and finally using the 0.25μm diamond paste which is the finest particle size available before etching in the appropriate solution to remove the surface damage. 'Syton' which is an alkaline silica solution can also be used for the final

preparation. It has the advantage of having a smaller particle size of 0.025μm and it acts both mechanically and chemically. This diamond sawing and handlapping technique produces good surface finish but it needs skill and is very time consuming if large sizes and odd shapes are required.

The following experiment aims to investigate whether all or part of the above process can be replaced by machining with a diamond tool in view of the success of diamond machining in fields of laser optics, astronomy and infrared optics (Frank et al. 1976, Frank 1977, Lester et al. 1977, Gerth et al. 1978 and Benjamin 1978).

5.2 Diamond Turning

Diamond turning is the shaping of material on a precision lathe under controlled machine and environmental conditions by using a single point diamond tool. The quality of the finished surface produced by the machining process depends on several factors such as the rigidity of the machine; the quality, orientation and shape of tool; the type of material to be shaped and the surface interaction between tool and workpiece.

As diamond is an extremely hard material, sharp cutting edges could be made which will produce a surface with a high reflectivity. The accuracy of diamond turning together with the reduction in cost and time is particularly attractive in the production of components with odd shapes and sizes. For example, Frank (1977) found that he took 3 weeks to diamond turn an optical off-axis parabola compared to a year if done by conventional lapping and polishing technique with a

tremendous saving of about 90% in cost. In infrared systems the reflectivity of diamond turned metal is high and has a good resistance to reflectivity degrading due to ageing.

The type and rate of tool wear will change the shape of the tool in contact with the workpiece (silicon in this case) and this affects the surface produce. Generally the depth of cut must be deep enough so that over-riding does not occur. Too deep a cut would increase the cutting force unnecessarily. A spiral of uncut ridges will be left if the tool feed rate is fast with respect to the plate rotation but too slow a tool feed rate will unduly wear and heat the diamond tool.

The performance of diamonds as a cutting tool has been discussed by Wilks (1980) and a study of the reflectivity and imperfection of diamond turned copper surfaces and motor car pistons have been carried out by King and Wilks (1976).

5.3 Experimental Procedure

The preparation of the samples and the initial measurements were carried out at Warwick University (McKenney) and an extensive series of rocking curve measurements to study the depth of distribution of damage was performed at Durham.

5.3.1 Preparation of Sample

The silicon used was provided by Motorola Inc. and guaranteed "zero D". The crystal was 2 inches in diameter and grown by the float zone technique along the [111] direction. It was doped with phosphorus and has a resistivity of 500 Ω cm. A number of 2.5 mm thick slices cut perpendicular to the

growth axis were obtained using an annular saw. Each slice was polished manually on a flat glass plate using 500 grit silicon carbide and water until all the saw marks were removed before being waxed on a lapping block. This was to ensure that it lay flat on the polishing plate and an even pressure applied during polishing. The slices were then polished on rotating cloth pads with a 6, 1 and 0.25 μm diamond paste at a speed of 150, 300 and 300 rpm respectively until a scratch-free and mirror-polished surface was obtained when viewed with a microscope of 5 times magnification. Between each polishing the slices were washed in acetone and ultrasonically cleaned. They were then melted out of the wax, soaked in dichloromethane to remove the wax and then etched in a 20:1 solution of nitric acid and hydroflouric acid for 10 seconds. A back reflection Laue photograph was taken before each slice was cut into six sections along known crystallographic directions (Figure 5.1). This is to permit easy orientation for rocking curve measurements.

Each set of 6 specimens was waxed on a steel plate (Figure 5.2). The specimens were labelled across the plate that is 1 and 6 were outer, 2 and 5 middle and 3 and 4 were the inner pair. The specimens were arranged such that 2 specimens will have each of the 3 radii. The outermost silicon (1 and 6) is 7cm from the centre of the plate. Epoxy resin was poured over the specimen and left to cure at room temperature. Use of resin helps to reduce the impact of the diamond tool which might damage the specimen or fracture the expensive diamond tool.

The machining was done at the City Polytechnic in London

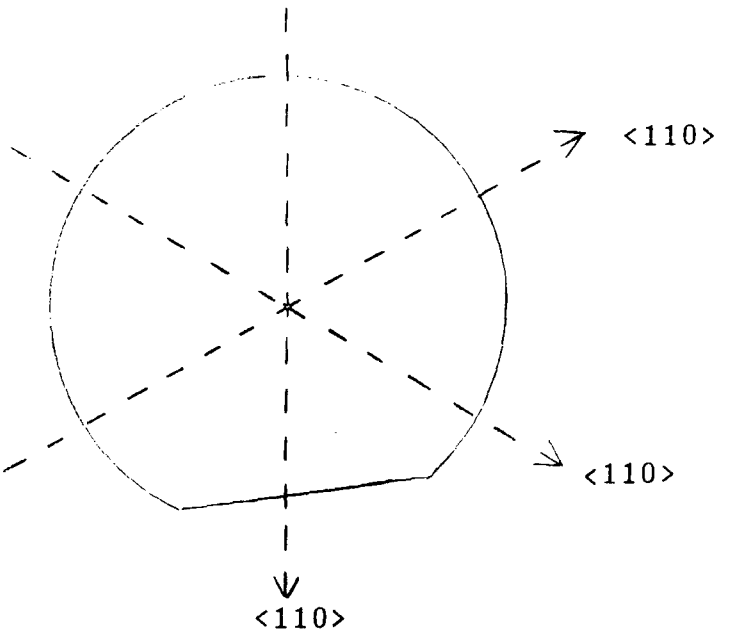

Fig. 5.1 Crystallographic orientation of the cuts.

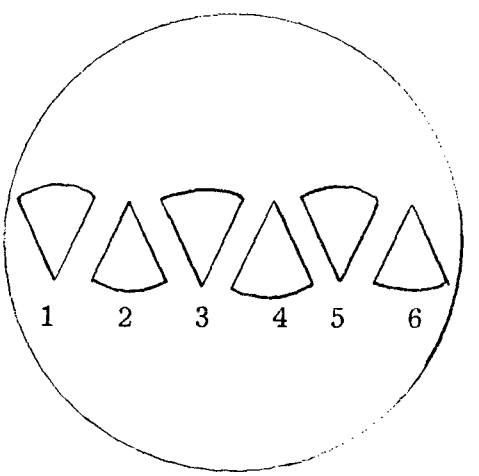

Fig. 5.2 A set of specimens mounted and embedded in epoxy resin ready for machining.

on a VDF Boehringer 48C CNC lathe. It is a rigid and massive machine designed for diamond turning and is computer controlled. The performance of any machining process is very much dependent on the physical and chemical interaction between the cutting tool and the workpiece and this varies from one material to another. The machining parameters were judged from experience with other materials since there does not appear to have been any previous work on silicon single crystals.

For all the 3 sets of specimens the depth of cut was 200 μm and the tool feed rate was 0.01 mm per rev. (10 μm per rev). The round-nosed tool with a radius of 450μm at the tip was used for the first set of specimens. A flat-nosed tool was used for the other 2 sets, one without lubrication and the other with Cimicool S4 with 25:1 mist application. The flat-nosed tool was brand new with a 2.5 mm facet width and was set with zero top rake. Table 5.1 shows the conditions for each of the specimens.

The flatness of the silicon surface was measured using a Talysurf 5 machine in the Warwick Centre for micro-mechanics with the stylus run normal to the turning grooves. The measurements were taken from the edges of the specimen as it leaves a mark which will interfere with the rocking curve measurements. Sensitivity to height fluctuations was about 20 nm.

5.3.2 Rocking Curve Measurements

The depth of damage introduced by the diamond turning was studied by rocking curve measurements using the double axis camera, the EGG. The sensitive non-dispersive (+,-) parallel setting was used; that is the reference and sample

Table 5.1 Machining parameters of the specimens cut with the different types of tool.

Specimen	Tool Type	Revs/min	Greatest speed of cut of outer specimens m/min	Slowest speed of cut of inner specimens m/min
RN	Round-nosed	1400	616	44
FN	Flat-nosed	1200	528	37
FNL	Flat-nosed with lubricant Cimicol S4 mist application 25:1	800 to 1250	352	39

crystal have identical lattice spacings and set for hkl and $\bar{h}\bar{k}\bar{l}$ reflection respectively. Bonse and Hartman (1981) have recently exploited this sensitivity to measure strain variations of parts in 10^8 in silicon from double crystal X-ray topograph. The Si(333) reflection using Mo Kα radiation whose theoretical FWHM is 0.88 arc seconds (assuming Gaussian distribution) was used throughout the experiment. The diffractometer sensitivity limits the use of the more sensitive higher order reflections. For our purpose the Si(333) reflection is adequate. It gave sufficient sensitivity and good counting statistics together with a convenient Bragg angle of 19.9 degrees. The reference crystal is a highly perfect silicon crystal with a (111) surface and placed on the first diffractometer axis.

A holder constructed for the sample is placed on the second axis (Figure 5.3). It consists of L-shaped flats onto which the specimen was rested. As the specimens were generally 2 mm thick and 2 cm long measured vertically (when specimen placed in holder), the specimen do not need a clip to keep them in place. The 2 mm well at the bottom is sufficient to keep the specimen in place. Nevertheless a soft clip was placed at the top of the specimen holder (but not touching the specimen) as a safety device. The sample can be changed easily for etching without removing the sample holder from the axis. This ensures that the subsequent rocking curve is within ± 1^o away from that of the previous one. The minimum rocking curve width was obtained by adjusting the azimuthal tilt under software control using the automatic routine. Each rocking curve measurement is repeated at least 4 times and the average value of the half width

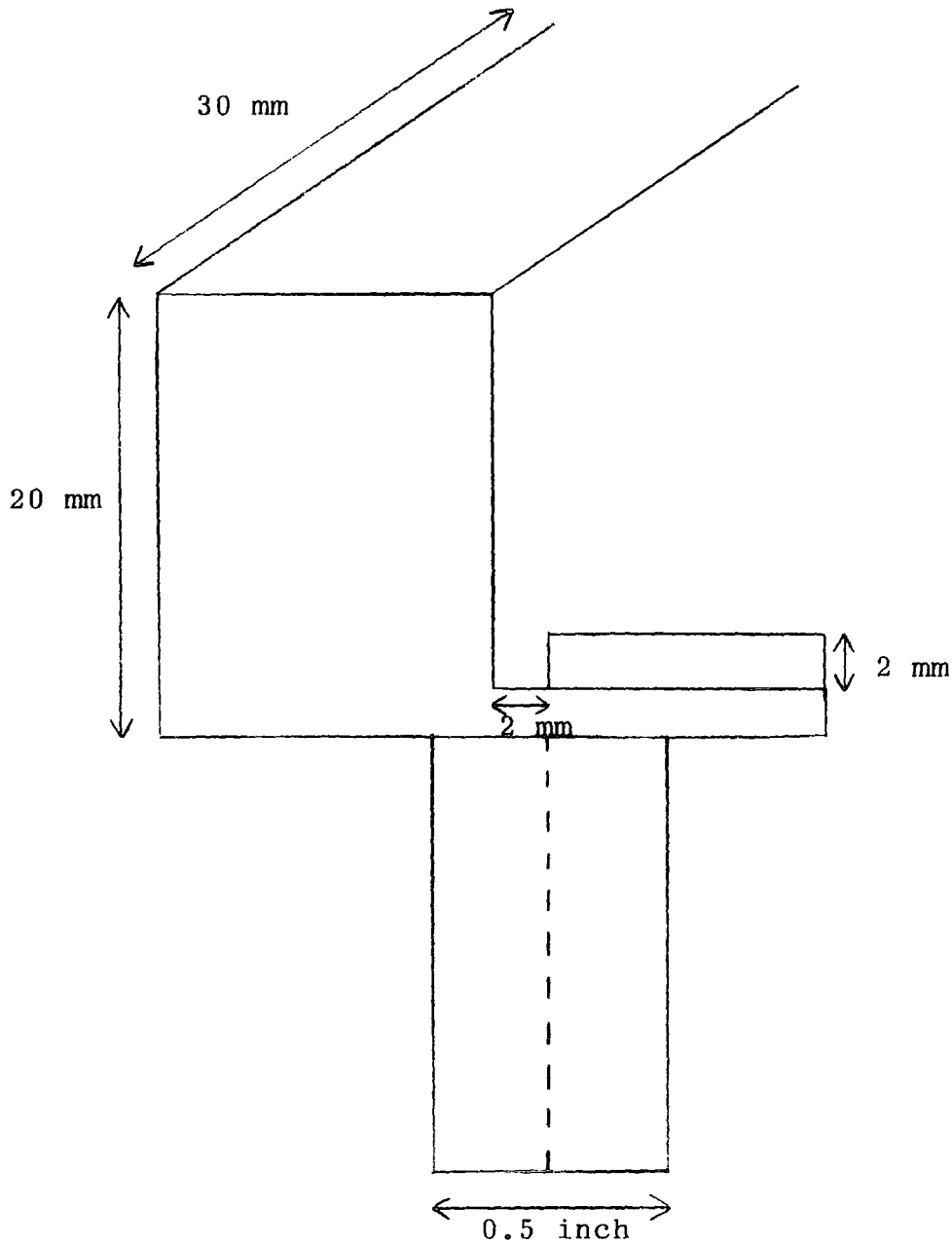

Fig. 5.3 Cross-section of the crystal holder.

evaluated.

A 20:1 solution of concentrated nitric acid (75%) and hydroflouric acid (45%) was used to etch away the silicon. The solution was continuously stirred with the aid of a motor during the etching process and the thickness of the sample was measured with a micrometer gauge after each etching. The amount of material removed was calculated in each case. The average rate of removal of 1-2 μm per minute cannot be used as the etching solution gets diluted.

Strains associated with diamond turning results in an increase of the rocking curve FWHM and an increase in the integrated intensity. The FWHM and integrated intensity was monitored as the surface layer is etched away and this gives a quantitative measure of the damage profile with depth. The turning damage can be described as "removed" when the rocking curve FWHM was reduced to that of the control sample.

5.4 Results

The first encouraging result was that the specimens or the diamond tool was not broken during the machining process. Visually, the surface finish was inferior to the hand lapped silicon or diamond turned metals such as brass, aluminium and molybdenum. This maybe due to the more abrasive nature of silicon.

The specimens turned using the round-nosed tool RN1-6 appeared shiny but the machining marks were obvious. This is typical of a round-nosed tool (Figure 5.4) which leaves behind grooves with the profile of their cross-section. The

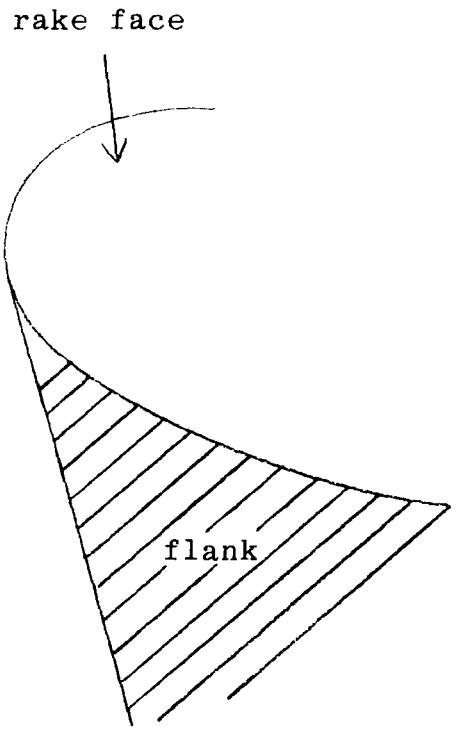

Fig. 5.4 Round-nosed tool.

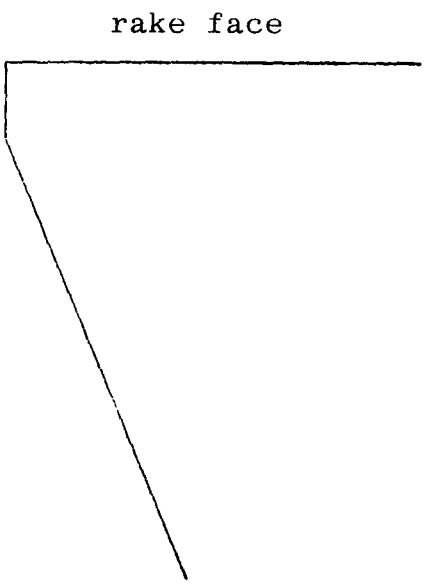

Fig. 5.5 Flat-nosed tool.

specimens turned by the flat-nosed tool (Figure 5.5), FN1-6 also appears shiny but the surface is smoother as the tool has a different cutting action. The cut surface is wiped by the flat edge of the tool as machining continues thus producing a smearing effect. Therefore the density of damage is expected to increase. Although the surface is smoother the machining marks are still visible. When a lubricant is used with the flat-nosed tool (specimens FNL1-6) we expect the cutting forces to reduce and thus a reduced depth of damage. The surface appears flat and the turning marks were hardly visible but the surface finish was dull and slightly corroded.

Talysurf measurement of RN1-3 and FN1-3 were taken to measure the roughness of the specimen's surfaces. The roughness R_z of the round-nosed specimens is taken as one fifth of the sum of the 5 highest peaks less the sum of the 5 lowest trough.

RN1	R_z	=	1.06 μm
RN2	R_z	=	0.92 μm
RN3	R_z	=	0.96 μm

Although the flat-nosed tool gave a smooth finish it has a long range ($\sim$ 7 mm wavelength) waviness of amplitude 1 μm. The waviness is a more serious disadvantage than roughness since the roughness can be easily removed by etching.

For the rocking curve measurements, specimen RN6 which has been hand lapped, polished and etched was taken as the control specimen. It has a rocking curve FWHM of 1.2 arc seconds compared to the theoretical value 0.88 arc second

(Figure 5.6). Therefore any increase in rocking curve width above this figure for the other specimens are due to the imperfections in the crystals. The 1.2 arc second rocking curve corresponds to 2 motor-steps of the axis rotation. The value of 0.88 arc second is not obtainable due to the limitation of the axis sensitivity. However, as seen later the width was quite narrow enough to act as a control specimen.

There is a very significant difference in the initial damage introduced by the three types of tool. Table 5.2 shows the average FWHM and integrated reflecting power of the samples cut by the different tools prior to etching. The flat-nosed tool without lubricant introduces the least damage. Its 4 arc seconds FWHM is about half that of the samples cut by the round-nosed tool and the flat-nosed tool with lubricant. Although one would expect the flat-nosed tool with lubricant to introduce less damage compared to when it is used without lubricant, it appears otherwise. This result should however, be treated cautiously as the flat-nosed tool was brand new when used without lubricant as compared to when used with lubricant or the round-nosed tool.

Figures 5.7 a-e and 5.8 a-e shows the variation of the FWHM and integrated reflecting power of the samples RN1-5 cut with the round-nosed tool as successive layers of the sample was removed. The corresponding curves for the samples cut by the flat-nosed tool without and with lubricant are shown in Figures 5.9 a-c, 5.10 a-c, 5.11 a-d, 5.12 a-d respectively. As seen from the graphs there are no systematic

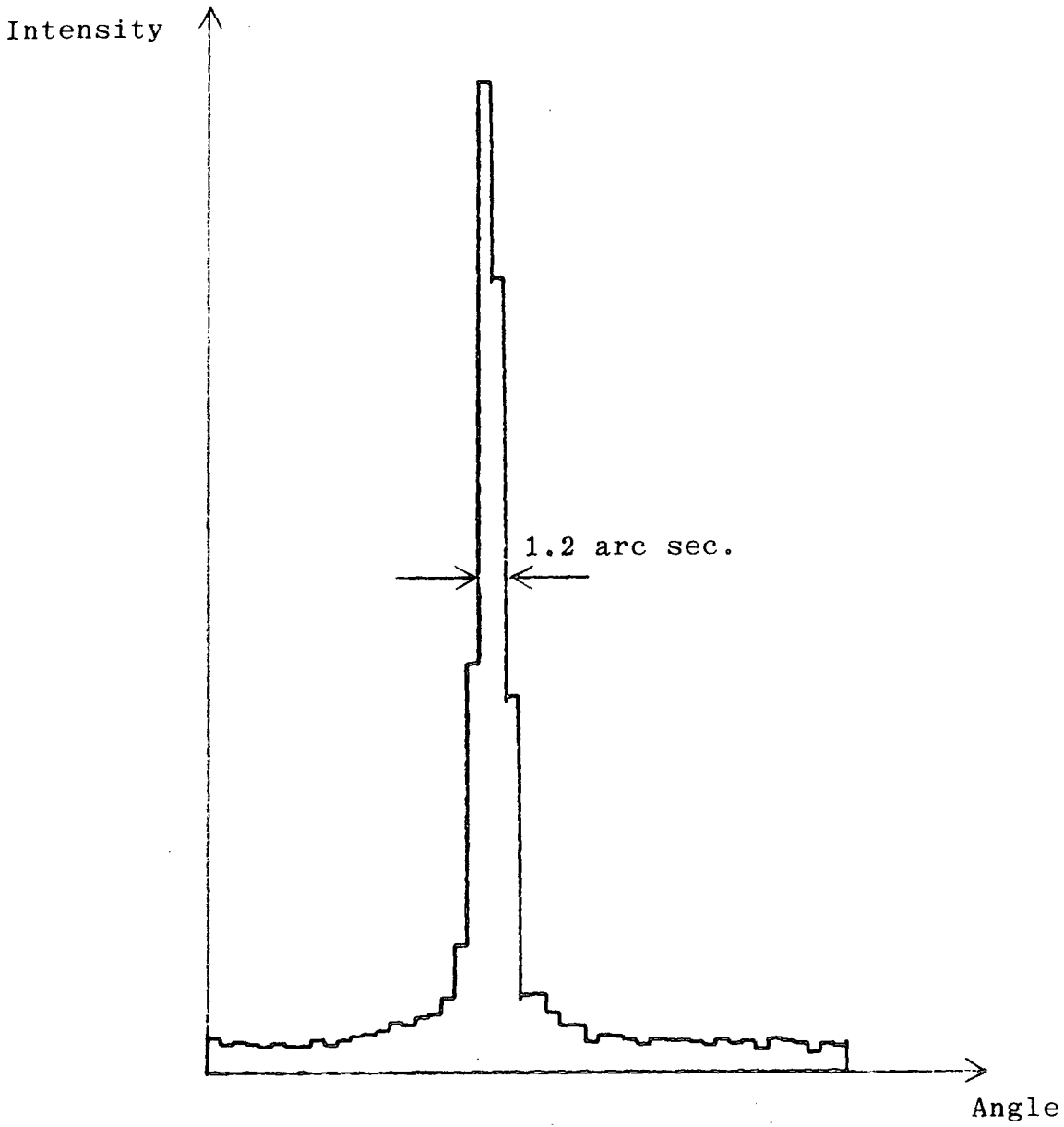

Fig. 5.6 333 double crystal rocking curve of the control specimen (Sample RN 6).

Table 5.2 The average FWHM and integrated reflecting power of the specimens cut with the 3 types of tool prior to etching.

Tool Type	FWHM (arc seconds)	Integrated reflecting power
RN	9 ± 1	$1.6 \times 10^{-5} \pm 0.2 \times 10^{-5}$
FN	4 ± 1	$0.6 \times 10^{-5} \pm 0.2 \times 10^{-5}$
FNL	9.5± 1	$1.2 \times 10^{-5} \pm 0.2 \times 10^{-5}$

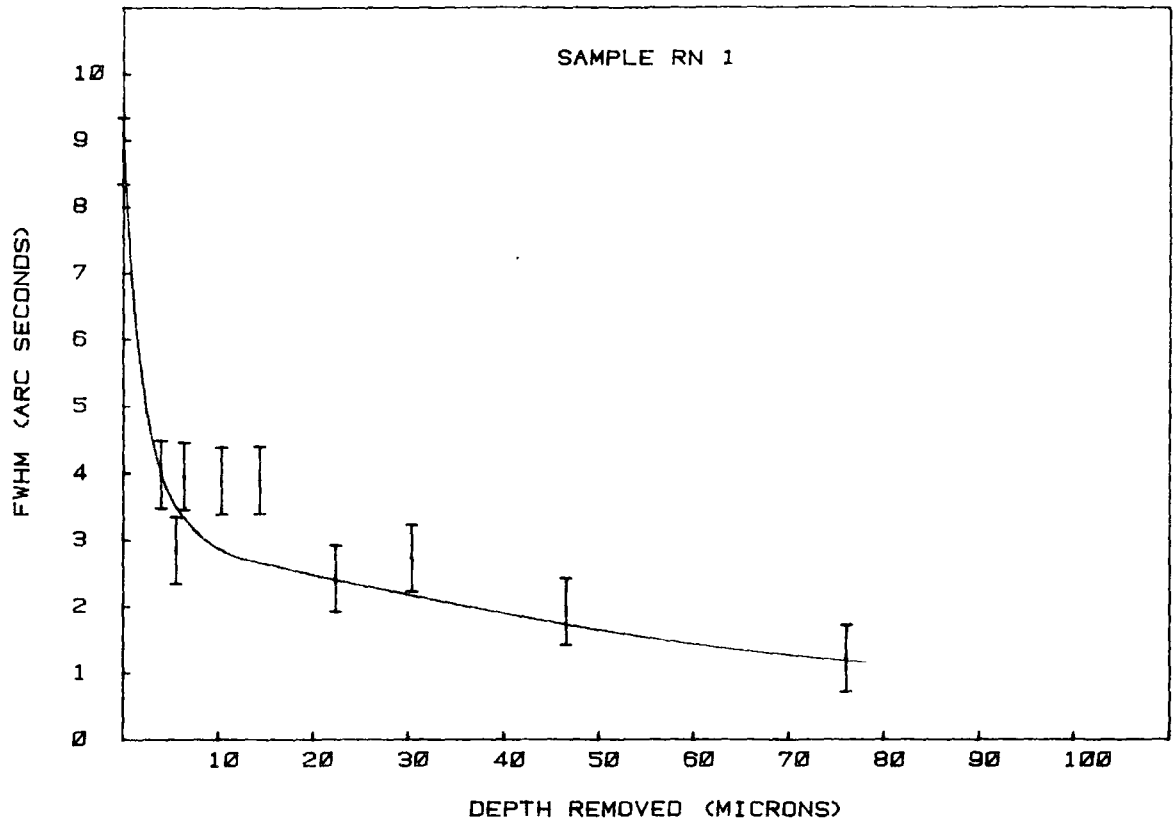

Fig. 5.7a

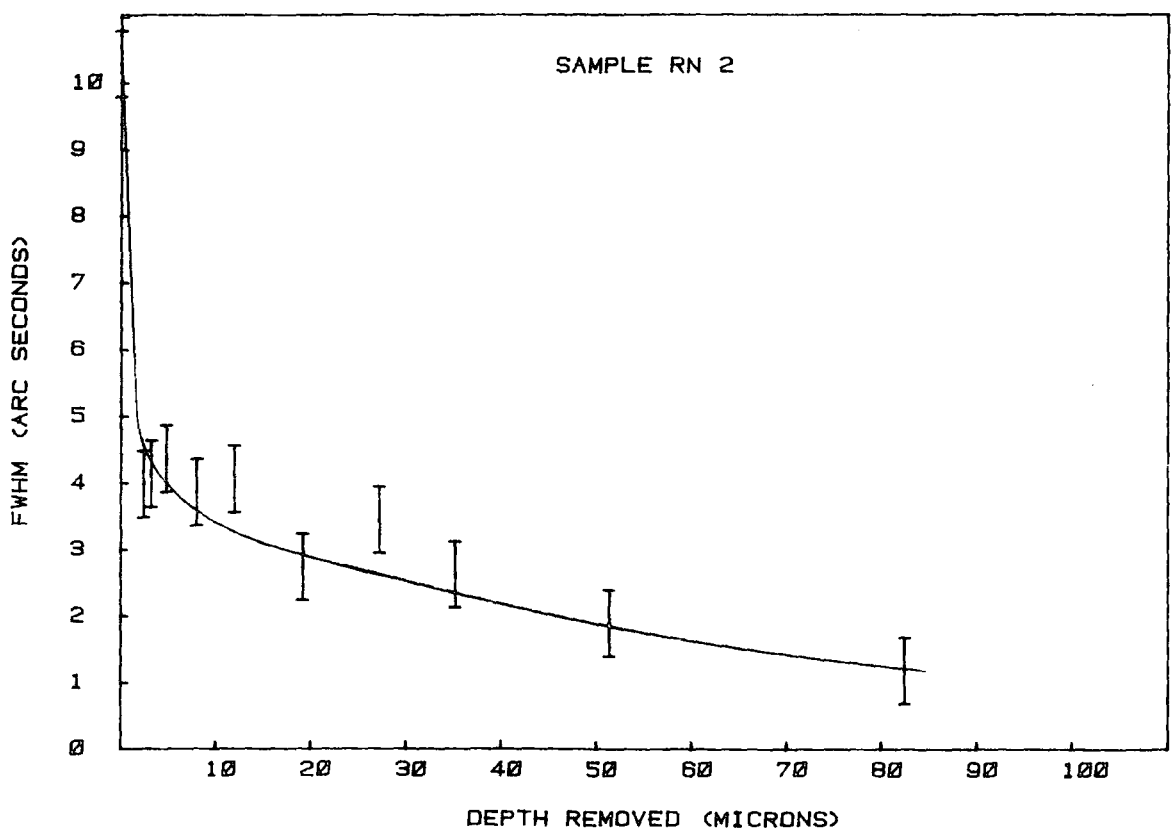

Fig. 5.7b

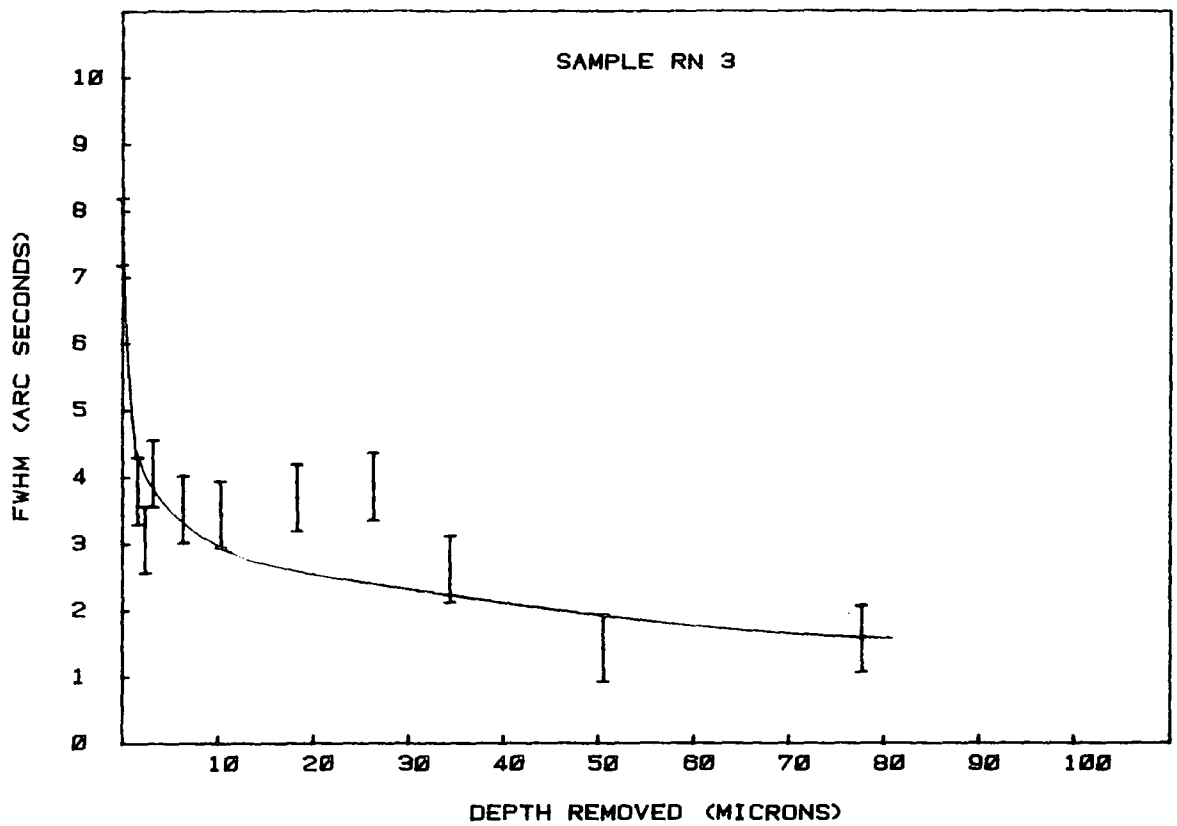

Fig. 5.7c

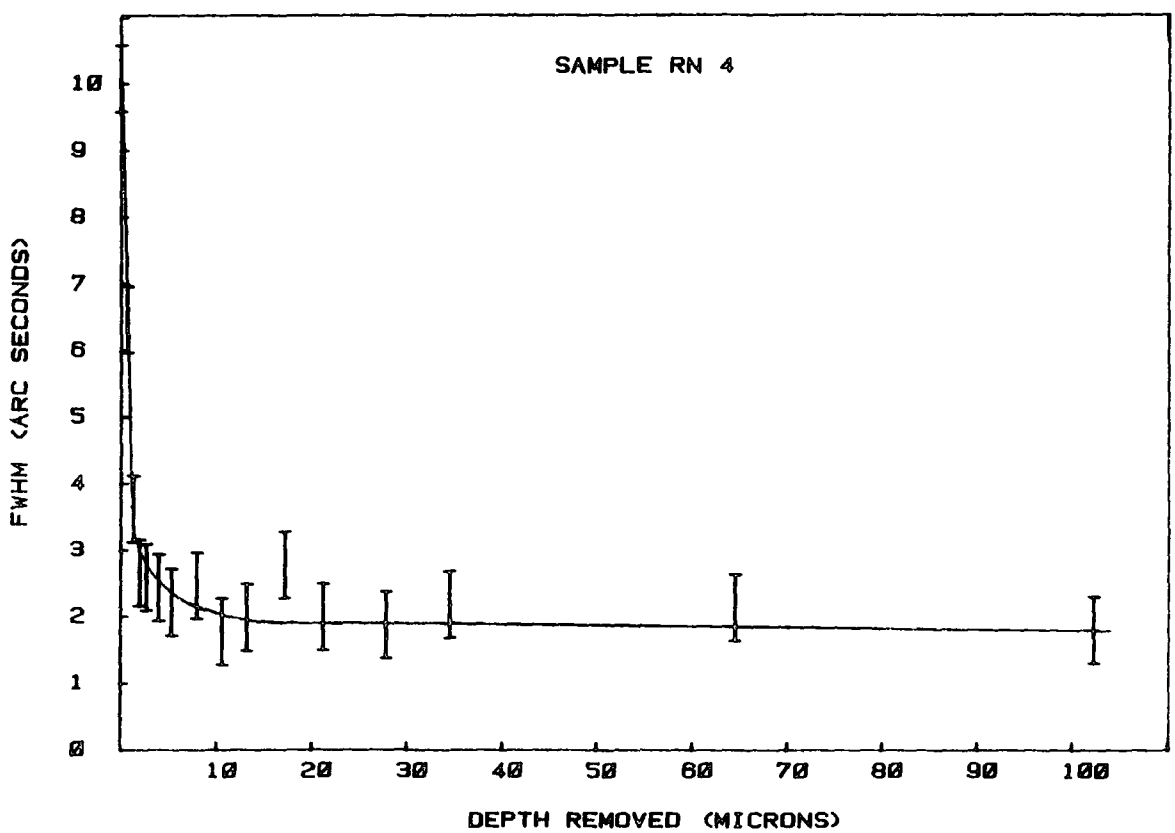

Fig. 5.7d

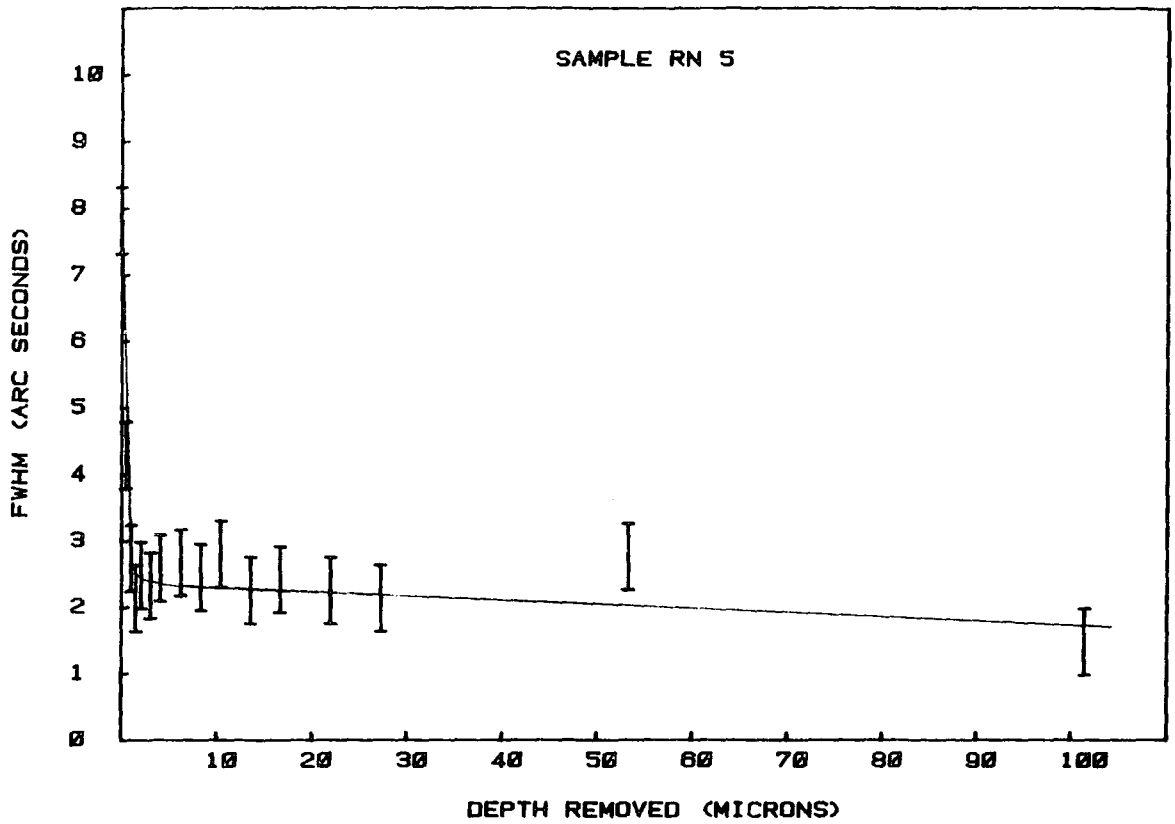

Fig. 5.7e

Fig. 5.7a-e Variation of the FWHM of specimens RN 1-6 cut with the round-nosed tool as they were etched.

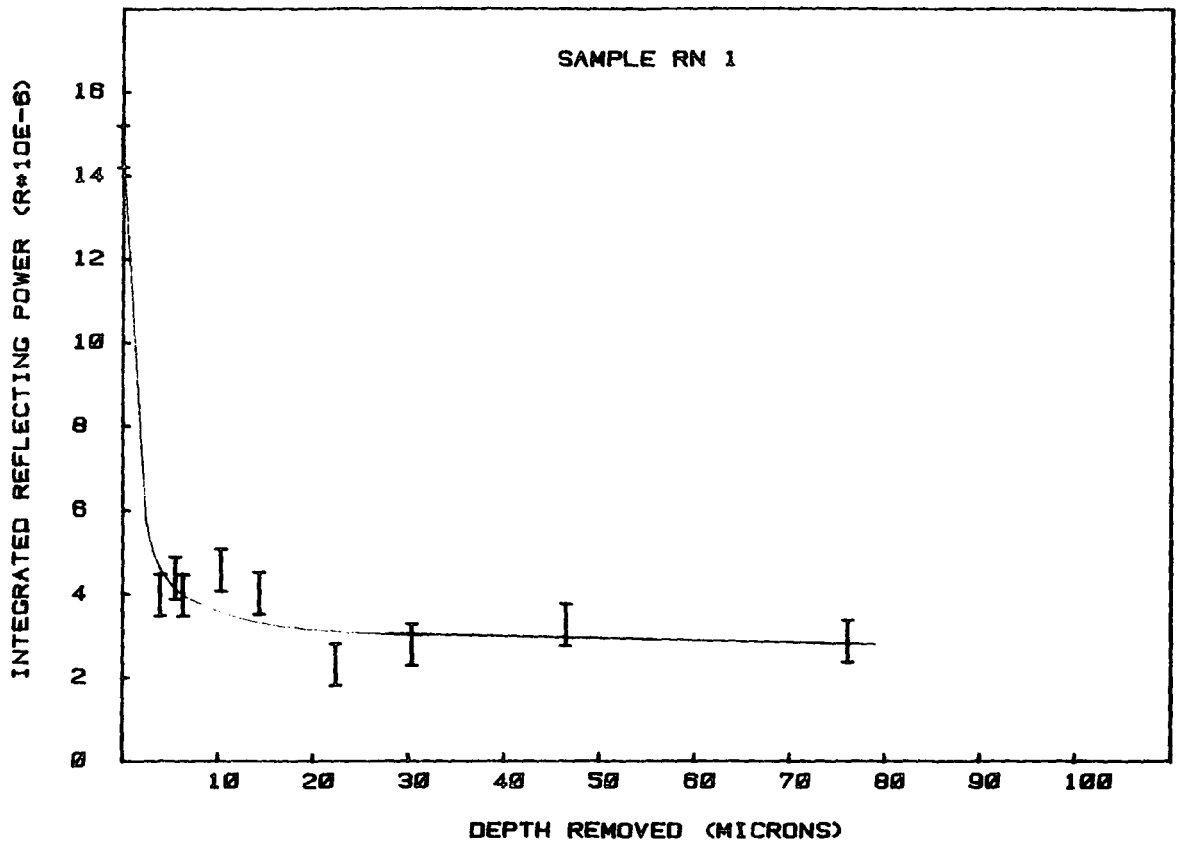

Fig. 5.8a

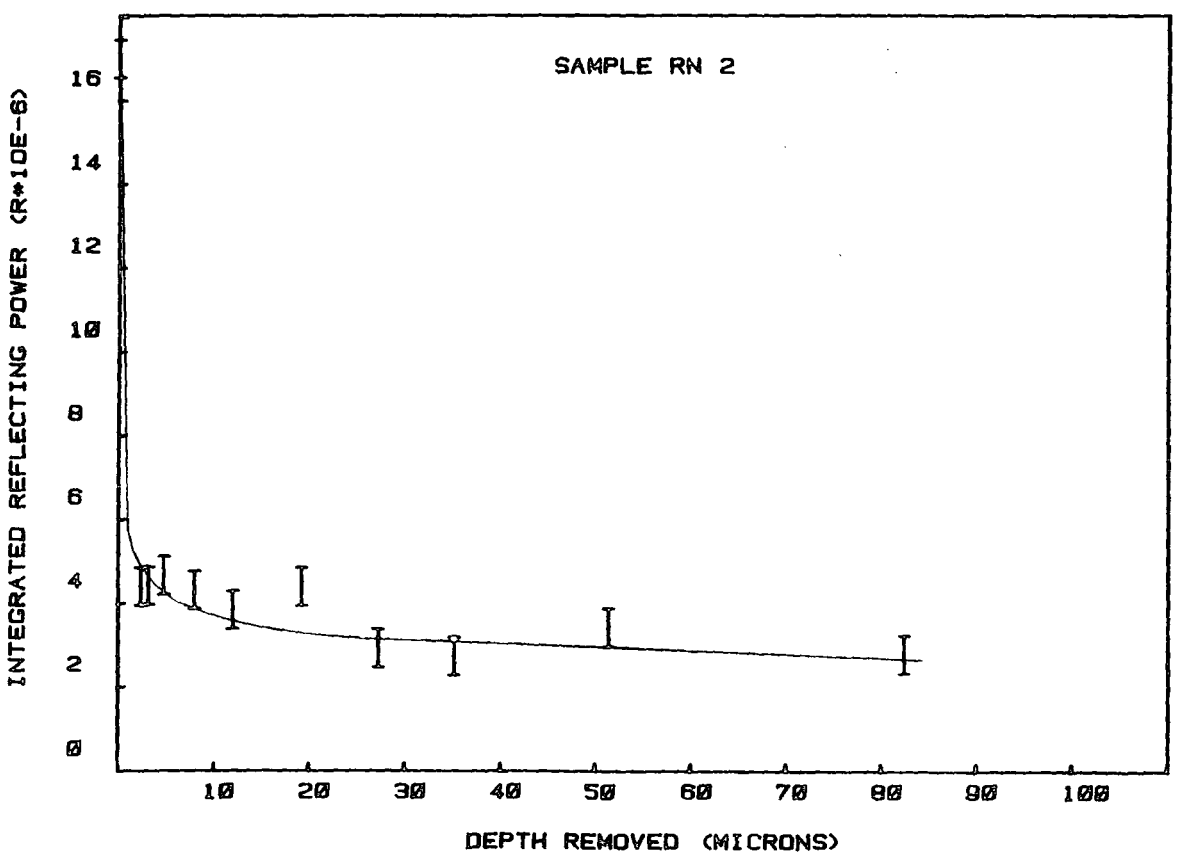

Fig. 5.8b

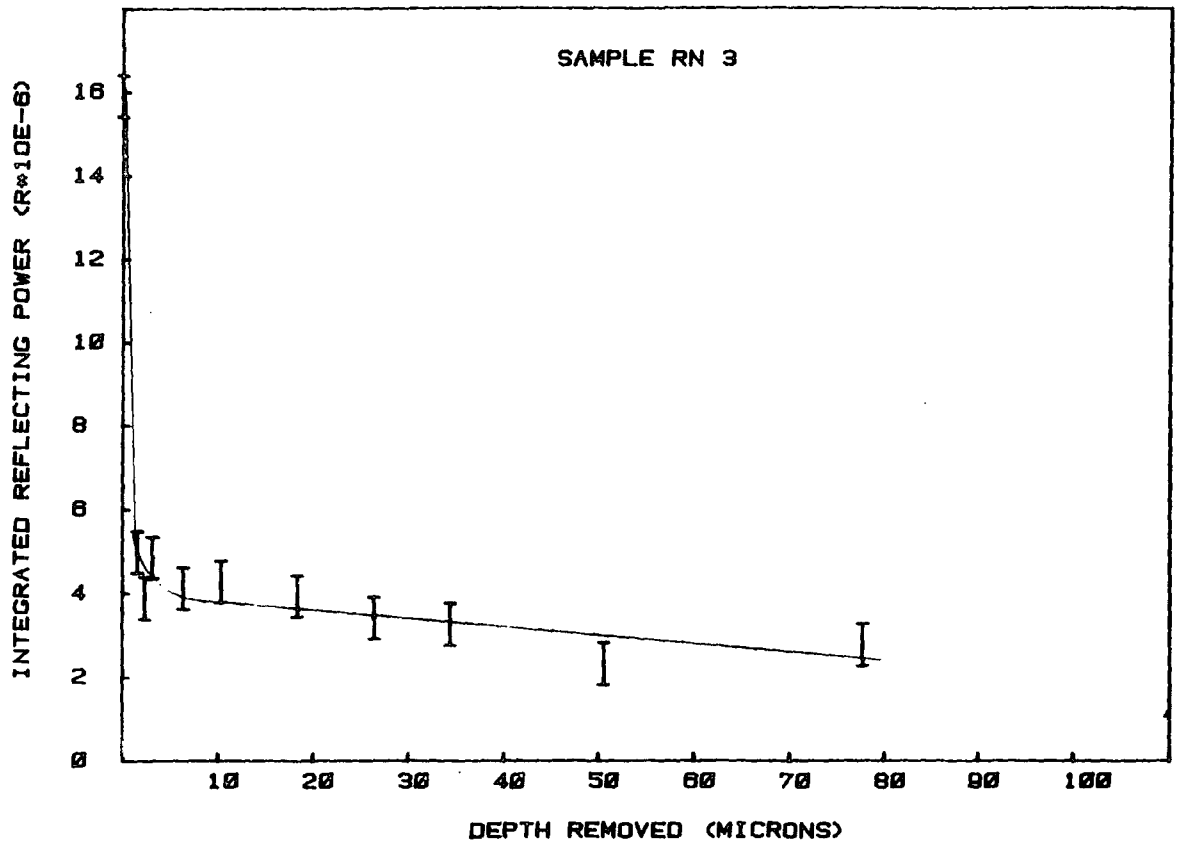

Fig. 5.8c

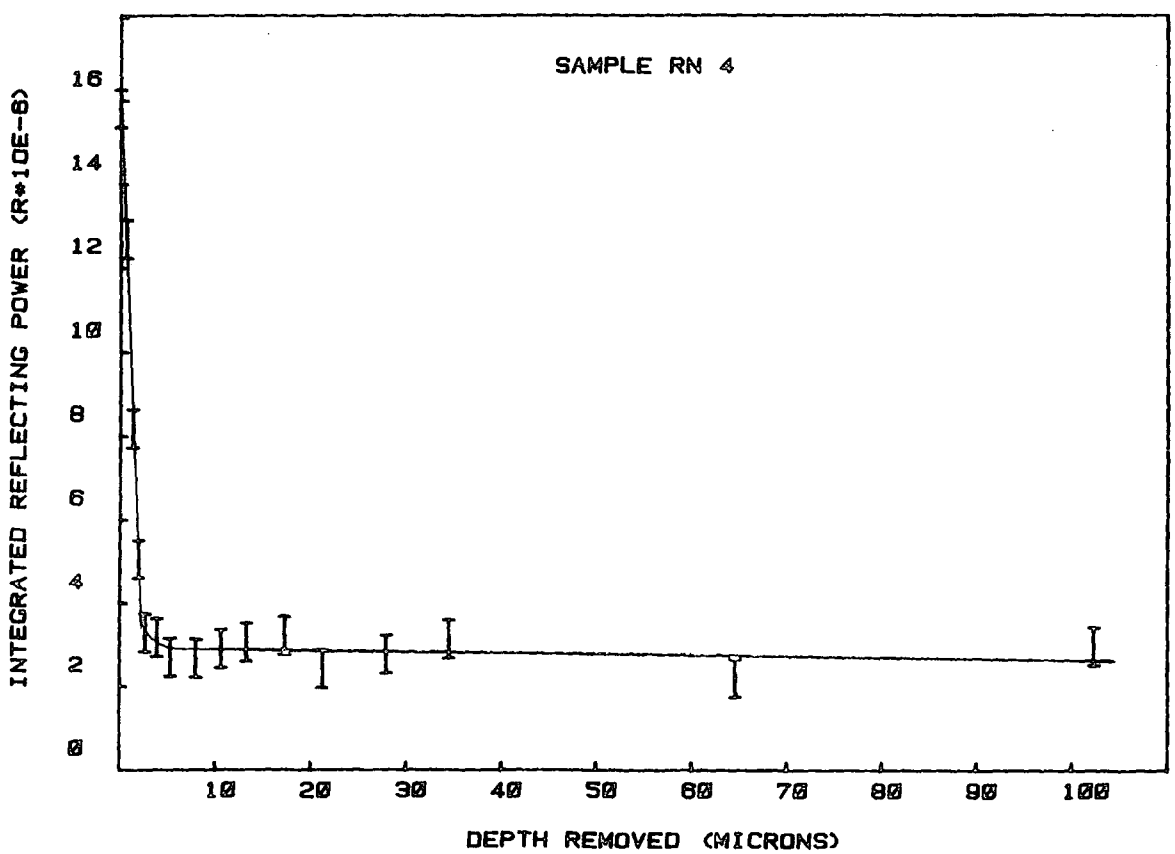

Fig. 5.8d

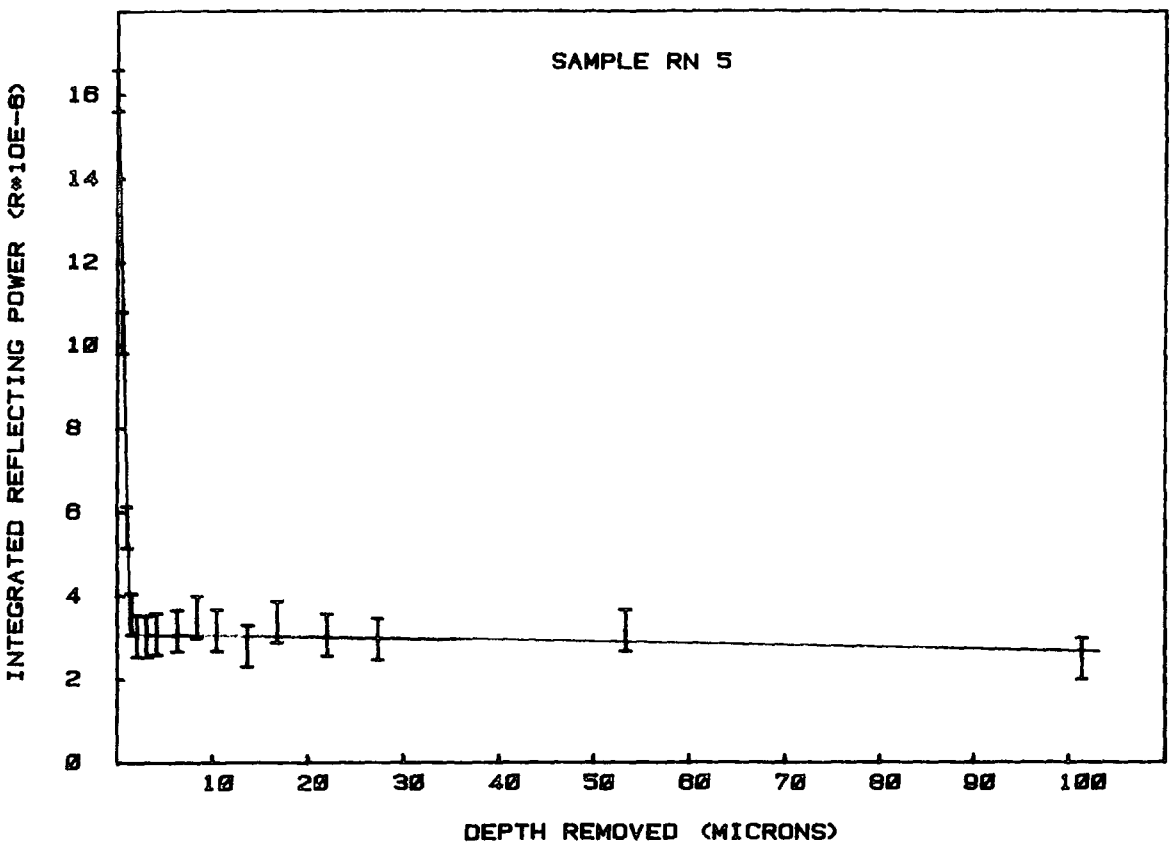

Fig. 5.8e

Fig. 5.8a-e Variation of the integrated reflecting power of specimens RN 1-6 cut with the round-nosed tool as they are etched.

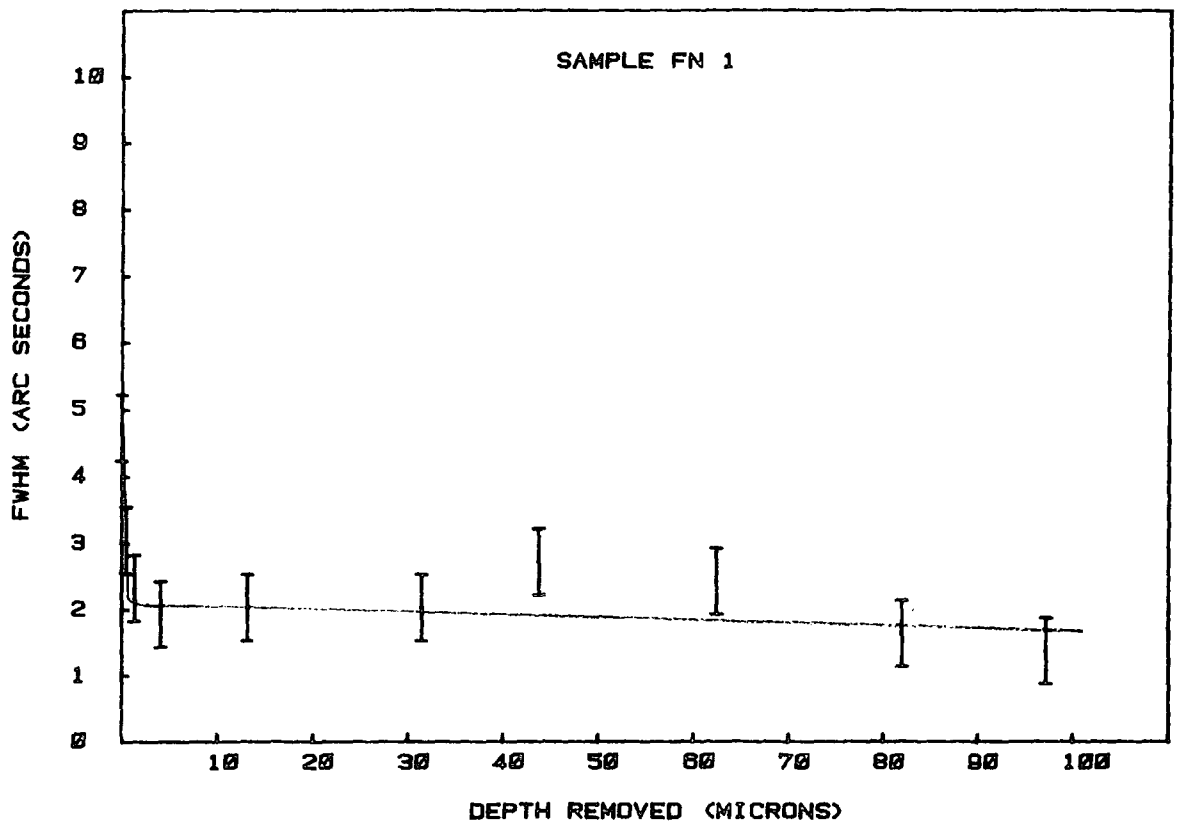

Fig. 5.9a

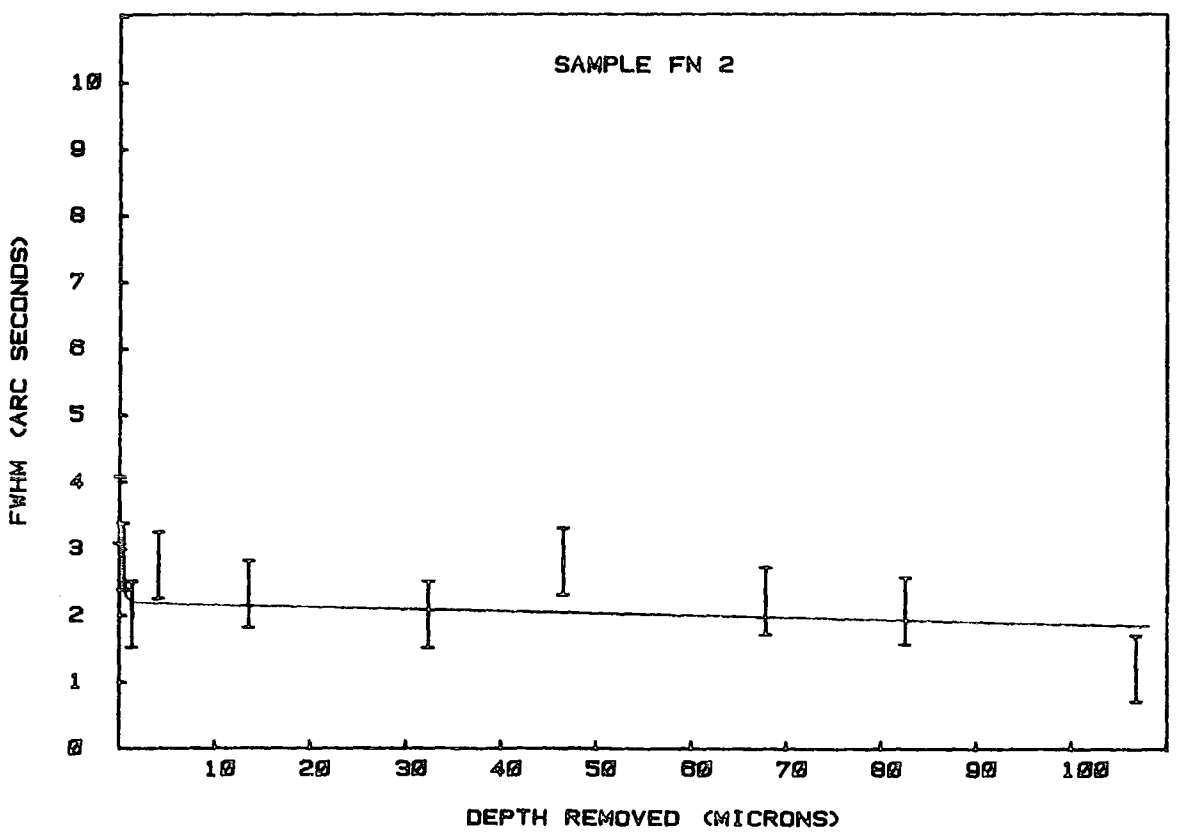

Fig. 5.9b

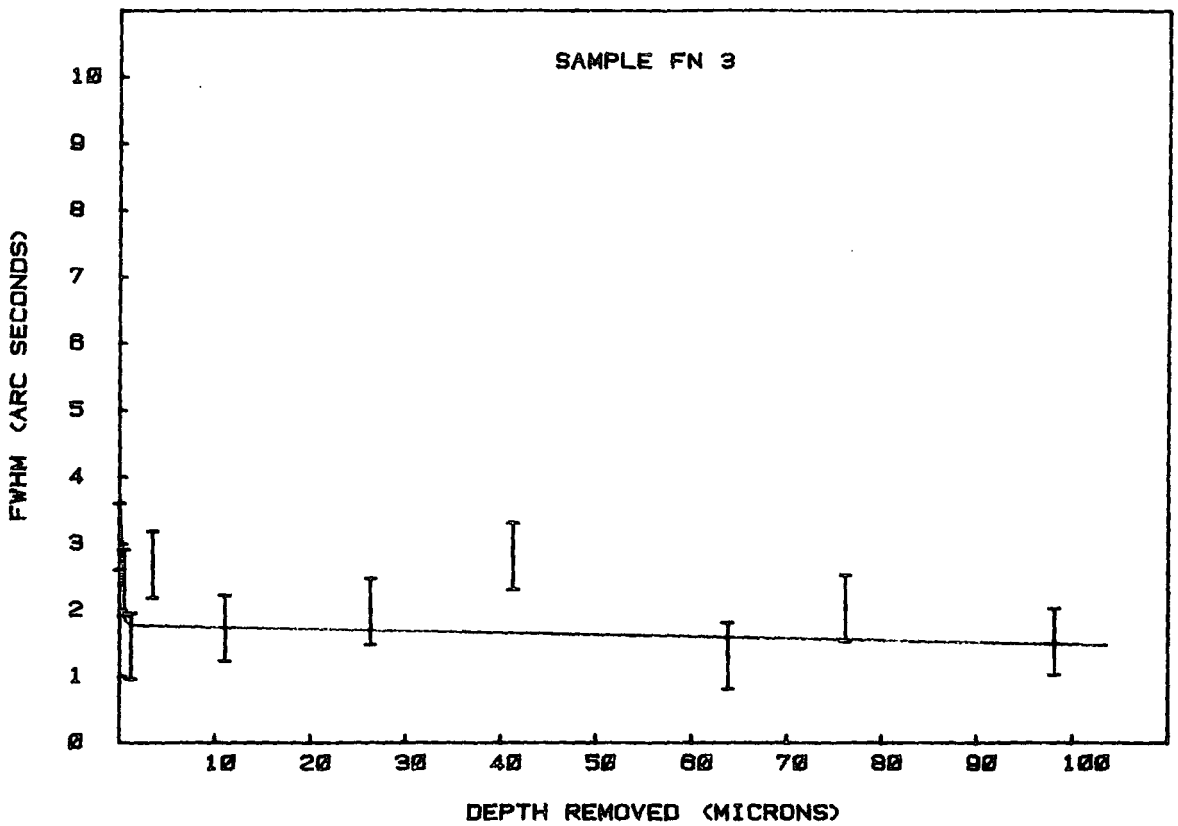

Fig. 5.9 c

Fig. 5.9 a-c Variation of the FWHM of specimens FN 1-3 cut with the flat-nosed tool as they were etched.

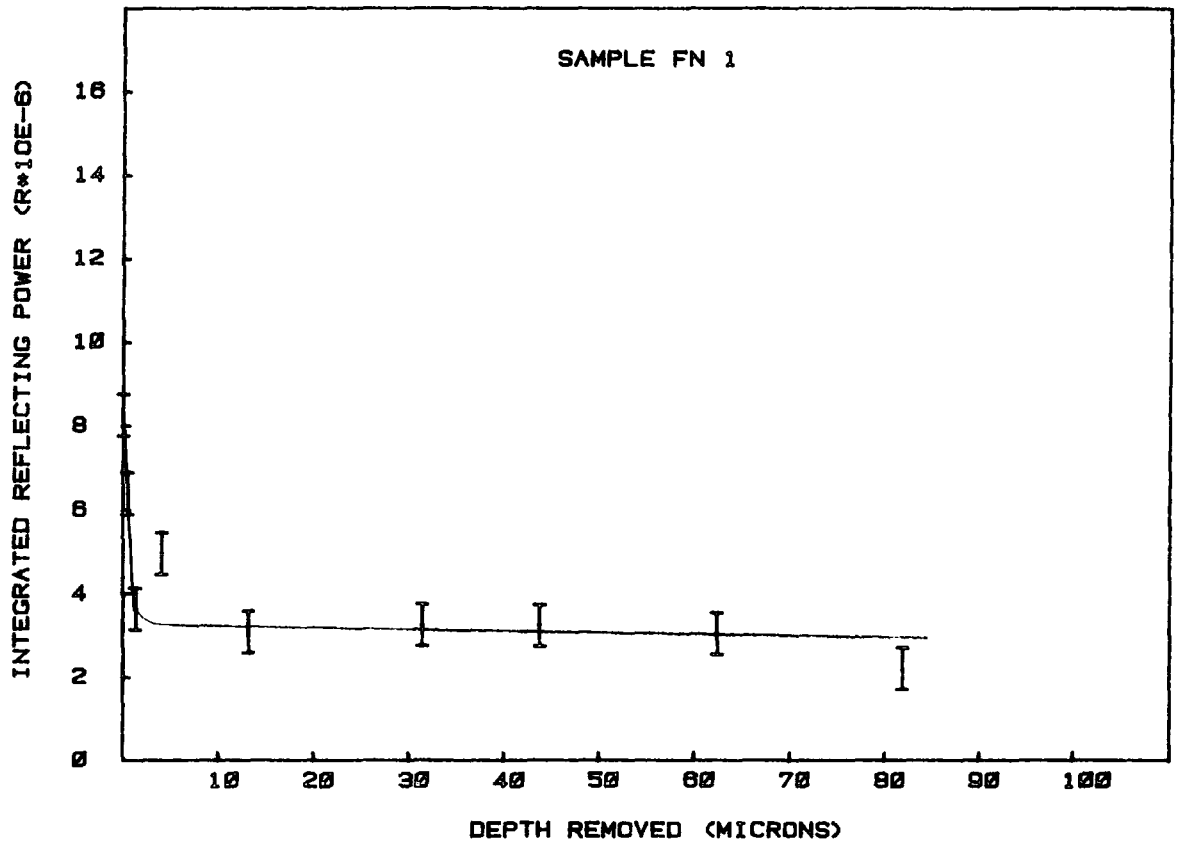

Fig. 5.10a

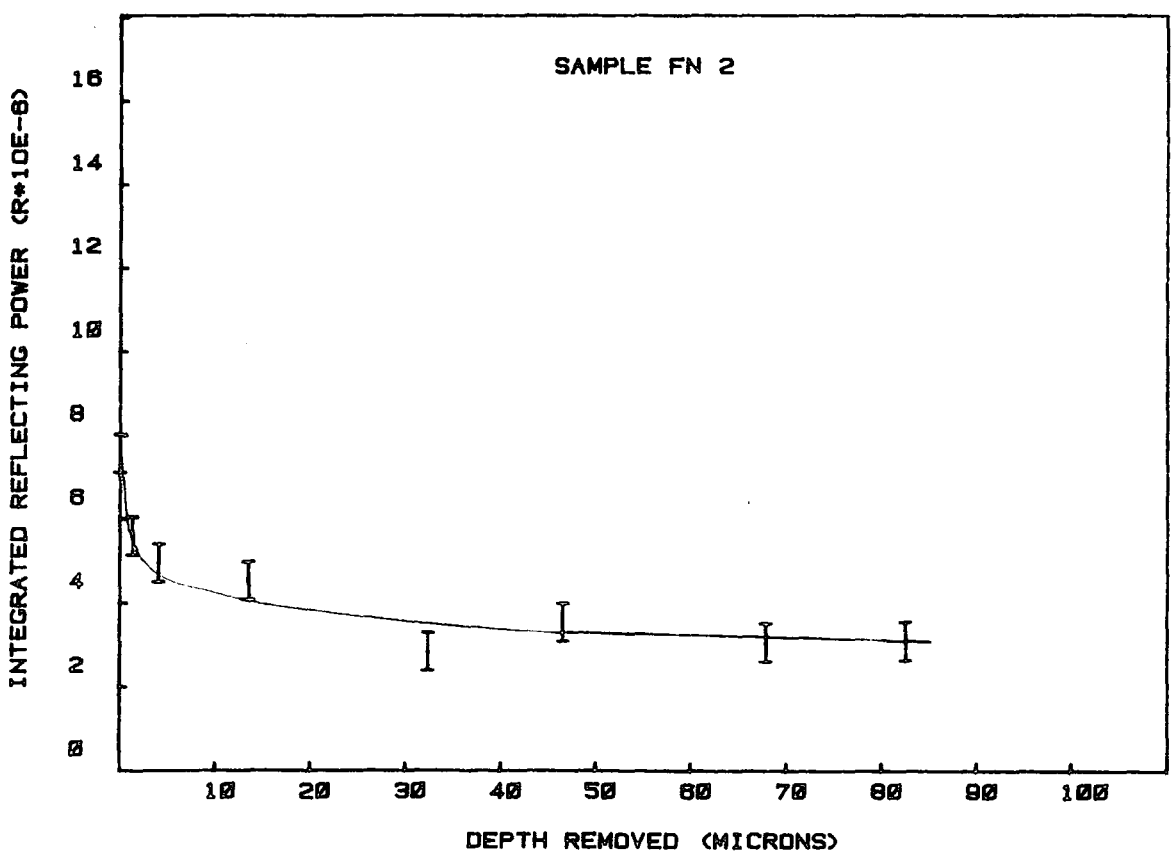

Fig. 5.10b

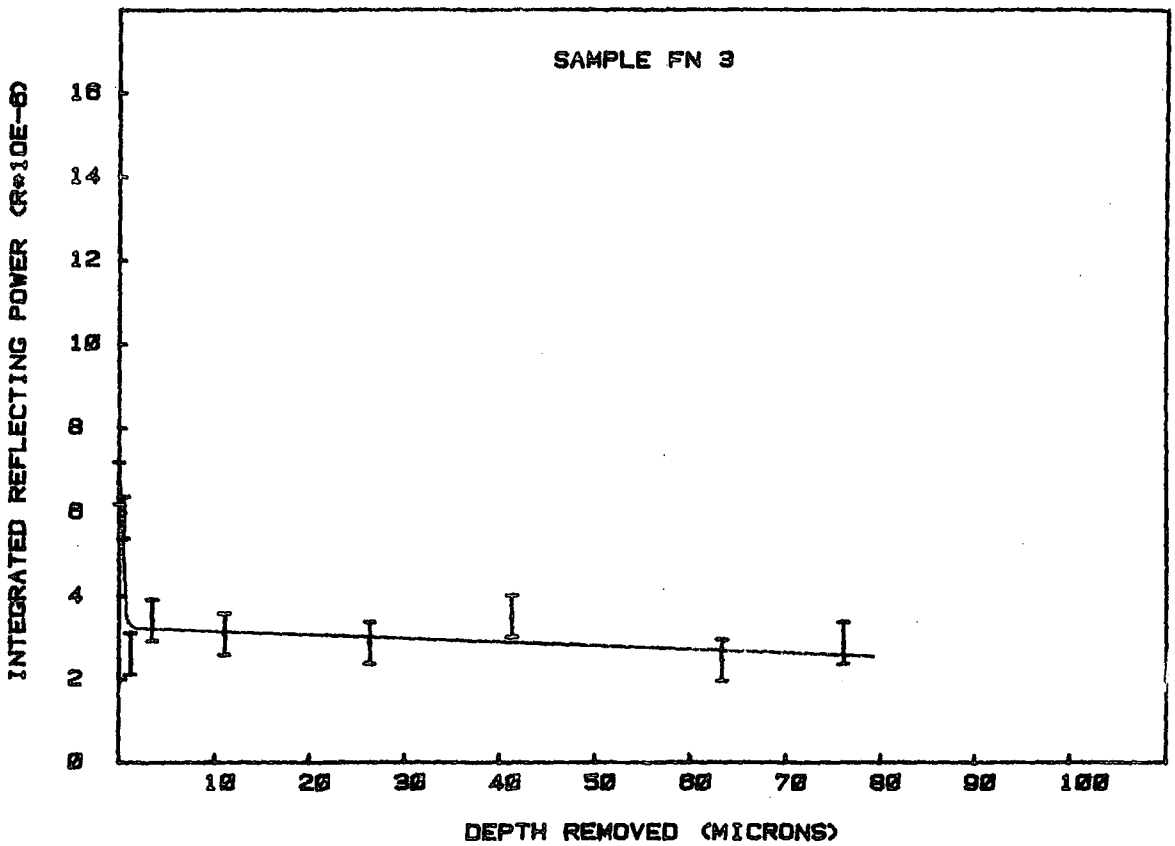

Fig. 5.10c

Fig. 5.10a-c Variation of the integrated reflecting power of specimens FN 1-3 cut with the flat-nosed tool as they were etched.

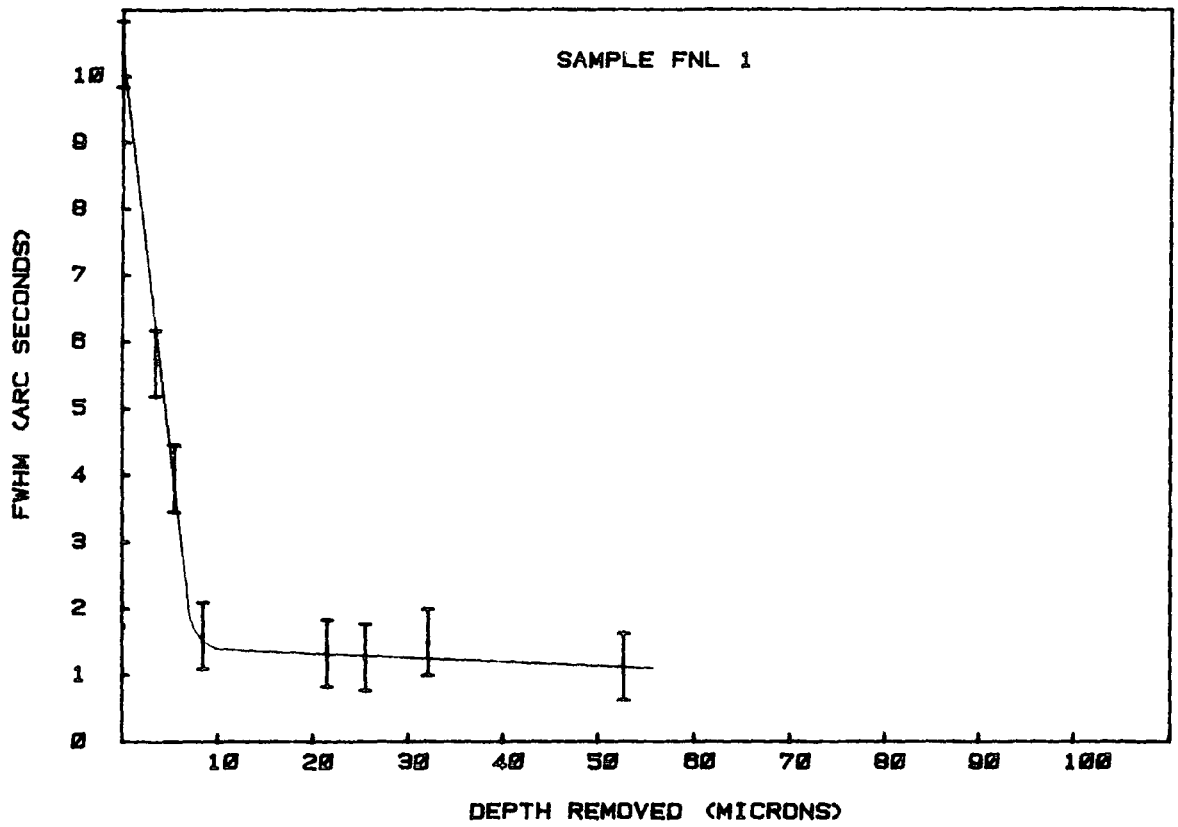

Fig. 5.11a

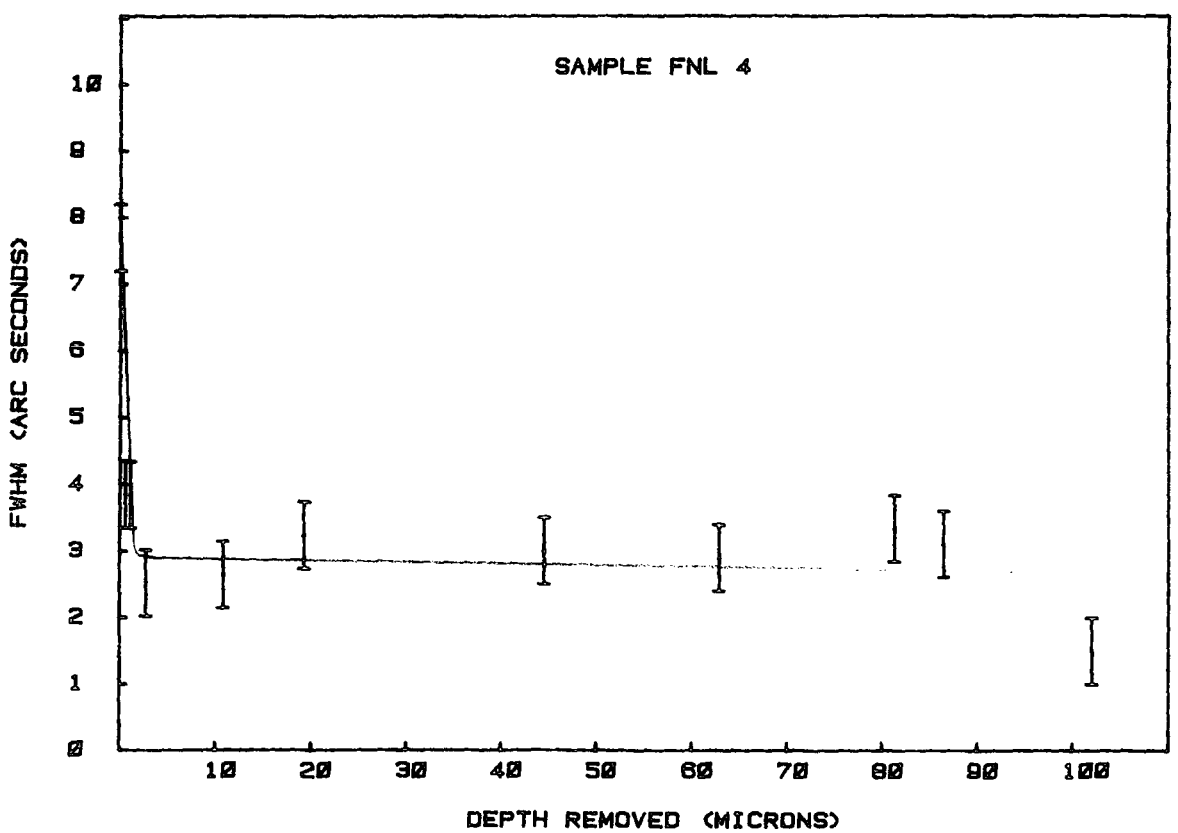

Fig. 5.11b

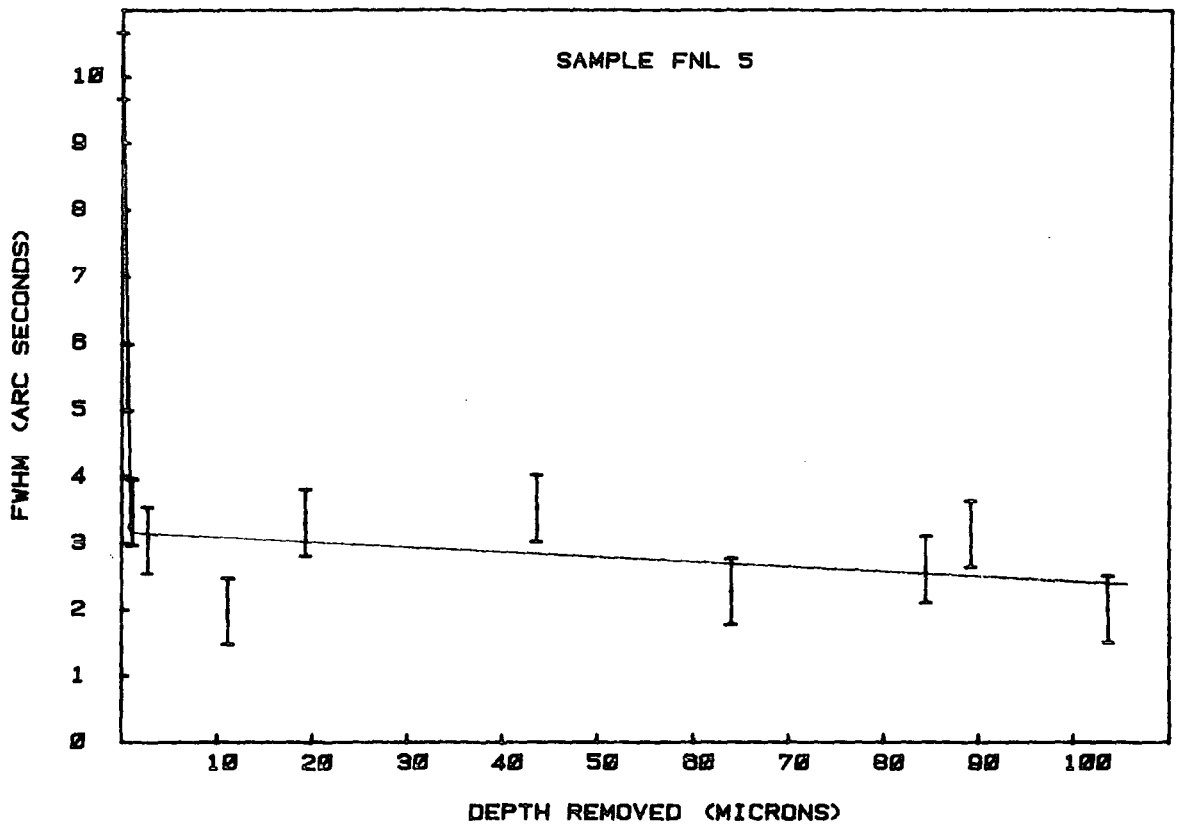

Fig. 5.11c

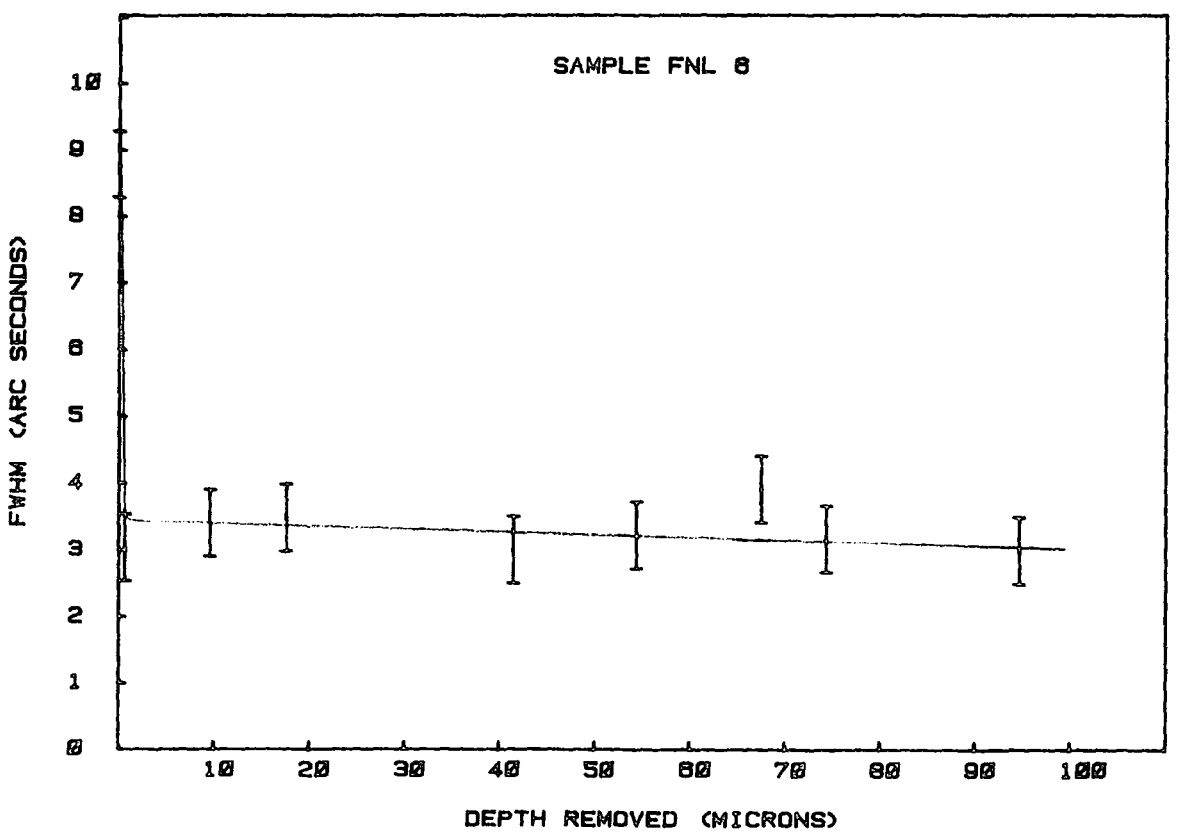

Fig. 5.11d

Fig. 5.11a-d Variation of the FWHM of specimens FNL 1 and FNL 4-6 cut with the flat-nosed tool

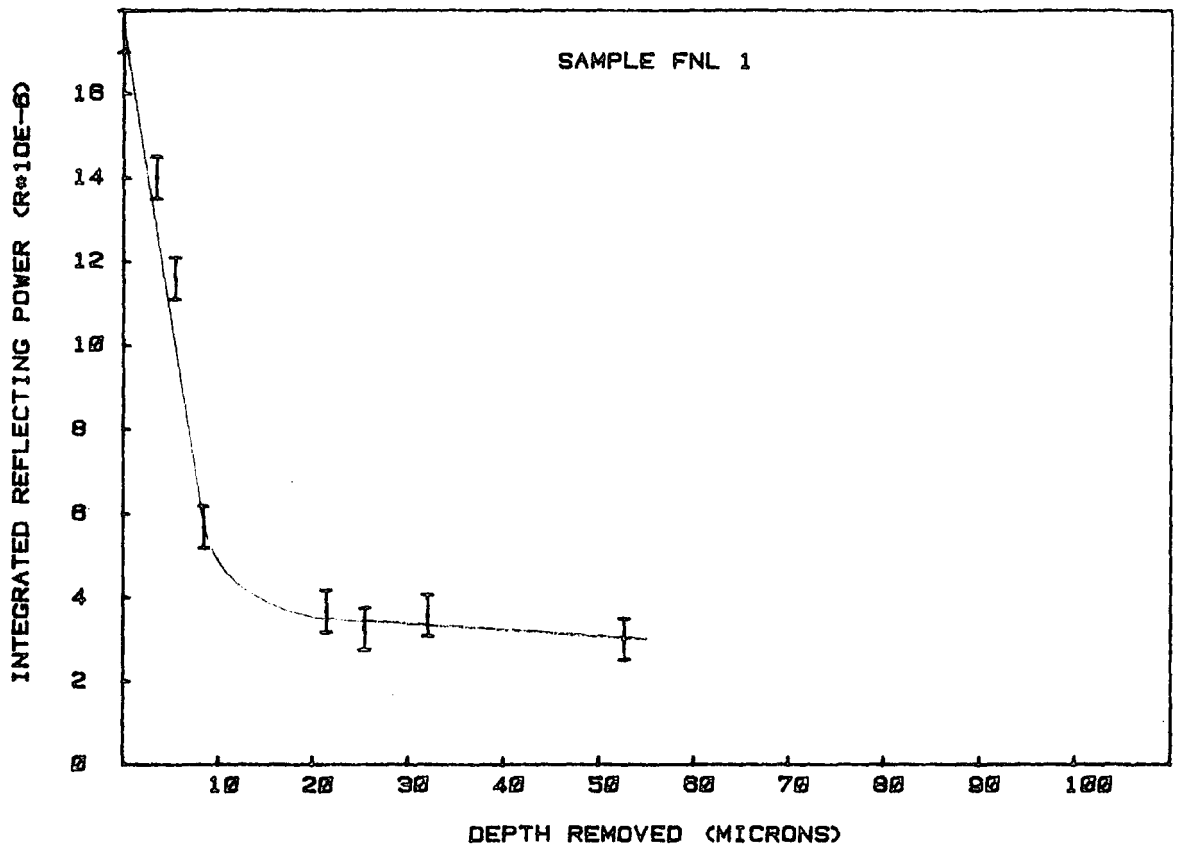

Fig. 5.12a

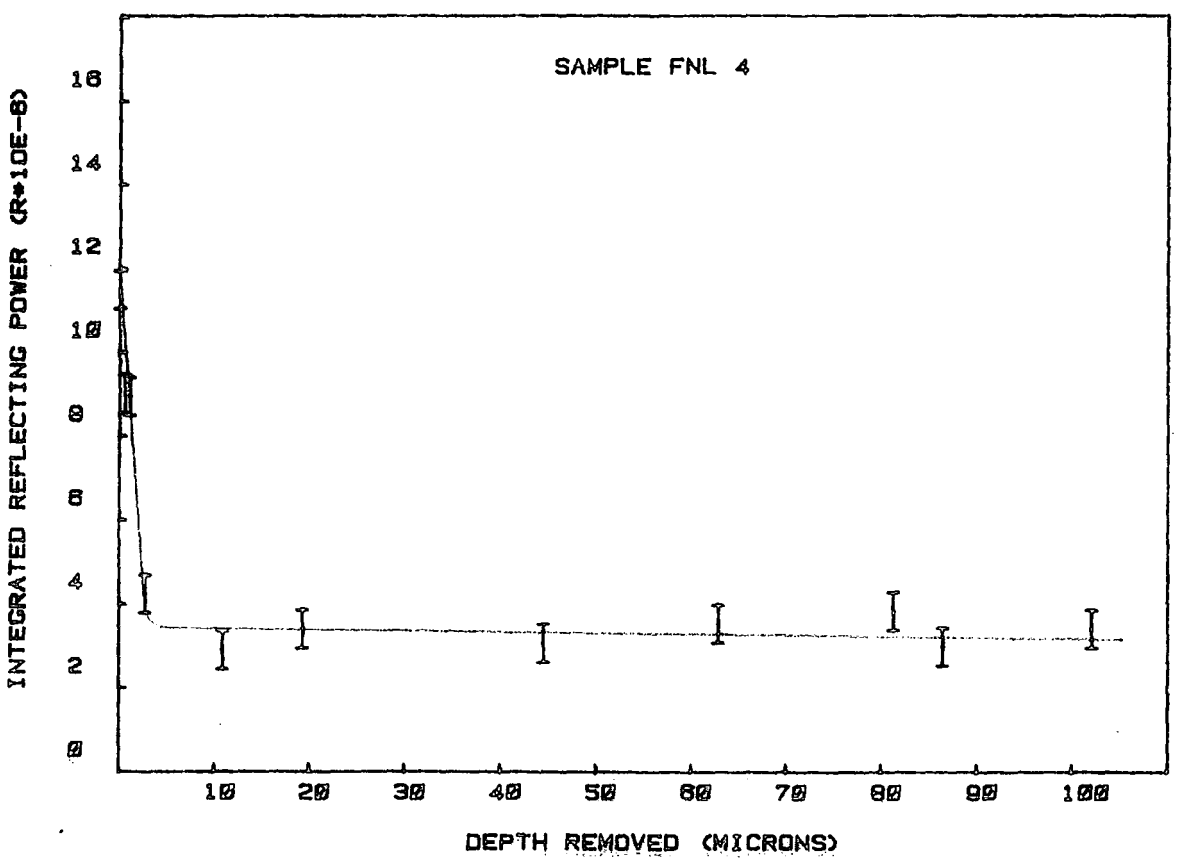

Fig. 5.12b

Fig. 5.12c

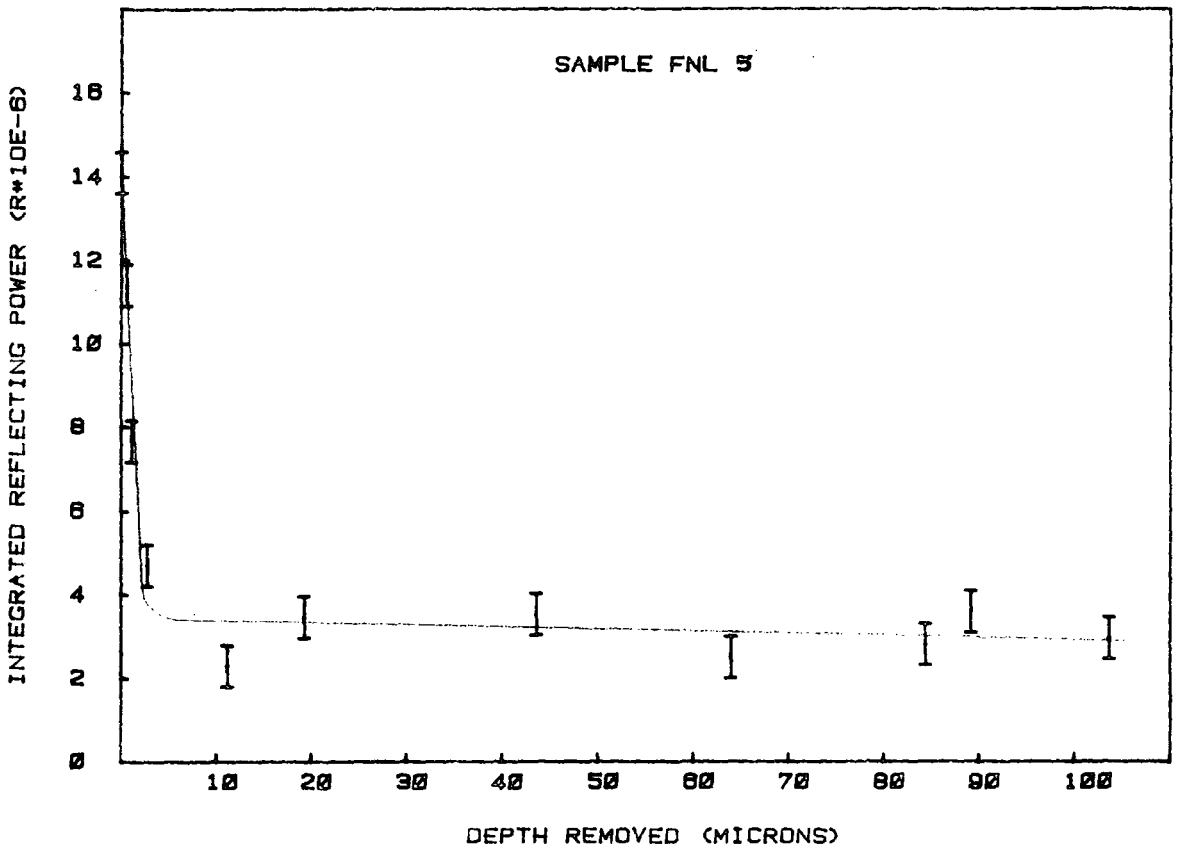

Fig. 5.12d

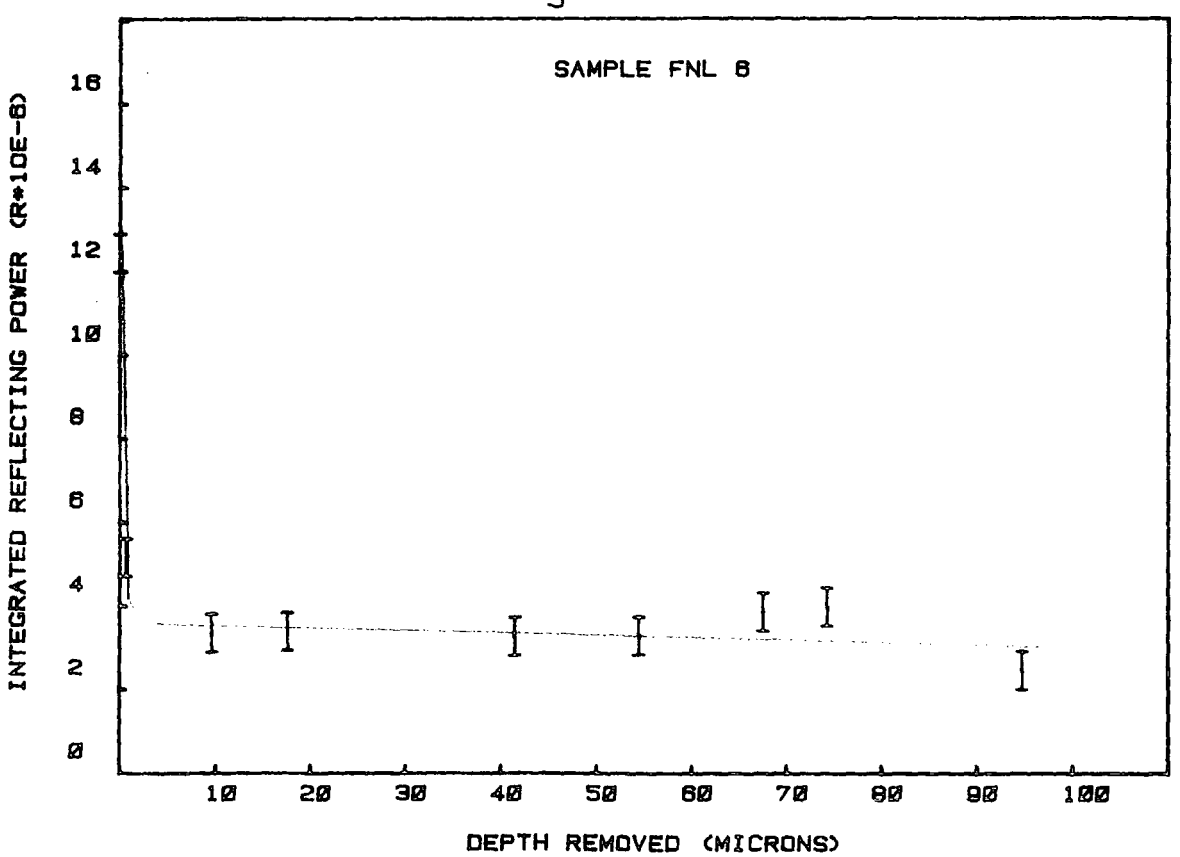

Fig. 5.12a-d Variation of the integrated reflecting power of specimens FNL 1 and FNL 4-6

variations of the FWHM and integrated reflecting power of the rocking curve with the position on the chuck indicating that the depth of damage and the damage profile is independent of the cutting speed between 40-620 m min^{-1}.

The most significant result is that in almost all the samples cut with the different types of tool, there is a sharp fall in the FWHM as the first few micrometers (0-5 μm) is etched away. This is followed by a slow decrease in the FWHM for a further 100 μm when it approaches the value of the control sample although for sample RN1 the fall is not so sharp. This was the first sample etched away and it was not anticipated that the FWHM would drop very sharply. Thus, readings were not taken until at least about 4 μm were removed. For sample FNL1 the fall is also not so sharp compared to the other samples cut by the same tool. The data for the FNL 1 was taken about 7 months later after that of samples FNL 4-6. During that period the microcracks introduced during the turning process might well have propagated through the sample giving a deeper damage layer, resulting in a gradual drop in FWHM as the sample is etched away. This factor is not a major problem as the damage is removed when a further 100 μm is etched away and the FWHM approach that of the control sample. The integrated reflecting power plots as the samples were etched for all the samples cut with the different types of tools have a similar characteristic, that is a sharp fall for the initial 5 μm etched and a slow fall as successive amounts were removed. The surface finish after about a 100 μm etch for all the samples is comparable to the hand-lapped control sample. As the rocking curve width and integrated reflecting power falls rapidly on removal of the first few micrometers

of material, Talysurf measurement were taken on two samples cut by the flat-nosed tool without and with lubricant before and after a 2 μm etch. The corresponding FWHM and integrated intensity were also measured and tabulated in Table 5.3. The results show that there is no change in the Talysurf measurements that is the surface flatness is preserved to better than 1 μm.

5.5 Conclusions

The important conclusion to be drawn from the results obtained, is that single crystal silicon can be diamond turned on a computer controlled milling machine and can replace the hand lapping and polishing process. As a good surface is obtained as well as the removal of all surface damages after about a 100 μm etch combined with a large reduction in cost and time, this is a promising method for the production of large figured X-ray optical elements for both diffraction and reflection geometries.

After machining, an increase by a factor of 8 and 3 was achieved in the rocking curve FWHM and integrated reflecting power for the round-nosed and flat-nosed tools respectively. The values of the FWHM (9 and 4 arc seconds respectively) are comparable to that of the lower order reflections with long wavelength (6.7 and 5.7 arc seconds for the σ and π polarization at 1.5Å respectively). Such as turned surfaces could find application in modest resolution high reflectivity experiments like protein crystallography.

Table 5.3 The FWHM and integrated reflecting power of specimens FN4 and FNL3 before and after a 2 m etch.

Specimen	FWHM (arc seconds)		Integrated intensity	
	Before 2μetch	After 2μetch	Before 2μetch	After 2μetch
FN4	2.3 ± 0.5	1.3 ± 0.5	$6.4 \times 10^{-6} \pm 0.2 \times 10^{-6}$	$3.2 \times 10^{-6} \pm 0.2 \times 10^{-6}$
FNL3	15.5 ± 0.5	6.7 ± 0.5	$2.1 \times 10^{-5} \pm 0.2 \times 10^{-5}$	$1.7 \times 10^{-5} \pm 0.2 \times 10^{-5}$

Other experiments could be carried out to determine whether use of other diamond turning parameters yields a better result. For example there is a need to investigate whether a brand new or worn off tool affects the initial damage produced and also a further study of the effect of lubricant on the machining process. In particular, further experiments are needed with a much smaller cut depth. When X-ray mirrors are produced, cut depths of only a few μm are used and it may be that such a technique introduces much less damage.

CHAPTER 6

GAMMA RAY DIFFRACTOMETRY

6.1 Introduction

This chapter describes the work carried out at Rutherford Laboratory to test the feasibility of γ-ray double crystal technique for the study of perfection of large as grown crytals. This technique has a very high sensitivity and might be very useful if it can be used as an on-line testing of silicon crystals prior to slicing for silicon device fabrication.

A feature of γ-ray experiment is the large separation between the crystals and the detector which, because of the small Bragg angles, is necessary to separate the Bragg reflected beam from the transmitted beam. This large separation is tolerable since the absorption of the 412 keV γ-rays in air is negligible.

6.2 Review of Past Work on γ-ray Diffractometry

Experiments on crystal diffraction by γ-rays date back as early as 1914. Most of the experiments were aimed at the measurement of energy and wavelength. Rutherford and Andrae (1914) measured the energies and intensities of the γ-rays as low as 70 mÅ by transmission through RaB and RaC crystals in lamina form. This was followed by Thibaud (1925) eleven years later. Frilley (1929) made use of Thibaud's arrangement and measured wavelength as low as 16 mÅ. The gamma rays were Bragg reflected at grazing incidence, also using a flat

crystal lamina, and the diffracted beam was recorded photographically. The resolution and precision obtained is poor especially at small angle of incidence as the direct and diffusely scattered beam result in a high background. Hulubei and Cauchois (1934) improved the geometry by using a curved crystal which diffracted X-rays from an extended source and the photographic plate was placed such that the X-rays were focussed on it. The shortest wavelength measured was about 160 mÅ.

A major breakthrough was made by Du Mond (1947). He constructed a curved crystal spectrometer with a 2m radius of curvature with the source placed at its focal circle. Each position on the focal circle corresponds to one particular wavelength. A wide detector was used to detect the transmitted beam which is a function ofthe source position. Soller slits were used to shield the direct and scattered radiation from reaching the detector especially for low wavelength measurements. The spectrometer is capable of measuring a wide range of energies between 40 keV and 1.3 MeV. A precision of 1 part in 10,000 is attainable for energy below 500 keV.

Following the breakthrough and the availability of neutron reactors, a number of similar instruments have been constructed for the same purpose. Examples are the spectrometer built by Ryde and Anderson (1955), Knowles (1957), Sumbaev (1957), Beckman et al. (1958), Piller et al. (1973) and Borchert etal. (1975). The 7.7 m and 2.2 m focal length line focus transmission spectrometers built at Argonne (1957)

and Leningrad are used for neutron capture γ-ray studies, as well as the 4.6 m and 5.7 m spectrometers at Munich and Riso (1962) and the 24 m spectrometer at Grenoble (1975).

Knowles (1959) made use of the successive reflection from a pair of crystals to measure γ-ray energies. The double flat crystal spectrometer as it is called has the advantage that the doubly diffracted beam depends only on the relative angle between the two crystals and is therefore independent of the position of the axes of the crystal turntables. An optical device which is insensitive to translation of the crystal turntables was used for the angle measurement. This method has a high resolution and extensive energy range but it has a disadvantage of lower efficiency.

Besides the measurement of energy and wavelength, γ-rays have been used as a tool for the assessment of crystal perfection. As γ-rays have a rather weak absorption, the property is exploited to study the mosaic structure of large as-grown single crystals and monochromators used in neutron scattering experiments (Schneider 1974 a,b). The advantage of γ-ray experiments is that it can be carried out at high or low temperature or under pressure without additional experimental difficulties since the oven, cryostat or high pressure device need not have any windows.

γ-ray diffraction have also been used to test Darwin's theory of diffraction in mosaic crystal (Schneider 1975) and the measurement of structure factor from absolute intensity of high order diffracted beams(Schneider 1978). An excellent review of the work has been published by Schneider

(1980).

Typical resolution of a single axis experiment is between 30 and 60 arc seconds. Higher resolution is limited to about 10 arc seconds due to the low intensity of γ-ray sources (250 Ci) and hence collimator length above 5 m is not practical.

The study of Jahn Teller phase transition in $TbVO_4$ using γ-rays have been carried out by Smith and Tanner (1978) and also by Bastie et al. (1975, 1976, 1978, 1979) to investigate the ferroelectric system of KH_2PO_4.

6.3 Sensitivity of γ-ray Diffraction

From dynamical diffraction theory, the extinction distance ξ_g for a perfect crystal is given by

$$\xi_g = \frac{\pi V_c \cos\theta_B}{r_e \lambda C F} \qquad 6.1$$

where V_c is the volume of the unit cell, θ_B is the Bragg angle, r_e is the classical electron radius, λ is the wavelength, C is the polarization factor and F the structure factor. As the extinction distance for γ-ray is very long, (Table 6.1) the full width at half height maximum $\Delta\theta_{\frac{1}{2}}$ over which the crystal will diffract an incident plane wave is very narrow.

$$\Delta\theta_{\frac{1}{2}} \simeq \frac{2}{g\xi_g} \qquad 6.2$$

Table 6.1 The Bragg angle, extinction distance and FWHM of the reflecting and rocking curves for 0.03 Å gamma ray.

Reflection	Bragg angle (degrees)	Extinction Distance (μm)	FWHM of reflecting curve (sec)	FWHM of rocking curve (sec) *
Si (111)	0.274	991	0.13	0.18
Si (220)	0.448	856	0.09	0.13
Si (311)	0.525	1281	0.05	0.07
Si (400)	0.633	995	0.06	0.08
Si (422)	0.776	1121	0.04	0.06
Si (333)	0.823	1751	0.03	0.04
Ge (111)	0.263	450	0.3	0.42
Ge (333)	1.579	751	0.06	0.08

* Assuming (+ -) parallel geometry and Gaussian lineshapes

As seen in Table 6.2 γ-ray experiments have a higher sensitivity as the FWHM of the reflecting curve for the higher order and therefore weak reflection for 0.7Å radiation is comparable to the low order and thus strong reflection for γ-rays.

An imperfect crystal contains both tilts and dilations in its lattice. The effect of the tilt can be characterized by a misorientation angle η and the strain by the change $\frac{\Delta h}{h}$ of the reciprocal lattice vector h.

Differentiating Bragg's law $2d\sin\theta_B = \lambda$ where $d = \frac{1}{h}$

$$\Delta\theta = \frac{\Delta h}{h} \tan \theta_B \qquad 6.3$$

From equations 6.1 to 6.3

$$\frac{\Delta h}{h} = \frac{4rd^2FC}{\pi V} \qquad 6.4$$

The change in Bragg angle Δθ due to the imperfection can therefore be written as

$$(\Delta\theta)^2 = (\frac{\Delta h}{h} \tan\theta_B)^2 + \eta^2 \qquad 6.5$$

assuming a Gaussian distribution for the lattice tilt and strain.

In γ-ray experiments the effects of strain are not detected due to the very small Bragg angle but the effect of tilt is seen as a broadening of the rocking curve if the tilt is greater than the theoretical FWHM of the rocking curve. The rocking curve full width at half height maximum is the convolution of two perfect crystal reflecting

Table 6.2 Comparison of the Bragg angle and the FWHM of the reflecting curve for a 0.03 Å and 0.7 Å radiation.

Reflection	λ = 0.03Å		λ = 0.7Å	
	Bragg angle (degrees)	FWHM of reflecting curve (sec)	Bragg angle (degrees)	FWHM of reflecting curve (sec)
111	0.274	0.18	6.412	3.1
333	0.823	0.04	19.575	0.61
444	1.097	0.03	26.533	0.53
555	1.371	0.01	33.945	0.24
777	1.920	0.006	51.421	0.15

curves if reflection is from the $(hk\ell)$ and $(\bar{h}\bar{k}\bar{\ell})$ planes of identical reference and specimen crystals. The FWHM is typically 40% larger than the perfect crystal reflecting range which is a fraction of an arc second. For Gaussian lineshapes the FWHM is $\sqrt{2}$ times the plane wave FWHM. Therefore lattice tilts less than an arc second can theoretically be detected.

6.4 Diffracted Intensity For Plane Parallel Crystal Plates in the Laue Case

As derived in Section 1.3.3a the ratio of the intensities of the external diffracted wave I_H and the external incident wave I_O (Figure 1.10a) is given by

$$\frac{I_H}{I_O} = b^2 |\chi_H|^2 e^{-\mu_o t} \frac{\sin^2(av)+\sinh^2(aw)}{|q + z^2|} \qquad 6.6$$

where $v + iw = \sqrt{q + z^2}$ 6.7

$$a = \pi k_O t_O / \gamma_O \qquad 6.8$$

$$t = \tfrac{1}{2}\left(\frac{1}{\gamma_O} + \frac{1}{\gamma_H}\right) t_O \qquad 6.9$$

$$z = \frac{1 - b}{2} \chi_O + \frac{b}{2} \alpha \qquad 6.10$$

$$q = b \chi_H \chi_{\bar{H}} \qquad 6.11$$

The quantities used have already been defined in Section 1.3.3.

For the case of zero absorption, the polarizability per unit volume is real. The Fourier coefficient of χ_H are such that $\chi_{\bar{H}} = \chi_H^*$, that is $\chi_H \chi_{\bar{H}} = |\chi_H|^2$ and q and z are real

quantities. Therefore $u_o = 0$, $w = 0$ and $v = \sqrt{b|\chi_H|^2 + z^2}$.

Let

$$A = a\sqrt{|b|}\ K\ |\chi_H|$$

$$A = \frac{\pi k_o K |\chi_H| t_o}{\sqrt{\gamma_o \gamma_H}} \qquad 6.12$$

and

$$y = \frac{z}{\sqrt{|b|} K |\chi_H|}$$

$$= \frac{\frac{1-b}{2}\chi_o + \frac{b}{2}\alpha}{\sqrt{|b|}\ K\ |\chi_H|} \qquad 6.13$$

K is the polarization factor where

$K = 1$ for normal polarization.

$= |\cos 2\theta_B|$ for parallel polarization.

Using equations 6.7 to 6.13, equation 6.6 simplifies to

$$\frac{I_H}{I_o} = \frac{b \sin^2 \left[A\sqrt{1 + y^2}\right]}{1 + y^2} \qquad 6.14$$

The power of the diffracted beam P_H and the incident beam P_o are given by

$$P_H = S_H I_H \qquad 6.15$$

$$P_o = S_o I_o \qquad 6.16$$

S_H and S_o are the cross section of the diffracted and incident beam respectively.

$$\frac{S_H}{S_o} = \left|\frac{\gamma_H}{\gamma_o}\right| = \frac{1}{b} \qquad 6.17$$

Thus the reflecting power P_H/P_o is given by

$$\frac{P_H}{P_o} = \frac{1}{|b|}\frac{I_H}{I_o}$$

$$= \frac{\sin^2\left[A\sqrt{1 + y^2}\right]}{1 + y^2} \qquad 6.18$$

The diffraction pattern is obtained by plotting a graph of P_H/P_o as a function of y. The nature of the diffraction curve is therefore dependent on the value of A which is proportional to the crystal thickness t_o and inversely proportional to the extinction distance ξ_g. The shape of the diffraction pattern can therefore be divided into three categories according to whether $A>>1$, $A<<1$ or $A\simeq 1$. A detailed discussion of the dependence of the diffraction pattern on A has been given by Zachariasen (1945).

The crystal dealt with in the experiment falls in the first category that is $A>>1$. For a given value of y the reflecting power P_H/P_o oscillates between zero and $\frac{1}{1 + y^2}$ as A tends to infinity. This is due to the term $\sin^2\left[A\sqrt{1 + y^2}\right]$ which exhibits interference fringes which gets closer as A increase. It is reasonable to assume that the interference fringes are smeared out for large values of A due to variations in sample thickness and the fact that the $\sin^2$ term oscillates extremely rapidly. The term $\sin^2\left[A\sqrt{1 + y^2}\right]$ can therefore be replaced by its average value of $\frac{1}{2}$. Then

$$\frac{P_H}{P_o} = \frac{1}{2(1 + y^2)} \qquad 6.19$$

The integrated reflecting power R^{y}_{H} is the area under the diffraction curve

$$R^{y}_{H} = \int_{-\infty}^{\infty} \frac{P_H}{P_O} \, dy \qquad 6.20$$

For $A \gg 1$, $R^{y}_{H} = \frac{\pi}{2}$ since $\int_{-\infty}^{\infty} \frac{1}{1+y^2} \, dy = \pi$

As derived in Section 2.4 the reflecting power P(y') for a double crystal (+,-) parallel arrangement where $\theta_B = \theta_B'$

$$P(y') = \int_{-\infty}^{\infty} n\left[\frac{I_H}{I_O}(y)\right] n\left[\frac{I_H}{I_O}(y' - by)\right]' dy \qquad 6.21$$

$$+ |\cos 2\theta_B| \int_{-\infty}^{\infty} p\left[\frac{I_H}{I_O}(y)\right] p\left[\frac{I_H}{I_O}\left(\frac{y'}{|\cos 2\theta_B|} - by\right)\right]' dy$$

$$\frac{}{|bb'|\{^{n}[R_H{}^{y}] + |\cos 2\theta_B| \, {}^{p}[R_H{}^{y}]\}}$$

If the reference and sample crystal are identical and a symmetrical reflection is used $\frac{I_H}{I_O}(y) = \frac{I_H'}{I_O}(y)$ and $b = b' = 1$. Thus P(O) is the maximum value of P(y').

$$P(O) = \frac{\int_{-\infty}^{\infty} {}^{n}\left[\frac{I_H}{I_O}(y)\right]^2 dy + |\cos 2\theta_B| \int_{-\infty}^{\infty} {}^{p}\left[\frac{I_H}{I_O}(y)\right]^2 dy}{{}^{n}[R_H{}^{y}] + |\cos 2\theta_B| \, {}^{p}[R_H{}^{y}]} \qquad 6.22$$

The percent reflection is given by 100 P(O). A P(y') versus y' plot gives the diffraction pattern for the double reflection and the integrated reflecting power R is obtained by integrating equation 6.21 from $-\infty$ to $+\infty$

$$R = \int_{-\infty}^{\infty} P(y') \, dy' \qquad 6.23$$

For A>>1 and the case of zero absorption R simplifies to

$$R = \frac{2(1 + \cos^2 2\theta_B)}{(1 + |\cos 2\theta_B|)^2} \overline{R^{\theta}}_H \qquad 6.24$$

The FWHM corresponds to the difference in the values of y' when the reflecting power is $\frac{1}{2}P(O)$.

In the interpretation of γ-ray rocking curves, the measured integrated reflecting power R_m is compared to R_{kin} and R_{dyn}. R_{kin} is calculated on the basis of the kinematical theory and R_{dyn} is determined from the dynamical theory for a perfect crystal of thickness t_o greater than the extinction distance ξ_g. For an ideally perfect crystal $R_m = R_{dyn}$ and if $R_m = R_{kin}$ the crystal is said to be ideally imperfect.

6.5 Diffractometer Design

As the experiment was carried out at Rutherford Laboratory the COFFIN (Jones and Tanner 1980) was transported from Durham together with its computer control system. The facility provided at Rutherford was a neutron goniometer, the Badger, used for single axis work. Due to the very small Bragg angles involved in γ-ray experiments, of the order of one degree (Table 6.1) it proves essential to use the COFFIN instead of the EGG. The larger axis separation of the COFFIN enables the direct beam to be separated from the doubly diffracted beam. The monolithic diffractometer provides the stability required for the measurement of very small angular rotations (a fraction of an arc second) and to maintain temperature stability, a large piece of expanded polystyrene

was hollowed out to surround the whole diffractometer.

The first diffractometer axis was placed concentric with the Badger. The Badger, which is stepper motor controlled, is capable of rotating the diffractometer to any required angle but it proved sufficient and easier to set the diffractometer manually and reading from a linear scale placed on the bench supporting the other end of the diffractometer. The bench is placed on guide bars 6 m long which also supports other benches used to mount the detector and the source slit system. The geometry of the arrangement can be varied by sliding the benches along the guide bars. Figure 6.1 is a photograph of the experimental arrangement.

6.5 Detector Characteristics

A standard scintillation counter was used as a detector. It consists of a photomultiplier tube and a NaI(Tℓ) scintillation crystal, 1.5 inches in diameter and length. A 3mm x 35mm high slit made from two lead blocks was placed in front of the detector to define the beam entering the detector. Lead sheets were wrapped round the detector to reduce the background count. The detector together with the slit system were supported on a holder which is micrometer driven so that it can be translated linearly across the direct beam and to the required $2\theta_B$ position which is normally less than 1^o. The output from the detector was fed to a programmable counter after pre-amplification and the whole system was controlled by a 32K byte Commodore PET microcomputer via a BESELEC Minicam Interface.

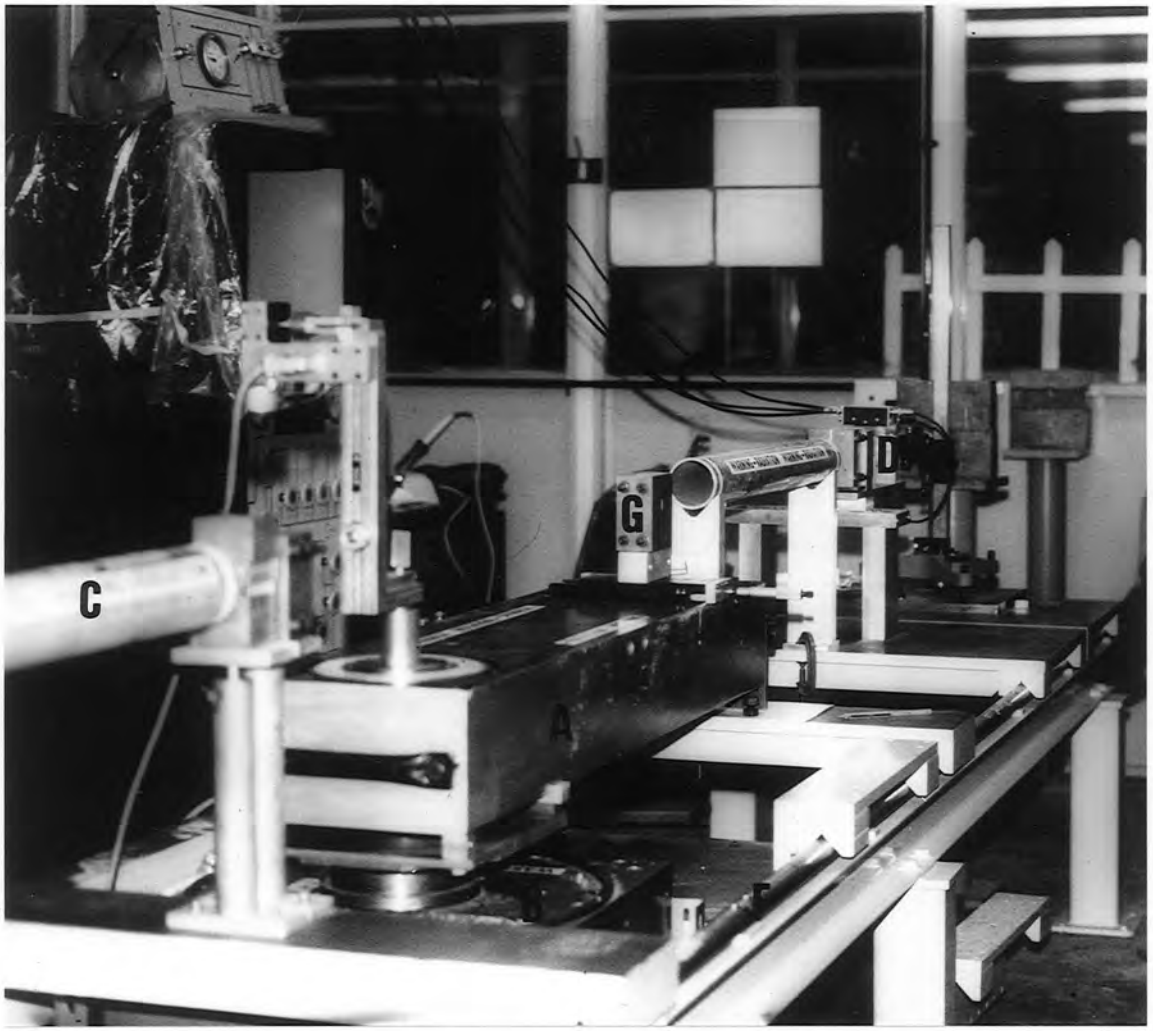

A - Diffractometer
B - Badger
C - Source collimator
D - Detector
E - Crystal on goniometer
F - Guide bars
G - Lead block on a linear bearing

Fig. 6.1 Photograph of the experimental arrangement.

Although precautions were taken to reduce the background count, a high background is still obtained which resulted in a very low signal to noise ratio for the doubly diffracted peak. A typical example is the double reflection from a pair of highly perfect silicon crystals (Figure 6.13). A peak count rate of 12 counts per second was obtained compared to a background of 7 counts per second. A slit placed between the first and second crystal does not improve the condition very much as much of the scatter still reaches the counter due to the very small scattering angles. A Si energy dispersive detector has been used but it failed to improve the signal to noise ratio due to its low efficiency and a Ge energy dispersive detector was not available.

6.7 Source Design

The source of γ-radiation is from a radioactive gold foil 0.25 x 6.5 x 6.5 mm irradiated in the DIDO reactor at AERE Harwell. An irradiation period of 3 to 4 days produced an activity of 120 Ci. The following reaction occurs which produces γ-rays of 3 different energies.

$$^{197}\mathrm{Au}(n,\gamma)^{198}\,\mathrm{Au} \xrightarrow[2.7\ \mathrm{days}]{\beta} \mathrm{Hg} + \gamma \begin{matrix} 412 \\ (676 \\ 1088 \end{matrix} \mathrm{kev})$$

The 412 keV line which is most intense was used. It has a wavelength of 0.03Å which is about 1/50 the wavelength of the Cu Kα radiation. It has a very low energy dispersion $\frac{\Delta E}{E} = \frac{\Delta\lambda}{\lambda} = 10^{-6}$ at room temperature, and a half life of about 2.7 days. The accepted safe limit of the source strength for the source container shown in Figure 6.2, was judged to

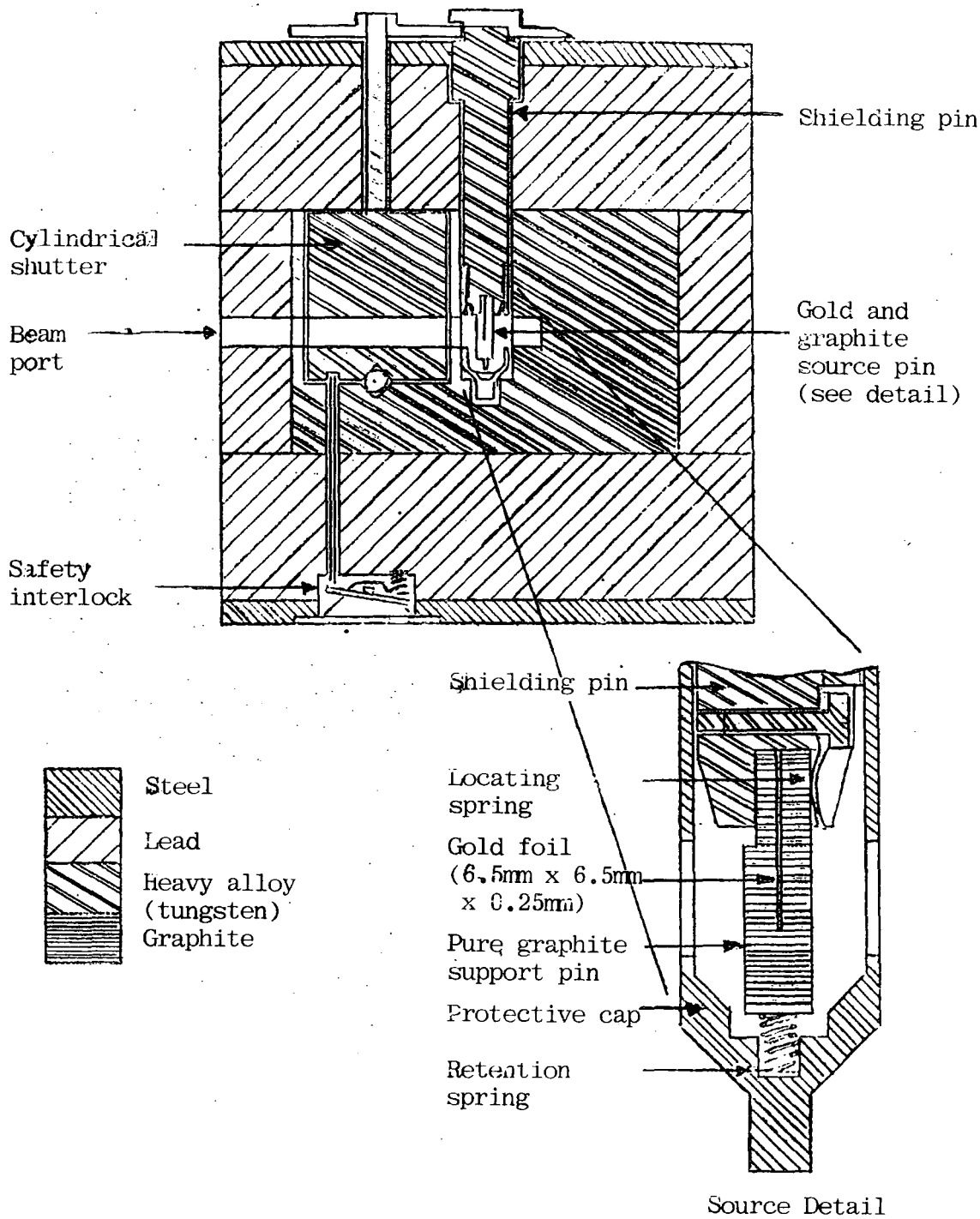

Fig. 6.2 The design of the container used to carry the gamma ray source.

be about 250 Ci but we used a source strength of 450 Ci in the earlier phase of the experiments with no hazards to personnel. With a new 250 Ci source the direct beam count rate of about 1.9 x 10^5 counts per second was obtained when a 1mm x 49mm slit was placed in front of the source.

After irradiation in the reactor, the gold foil which is supported on a pure graphite rod, is transferred to a special holder (Figure 6.2) for insertion in the shielded housing built from tungsten and lead at Rutherford Laboratory. Two slits are placed in front of the source, a 3 mm slit is about 1 m from the source and a 1 mm slit is placed near the first axis of the diffractometer. The distance between the two slits can be varied depending on the geometry required.

6.8 Experimental Procedure

The angular divergence of the incidence beam depends on the final slit in front of the diffractometer. In our arrangement the distance between the final slit which is 1mm and the source varies between 240 and 330cm. Thus the beam divergence varies between 86 and 63 arc seconds. A series of lead blocks are placed between the source and the 1mm slit to limit the angular divergence of the beam emerging from the source.

The zero position or the position where the detector receives the direct beam was initially determined by plotting the detector position versus source strength. The diffractometer is displaced by $2\theta_1$ from its zero position and this corresponds to $w\tan 2\theta_1$ on the linear scale. w is

the distance between the first axis and the linear scale and θ_1 is the Bragg angle for the first crystal.

As in all γ-ray experiments the Laue geometry is used. The specimen crystal can either be on the first or second axis. The direct beam will be incident on both crystals provided that the second crystal is large enough. It is thus easier to obtain the double reflection by first obtaining the single reflection from both crystals which is of the order of 60 arc seconds. The detector must be positioned accordingly to detect the first reflection from both crystals. As shown in Figure 6.3 the detector is displaced by $(x + y)\tan 2\theta_1$ to detect the first reflection from the first crystal and by $y\tan 2\theta_2$ for the second crystal. A lead block positioned on a linear bearing is translated between the first and second axis to cut off the direct beam from reaching the second crystal and to allow only the first crystal diffracted beam to reach the second crystal. In the later phases of the experiments a lead slit was used in order to reduce the high background count. In order to detect the doubly diffracted beam the detector is positioned $\left[(x + y)\tan 2\theta_1 - y\tan 2\theta_2\right]$ from the zero position. If both crystals are identical and reflection are from the same plane, the doubly diffracted beam is only a few arc seconds rotation away.

If non-identical crystals are used or the reflections are not from the same plane, the angle through which the second crystal has to be rotated from its first diffraction peak to obtain the double reflection can be calculated. As shown in Figure 6.4a,b if $\theta_1 > \theta_2$ the second crystal is rotated

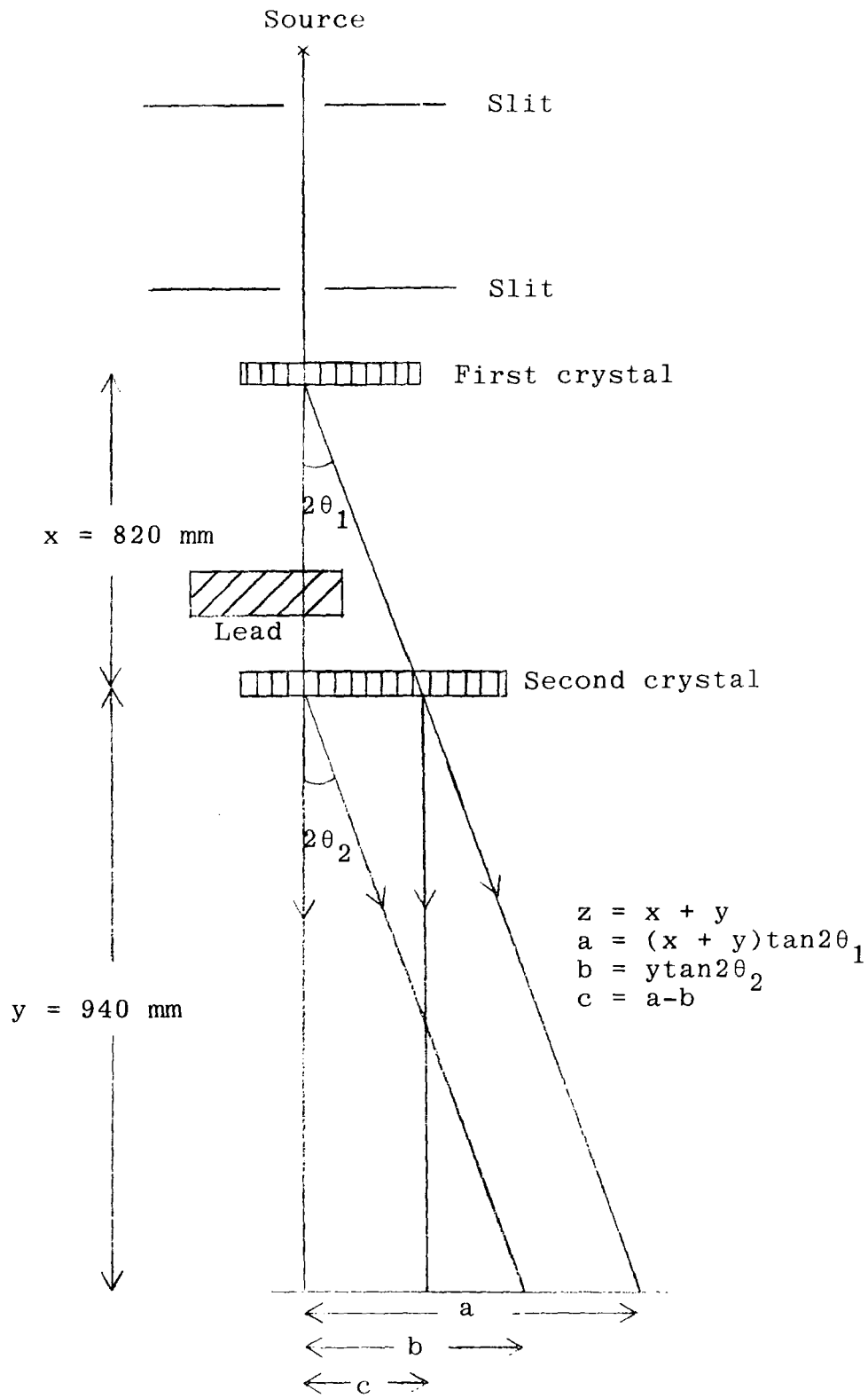

Fig. 6.3 Diffraction geometry showing detector position for the single and double diffracted beam.

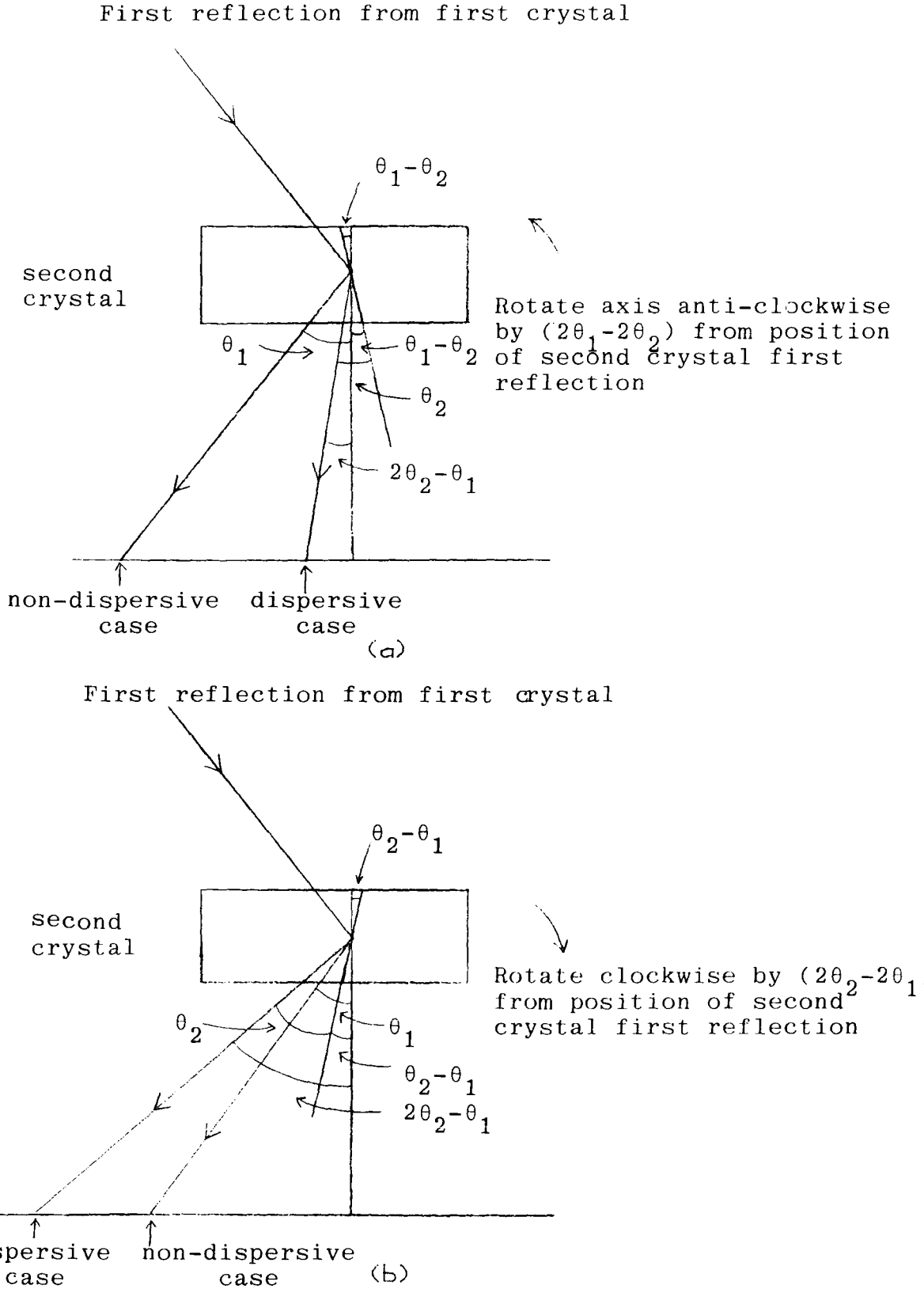

Fig. 6.4 Geometry showing the direction and angle of rotation for the sample crystal if
(a) $\theta_1 > \theta_2$
(b) $\theta_1 < \theta_2$

by $(2\theta_1 - 2\theta_2)$ anticlockwise and $(2\theta_2 - 2\theta_1)$ in a clockwise direction if $\theta_1 < \theta_2$. Once the double reflection is located the relative tilt of the crystal was adjusted using the motorized goniometer. It was necessary to locate the rocking curve after successive tilting of about 4 minute since the peak shifted during the process. It was found to be more convenient to scan and tilt the same crystal due to difficulties in aligning the goniometer tilt axis. Computer control is essential in this experiment due to the high background and low peak count. Typical counting time per point were between 10 to 360 secs.

The integrated reflecting power for the single and double reflection was also measured. With the first crystal in the path of the beam, the detector was positioned to receive the direct beam P_o and the count rate (sec^{-1}) noted. The detector was then displaced by $2\theta_1$ to receive the first crystal diffracted beam. To obtain a reasonable background count the crystal was initially positioned sufficiently far from its Bragg angle θ_1. The crystal was then rotated through its reflecting range at an angular velocity ω (rad sec^{-1}) and the total counts recorded is E. In each case the background intensity must be subtracted. The integrated reflecting power is then given by $R = \frac{E\omega}{P_o}$. The same method applies for the double reflection. P_o is then the peak intensity from the reflection of the first crystal and E is the total intensity obtained when the second crystal is rotated through its reflecting range with an angular velocity ω.

6.9 Effect of Temperature Variation

As the full width at half height maximum of the rocking curve is of the order of a fraction of an arc second, the temperature stability is a critical factor. The length of the aluminium lever used for the sensitive axis is about 53.7 cm and the micrometer used to push the lever has a maximum length of about 9 cm. Taking the coefficient of thermal expansion of aluminium and mild steel (micrometer) to be about 25×10^{-6} per ^{o}C and 15×10^{-6} per ^{o}C respectively at room temperature, we find that a temperature change of $1^{o}C$ causes the aluminium lever and micrometer to change its length by approximately 14.3 μm and 1.35 μm respectively. This corresponds to a change in angular rotation by about 0.3 arc second and is significant compared to 0.012 arc second.

6.10 Results

From Table 6.1 we see that the perfect crystal reflecting range for 0.03Å γ-radiation is less than 1 arc second and is much less than the divergence of the incident beam which is of the order of 70 arc seconds. Thus the single crystal diffraction pattern or more precisely the half width of the rocking curve is not a function of crystal property but is determined by the angular resolution of the diffractometer. The integrated reflecting power is independent of the resolution and can therefore be used to characterize crystal perfection. A survey of the integrated reflecting power of four silicon

crystals was made and compared with the theoretical value. Figure 6.5 shows the variation of the integrated reflecting power as a function of A (Zachariasen 1945). As the crystals studied fall into the category where A>>1, equation 6.18 was integrated numerically to obtain the theoretical or dynamical value R_{dyn}. Table 6.4 is a tabulation of the results obtained. Sample E has an average thickness of about 12 mm. Sample F which contains phosphorus is 8 mm thick. Samples G and H are LOPEX silicon with a thickness of 6 mm and 3.5 mm respectively. All the four samples have been chemically polished with a solution of hydrofluoric acid (48%), nitric acid (70%) and glacial acetic acid mix in a ratio 1:13:6. It can be seen that as the crystal perfection increases (Sample G and H) and the FWHM of the rocking curve decreases (Table 6.5) the integrated reflecting power approaches the dynamical value R_{dyn}. This verifies that measurement of R in a single crystal experiment can be used as an accurate measure of the perfection of highly perfect crystals (Schneider 1980).

The rocking curve shown in Figure 6.6 is the 111 reflection from a pair of moderately perfect germanium crystals 2 mm thick grown some years ago. The FWHM obtained is about 2 arc second compared to the theoretical value of 0.42 arc second (Table 6.1). Figures 6.7a and 6.7b are the single reflection rocking curves from the first and second crystal with a FWHM of 63 and 71 arc seconds respectively. The peak intensity of the single reflection is about 3½ times that of the double reflection. A higher order 333 reflection from the same pair of germanium crystals gives a

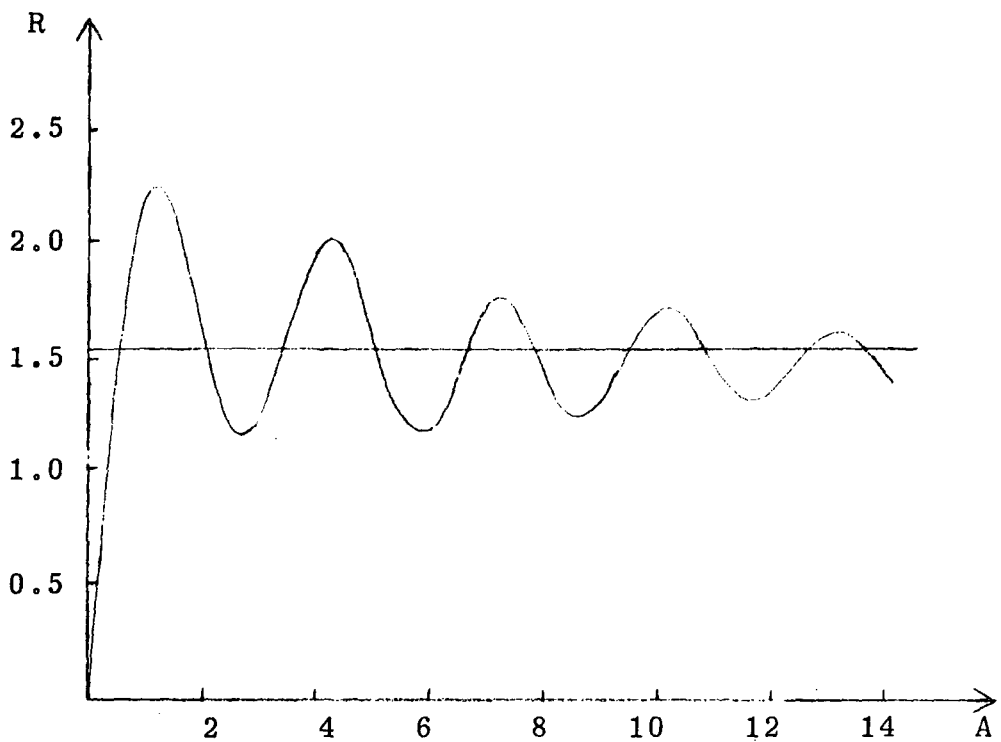

Fig. 6.5 The integrated reflecting power in the Laue case as a function of A.

Table 6.3 Description of the crystals used in the experiment.

Crystal	Description	Thickness (mm)
A	Germanium	2
B	Germanium	2
C	Silicon-Device Grade	3
D	Silicon-Device Grade	3
E	Silicon-From Mullard Semiconductor	12
F	Silicon-From Fairchild Semiconductor	8
G	Silicon-LOPEX	6
H	Silicon-LOPEX	3.5

Table 6.4 The theoretical and the measured integrated reflecting power for the single reflection.

Extinction distance is 991 μm for Si (111) reflection.

Crystal	Thickness mm	R_m	R_{dyn}
Sample E	12	0.59×10^{-6}	0.43×10^{-6}
Sample F	8	10.1×10^{-6}	0.43×10^{-6}
Sample G	6	0.57×10^{-6}	0.42×10^{-6}
Sample H	3.5	0.53×10^{-6}	0.53×10^{-6}

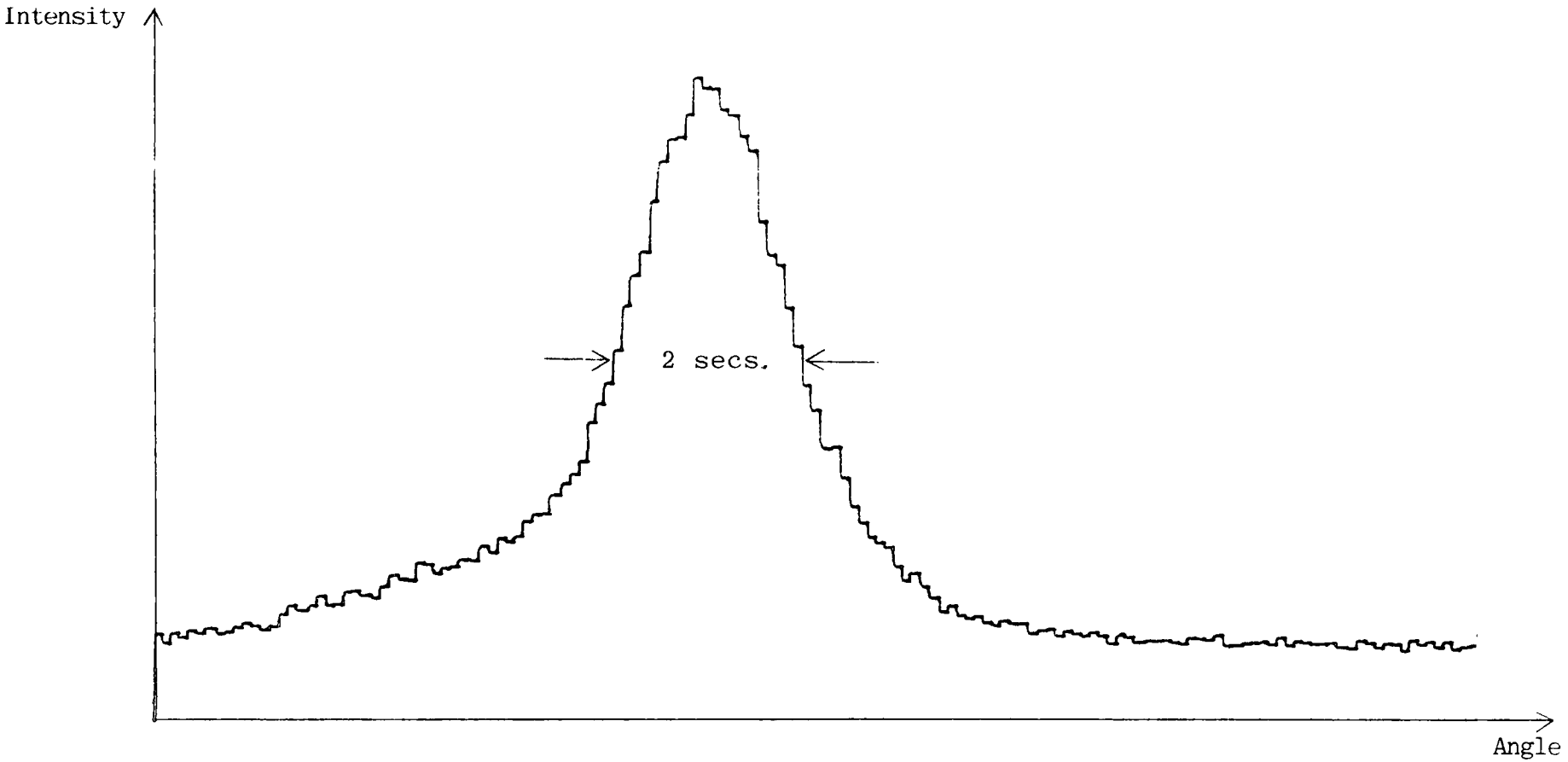

Fig. 6.6 111 double crystal rocking curve from a pair of germanium crystals (Sample A and B). Counting time per 0.1 arc sec. step was 12 sec. Peak height = 138 cps. Background = 33 cps.

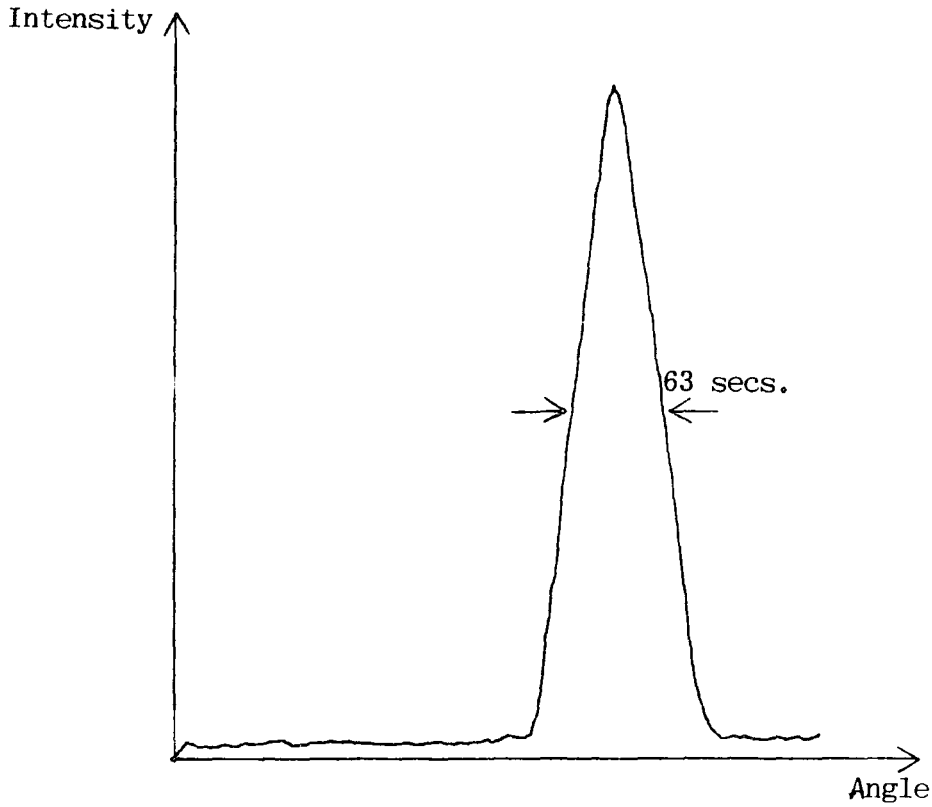

(a)

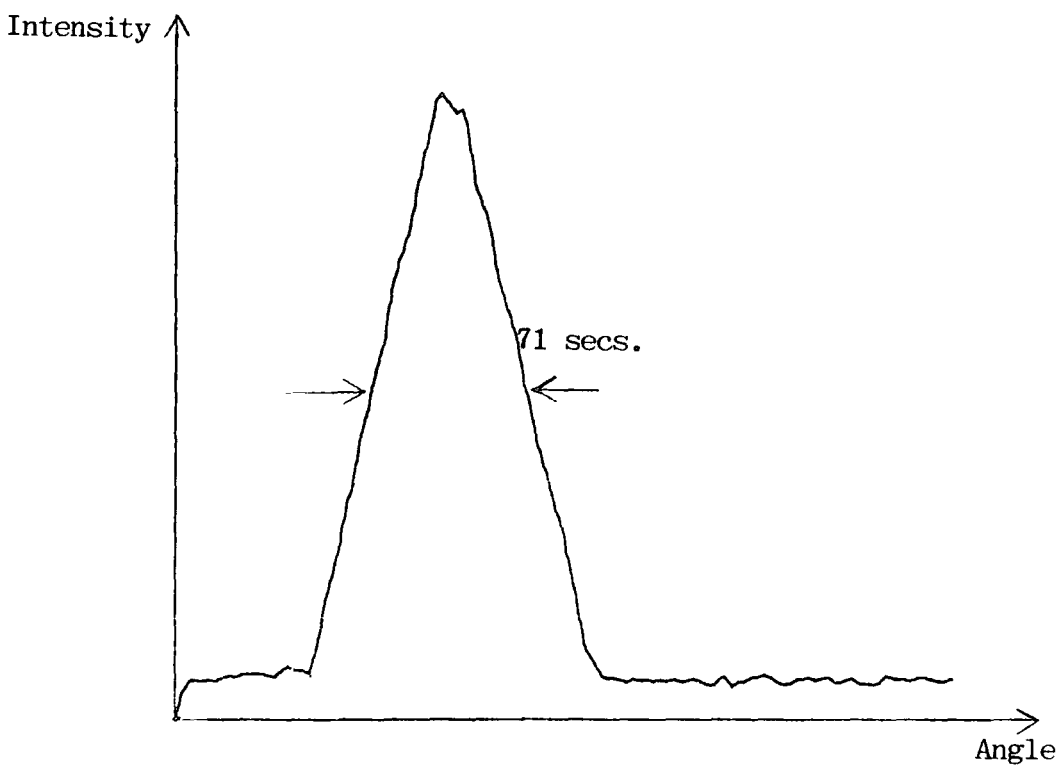

(b)

Fig. 6.7 Single crystal rocking curve from germanium crystals.
(a) Sample A. Counting time per 4.6 arc secs. step was 1 sec. Peak height= 978 cps.
(b) Sample B. Counting time per 3 arc secs. step was 1 sec. Peak height= 894 cps.

rocking curve width of 1.1 arc secondscompared to 0.08 arc second which was expected. The peak intensity of the 333 reflection is reduced by approximately a factor of 4 (Figure 6.8). In both cases the curves are not symmetrical. This could be due in part to surface damage as the crystals were not polished before the experiment.

Broadening of the rocking curve is significant if the reflecting planes of the sample and reference crystals are not exactly parallel as shown by the plot of the FWHM versus angle between the diffracting plane ϕ_c in Figure 6.9. As discussed in Section 2.6 the broadening of rocking curve $\Delta\theta_B$ is a function of the vertical divergence ϕ_v of the source and ϕ_c.

$$\Delta\theta_B = \phi_v\phi_c$$

The fractional broadening is

$$\frac{\Delta\theta_B}{\theta_B} = \frac{\phi_v\phi_c}{\theta_B} \qquad 6.25$$

This expression is similar to Knowles' equation (Knowles 1962) for the fractional broadening of rocking curve except for the first term where an approximation was taken in equation 2.52a in which the higher order term of ∂ and ψ are neglected (Section 2.6). Knowles expression is

$$\frac{\Delta\theta_B}{\theta_B} = -\frac{\phi_v^2 + \phi_c^2}{2} + \frac{\phi_c\phi_v}{\theta_B} \qquad 6.26$$

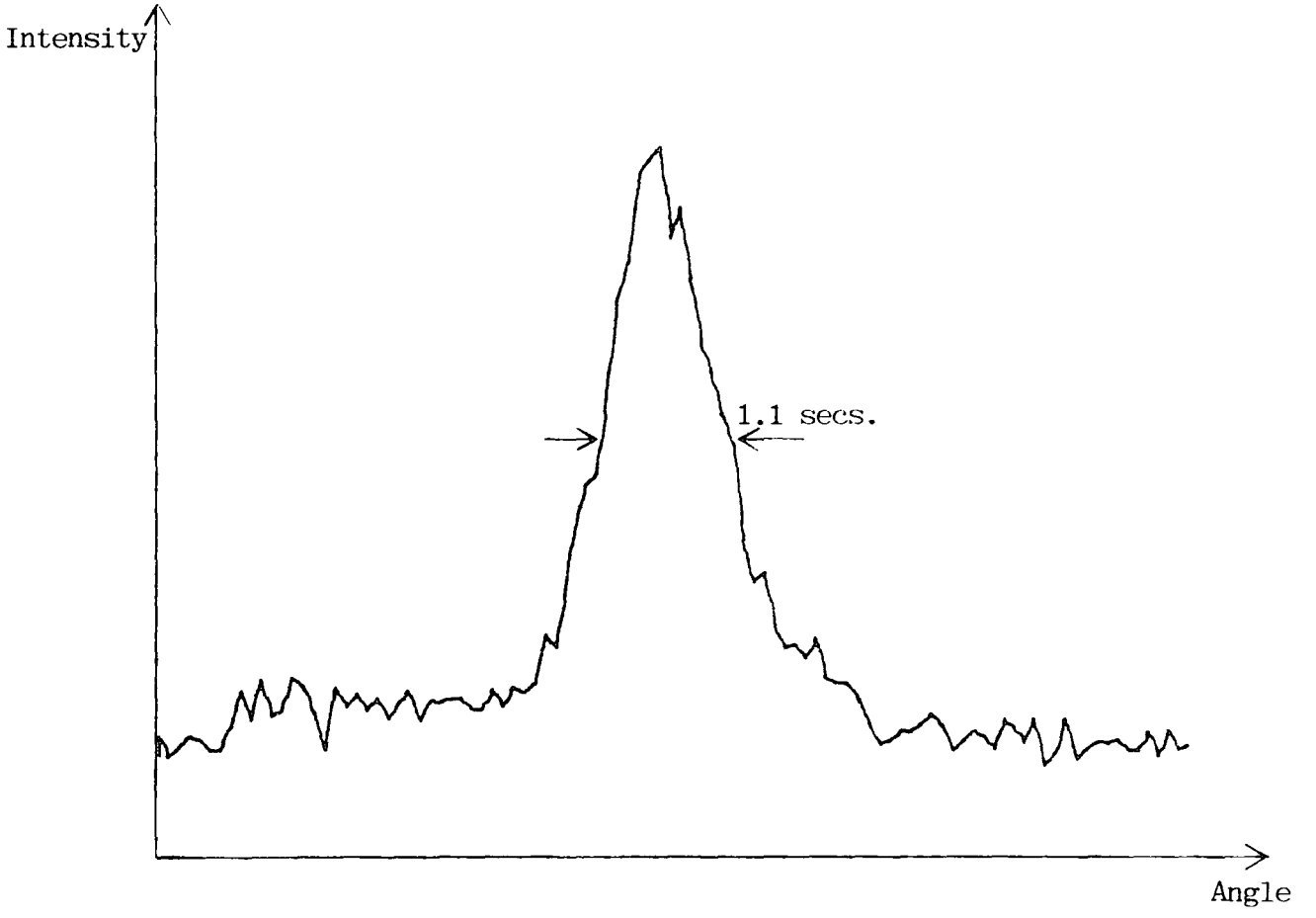

Fig. 6.8 333 double crystal rocking curve from a pair of germanium crystals (Sample A and B). Counting time per 0.1 arc second step was 5 seconds. Peak height=64 cps. Background=11 cps.

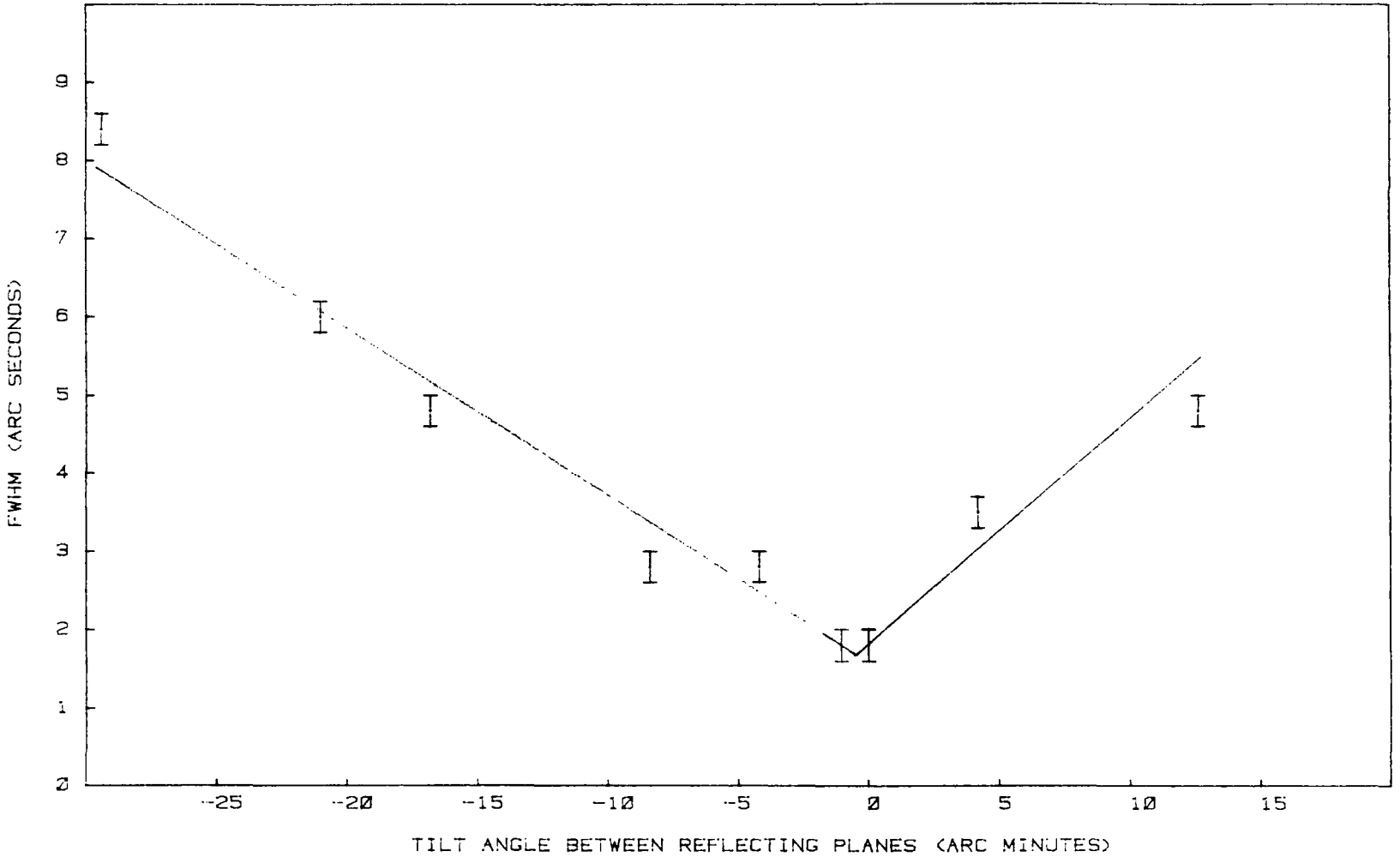

Fig. 6.9 Effect of the tilt between the reflecting planes of the reference and sample crystals on the FWHM for Ge(111) double crystal rocking curve (Sample A and B).

However, the first term of equation 6.26 is negligible for ϕ_v of the order of 1 degree which is approximately the vertical divergence of the set up used and ϕ_c greater than about 10 minutes. As the divergence for a particular arrangement is constant the broadening is therefore a linear function of the angle between the diffracting plane ϕ_c. The FWHM versus ϕ_c plot (Figure 6.9) satisfies this relation except in the region where ϕ_c approaches zero where the $(\phi_c^2 + \phi_v^2)/2$ term becomes significant. This linear relation could be used to aid rapid setting up of double crystal rocking curve, as in principle, only 4 curves are needed to find the minimum.

It was found that the narrow line width of the 412 keV ^{198}Au line ($\Delta\lambda/\lambda = 10^{-6}$) and the small Bragg angle eliminates the dispersion effect when the same reflection from different crystals were used. In spite of the 5% lattice parameter difference for the 111 reflection of germanium and silicon (sample H) the FWHM is still about 2 arc seconds (Figure 6.10). Clearly the "mosaic bending" in the germanium crystals is typically 1 arc second.

Figure 6.11 is the 111 rocking curve from a pair of device grade silicon crystals 3 mm thick. A 1 arc second rocking curve was obtained which is 5½ times the value for perfect crystals. A linear relationship is also obtained for the variation of tilt ϕ_c with FWHM (Figure 6.12).

Figure 6.13 is another 111 rocking curve from a different pair of silicon crystals. The reference crystal is a LOPEX silicon (Sample H) and the sample crystal

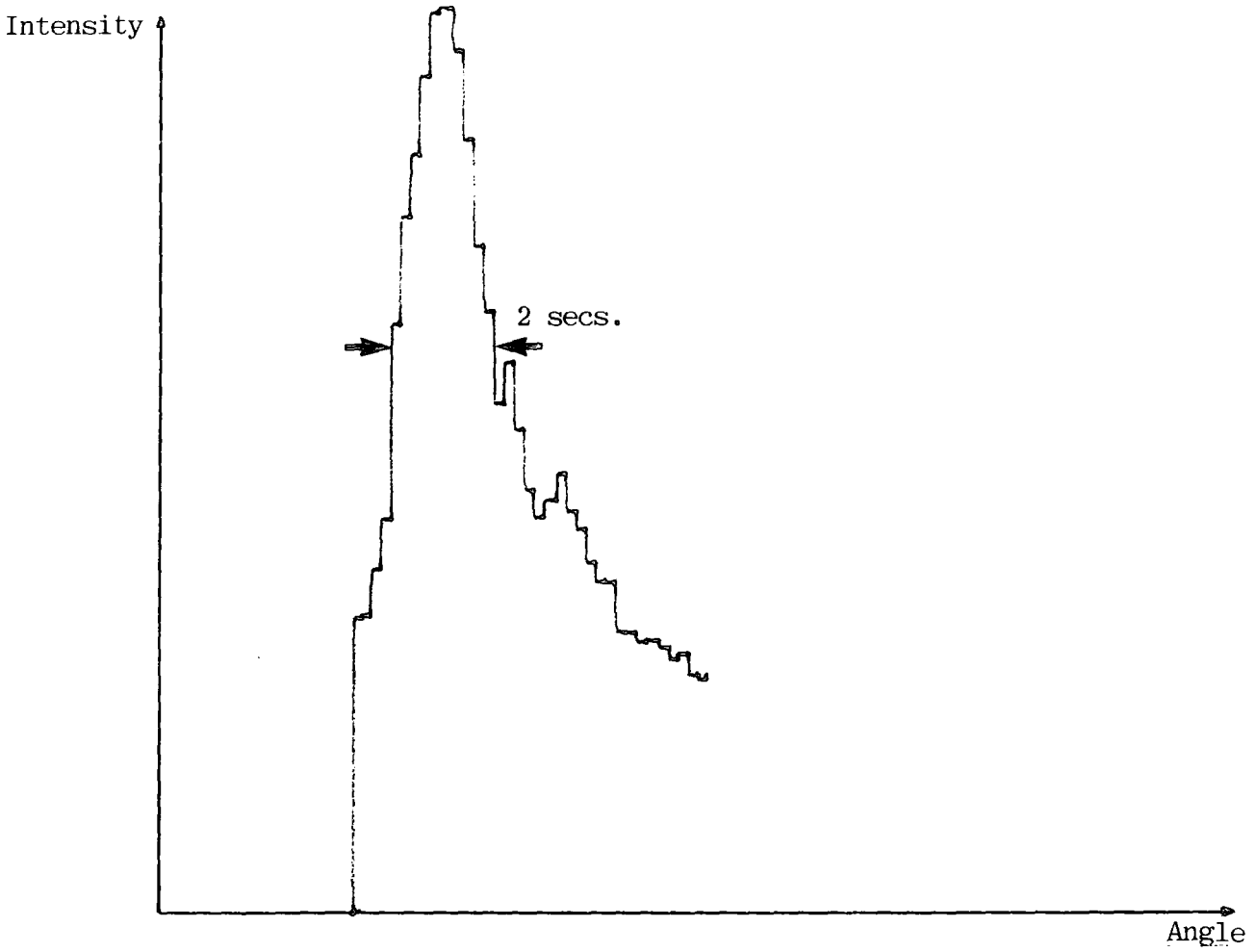

Fig. 6.10 111 double crystal rocking curve from a silicon crystal (Sample H) as reference and a germanium crystal as specimen. Counting time per 0.2 arc sec. step was 35 sec. Peak height = 57cps. Background = 17 cps.

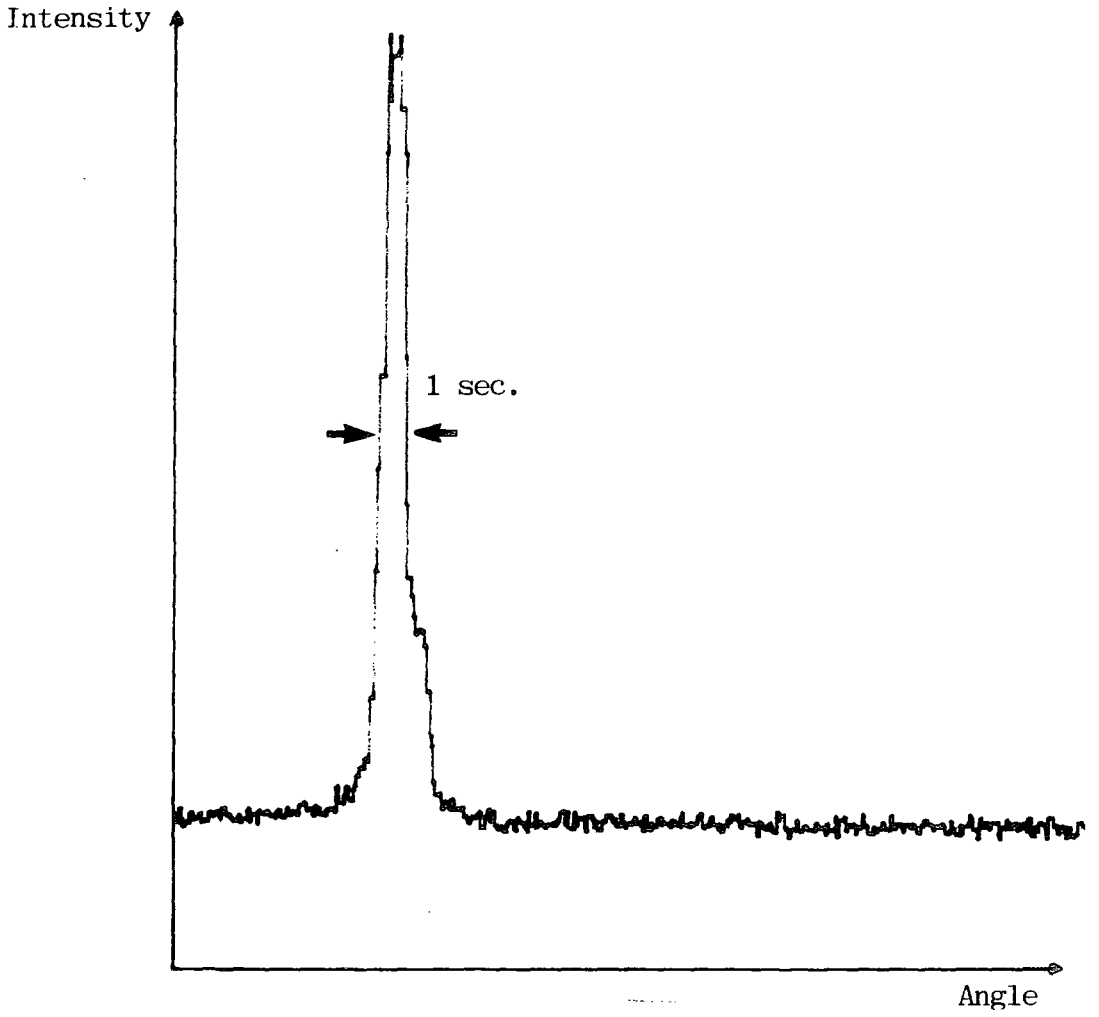

Fig. 6.11 111 double crystal rocking curve from a pair of device grade silicon (Sample C and D). Counting time per 0.1 arc sec. step was 40 secs. Peak height = 99 cps. Background = 15 cps.

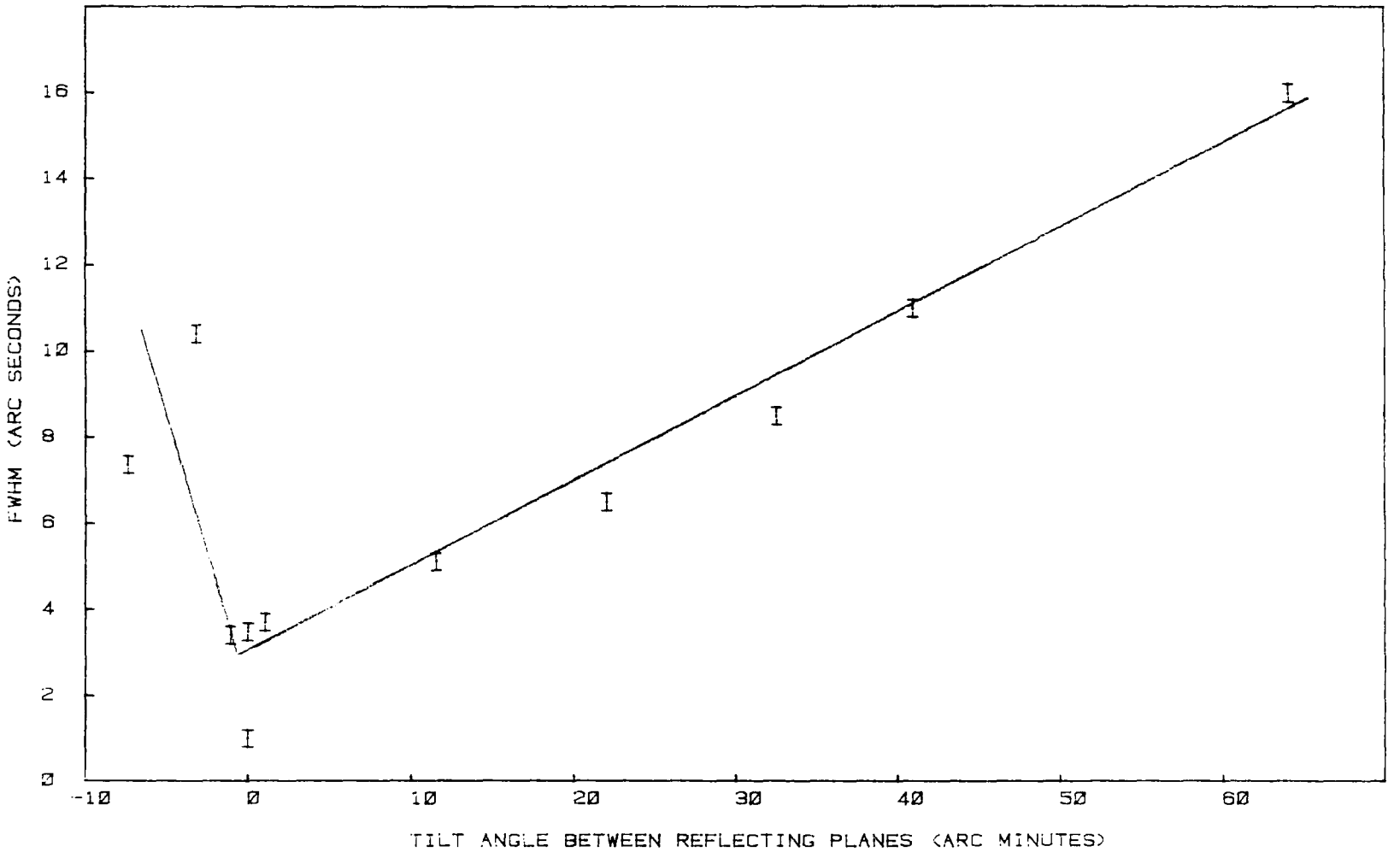

Fig. 6.12 Variation of the FWHM with the tilt angle between the reflecting planes of the reference and sample crystals for Si(111) reflection (Sample C and D).

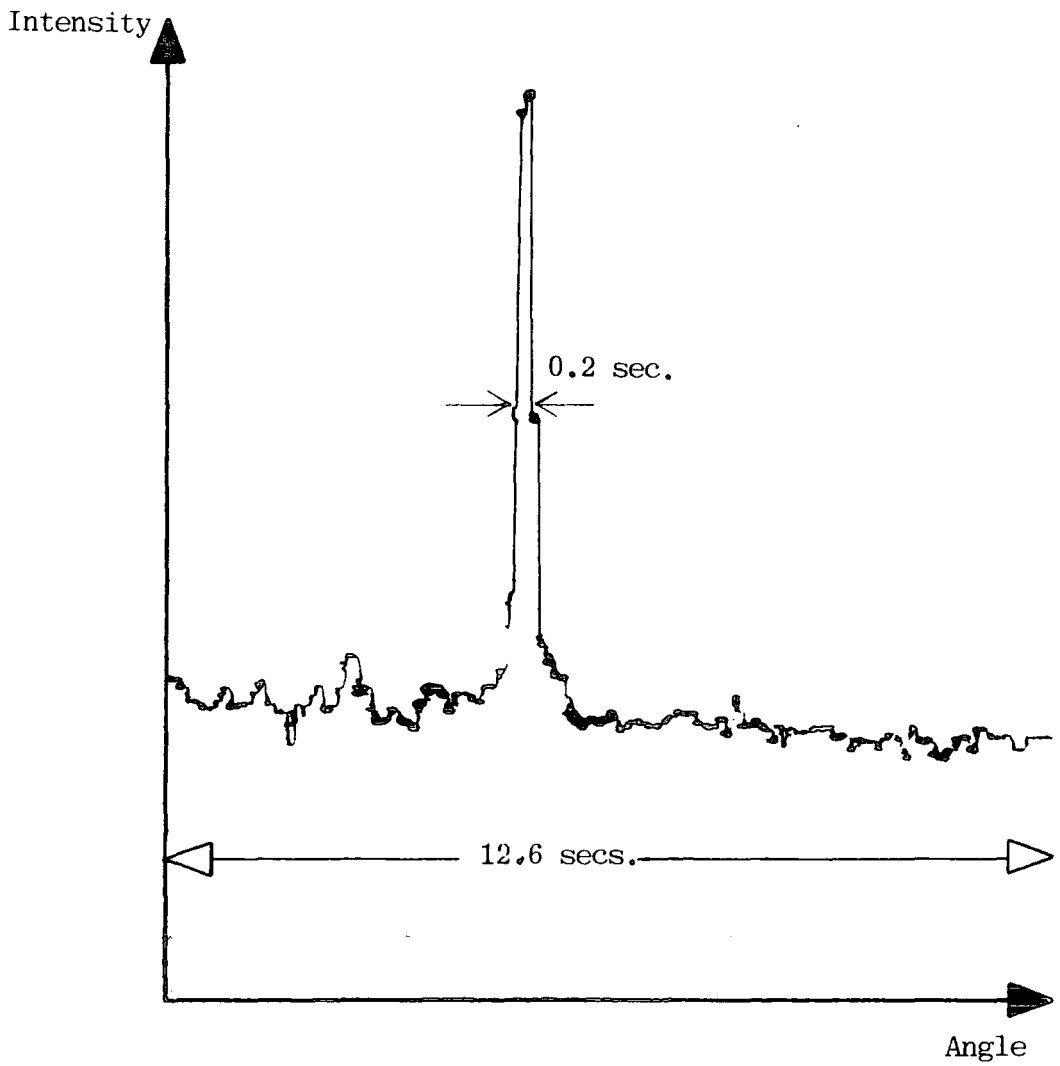

Fig. 6.13 111 double crystal rocking curve from a LOPEX silicon (Sample H) and silicon sample E. Counting time per 0.1 arc sec. step was 360 secs. Peak height = 12 cps. Background = 7 cps.

is sample E which originated from Mullard Semiconductor. The separation between points on the rocking curve is equivalent to 0.1 arc second. Due to the high background, a high counting time is necessary, in this case 6 minutes per point. The peak count is about 12 cps compared to a background of 7 cps.

The narrowest rocking curve obtained is shown in Figure 6.14 from a pair of LOPEX silicon (Sample G and H). As the crystal perfection increase the FWHM and the integrated reflecting power both decrease. We had very serious difficulty in locating the double reflection. The reflecting planes of both crystals must be set as nearly parallel as possible initially in order to locate the double reflection because small tilts become more significant as the FWHM goes down. When the double reflection was first obtained it was 6 arc seconds wide. The goniometer was tilted in steps of 4 minutes to narrow the rocking curve. As the rocking curve became narrower the til ting was performed in steps of 2 minutes and finally 25 arc seconds. At this stage the sensitive axis with an angular rotation of 0.012 arc seconds per step was used. It was a time consuming process as the counting time at each point must be at least 20 seconds to obtain a reasonable signal to noise ratio. A rocking curve FWHM between 0.04 to 0.06 arc second was obtained which was about 4 times smaller than the predicted value of 0.18 arc second.

The surprising narrowness of the rocking curve may be due to four factors.

(a) The rotation of the axis may not be exactly 0.012 arc second per motor step.

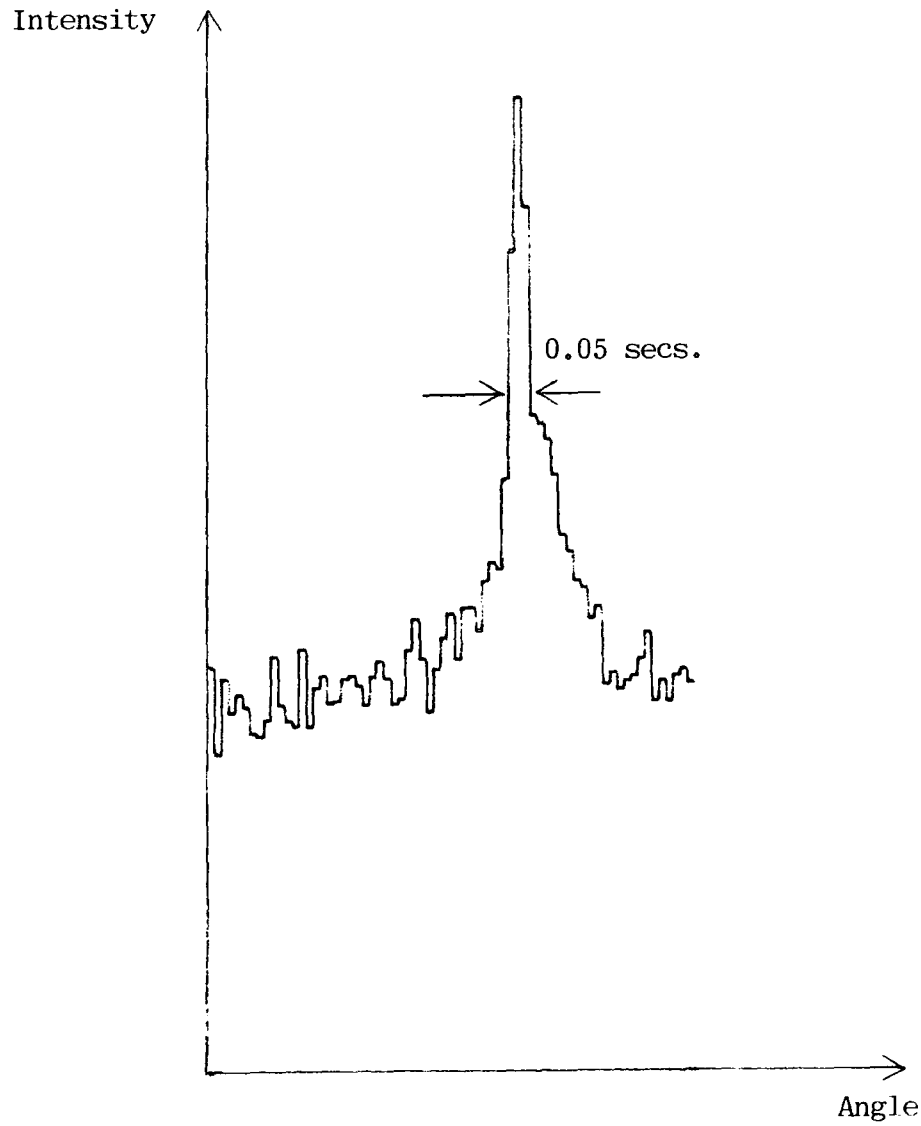

Fig. 6.14 111 double crystal rocking curve for a pair of LOPEX silicon (Sample G and H). Counting time per 0.012 arc sec. step was 50 secs. Peak height = 12 cps. Background = 5cps.

(b) The occurrance of Pendellosung fringes.

(c) The effect of temperature variation is significant, and (d) the effect of multiple reflections.

The four possibilities are discussed below.

The length of the lever used for the axis with 0.012 arc second per motor step was measured to be 57.3 cm. A 3 cm ($\sim$ 5%) error in the measurement of the lever will result in 5% error for the angular rotation and is quite insignificant compared to 0.18 arc second which is the value for perfect crystals. The reproducibility of the rocking curve eliminates the possibility of axis slop.

The second factor was ruled out since the crystal thickness t_o is much greater than the extinction distance ξ_g: $t_o \sim 3.5\xi_g$ for the reference crystal and $t_o = 6\xi_g$ for the sample crystal. Figure 6.15 is the theoretical curve for the double reflection obtained by numerical integration of equation 6.21 for the sigma polarization state and using equation 6.18 as the single crystal reflection function. The FWHM of this curve is about 0.23 arc second which is in fact some 28% larger than the FWHM calculated by assuming a Gaussian distribution for the single crystal reflection curve. The non-symmetry of Figure 6.15 is due to the truncation error of the numerical integration. Figure 6.16 is the rocking curve obtained if the approximation of a thick crystal is made where the sine squared term of equation 6.18 is equal to $\frac{1}{2}$. In all cases the theoretical FWHM is significantly greater than that measured.

When the diffractometer was surrounded by the poly-styrene the narrowest rocking curve obtained was 0.3 arc

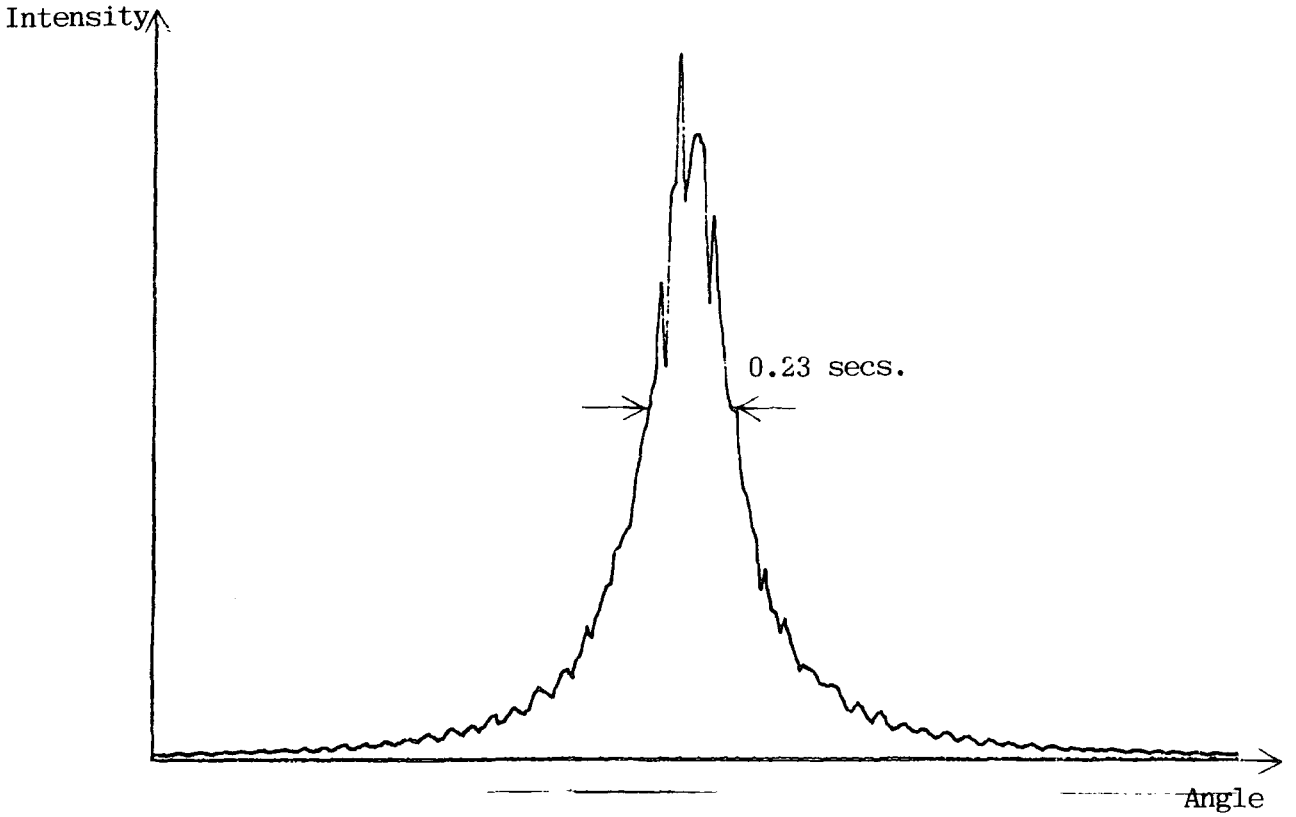

Fig. 6.15 Theoretical Si(111) double crystal rocking curve obtained by the convolution of the first and second crystal reflecting range.

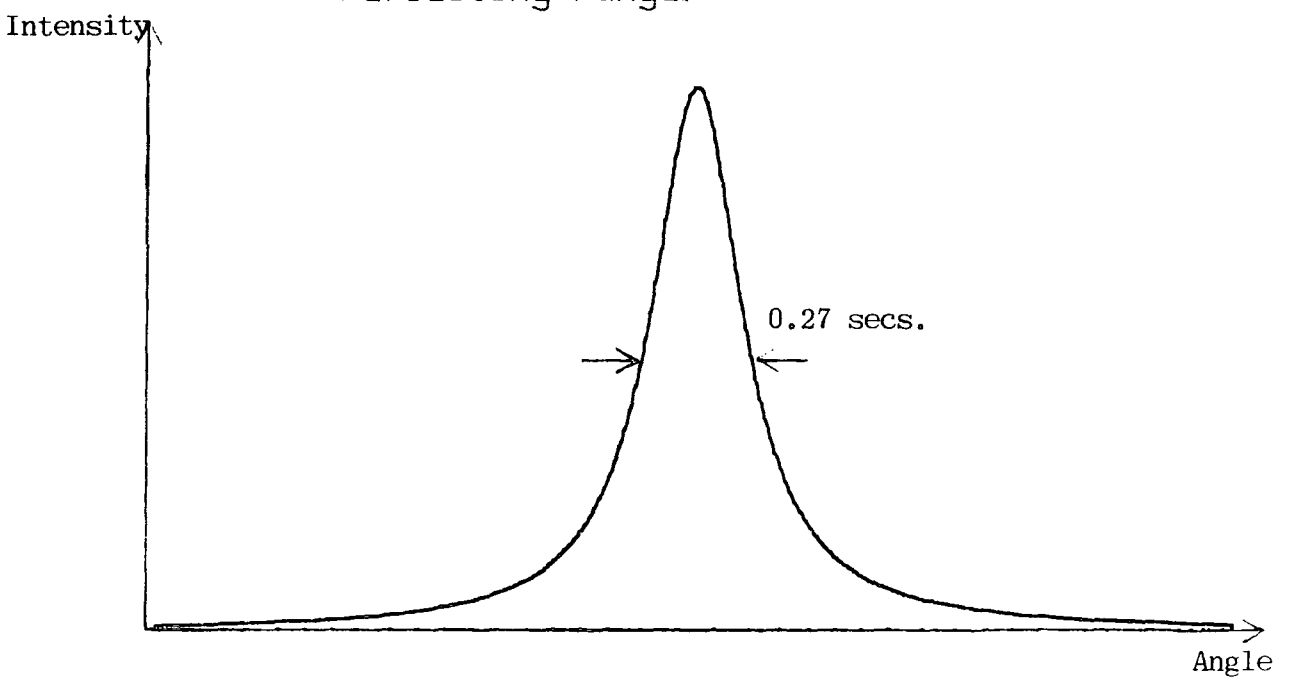

Fig. 6.16 Theoretical Si(111) double crystal rocking curve for a thick crystal in the Laue geometry.

second (Figure 6.17). This is 1.7 times larger than the FWHM based on a Gaussian distribution and 1.3 times larger if the FWHM is based on equation 6.21 and 6.18. Therefore the suggestion that temperature drift was occurring seems plausible as the measured FWHM of the rocking curve is closer to the theoretical value of 0.23 arc second (based on equation 6.21) when the polystyrene was on compared to 0.04 to 0.06 arc second when the polystyrene was not on. As discussed in Section 6.9 a temperature variation of $1^{o}C$ results in a 0.3 arc second change in angular rotation. As the polystyrene reduces the temperature variation to $\pm$ $0.1^{o}C$, a 0.03 arc second in angular rotation, a meaningful value of the half width could be obtained. As all scans were made in the same direction, it was by chance that the curves narrowed rather than broadened.

Due to the very short wavelength of γ-radiation the Ewald sphere has a radius of about $\frac{2\pi}{\lambda} = 209\ \text{Å}^{-1}$ and is about 180 times the mean distance between neighbouring reciprocal lattice points for silicon. Therefore the geometrical condition for multiple Bragg scattering, that is more than two reciprocal lattice points are located on the Ewald sphere, is often satisfied for γ-ray diffractometry. This may affect the shape and the integrated intensity of the single reflection. As shown by Schneider (1975) the effect of multiple scattering is avoided for Bragg reflections with $\sin\theta/\lambda \lesssim 0.8\text{Å}^{-1}$ where the atomic scattering factor decreases with increasing momentum transfer and the interaction of γ-radiation with the crystal is weak.

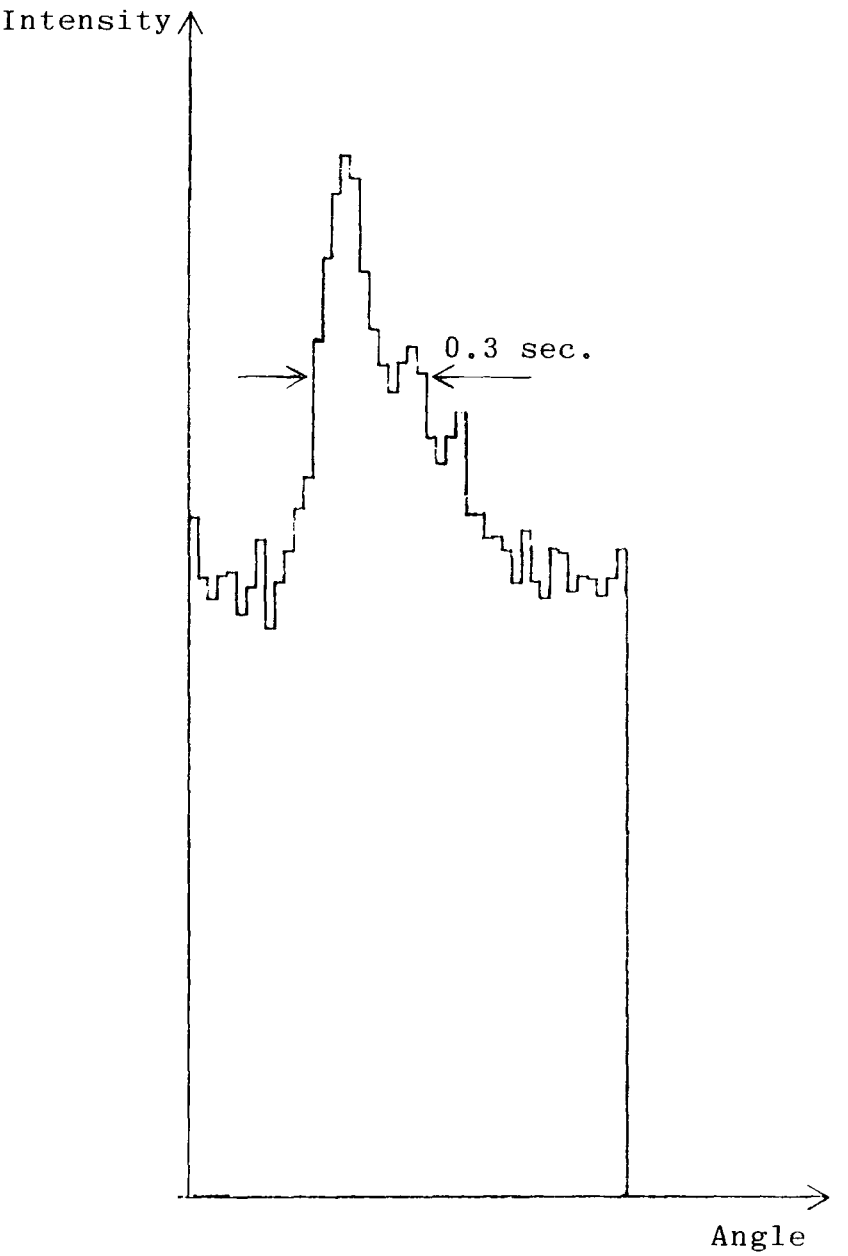

Fig. 6.17 111 double crystal rocking curve for a pair of LOPEX silicon (Sample H and G). Counting time per 0.024 arc second step was 100 seconds. Peak height=7 cps. Background=4 cps.

This assumption is justified as the reflections used in the experiment has $\sin\theta/\lambda < 0.8\text{Å}^{-1}$ and the single reflection integrated intensity R_m measured for the LOPEX silicon crystals (samples G and H) is approximately equal to the value R_{dyn} calculated for perfect crystals.

A rocking curve for the 333 reflection from the same pair of silicon crystals was also obtained but due to lack of time and the weakening source the best value obtained for the FWHM is between 0.06 to 0.072 arc second (Figure 6.18) compared to the theoretical value of 0.04 arc second (for Gaussian lineshapes) and 0.07arc seconds (equation 6.23). The polystyrene was on in this case.

Table 6.5 is a tabulation of the measured and theoretical integrated intensity and FWHM of the rocking curves mentioned above. The theoretical value of the integrated intensity was calculated using equation 6.24 and taking the single reflection integrated reflecting power as $\pi/2$ for a thick non absorbing perfect crystal. The theoretical FWHM was calculated assuming that the rocking curve has a Gaussian distribution and also by using the rocking curve obtained by equation 6.21.

The apparatus was also used to study the uniformity of crystal perfection of Sample F along its whole length. A germanium crystal (Sample A) was used as the reference crystal. The FWHM of the 111 reflection varies between 9 to 14 arc seconds along its whole length of 112 mm and a plot of FWHM versus position along the length of the crystal is shown in Figure 6.19. A feature of this experiment is that the crystal did not need to be remounted to obtain reflection from

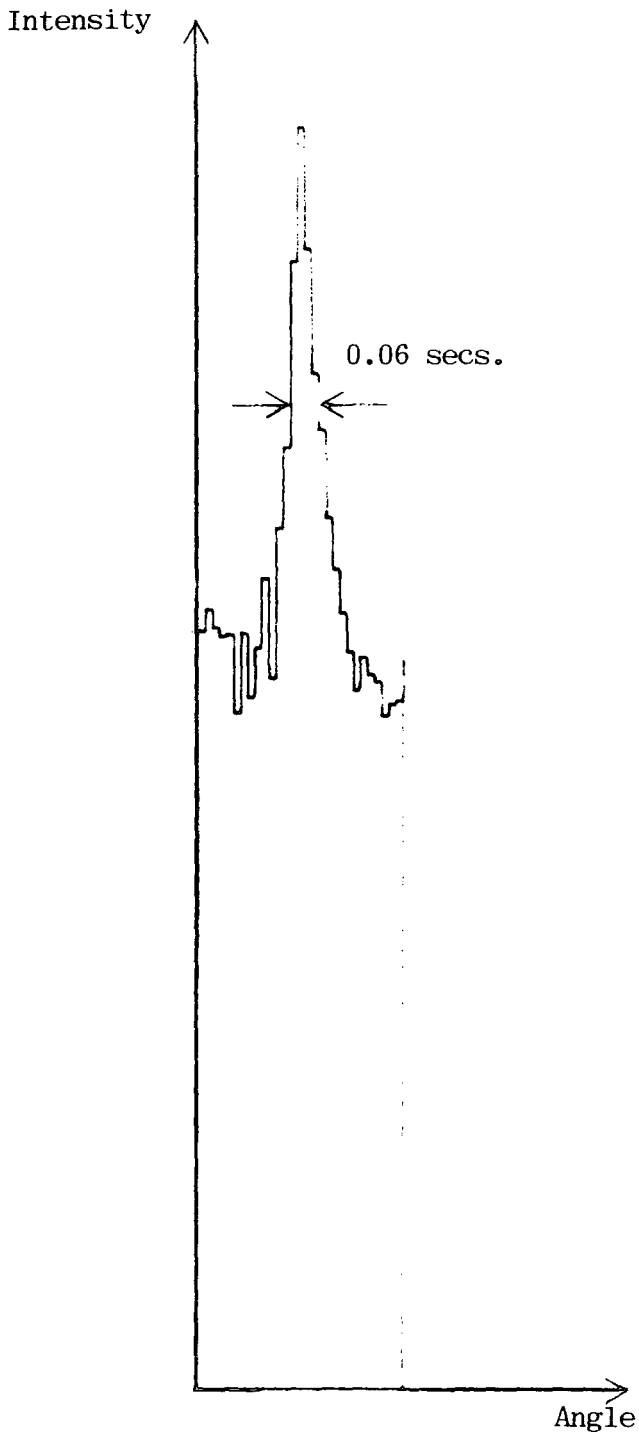

Fig. 6.18 333 double crystal rocking curve from a pair of LOPEX silicon (Sample G and H). Counting time per 0.012 arc sec. step was 100 secs. Peak height = 8 cps. Background = 4 cps.

Table 6.5 The theoretical and measured integrated reflecting power and FWHM of the different pairs of crystals.

Crystals	Position	R_m	R_{dyn}	FWHM (arc seconds)		
				measured	Gaussian	equation 6.21
Ge A,B	(1,-1)	2.9×10^{-6} $\pm0.5\times10^{-6}$	1.14×10^{-6}	2	0.42	
Ge A,B	(3,-3)	9.5×10^{-7} $\pm0.5\times10^{-7}$	2.28×10^{-7}	1.1	0.09	
Si C,D	(1,-1)	14.9×10^{-7} $\pm0.5\times10^{-1}$	5×10^{-7}	1	0.18	0.23
Si H,E	(1,-1)	1.6×10^{-7} $\pm0.5\times10^{-7}$	5×10^{-7}	0.4	0.18	0.21
Si H,G	(1,-1)	0.2×10^{-7} $\pm0.5\times10^{-7}$	5×10^{-7}	0.04-0.06	0.18	0.23
Si H,G with polystyrene	(1,-1)	0.2×10^{-7} $\pm0.5\times10^{-7}$	5×10^{-7}	0.3	0.18	0.23
Si H,G with polystyrene	(3,-3)	0.9×10^{-7} $\pm0.5\times10^{-7}$	0.94×10^{-7}	0.06-0.07	0.04	0.07

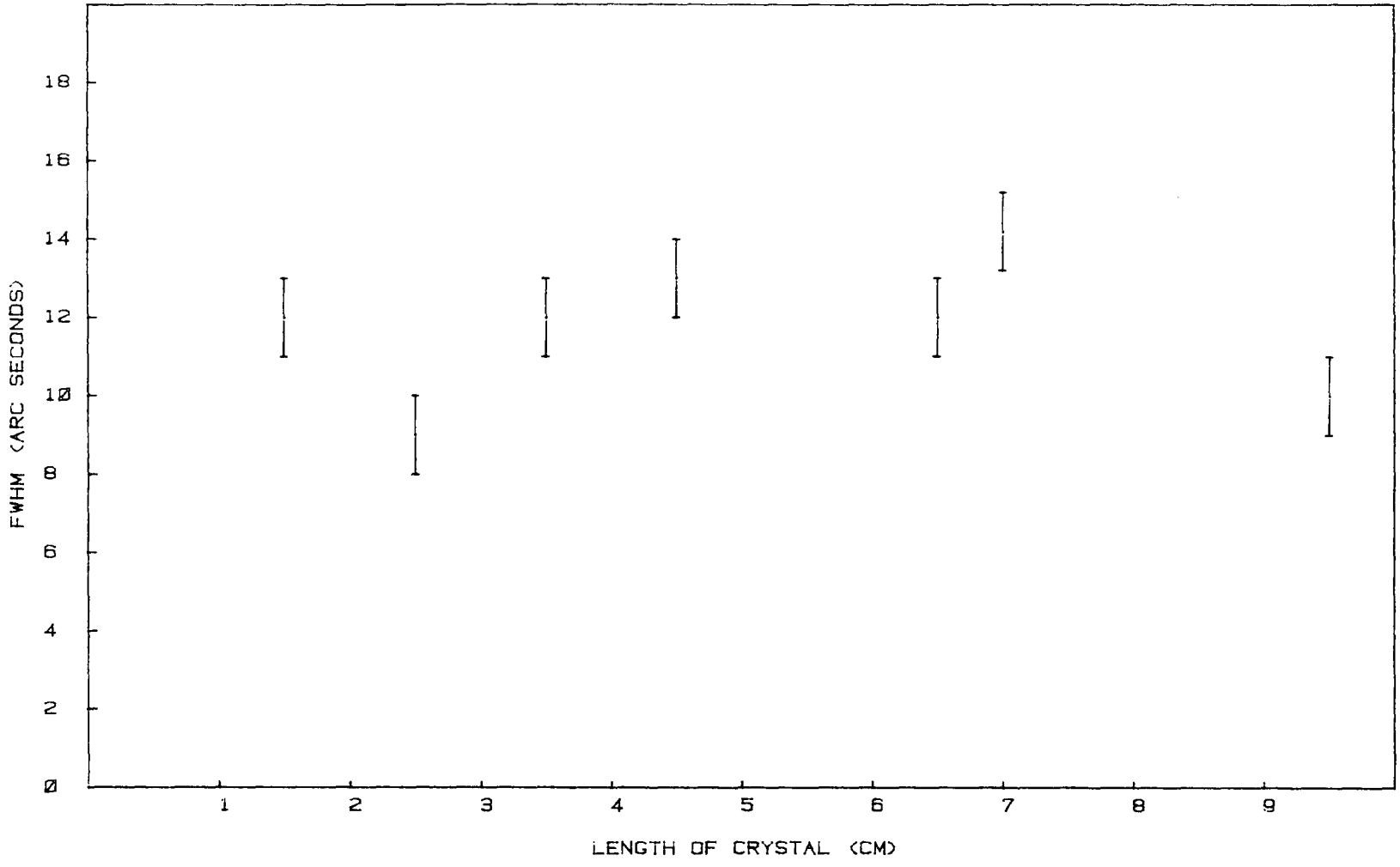

Fig. 6.19 Variation of the FWHM along the length of Sample F.

different parts of the crystal. Instead the diffractometer was displaced by a known amount such that the reflection from the reference crystal hit a different part of the sample. The first diffracted beam could be relocated quite easily after the diffractometer has been displaced. This technique could be quite useful in assessment of moderate perfection crystals prior to further processing, as employed for example with copper monochromators in the single axis mode (Schneider 1975).

6.11 Conclusion

Experiments show that tilts < 10^{-6} rads can be measured in highly perfect silicon crystals and there is a good agreement between the dynamically predicted FWHM and integrated reflecting power with respect to experiment.

The main disadvantage of γ-ray experiments especially in the double crystal arrangement is the long counting time involved, up to 6 minutes at each point. Thus the experiment is slow and tedious. A much higher source strength is desirable or better still the experiment is carried out at a synchrotron radiation source such as CHESS at Cornell where the synchrotron radiation will be very hard and intense when the new wriggler is installed. The intensity will increase by several orders of magnitude in the 40 to 100 keV range and will provide a major increase in flux particularly in the high energy range.

Although γ-ray double crystal diffractometry is a very good method for the study of the perfection of large crystals

due to it being a non-destructive method and having a high sensitivity to tilt, it is clearly not a practical method for on line testing of silicon crystals to be used for mass device fabrication. Another problem is that for device fabrication it is not tilt that needs to be measured accurately but lattice dilations. The oxygen and carbon segregation give rise to growth striae and it is these dilations which device engineers need to monitor. Gamma ray diffractometry, which is insensitive to dilations, is clearly not as good as X-ray diffractometry for this purpose.

CHAPTER 7

TRIANGULAR MONOCHROMATOR CRYSTALS

7.1 The Curved Crystal Monochromator

The diffracted intensity from a plane crystal monochromator is weak as an incident beam has a certain angular divergence and therefore only rays making the Bragg angle with the lattice planes will be diffracted. Johann (1931) and Cauchois (1932) make use of an elastically curved crystal whose reflecting planes form a cylinder of revolution to increase the reflected beam. The normals to the reflecting plane at different positions along the crystal surface converge on its centre of curvature of radius R and makes an angle $\pi/2-\theta$ with the diffracted beam. The diffracted beams do not converge to a single focus but converge to a zone of minimum width on a circle of radius R tangential to the crystal surface.

This chapter describes the study undertaken on the monochromator cyrstals used at the Protein Crystallography Station at Daresbury Laboratory. In the assessment of the degree of perfection of the crystals, double crystal rocking curves were obtained where the FWHM, peak count, peak position and the integrated intensity were monitored as the crystal was bent. Single reflection experiments to determine the variation of bending radius R as a function of position along the crystal was also carried out on the Lang camera. The effect of rocking curve width, focussing aberration and error in Guinier position on the energy resolution has been

discussed by Helliwell et al. (1981).

The use of synchrotron radiation for protein crystallography provides an intense, tunable and collimated X-ray beam compared to conventional sources. The monochromator used at Daresbury (Helliwell et al. 1981) is basically the same design as that used at LURE (Lemonnier et al. 1978, Kahn et al. 1981) and DORIS (Hendrix et al. 1979). It consists of a horizontal focussing triangular shaped crystal bent to an arc of a circle of curvature radius R, which made it possible to image the horizontal source width h at the sample. The base of the triangle is mounted as a cantilever and the free end is displaced to obtain the curvature. To obtain a reasonable focal length the bending radius is usually 10 m or more. As the point of incidence on the bent crystal (Figure 7.1) moves along the arc MN, the envelope of the diffracted beam for an asymmetric reflection is the circle of radius R cos $(\theta-\alpha)$ centred at the centre of the circle of radius R. The divergent incident beam correspondingly lies on the arc of the circle of radius R cos $(\theta+\alpha)$. α is the angle made by the surface to the reflecting plane. An asymmetric reflection with an asymmetry factor $b>1$ is used to produce a compression effect on the width of the reflected beam. Although the total integrated intensity will be less than the symmetric cut monochromator, the intensity (photons per unit area) will be $\sqrt{b}$ times larger and this geometry is preferable for the usually small protein samples. The source size effect, the crystal rocking curve width and the imperfection in the Rowland focussing geometry contributes to the finite size of the image produced (Lemonnier et al. 1978). The

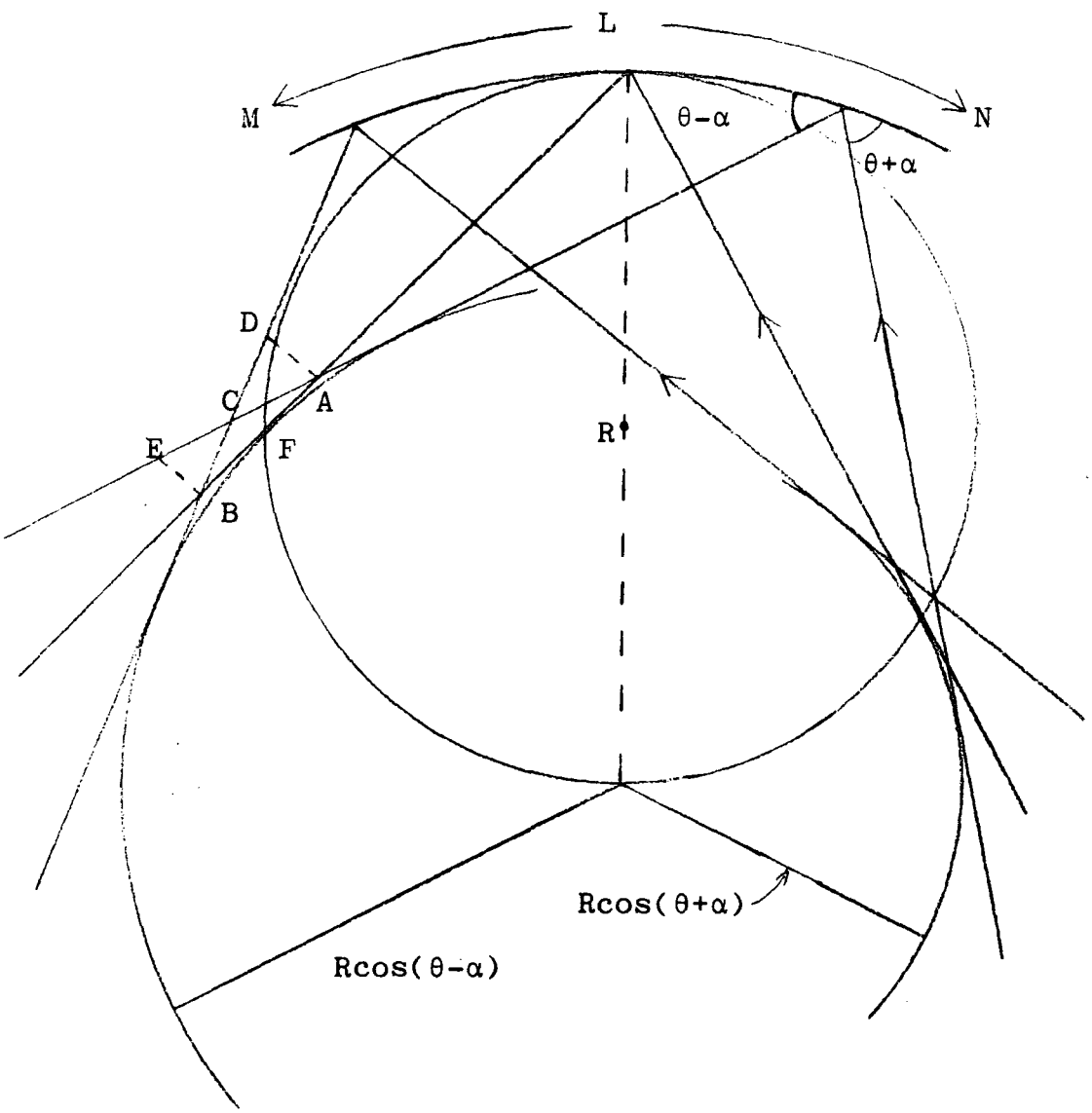

Fig. 7.1 Principle of a bent crystal focussing monochromator for an asymmetric reflection showing the focussing aberration (CF) and depth of focus (≈AB).

wavelength spread in the reflected beam $(\delta\lambda/\lambda)_{TOT}$ is the convolution of the crystal rocking curve contribution of $\omega_o \cot\theta$ spread over a distance $\omega_h p'$ with the source size contribution of $\delta\theta \cot\theta$ where $\delta\theta = h/p$ and the monochromator curvature contribution of $\frac{L}{2}\left|\frac{\sin(\theta-\alpha)}{p'} - \frac{\sin(\theta+\alpha)}{p}\right| \cot\theta$. Thus

$$\left(\frac{\delta\lambda}{\lambda}\right)_{TOT} = \sqrt{\left(\frac{h}{p} + \frac{L}{2}\left|\frac{\sin(\theta-\alpha)}{p'} - \frac{\sin(\theta+\alpha)}{p}\right|\right)^2 + \omega_o^2}\cot\theta \qquad 7.1$$

where h and h' are the horizontal extension of the source and focus respectively, p is the distance between the source and monochromator, p' is the monochromator to focus distance, L is the length of the monochromator, $\omega_o = \omega_{sym}/\sqrt{b}$ is the angular width of the beam incident on the monochromator and $\omega_h = \omega_{sym}\sqrt{b}$ is the angular width of the diffracted beam.

If the sample is smaller than the focus or a slit is placed at the focus, a fraction of $(\delta\lambda/\lambda)_{TOT}$ is received by the sample. As shown in Figure 7.2 there is an energy gradient across the focus due to the source size. Rays from points A, B and C on the source make the same angle θ_1, θ_2 and θ_3 respectively at different positions along the monochromator thus coming to the respective foci A', B' and C' (neglecting aberration). A sample or slit x_H at the focus thus receives $x_H \cot\theta/p'$ of the contribution of source size $(\frac{h}{p} \cot\theta)$ to $(\delta\lambda/\lambda)_{TOT}$. hp'/p is the total focus width. A wavelength spread $\delta\lambda/\lambda = 5 \times 10^{-4}$ can therefore be achieved at the Guinier position which is important for

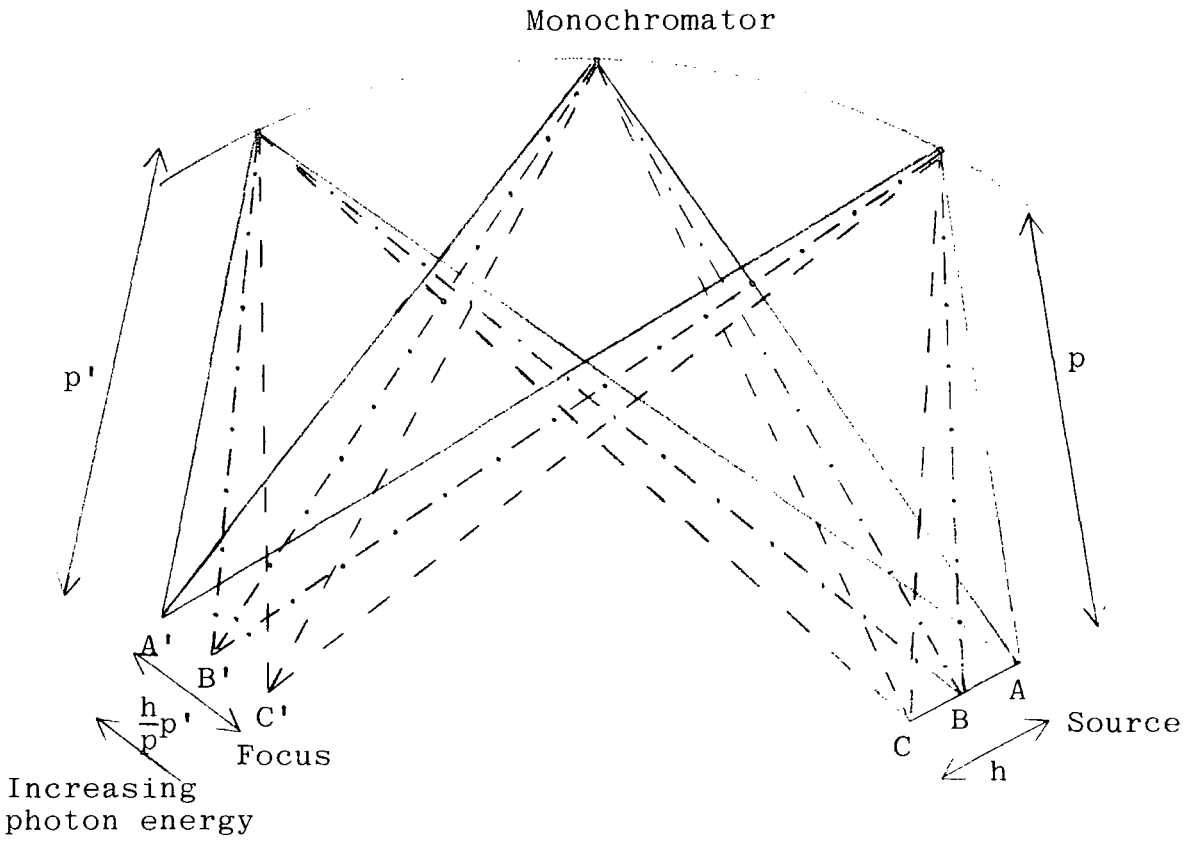

Fig. 7.2 A bent triangular monochromator at the Guinier position showing the energy gradient at the focus due to the source size.

absorption edge fine structure studies. Helliwell et al. (1981) used samples of cobalt foil and Dy_2O_3 powder and obtain K and L_{III} absorption edges respectively.

Away from the Guinier point where $\frac{\sin r}{p'} \neq \frac{\sin i}{p}$ the contribution to the total wavelength spread due to the monochromator curvature is significant. Assuming $\omega_{sym} = 0$ and $\alpha = 0$ for convenience, rays from point A (Figure 7.2) on the source form different angles along the monochromator surface, that is $\theta_1 \neq \theta_2 \neq \theta_3$. Thus the reflected rays which form at the focus A' has a correlation between their direction and energy and an energy gradient also exist due to the finite source size. This effect was illustrated by Helliwell et al. (1981). A photographic film was placed about 0.5 m behind a 70 μm slit at the focus. The diverging beam which reaches the film produced streaks with an energy gradient across its length.

7.1.1 Effect of Rocking Curve Width

So far the rocking curve width and the focussing aberration has been neglected and the oblique cut angle α is assumed to be without error.

Referring to Figure 7.3 to illustrate the effect of rocking curve width, CY is the incident beam on the monochromator producing a reflected beam CY'. The angular spread of the incident and reflected beams are $\omega_o = \omega_{sym}/\sqrt{b}$ and $\omega_h = \omega_{sym}\sqrt{b}$ about CY and CY' respectively. The reflected beam has a wavelength spread of $\omega_o \cot\theta$ (Lemmonier et al. 1978). Incident beams CP and CQ which are at an angle $\omega_h/2$ with CY will also have an incident angular spread of ω_o about CP

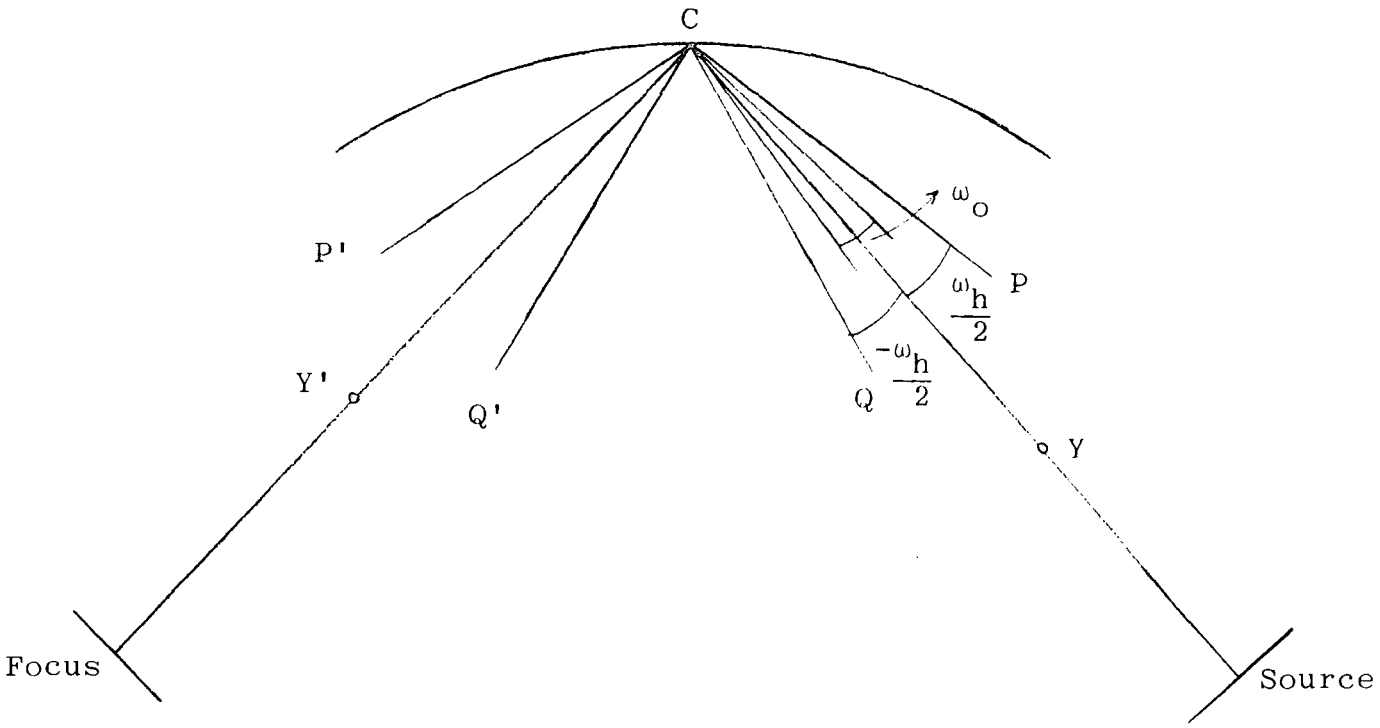

Fig. 7.3 Effect of rocking curve width on point to point resolution.

and CQ and an emergent angular spread about CP' and CQ' respectively. In both cases $\langle P'C\ Y' = \langle PCY = \omega_h/2$ and $\langle Q'C\ Y' = \langle QCY = \omega_h/2$.

The range of wavelengths passing along CY' is therefore $\omega_h \cot\theta$ if the bundles of ray centred on CP', CY' and CQ' are monochromatic and separated in absolute wavelength by $\omega_h \cot\theta/2$. This is only valid if CP or CQ intercept the finite source size h. For example, for Ge(111) where $\alpha = 10.5^{o}$, $\omega_h p \overset{\sim}{\sim} 4.1$ mm for Cu radiation. As h = 13.7 mm (measured FWHM) then for rays from the edges of the source, CP and CQ falls outside the FWHM range and is weak in flux. The energy resolution thus increases towards the edge of the focus.

7.1.2 Focussing Aberration

FC in Figure 7.1 represent the focussing aberration at the focus and is given by

$$FC = \frac{\rho L^2}{8R^2} \quad \text{(Martin and Cacak 1976)}$$

$$= \frac{L^2 \cos(\theta-\alpha)}{8R} \qquad 7.2$$

as $\rho = R \cos(\theta-\alpha)$

7.1.3 Error in Guinier Position

An error in the angle α will produce an error $\delta p_G'$ in the Guinier position p_G'. As

$$p_G' = \frac{\sin(\theta-\alpha)}{\sin(\theta+\alpha)} p$$

$$\delta p_G' = -\frac{p}{\sin^2(\theta+\alpha)} \sin 2\theta \, \delta\alpha \qquad 7.3$$

An error in p_G' will also cause an error in the $(\frac{\delta\lambda}{\lambda})_{TOT}$ due to the curvature component of

$$\frac{L}{2} \left| \frac{\sin(\theta-\alpha)}{p'} - \frac{\sin(\theta+\alpha)}{p} \right| \cot\theta$$

from zero at p_G' to

$$\delta(\frac{\delta\lambda}{\lambda}) = \frac{L}{2} (\frac{\cos(\theta-\alpha)}{p'} + \frac{\cos(\theta+\alpha)}{p}) \delta\alpha$$

7.2 Elasticity Theory For a Bending of Beams Clamped at One End

A bent rod returns to its original form if it is not bent beyond its elastic limit. Figure 7.4a shows a beam OB clamped at one end and the free end is supporting a load W. At position A along the rod the internal forces at A due to AO must balance the forces due to AB and the load W for equilibrium to exist. The force W acting vertically downwards at B is balanced by an equal vertical force at A which forms a couple of bending moment W x AB. Thus an internal couple of equal magnitude but opposite in direction exists at equilibrium.

If an elastic beam of thickness b is bent to a radius R where R>>b, the deformation in the simple case consists only of the extension or contraction of the longitudinal fibres

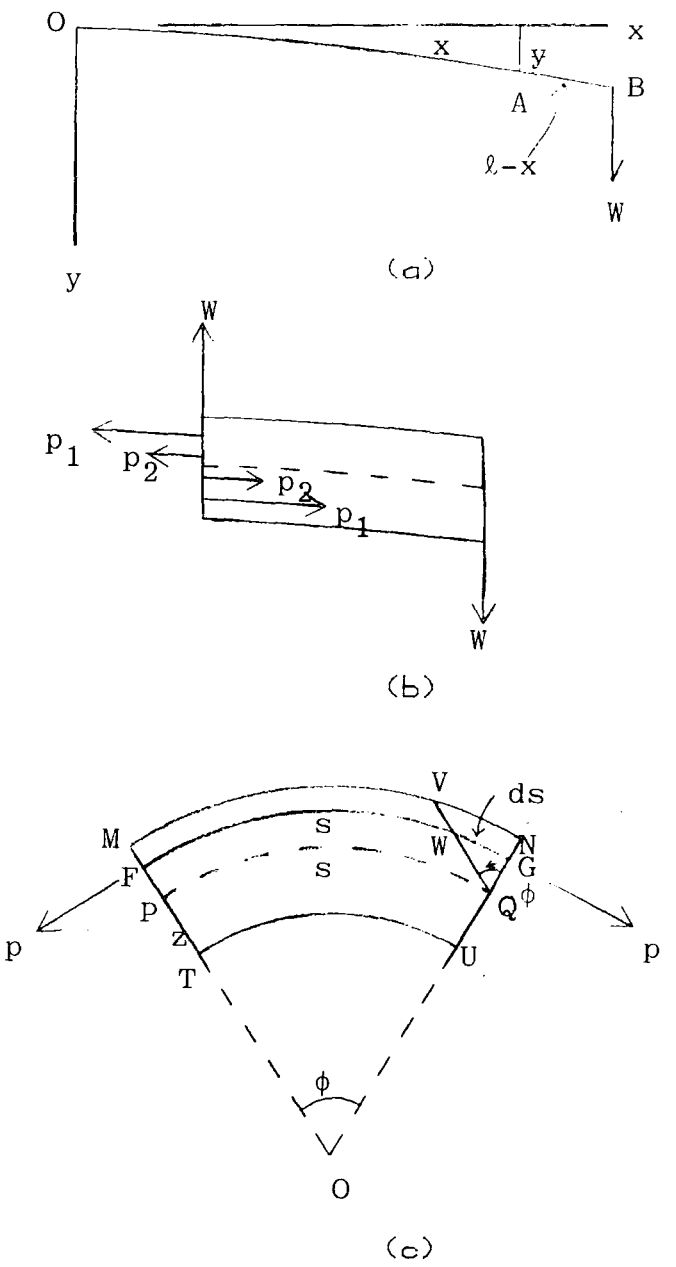

Fig. 7.4 (a) A beam clamped at one end with the free end supporting a load W.
(b) A section of the beam at point A.
(c) An element of the beam where the neutral surface subtends an angle at its centre of curvature.

of the beam in proportion to their distance from a central neutral surface which retains its original length (Figure 7.4b). The resultant elastic reaction produces forces such as p_1, p_2 in both parts of the beam (above and below the neutral surface) and form couples which balance the bending moment W x AB. The internal forces give rise to a shearing stress W/ab where a is the width of the beam and b is its depth. The shearing stress W/ab produces a deflection δ_1 of B relative to O but is small compared to the depression of B due to bending.

Figure 7.4c shows an element MNUT of the beam. The neutral surface PQ subtends an angle ϕ at the centre of curvature O. If QV is drawn parallel to MT then arc FW is equal to the normal length s (arc PQ) of the beam and arc WG is an extention of the beam at a distance z from P. Then the tensile strain is $\frac{ds}{s}$ and if the magnitude of the internal force that produce the extension is p

$$\frac{p}{\alpha} = Y \frac{ds}{s} \qquad 7.4$$

where α is the cross section of the fibre and Y is the Young's Modulus.

But

$$s = R\phi$$

$$ds = z\phi$$

$$\frac{ds}{s} = \frac{z}{R} \qquad 7.5$$

From equations 7.4 and 7.5

$$p = \frac{Y}{R} z\alpha \qquad 7.6$$

Moment of p about Q is $pz = \frac{Y}{R} z^2 \alpha$ 7.7

Therefore the total internal bending moment

$$\Sigma pz = \frac{Y}{R} \Sigma z^2 \alpha \qquad 7.8$$

$\Sigma \alpha z^2$ is analogous to the moment of inertia about the neutral axis and is called the geometrical moment of inertia of the cross-section about that axis and is equal to Ak^2 where A is the area of cross-section and k is the radius of gyration.

$$\therefore \text{Internal Bending Moment} = \frac{Y}{R} Ak^2 \qquad 7.9$$

In Figure 7.4a Ox, Oy are axes along and perpendicular to the unstrained position of the beam. Let the co-ordinate of A be (x,y). The co-ordinate of B is (ℓ,δ) where δ is the depression of B due to bending and ℓ is the length of the beam. The external bending moment at A is $W(\ell-x)$ and the curvature at a point is $\frac{d\psi}{ds}$ where ds is a short length of the beam and ψ is the angle the tangent makes with the x-axis. Therefore the curvature is

$$\frac{1}{R} = \frac{d\psi}{ds} = \frac{d}{ds} (\tan \psi) = \frac{d^2y}{dx^2} \qquad 7.10$$

Since ψ is small $\tan \psi = \psi$

$$W(\ell-x) = \frac{Y}{R} Ak^2 = YAk^2 \frac{d^2y}{dx^2} \qquad 7.11$$

The cross sectional area A is $b(\ell-x)$. From equation 7.11

$$W(\ell-x) = \frac{Y}{R} Ak^2$$

$$R = \frac{Ybk^2}{W} \qquad 7.12$$

which is independent of the position along the length of the beam.

7.3 Radius of Curvature For a Bent Triangular Monochromator Crystal

The monochromator crystals are triangular in shape with a thickness of 1 mm. The length is about 200 mm and the width at one end is between 30 to 35 mm and at the other is about 1 mm. The (111) plane is inclined at an angle α to the crystal surface (Table 7.1).

The crystal is mounted on a special holder with the reflecting surface vertical (Figure 7.5). The crystal is pivoted at the wider end by sandwiching it between pieces of teflon and photographic film. The sandwich is kept in place by three screws. The narrow end of the crystal is tangential to an eccentric cam such that as the cam is rotated with the aid of a stepper motor it pushes against the tip of the triangle. An advantage of using an eccentric cam is that it is impossible to break the crystal. The amount of the rotation of the cam determines the radius of curvature of the arc form by the bending. The minimum radius of curvature is fixed by the eccentricity of the cam and it is about 20 m. Referring to Figure 7.6 the arc BC is the length of the crystal which form part of the circle of radius R. As the minimum radius R is large compared to the length of the crystal, BC is approximately equal to arc BC which is the length of the crystal. β is the angle made by the two radii of the circle AB and AC. x is the displacement of the cam.

Table 7.1 Description and data for the monochromator crystals.

Sample	Description	α (degrees)		b		FWHM of reflecting curve for 111 symmetric reflection with Cu radiation (sec.)
		Nominal	Measured	111 reflection with Cu rad.	333 reflection with Mo rad.	
1	Silicon	7	6.73	2.738	1.968	6.9
2	Silicon	7	6.74	2.743	1.970	6.9
3	Silicon	10.5	10.2	5.870	2.979	6.9
4	Silicon	10.5	10.29	6.024	3.015	6.9
5	Germanium	10.5	10.44	7.285	3.289	15.8
6	Germanium	10.5	10.39	7.160	3.265	15.8
R	Silicon	0	0	1	1	6.9

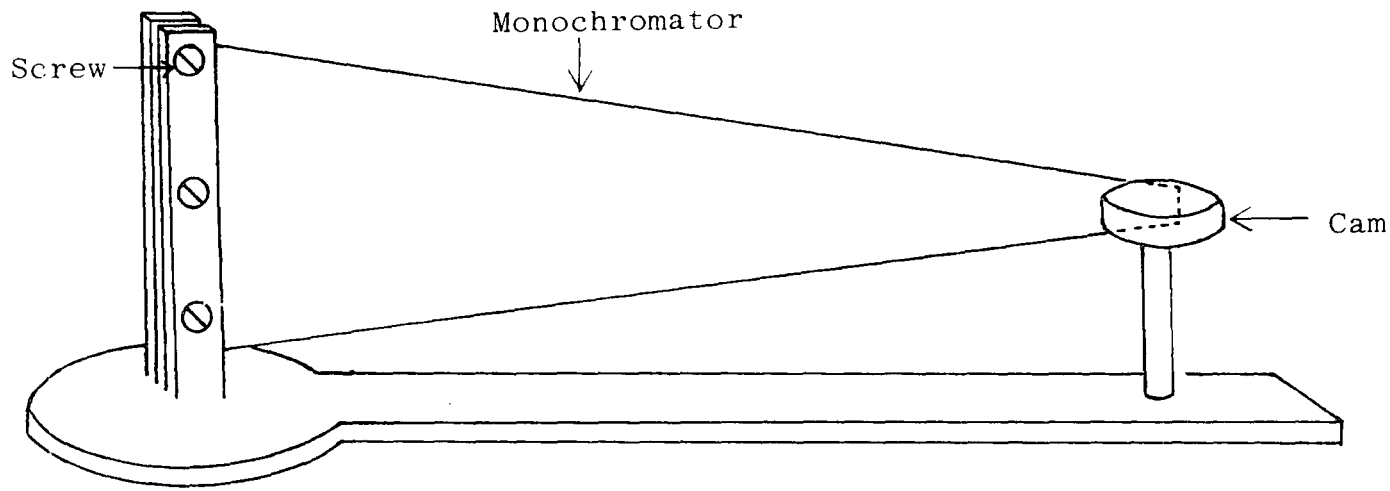

Fig. 7.5 The monochromator mounted on a special holder with the reflecting surface vertical.

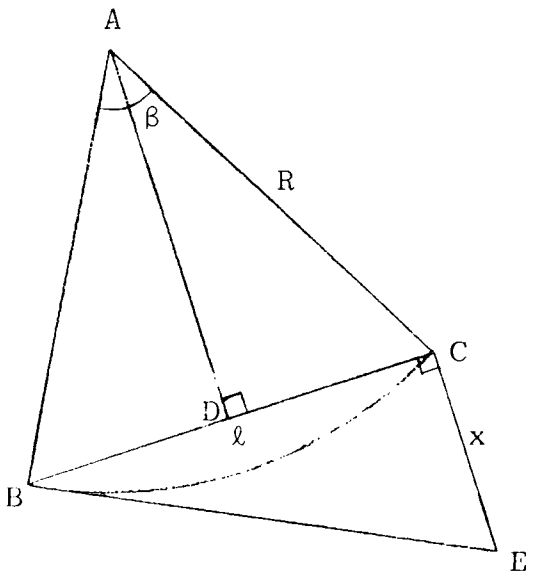

Fig. 7.6 Geometry of the bent triangular monochromator used for the derivation of the radius of curvature.

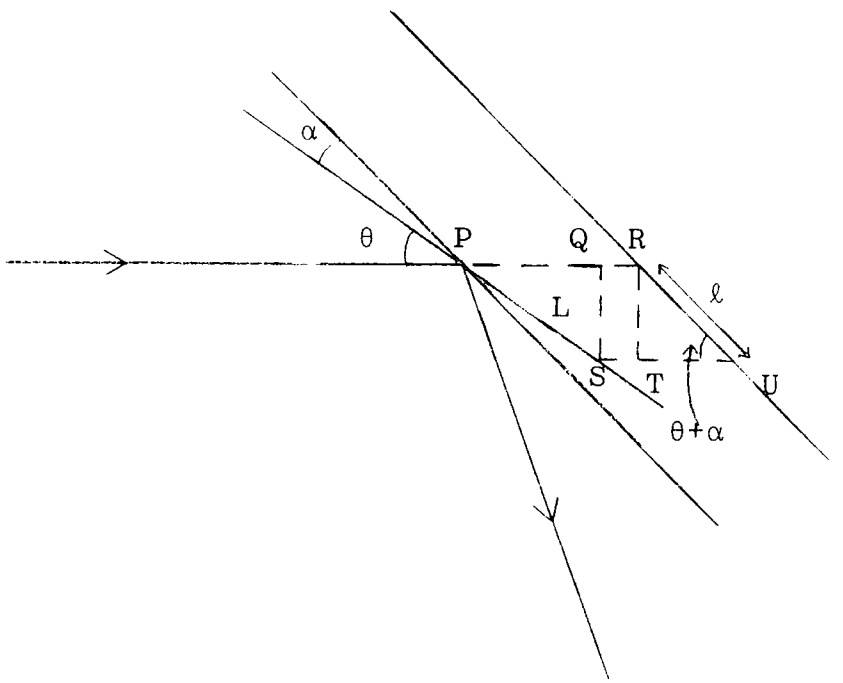

Fig. 7.7 Ray diagram for an asymmetric reflection for the determination of the radius of curvature.

From ΔADC,

$$\text{Sin } \frac{\beta}{2} = \frac{\ell}{2R}$$

$$\ell = 2R \sin \frac{\beta}{2} \qquad 7.13$$

From ΔBCE,

$$\tan \frac{\beta}{2} = \frac{x}{\ell}$$

$$x = \ell \tan \frac{\beta}{2} \qquad 7.14$$

As θ is small $\sin \beta/2 = \tan \beta/2 \overset{\sim}{\sim} \beta/2$.

Therefore equation 7.13 becomes $\ell = R\,\beta$ 7.15

and equation 7.14 becomes $x = \ell\beta/2$ 7.16

From 7.15 and 7.16

$$R = \ell/\beta \qquad 7.17$$

$$R = 2x/\beta^2 \qquad 7.18$$

$$R = \ell^2/2x \qquad 7.19$$

The radius of curvature R given by equations 7.17 to 7.19 is for a symmetric reflection where the reflecting plane is parallel to the crystal surface. For an asymmetric reflection R is increased or decreased depending whether α is positive or negative. Figure 7.7 shows the ray diagram for an asymmetric reflection where the reflecting plane is at an angle α to the crystal surface and θ is the Bragg angle.

From ΔPQS $\sin \theta = \frac{QS}{PS}$ 7.20

From ΔRTU $\sin (\theta+\alpha) = \frac{RT}{RU} = \frac{QS}{RU}$ 7.21

From equations 7.20 and 7.21, $PS \sin \theta = RU \sin (\theta+\alpha)$.

Let PS = L and RU = ℓ

$$L = \frac{\ell \sin(\theta+\alpha)}{\sin\theta} \qquad 7.22$$

Radius of curvature of the reflecting plane

$$R = \frac{L}{\beta} = \frac{\ell \sin(\theta+\alpha)}{\beta \sin\theta} \qquad 7.23$$

7.4 Double Crystal Rocking Curves

The FWHM of the double crystal rocking curves for all the samples were measured to determine their perfection. The automatic routine was used to obtain the minimum rocking curve width. The experimental value was compared to the theoretical value which was calculated on the assumption that the rocking curve has a Gaussian distribution. Table 7.2 shows the results tabulated for the 111 and 333 reflections for Cu and Mo Kα radiation respectively.

The experimental and theoretical values for the 111 reflection from Samples 1 and 2, 5 and 6 and R and 3 are comparable within limits of experimental error. As Sample 4 has its surface unpolished the FWHM of the rocking curve for both the 111 and 333 reflection are expected to be higher than the predicted value. Two peaks were observed when the higher resolution 333 reflection was used. The occurrence of Pendellosung fringes is eliminated as the crystal is too thick, that is $t >> \xi_g$. It is unlikely that all the five crystals are imperfect and a lattice misorientation of less than 15 arc seconds exist which is not resolved

Table 7.2 Tabulation of the theoretical and experimental FWHM of the rocking curve.

Reflection	First Crystal	Second Crystal	Theoretical FWHM of rocking curve (sec)*	Experimental FWHM of rocking curve (sec)	Peak Separation (sec)
Si(111)	2	1	12.2	15 ± 1	
Si(333)	2	1	0.98	3.7 ± 0.5	8.8 ± 0.5
Si(111)	3	R	18.1	24 ± 1	
Si(333)	3	R	1.2	3.3 ± 0.5	3.9 ± 0.5
Si(111)	4	R	18.3	276 ± 5	
Si(333)	R	4	0.72	68 ± 3	
Ge(111)	5	6	43.2	51 ± 3	
Ge(333)	5	6	2.8	6.5 ± 0.5	11 ± 0.5

* Assuming Gaussian lineshapes

$$(\mathrm{FWHM})_{\mathrm{Theo.}} = \sqrt{(\omega_h^2)_{\mathrm{first}} + (\omega_o^2)_{\mathrm{second}}}$$

in the 111 reflection. Although the intensity of the two peaks is in the ratio of approximately 1:2 it could not be the $K\alpha_1$ and $K\alpha_2$ peaks as the non-dispersive (+,-) parallel arrangement was used and refraction effect could not account for the peak separation between 4-11 arc seconds for the 3 pairs of samples compared to the calculated value for the $K\alpha_1$ and $K\alpha_2$ peak separation of about 450 arc seconds.

7.5 Integrated Reflecting Power for a Polished and Unpolished Crystal Surfaces

The integrated reflecting power of Sample 3 was compared with that of Sample 4. Both samples were cut from the same source with the (111) plane at an angle of about 10.5 degrees to the crystal surface. Sample 3 has a polished reflecting surface but the surface of Sample 4 was left unpolished. The Si (333) non-dispersive (+,-) parallel arrangement with Mo radiation was used. The first reflection is a symmetric reflection from a perfect silicon crystal (Sample R). The asymmetry factor b for Sample 3 and 4 are 2.979 and 3.015 respectively.

Figure 7.8 is the double crystal rocking curve for Sample 3 and has a FWHM of 3 arc seconds compared to 0.72 arc seconds for a Gaussian profile. A subsidiary peak was obtained about 6 arc seconds from the main peak. Similarly a double crystal rocking curve was obtained for Sample 4 (Figure 7.9). As expected the FWHM of the rocking curve is very much wider, about 1.28 minutes due to the surface damage of the unpolished crystal and the subsidiary peak was

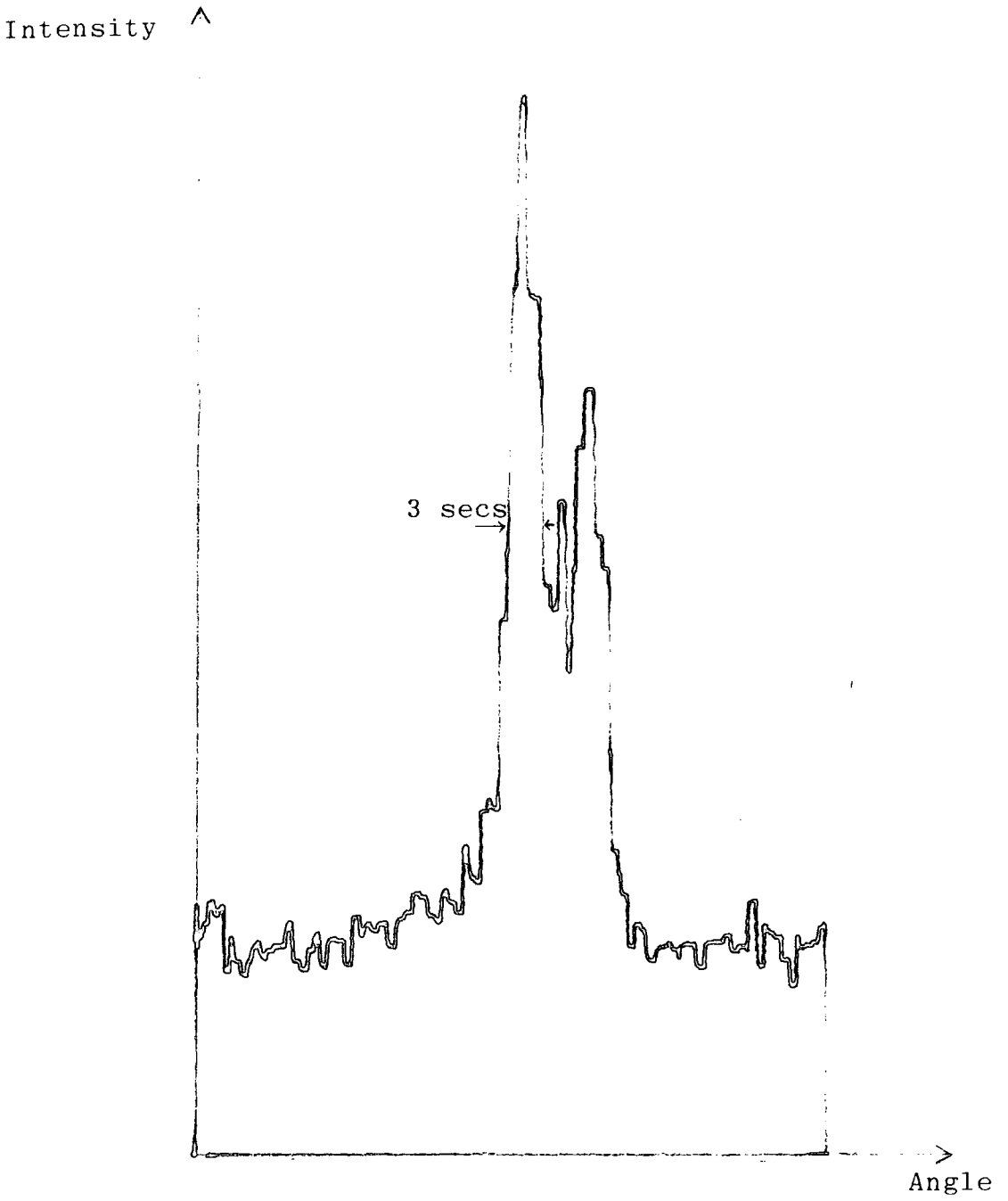

Fig. 7.8 333 double crystal rocking curve of Sample 3 with Mo radiation.

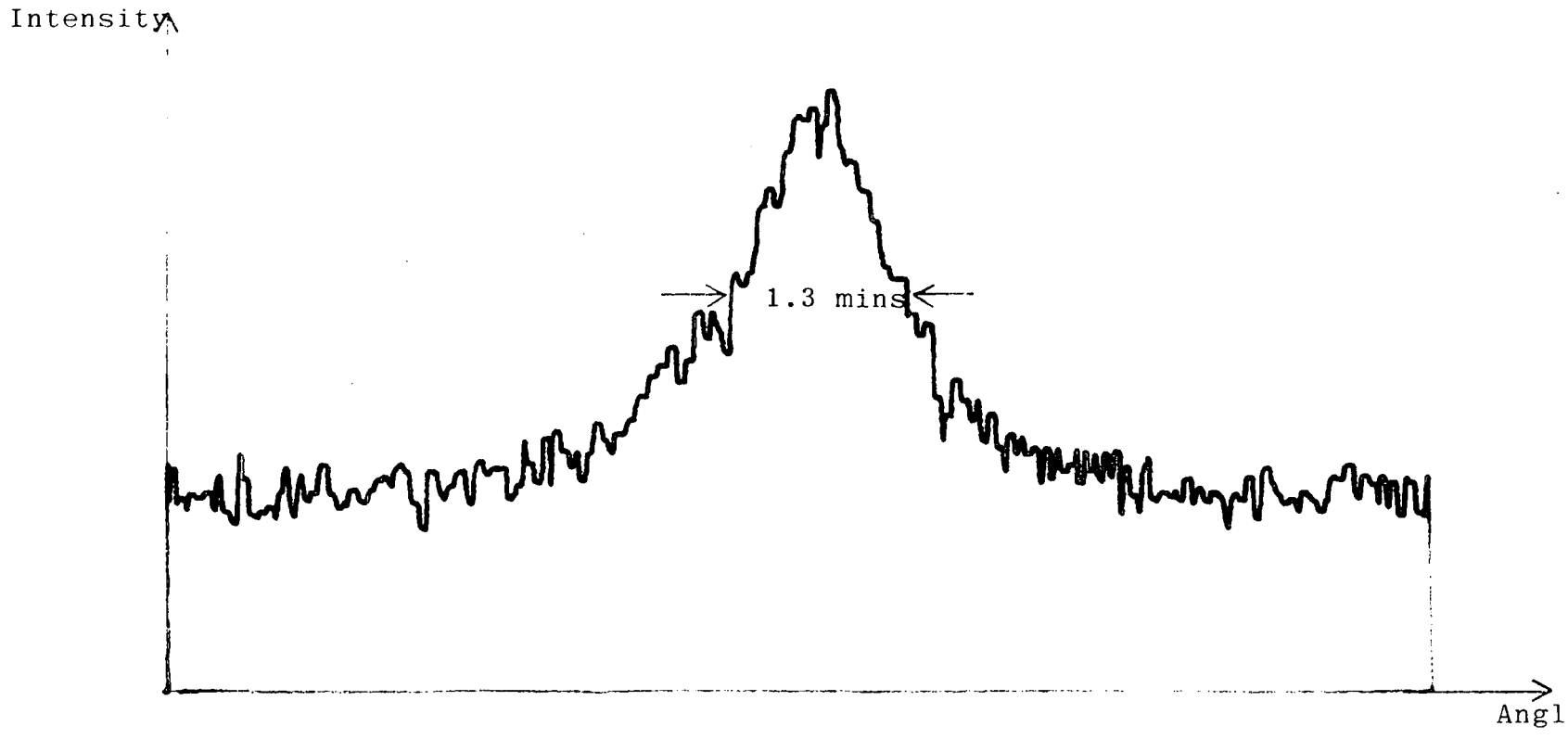

Fig. 7.9 333 double crystal rocking curve of Sample 4 with Mo radiation.

not resolved. The integrated reflecting power for Samples 3 and 4 are 4×10^{-6} and 2.5×10^{-5} respectively and about a 6 fold increase in intensity is obtained for the crystal with an unpolished surface. Although the defocussing effect reduces the integrated intensity by a factor of 0.5, the 3 fold increase in intensity obtainable using an unpolished monochromator is a great advantage in protein crystallography experiments. This monochromator is scheduled to be tested on the synchrotron radiation source during the next cycle.

7.6 Effect of Variation of Curvature on the Double Crystal Rocking Curves

The effect of bending or varying the radius of curvature on FWHM, peak count, peak position and integrated reflecting power was determined from the double crystal rocking curve for the asymmetric reflection from various pairs of crystals set in the (+,-) parallel arrangement. The first pair were the silicon crystals, Sample 1 and 2 where $\alpha \approx 7^{o}$, the second pair were germanium crystals, Sample 5 and 6 where $\alpha \approx 10.5^{o}$ and the third and last pair has a symmetric first reflection from a silicon crystal (Sample R) and the second crystal was from Sample 3 and 4 respectively where $\alpha \approx 10.5^{o}$. Each experiment was repeated twice using the 111 reflection with Cu radiation and the 333 reflection with Mo radiation. In each case rocking curves were obtained by rotating the bent sample. Graphs of radius of curvature versus FWHM and integrated reflecting power were plotted for every set of data. The

radius of curvature was calculated using equation 7.23. There is usually a small gap between the cam and the crystal initially, that is before bending as it is difficult to place the cam just touching the crystal. Therefore the displacement x of the cam when the crystal was just touching the crystal was determined from the peak position of the double reflection as it varies as the crystal is bent. This allows the minimum radius of curvature to be determined in each case.

The integrated reflecting power for the double reflection from the pair of germanium crystals does not vary as the curvature changes for both the 111 and 333 reflections (Figures 7.12b and 7.13b) but the FWHM for the 333 reflection (Figure 7.13a) increases as the curvature increases whereas it remains unchanged for the 111 reflection (Figure 7.13a). The increase in FWHM is sharp for bending steps between 2000 and 3000. A comparison was made with the third and fourth pair of silicon samples where one of the crystals in each pair has about the same α value of 10.5^{o} as that of the germanium crystals. It shows a similar variation in integrated reflecting power and FWHM with curvature for the 111 reflection (Figures 7.14a,b and 7.16 a,b). The 333 reflection for the third pair has both the integrated intensity and FWHM increasing as the curvature increase (Figures 7.15a and b) but both values remain unchanged for the fourth pair (Figure 7.17a and b). Note that the silicon sample in the fourth pair where $\alpha = 10.5^{o}$ has its reflecting surface unpolished. For the first pair of silicon crystals with $\alpha = 7^{o}$, the integrated reflecting power and FWHM both increase as the curvature

(a)

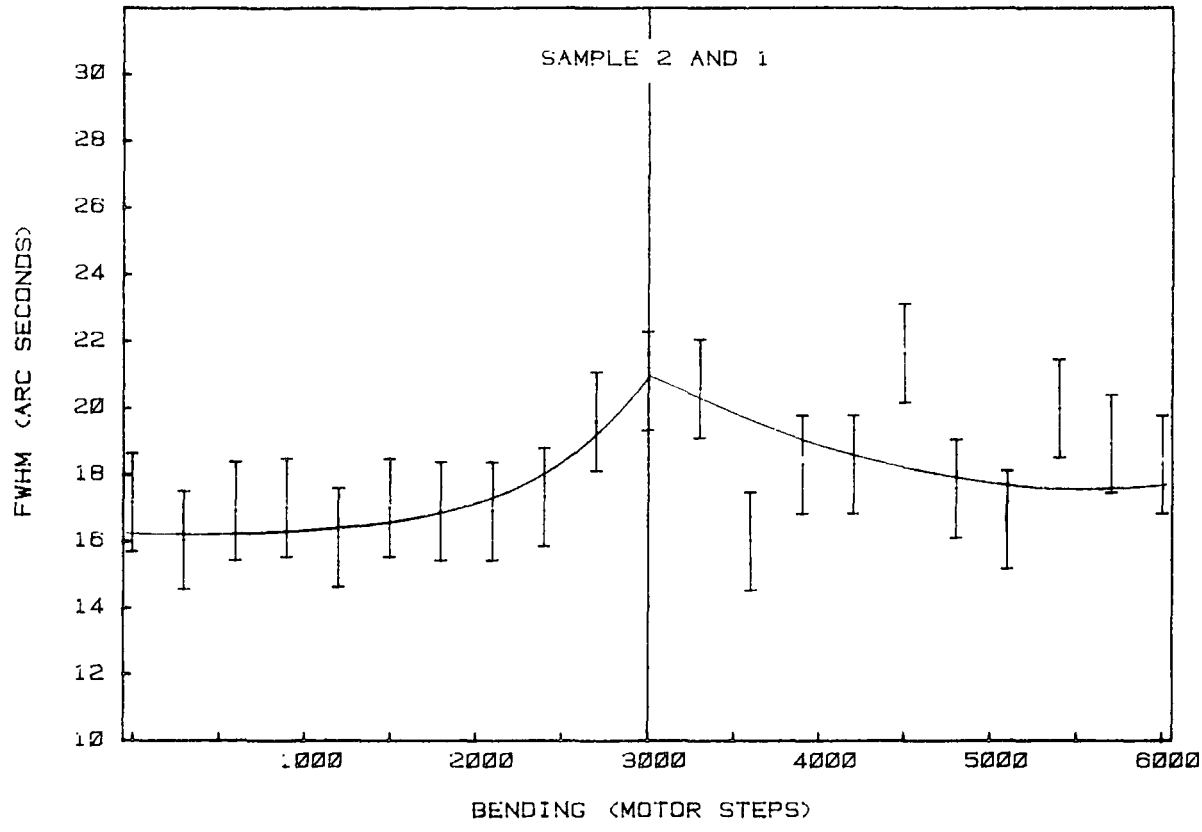

(b)

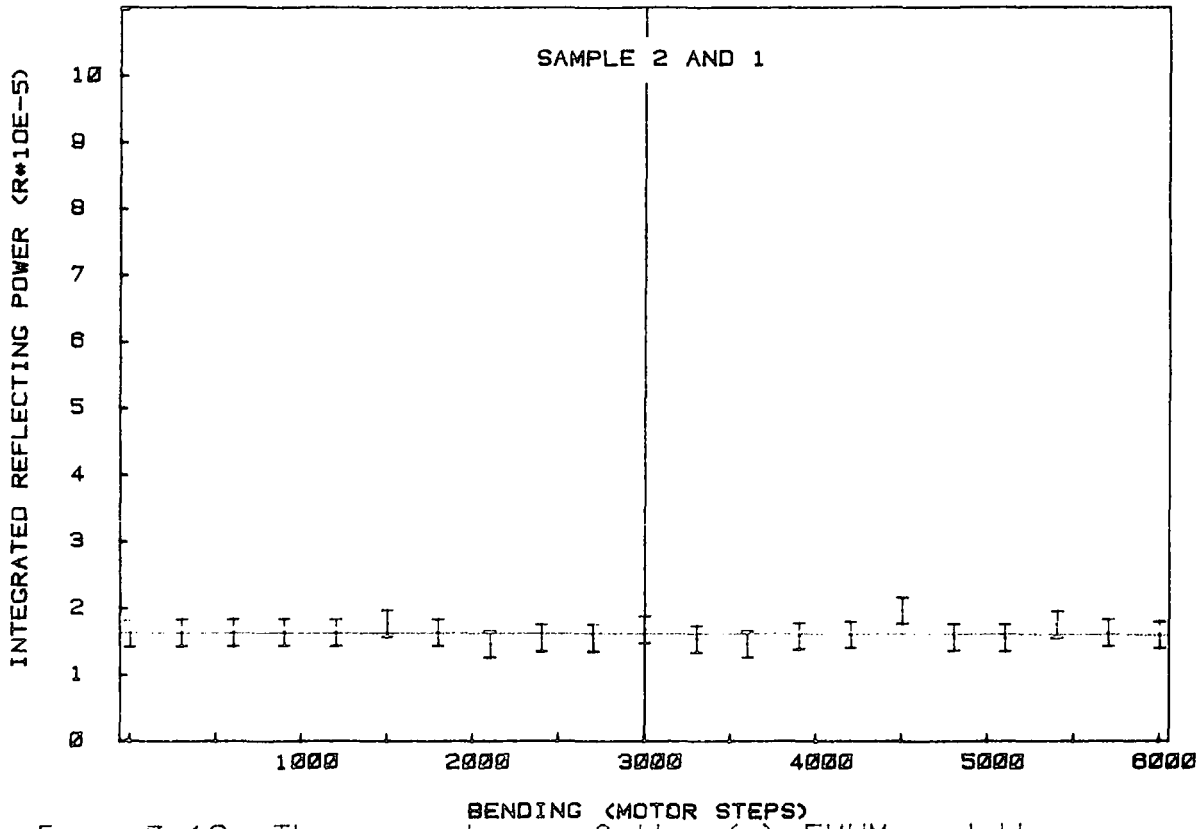

Fig. 7.10 The variation of the (a) FWHM and the (b) integrated reflecting power as the curvature was increased for the 111 reflection using Cu radiation.

(a)

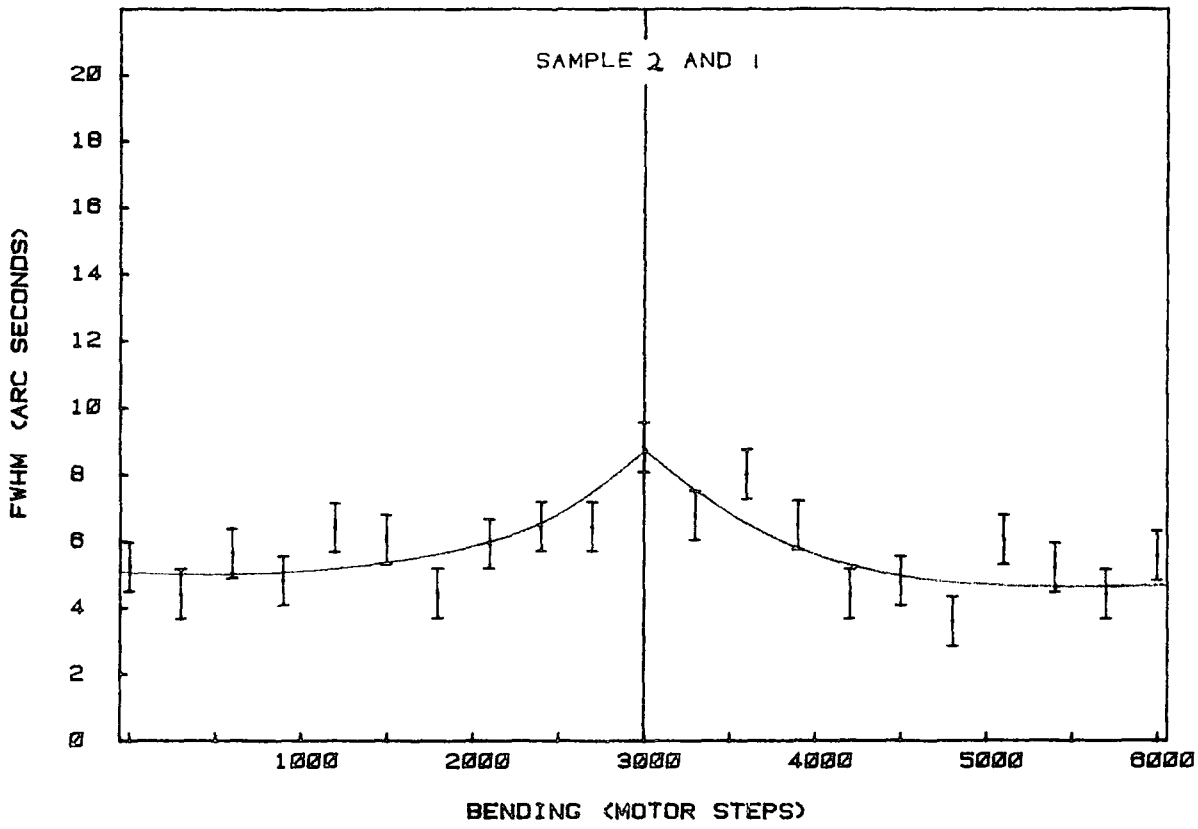

(b)

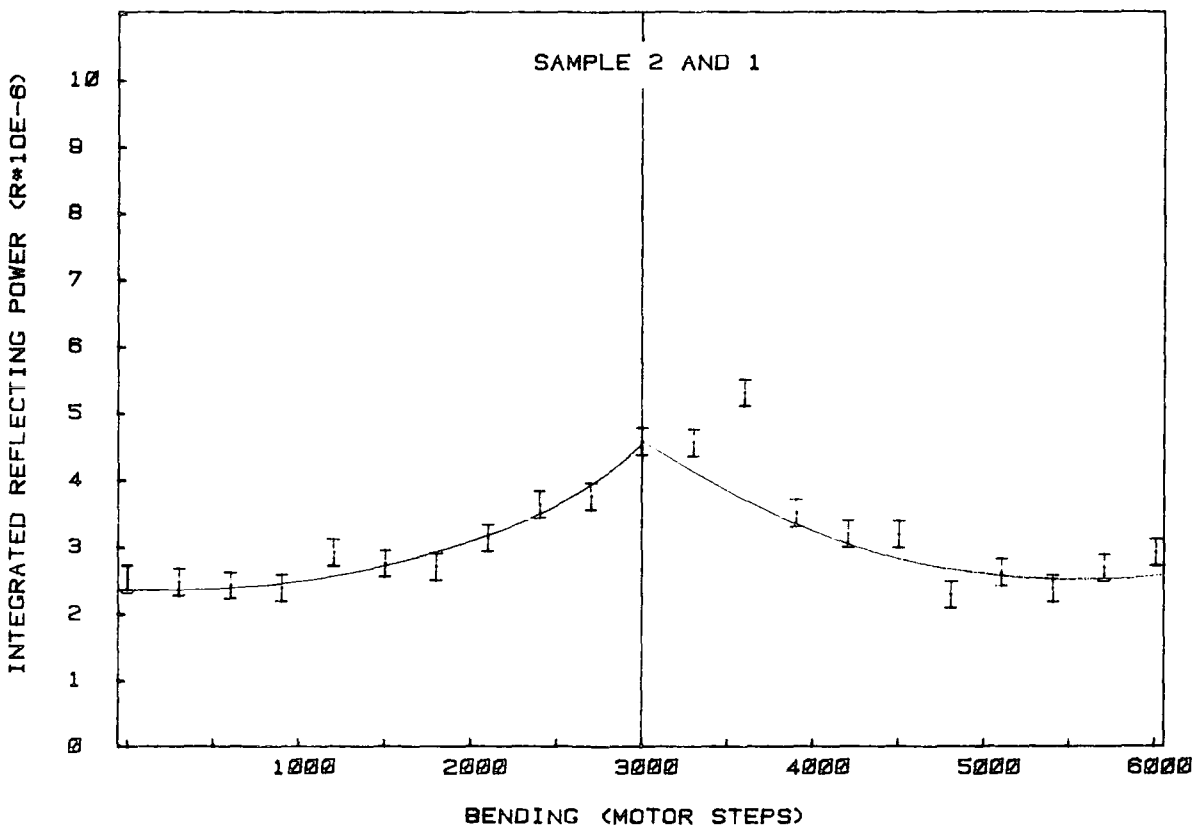

Fig. 7.11 The variation of the (a) FWHM and the (b) integrated reflecting power as the curvature was increased for the 333 reflection using Mo radiation.

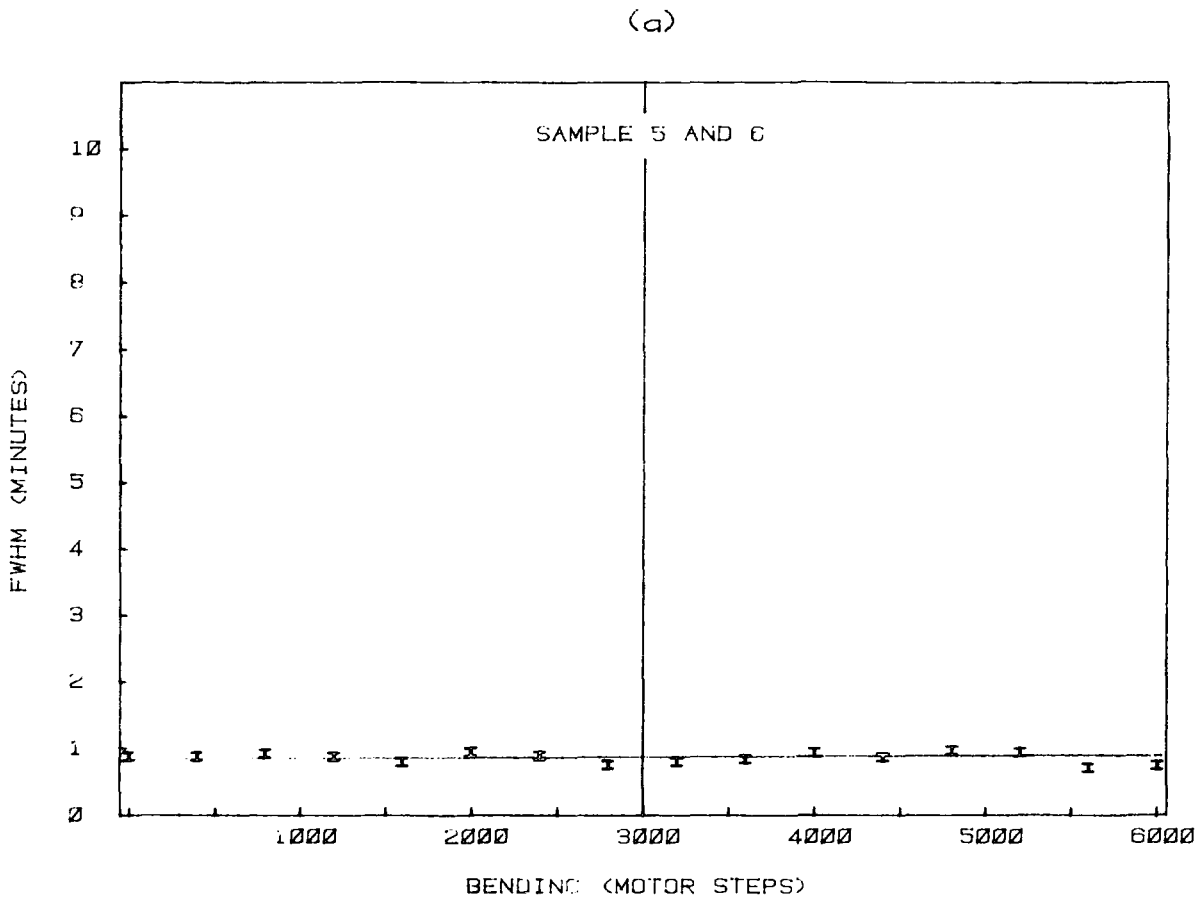

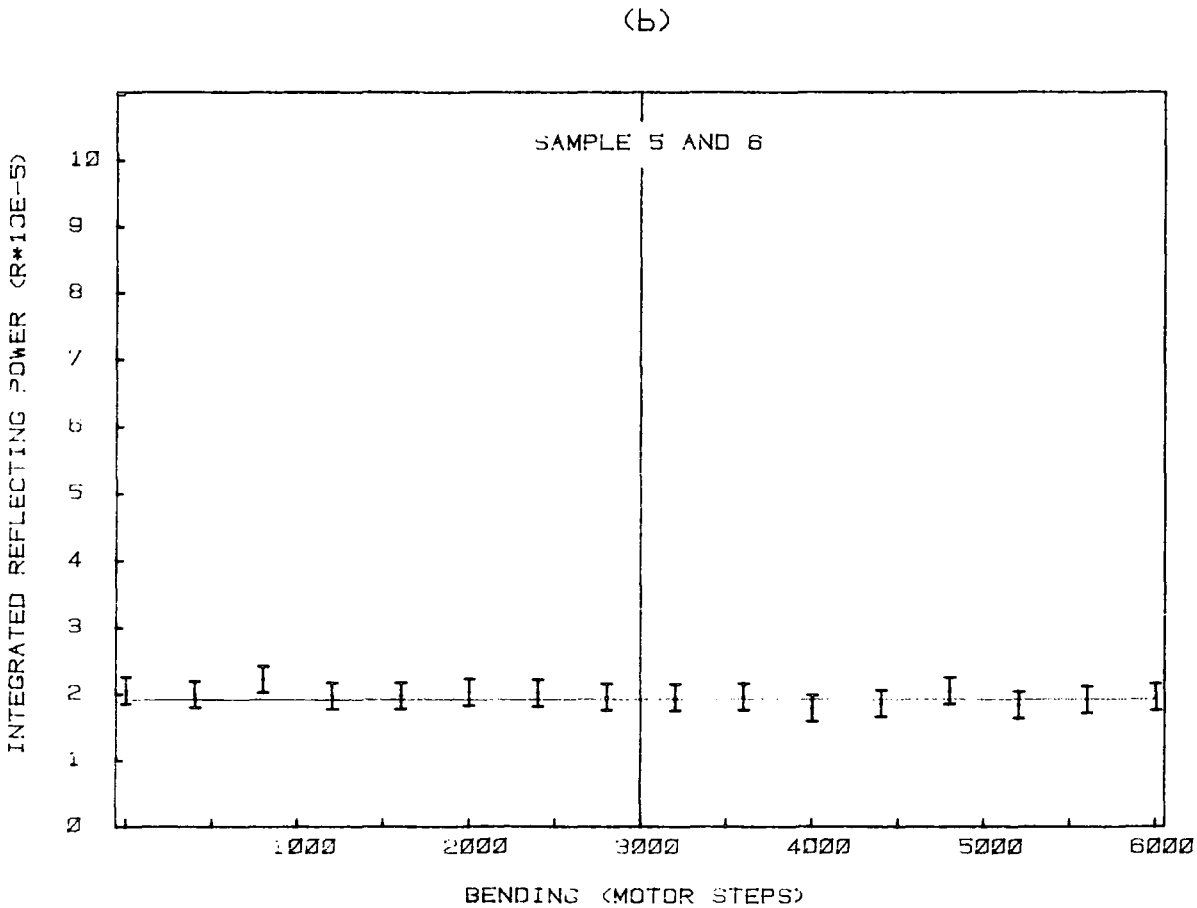

Fig. 7.12 The variation of the (a) FWHM and the (b) integrated reflecting power as the curvature was increased for the 111 reflection using Cu radiation.

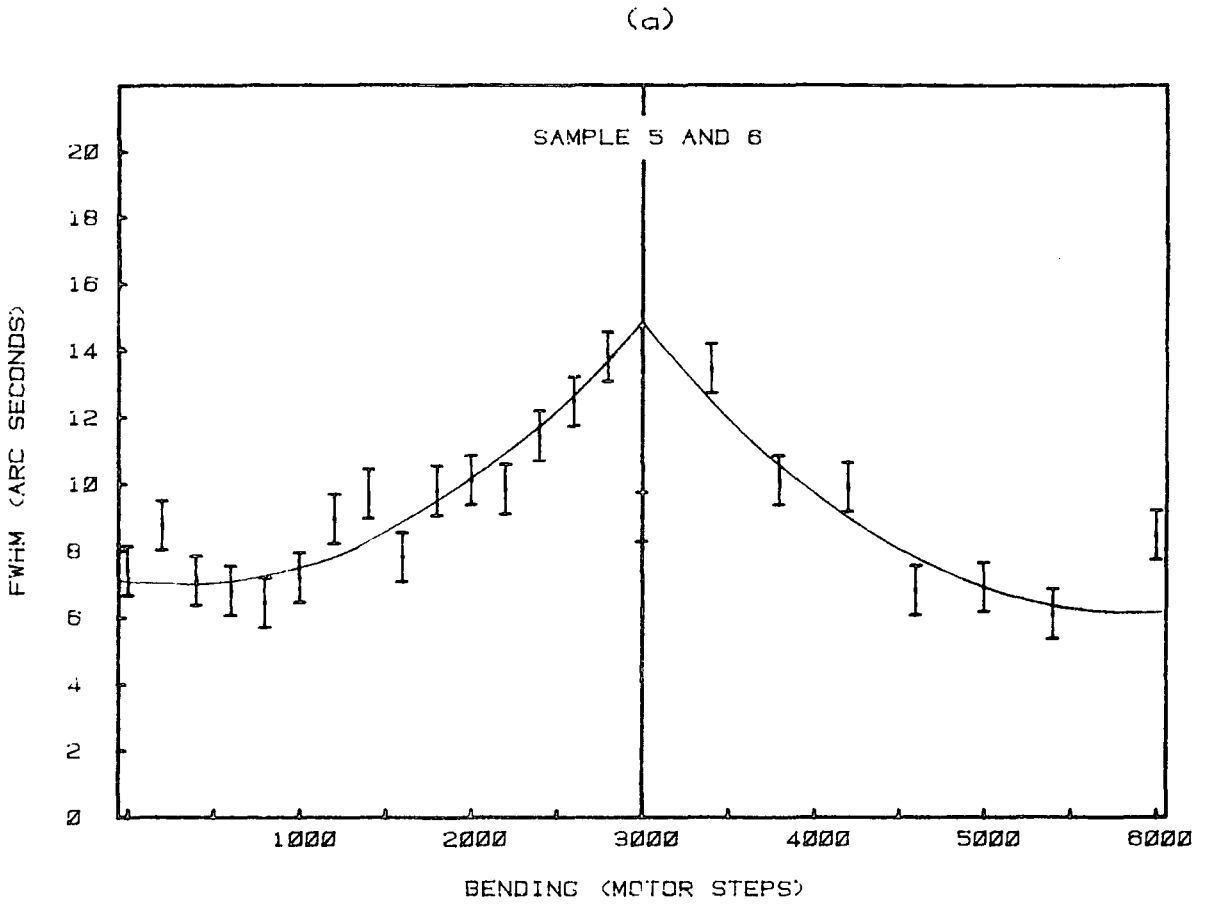

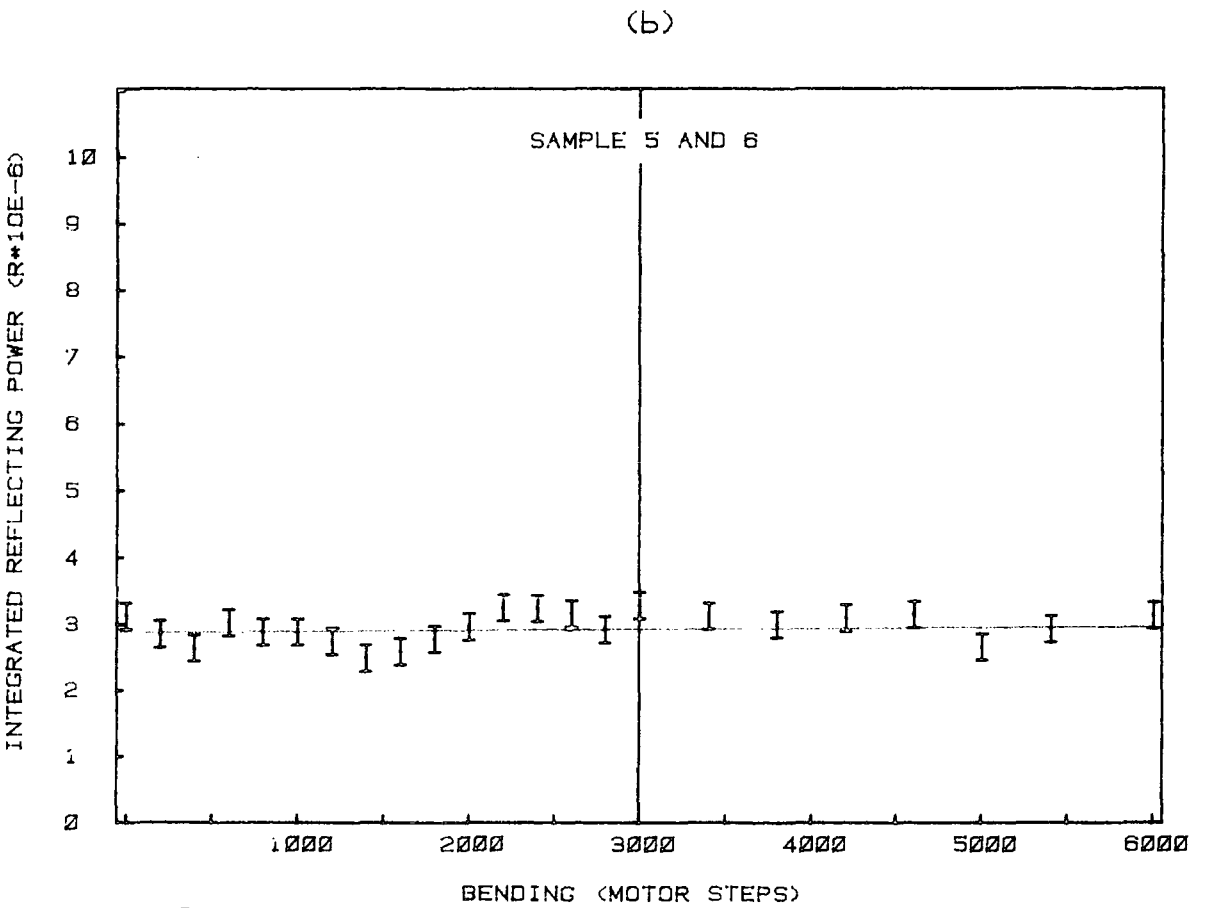

Fig. 7.13 The variation of the (a) FWHM and the (b) integrated reflecting power as the curvature was increased for the 333 reflection using Mo radiation.

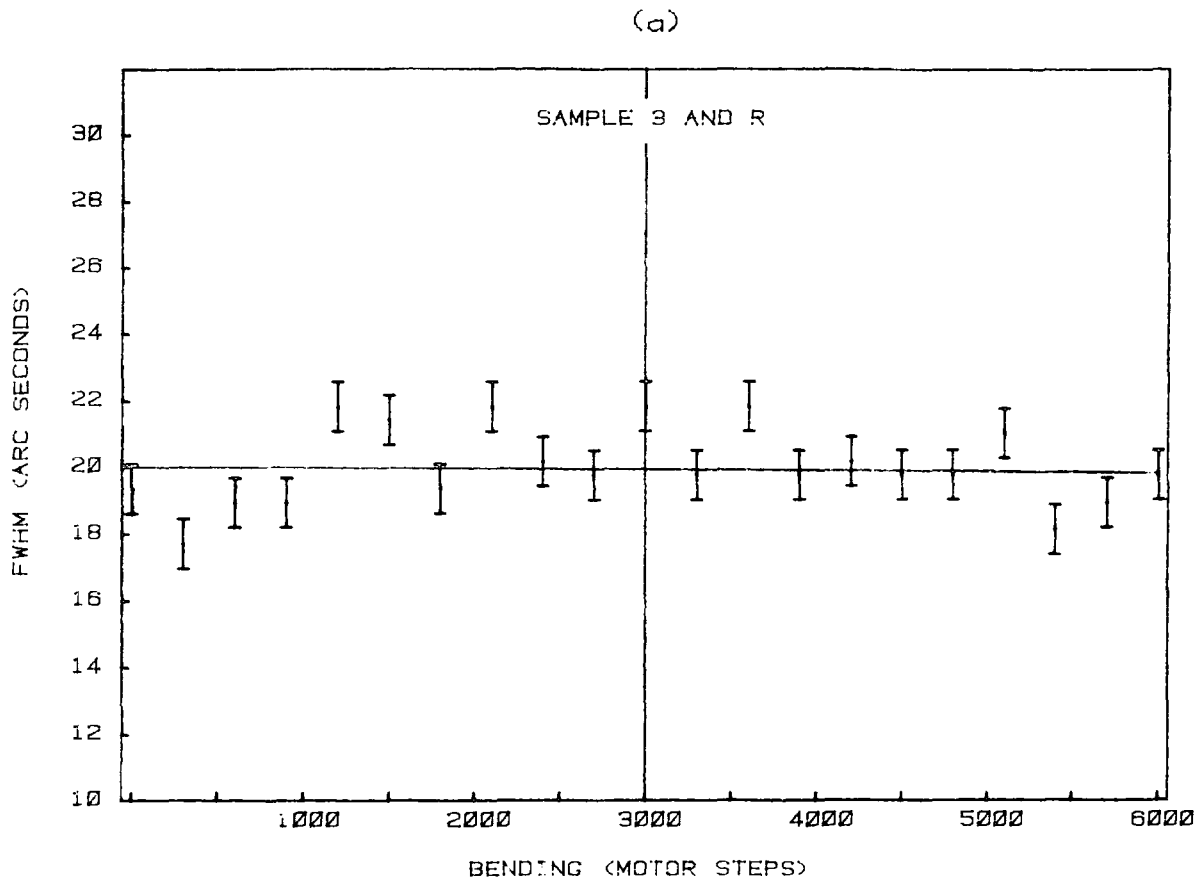

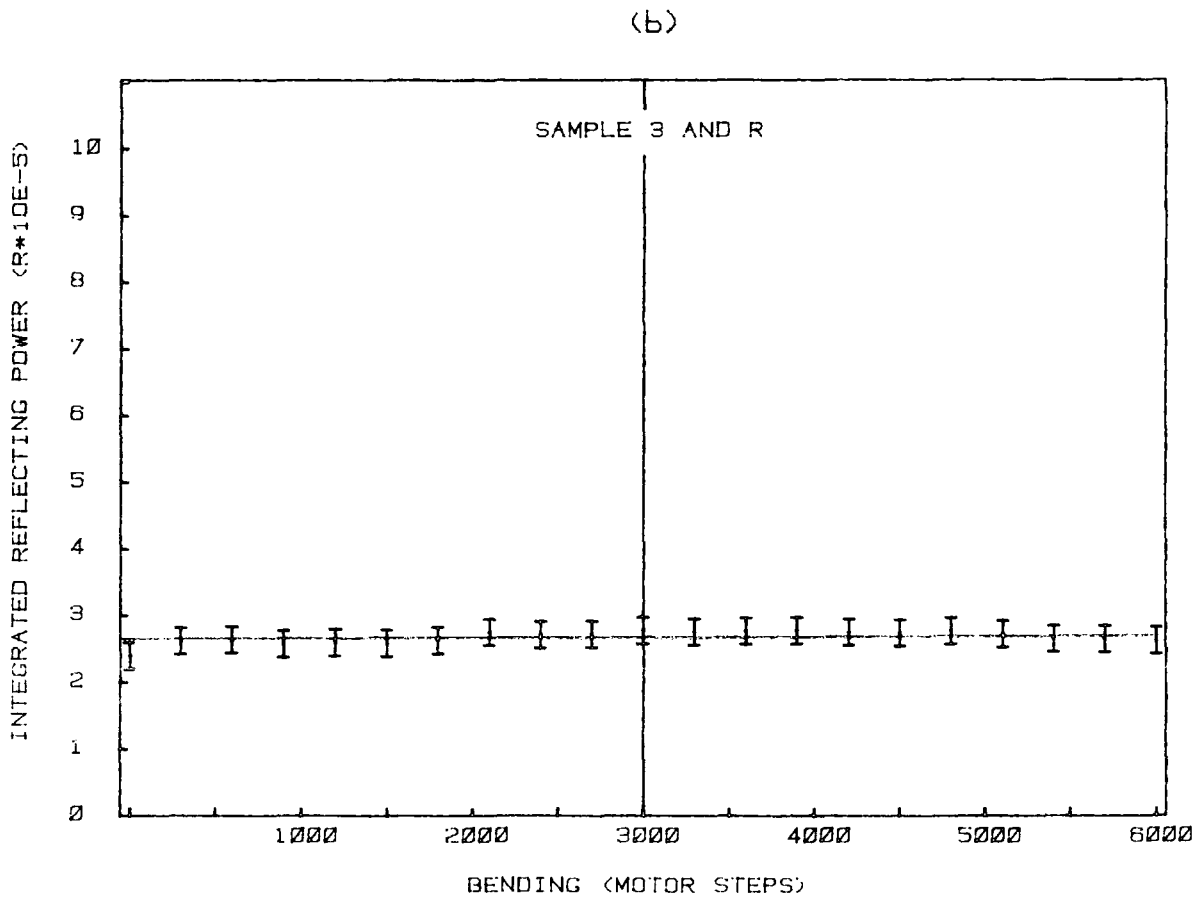

7.14 The variation of the (a) FWHM and the (b) integrated reflecting power as the curvature was increased for the 111 reflection using Cu radiation.

(a)

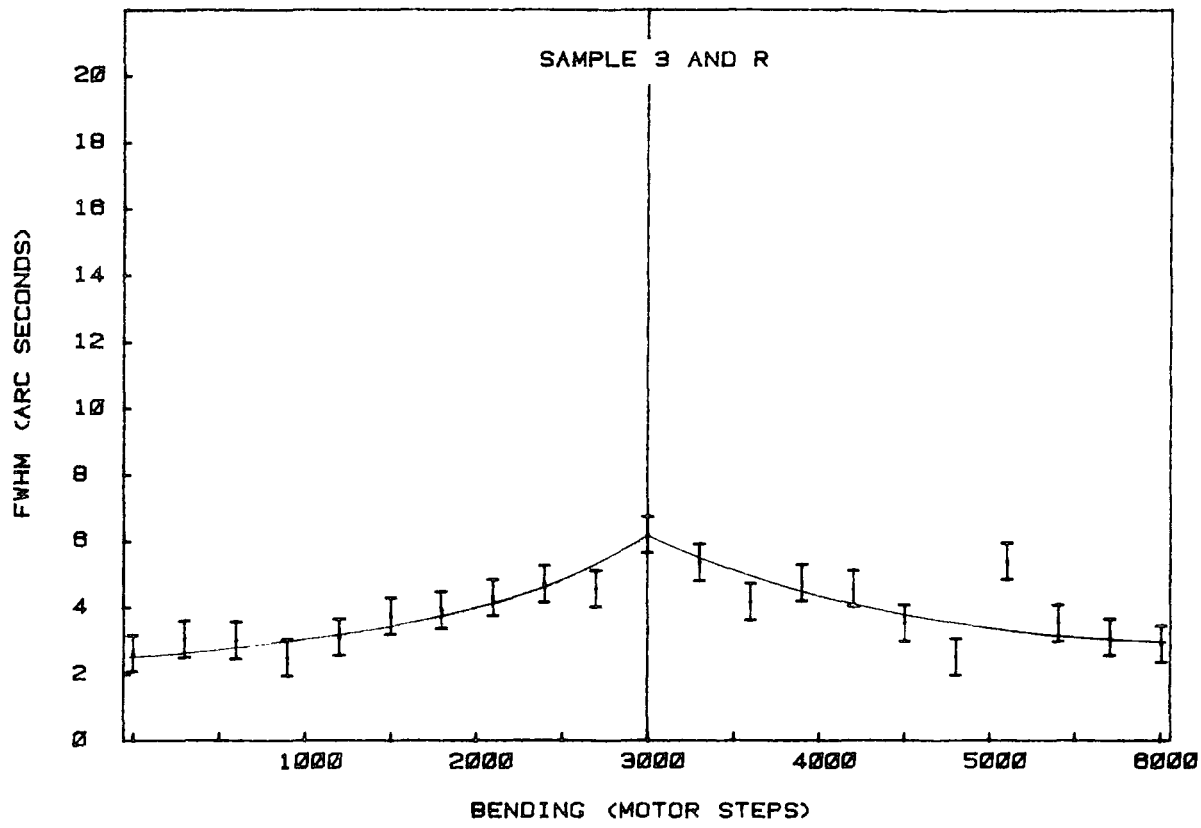

(b)

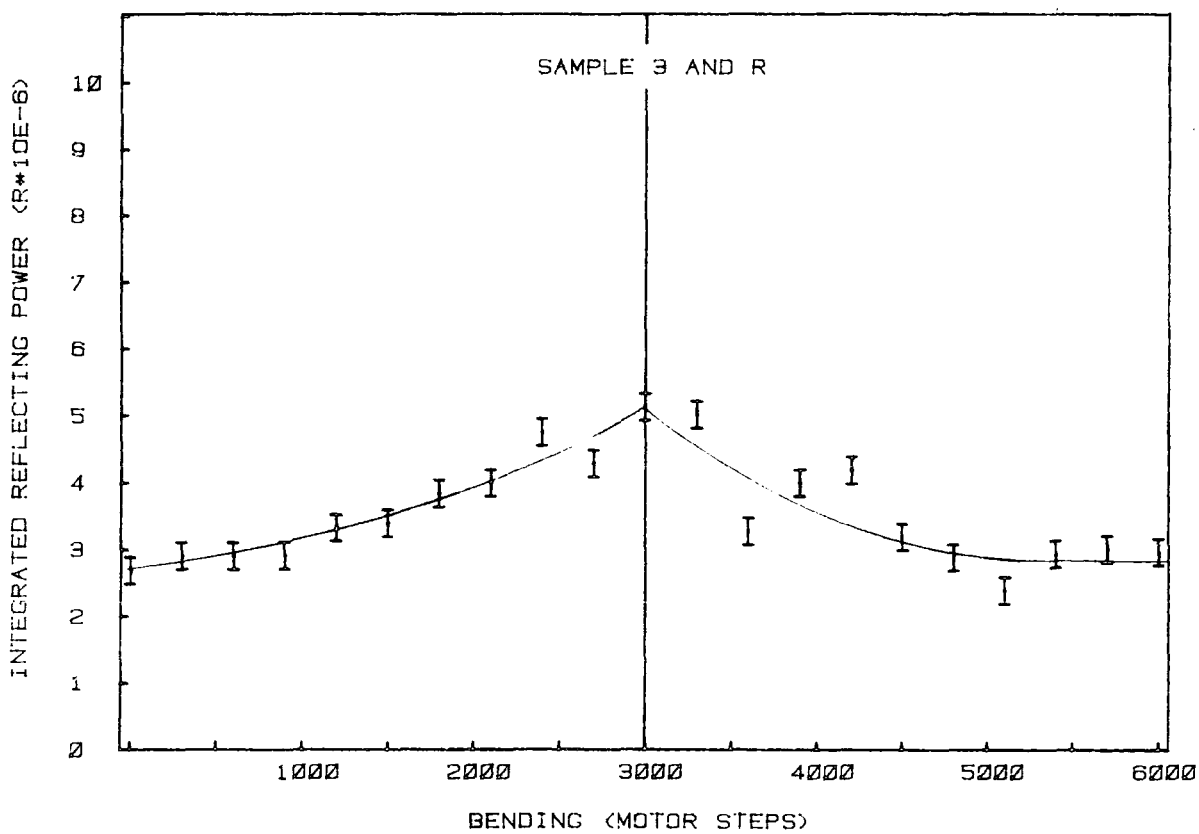

Fig. 7.15 The variation of the (a) FWHM and the (b) integrated reflecting power as the curvature was increased for the 333 reflection using Mo radiation.

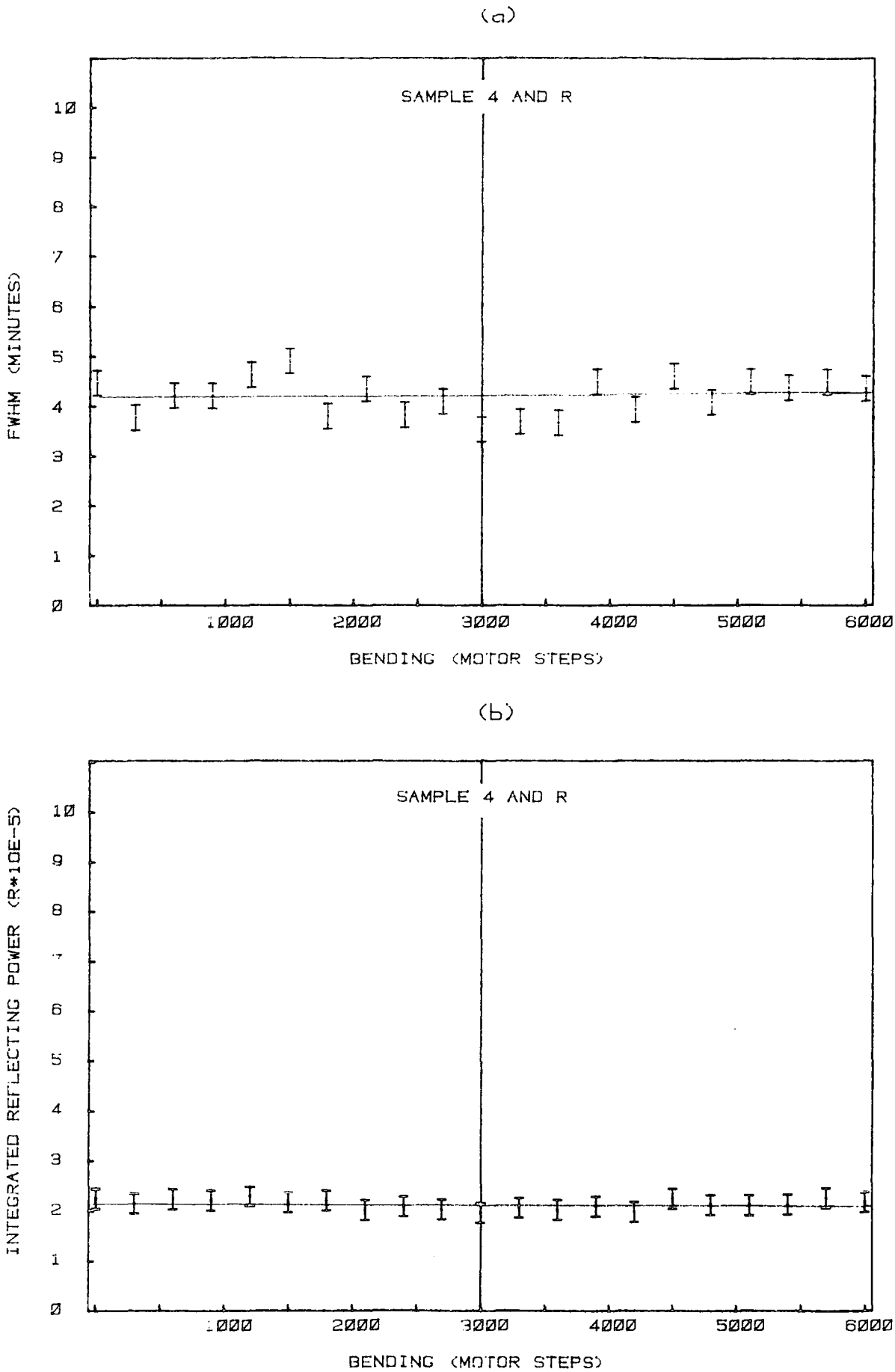

Fig. 7.16 The variation of the (a) FWHM and the (b) integrated reflecting power as the curvature was increased for the 111 reflection using Cu radiation.

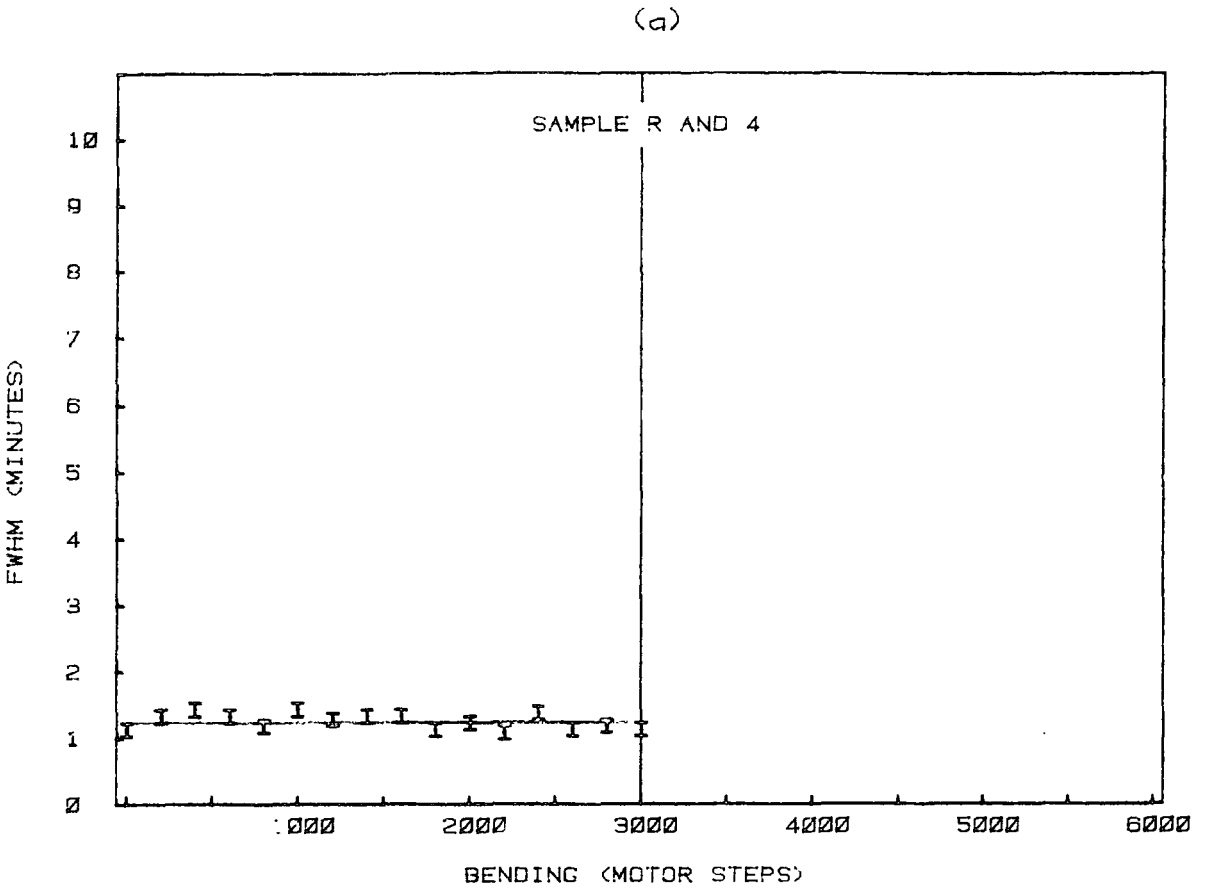

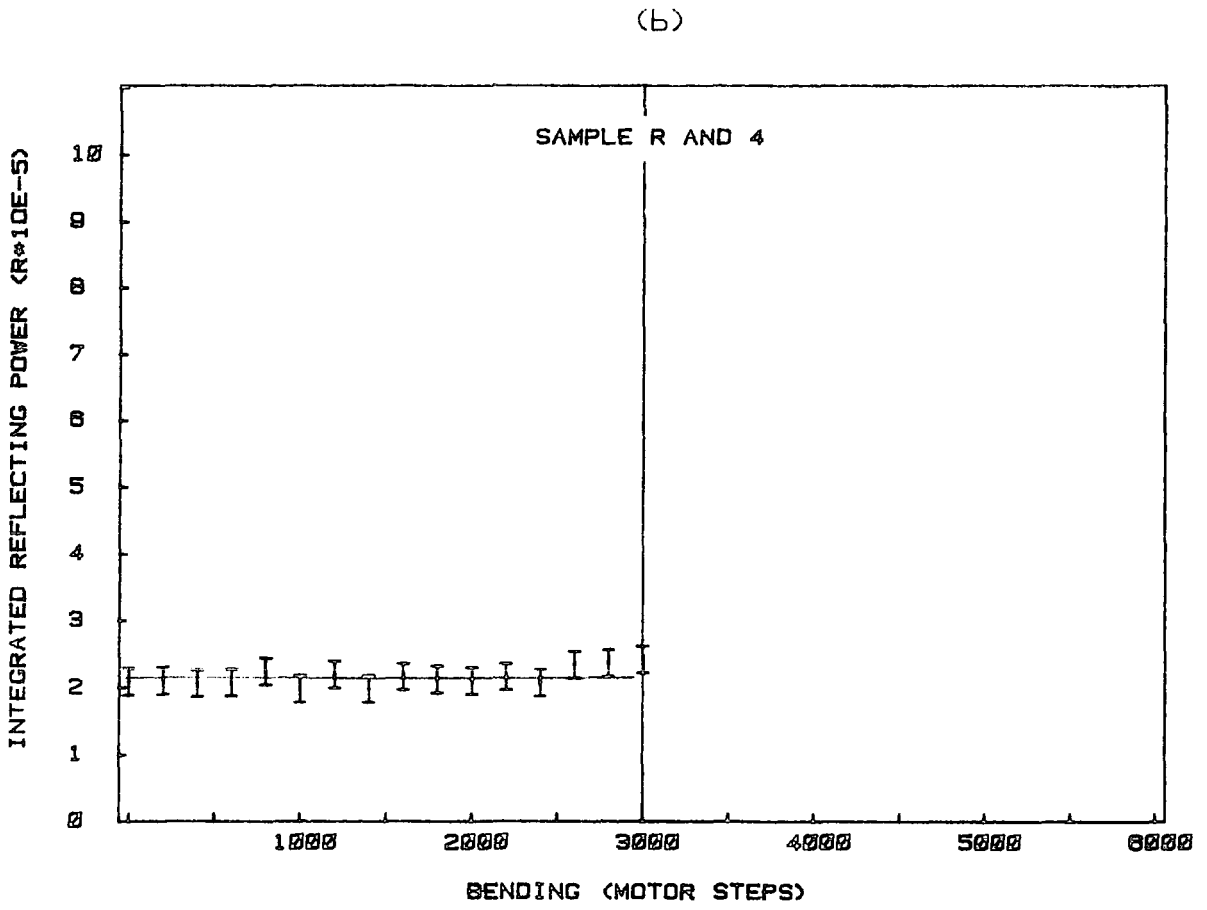

Fig. 7.17 The variation of the (a) FWHM and the (b) integrated reflecting power as the curvature was increased for the 333 reflection using Mo radiation.

increases (Figures 7.11a,b) when set for the 333 reflection whereas only the FWHM increase with curvature for the 111 reflection (Figures 7.10a and b). A summary of the result is tabulated in Table 7.3.

The peak position for the double reflection for all the pairs of crystals shifted towards higher Bragg angle as the curvature increased. The results for each pair are tabulated in Table 7.4.

7.7 Energy Resolution

As stated in Section 7.1.1. the energy resolution improves towards the edge of the focus and is given by

$$\frac{\delta E}{E} = \omega_h \cot \theta$$

As b>1, the resolution will improve if a symmetric cut crystal is used as $\omega_h > \omega_s$, but the focal width h is too large ($h_{meas.}$ = 9.87 mm FWHM) for experiments with protein samples. From Table 7.1 it is clear that by using a Si(111) monochromator the energy resolution will improve by about $\frac{1}{3}$ for the same reflection from Ge(111) monochromator as the FWHM of the reflecting range for silicon is much narrower. This higher energy resolution is achieved at the expense of intensity.

For an Fe absorption edge where λ = 1.743Å, δE = 5.1eV for Ge(111) crystal ($\alpha = 10.44^{o}$, $(\delta E/E)_{sym} = 3.2 \times 10^{-4}$) and δE = 1.9 eV for Si(111) ($\alpha = 10.29^{o}$, $(\delta E/E)_{sym} = 1.2 \times 10^{-4}$);

Table 7.3 A summary of the results obtained for the variation of the FWHM and integrated reflecting power as the curvature was increased.

Sample	Reflection	Variation as Curvature Increase	
		FWHM	Integrated reflecting power
1 and 2	111	increase	unchanged
	333	increase	increase
5 and 6	111	unchanged	unchanged
	333	increase	unchanged
R and 3	111	unchanged	unchanged
	333	increase	increase
R and 4	111	unchanged	unchanged
	333	unchanged	unchanged

Table 7.4 Tabulation of the peak shift as the curvature was increased and the minimum radius of curvature obtainable.

Sample	Peak shift (deg)		Minimum radius of curvature (m)
	111	333	
1 and 2	0.23	0.09	33
5 and 6	1.2	0.16	20
R and 3	0.11	-	29
R and 4	-	-	20

assuming that ω_{sym} measured for Cu Kα (λ = 1.542Å) can be used for λ = 1.743Å.

The focussing aberration which limits the energy resolution of the monochromator can be improved by reducing the length L of the monochromator and using a 10.5° oblique cut monochromator instead of a 7° cut. For example, a Ge(111) crystal where α = 10.44° and R = 50 m at the Guinier position has a focussing aberration FC = 0.1 mm. Then

$$\omega_{effective} = \left[\omega_h^2 + \left(\frac{FC}{p'}\right)^2\right]^{\frac{1}{2}} = 40.5 \text{ secs}$$

instead of 40 secs (ω_h). If L is reduced to 100 mm, FC = 25 μm and is negligible compared to $\omega_h p'$ = 0.65 mm at the Guinier position. For cobalt hp'/p calculated is 2 mm with an energy width of 20 eV. Therefore 0.65 mm is equivalent to 6.5 eV and is comparable with 5.1 eV calculated earlier.

Table 7.5 shows the effect of an error in the oblique cut angle $\delta\alpha$ on δE for Ge(111) at 1.5Å. If $\delta\alpha$ = 0.25° which is the maximum difference between the crystal supplier's estimate and the measured value, the error in the Guinier position, $\delta p_G'$ is 250 mm and $\delta(\delta\lambda/\lambda)$ = 7.5 eV. For $\delta\alpha$ = 0.05°, $\delta p_G'$ = 50 mm and $\delta(\delta\lambda/\lambda)$ = 1 eV. By reducing the length of the monochromator $\delta(\delta\lambda/\lambda)$ can be reduced at the expense of flux and there is a difficulty of obtaining a minimum width at the Guinier position. The depth of focus AB (Figure 7.1) is less than $L\cos\theta/2$, but there is a contribution from the depth of the source due to the acceptance angle β = 4 mrad. of the SRS beam which is equal to βR_b = 22.5 mm for a bending radius R_b = 5.5 m. For L = 200 mm for Co K edge where θ = 14.25°, the total depth of focus is

Table 7.5 Effect of an error in the measurement of on E for Ge(111) reflection at 1.5A.

Error in α $\pm$ $\delta\alpha$ (degrees)	Error in Guinier position $\pm$ $\delta p'_G$ (mm)	Effect on energy resolution $\pm$ δE (eV)
0.05	50	1.2
0.1	100	2.4
0.15	150	3.6
0.20	200	4.8
0.25	250	6.0

$$\frac{L\cos\theta}{2} + \beta R_b = 119 \text{ mm}$$

and for L = 100 mm it is 60 mm. Therefore $\delta(\delta\lambda/\lambda)$ is in the range 1-3 eV for L between 100 - 200 mm.

Therefore for Si(111) at the Guinier position with $\alpha = 10.5^{\circ}$ and for Fe K wavelength $\delta E_{TOT} = 5.9$ eV for L = 200 mm and 3.9 eV for L = 100 mm where the contribution of $\omega_h \cot\theta$ is 1.9 eV, $\delta\alpha = 0.05^{\circ}$ is 1 eV and depth of focus is 1-3 eV for L = 100 - 200 mm. For Ge(111) it would be 9.1 eV and 7.1 eV respectively.

7.8 Determination of Radius of Curvature

A single reflection experiment was carried out on the Lang camera to determine the variation of curvature along the length of the monochromator. Cu $K\alpha_1$ radiation with a beam divergence of approximately 5×10^{-4} radian was used. The asymmetric Si(333) reflection used provide a suitable Bragg angle of 47.6 degrees and about 70 mm of the crystal can be translated across the incident beam using the transverse mechanism. By bending the crystal using the cam to obtain a fixed value of the curvature, the angular position of the peak intensity was noted for various positions along the length of the crystal. Similar data were taken as the curvature was increased up to the maximum and then decreased back to zero again. For the evaluation of the radius of curvature R the angular position of the peak intensity for one position ℓ_A along the crystal is used as a reference. The value of β in equation 7.26 is therefore the angular difference between

peak positions for different positions along the crystal, say ℓ_B, and that at position A.

Three graphs were plotted from each set of data taken.

(a) a graph of β versus ℓ for each radius of curvature R,

(b) a graph of R versus ℓ,

(c) a graph of R versus x for each value of ℓ.

Theoretically graph (a) should be a straight line with a positive gradient which is equal to the curvature $(\frac{1}{R})$ of the crystal surface. Graph (b) determines the variation of the radius of curvature along the length of the crystal for a particular bending step and graph (c) is the variation of R with x when ℓ is constant.

Data was obtained for the silicon Samples 2 and 3. Two similar sets of data were obtained for Sample 2 in which the second set was taken at a different part of the crystal further from the clamped end and the crystal was remounted. Graphs of β versus ℓ (Figures 7.18 a,b,c) for the three sets of data are linear as predicted theoretically. The radius of curvature obtained from the gradient agrees within experimental errors with the average value calculated from the data obtained except at a bending step of about 1200 for the first and third set of data where the average radius of curvature varies by a large range as it changes its sign (Table 7.6). From Figures 7.19a, b and c, within limits of experimental errors the radius of curvature is constant along the length of the crystal and corresponds to the average value and that obtained from Figures 7.18a, b and c except at a bending step of about 1200 as discussed above

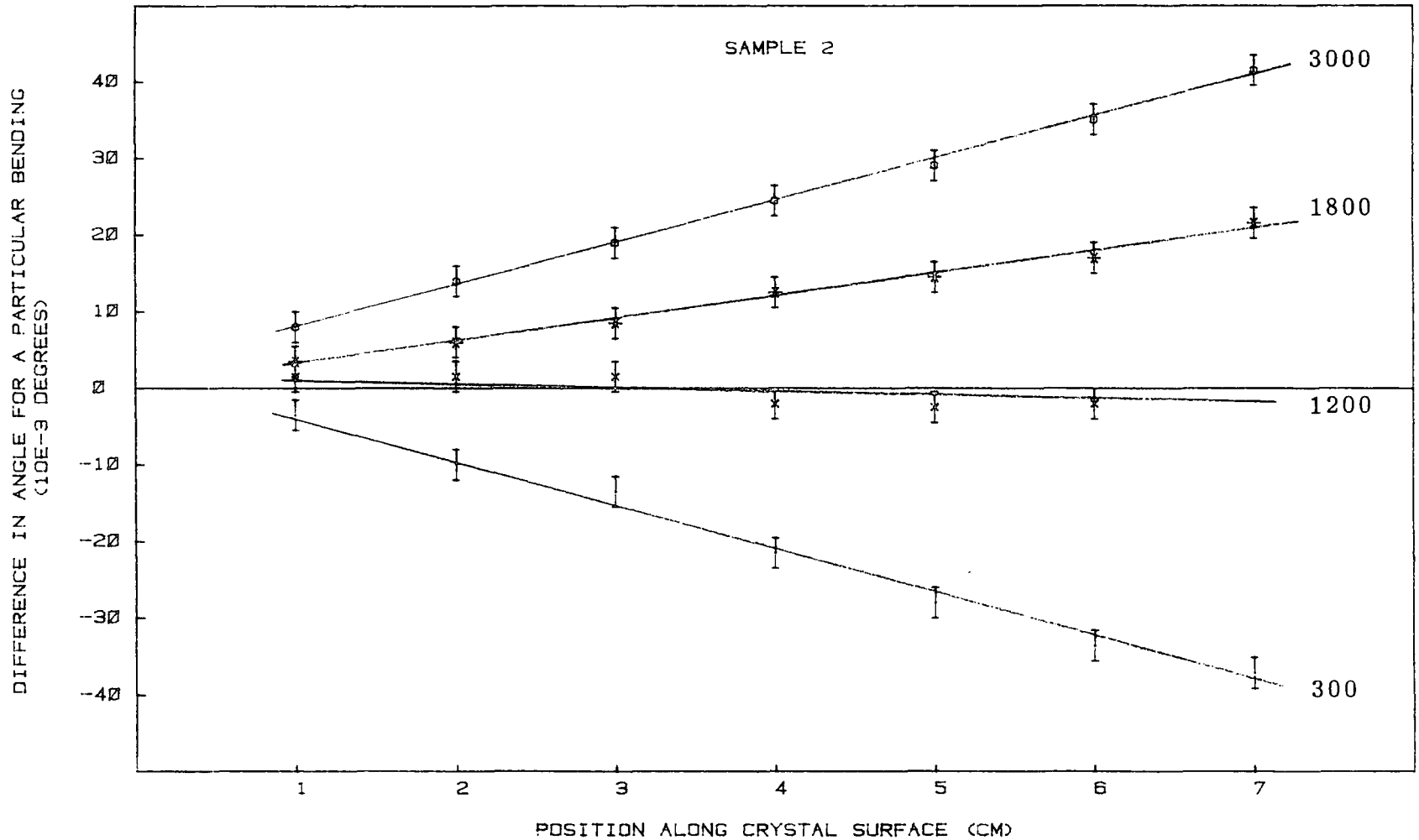

Fig. 7.18 (a) Variation of the angle β along the length of the Sample 2.

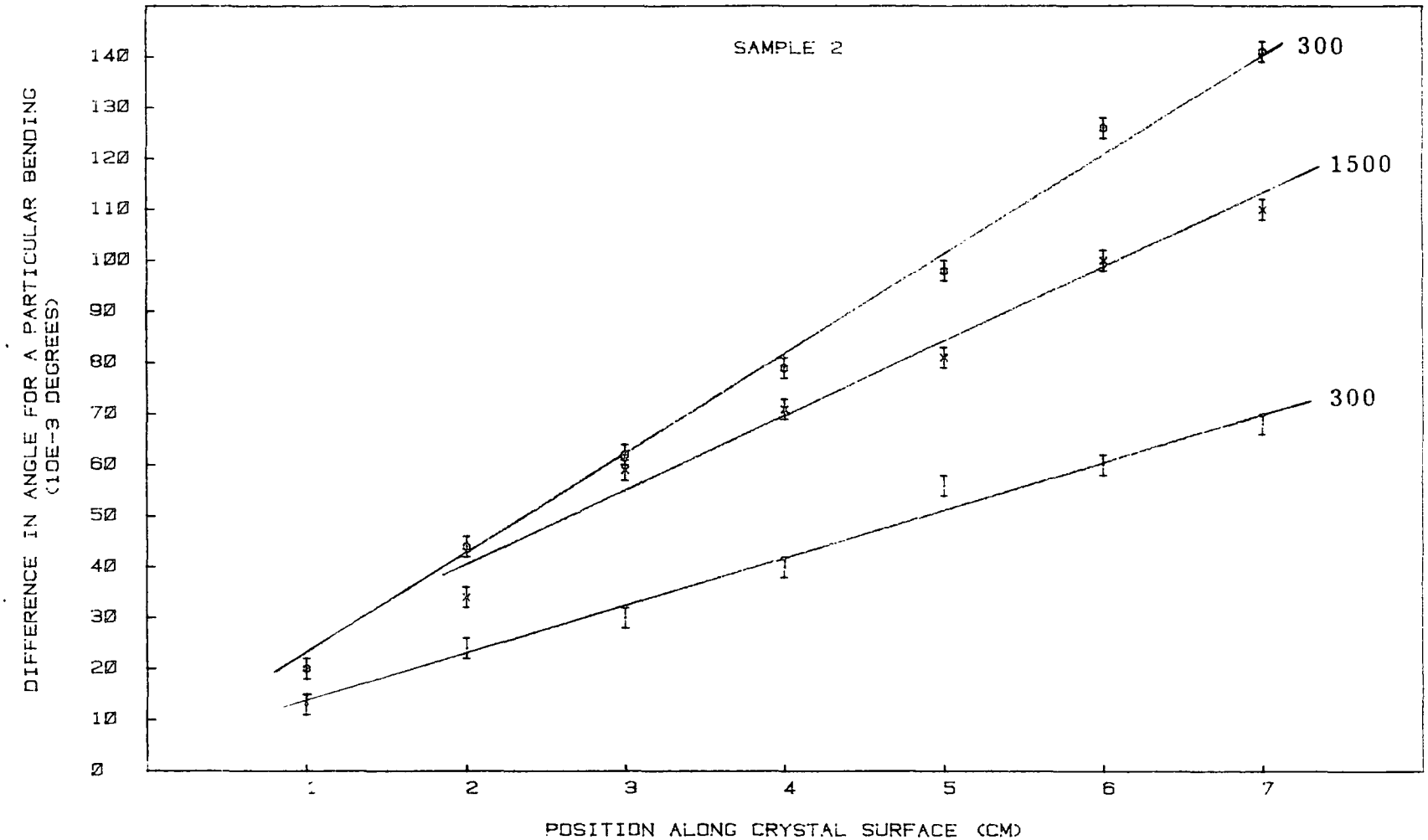

Fig. 7.18 (b) Variation of the angle β along the length of Sample 2 (remounted).

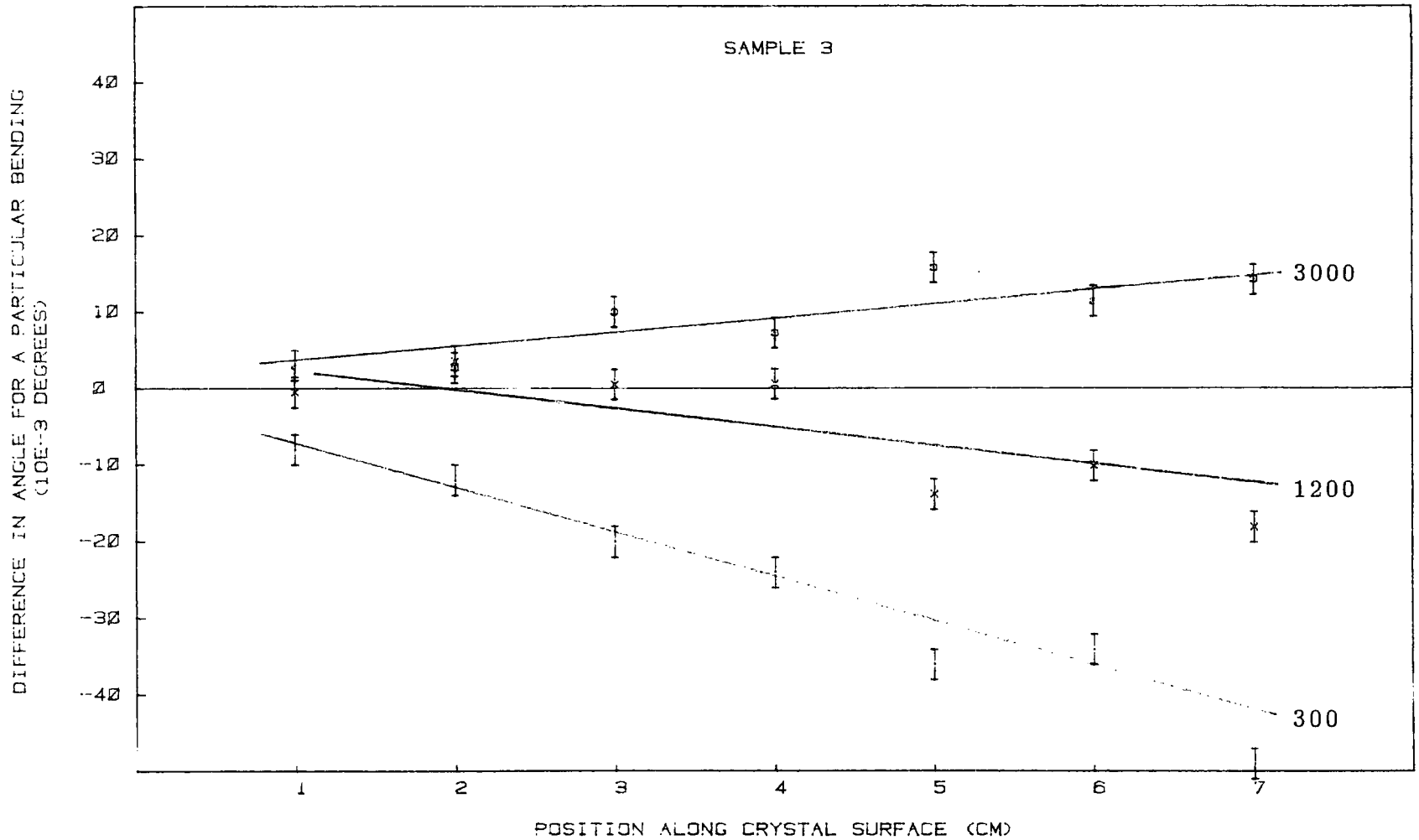

Fig. 7.18 (c) Variation of the angle β along the length of Sample 3.

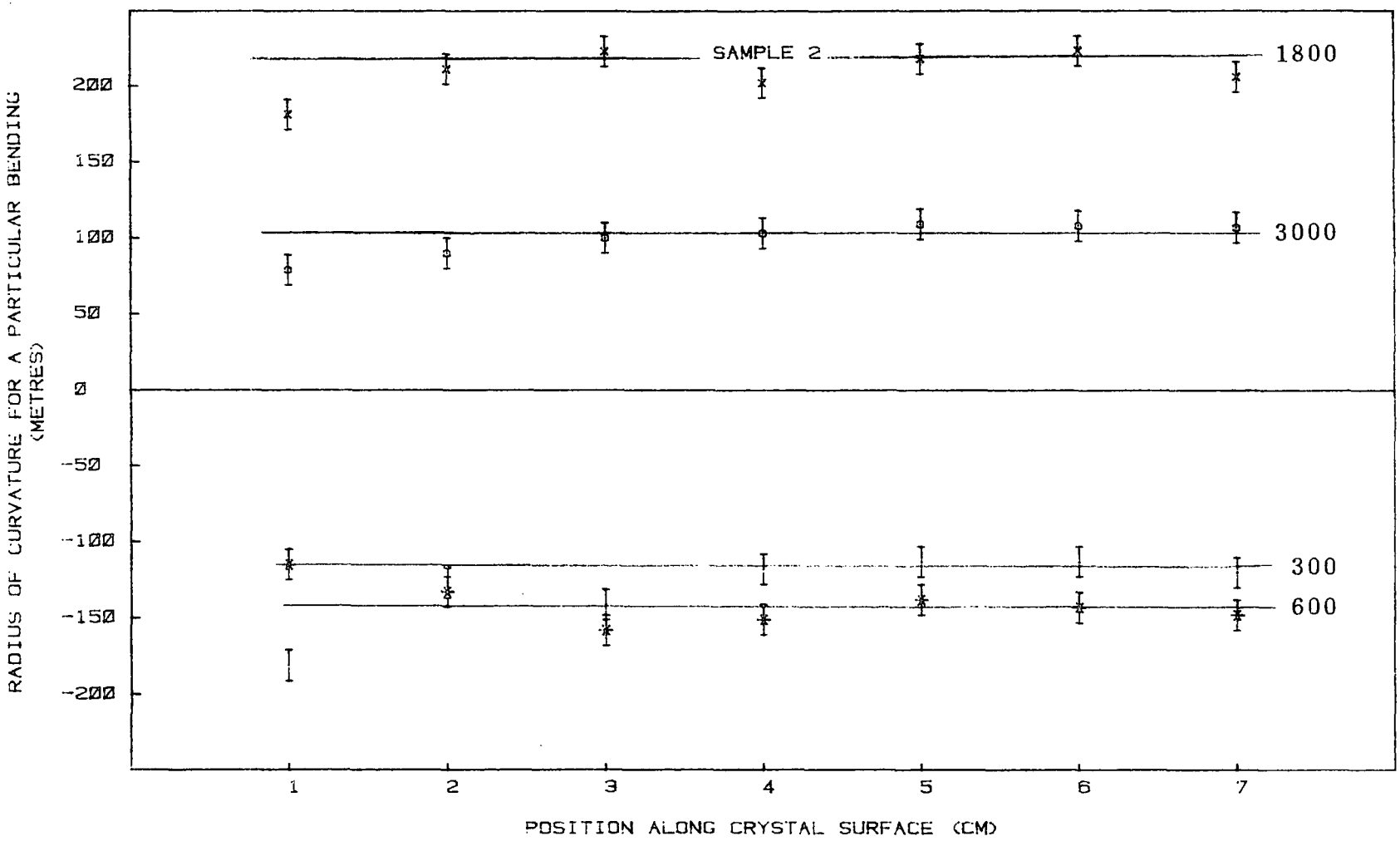

Fig. 7.19 (a) Variation of the radius of curvature R along the length of Sample 2.

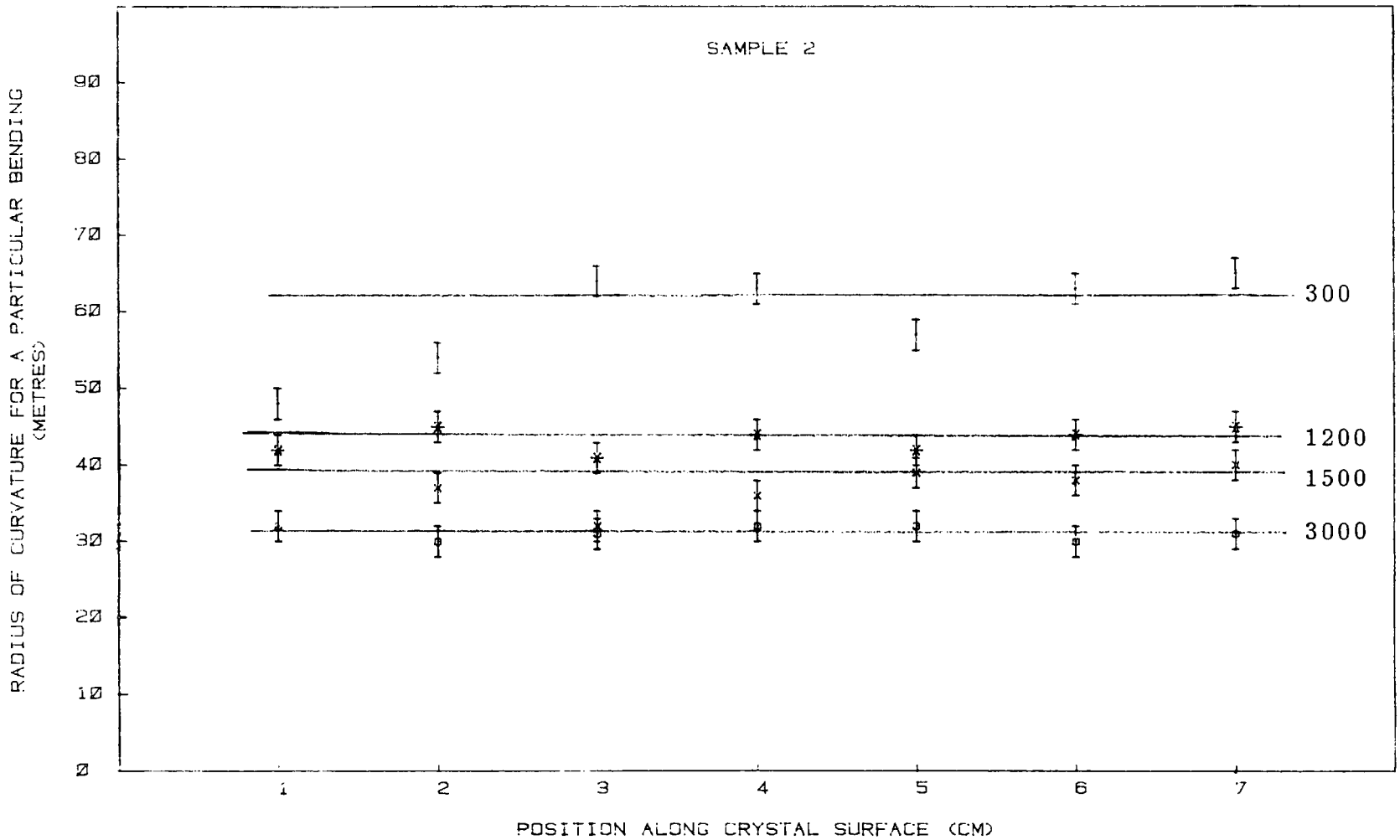

Fig. 7.19 (b) Variation of the radius of curvature R along the length of Sample 2 (remounted).

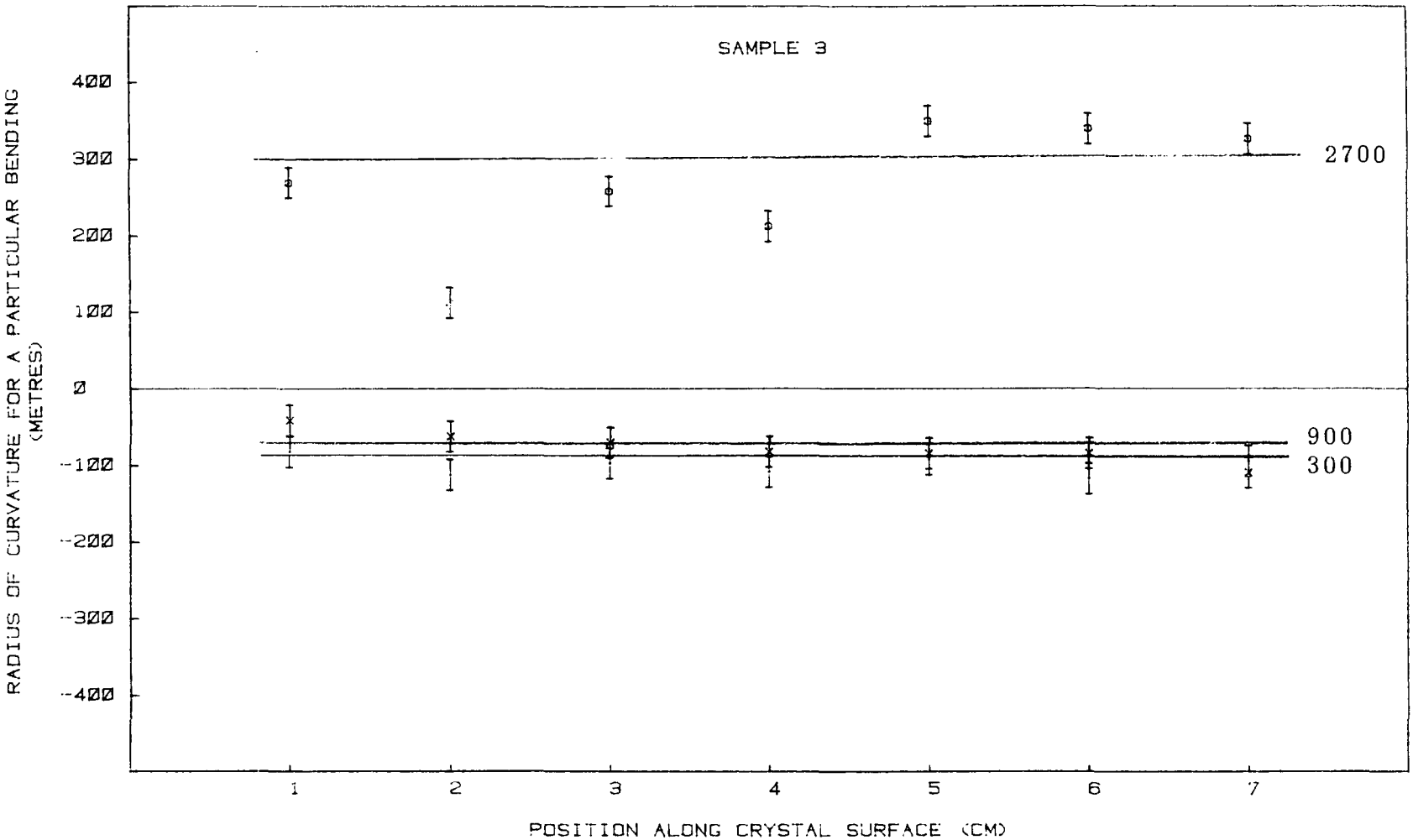

Fig. 7.19 (c) Variation of the radius of curvature R along the length of Sample 3.

Table 7.6 Tabulation of the radius of curvature for different bending steps.

A bending step of 3000 is equivalent to a 1mm displacement of the cam.

Bending Steps	Sample 2			Sample 2 (remounted)			Sample 3		
	Average	Graph 7.19a	Graph 7.20a	Average	Graph 7.19b	Graph 7.20b	Average	Graph 7.19c	Graph 7.20c
300	- 130 ± 45	- 101	- 115	59 ± 6	61	63	-100 ± 12	-108	-88
600	- 141 ± 15		- 142						
900							-76 ± 20		-67
1200	-1160 ± 500	-1375		43 ± 2		45	-930 ± 2000	-726	
1500				37 ± 3	39	40			
1800	209 ± 15		219						
2700							266 ± 85		300
3000	100 ± ±0	103	102	31 ± 1	29	32	292 ± 110	272	

(Table 7.6).

The graphs of R versus x for both samples (Figures 7.20 a,b,c) show an important feature. It is clear that graphs (Figure 7.20 a,b) for Sample 2 have different features. In Figure 7.20a, the radius of curvature takes negative values for a bending step between 300 to 1200 and it occurs again at about the same bending as the curvature is decreased to minimum. This feature does not occur in Figure 7.20b when the sample was remounted. The radius of curvature decreases as the crystal was bent to a maximum displacement of the cam which is 1mm. The graph in Figure 7.20a suggests that buckling of the crystal occurs and it is certainly due to improper mounting. The graph for Sample 3 (Figure 7.22c) also shows that buckling occurs. Therefore it is very important to note that the curvature along the crystal should be checked for each bending before it is used as a monochromator for further experiments. Nevertheless following careful mounting, experiments carried out at the Protein Crystallography Station using these monochromators give excellent results and no problem in focussing the monochromator has so far been encountered (Helliwell et al. 1981).

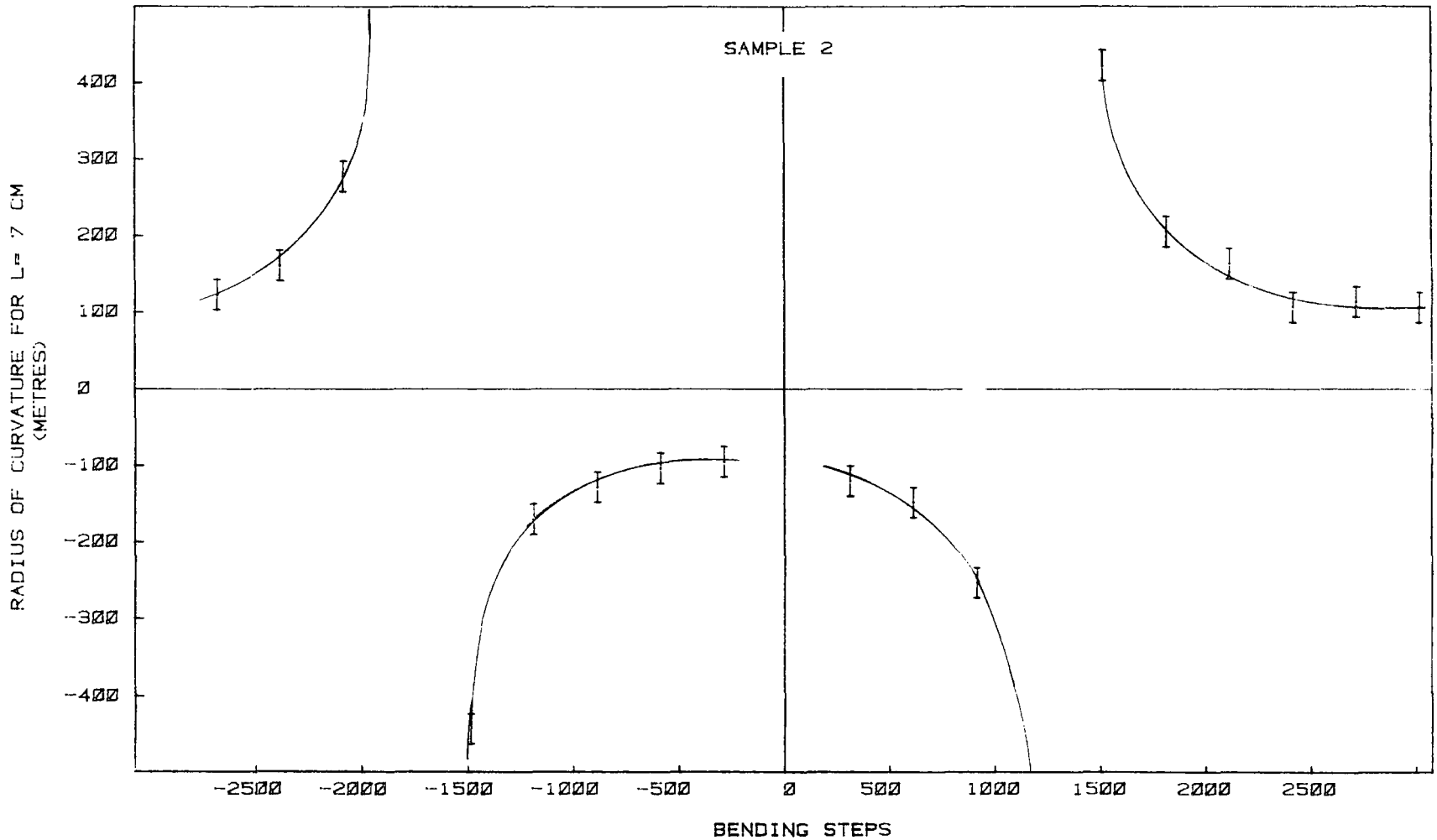

Fig. 7.20 (a) Variation of the radius of curvature as Sample 2 was bent.

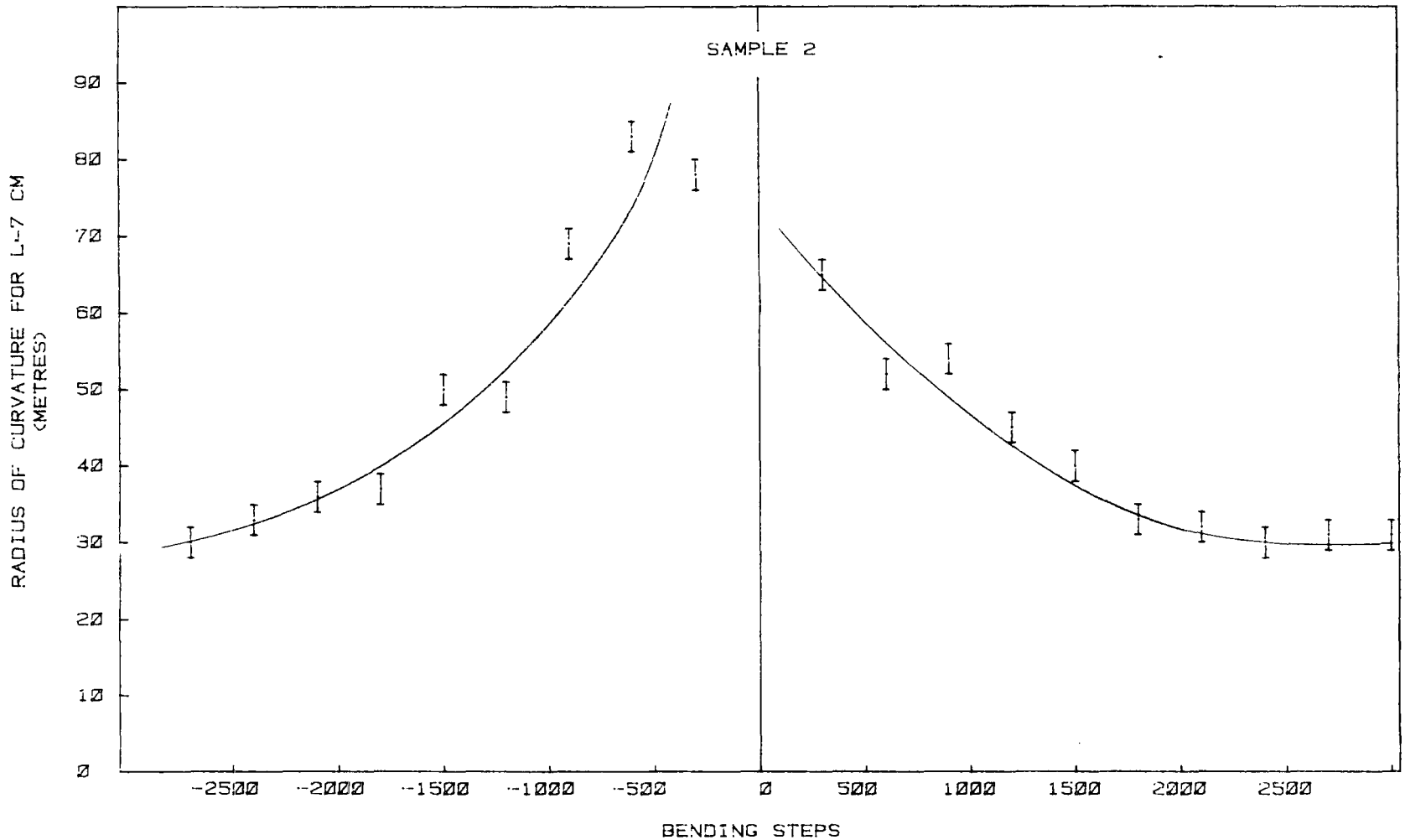

Fig. 7.20 (b) Variation of the radius of curvature as Sample 2 (remounted) was bent.

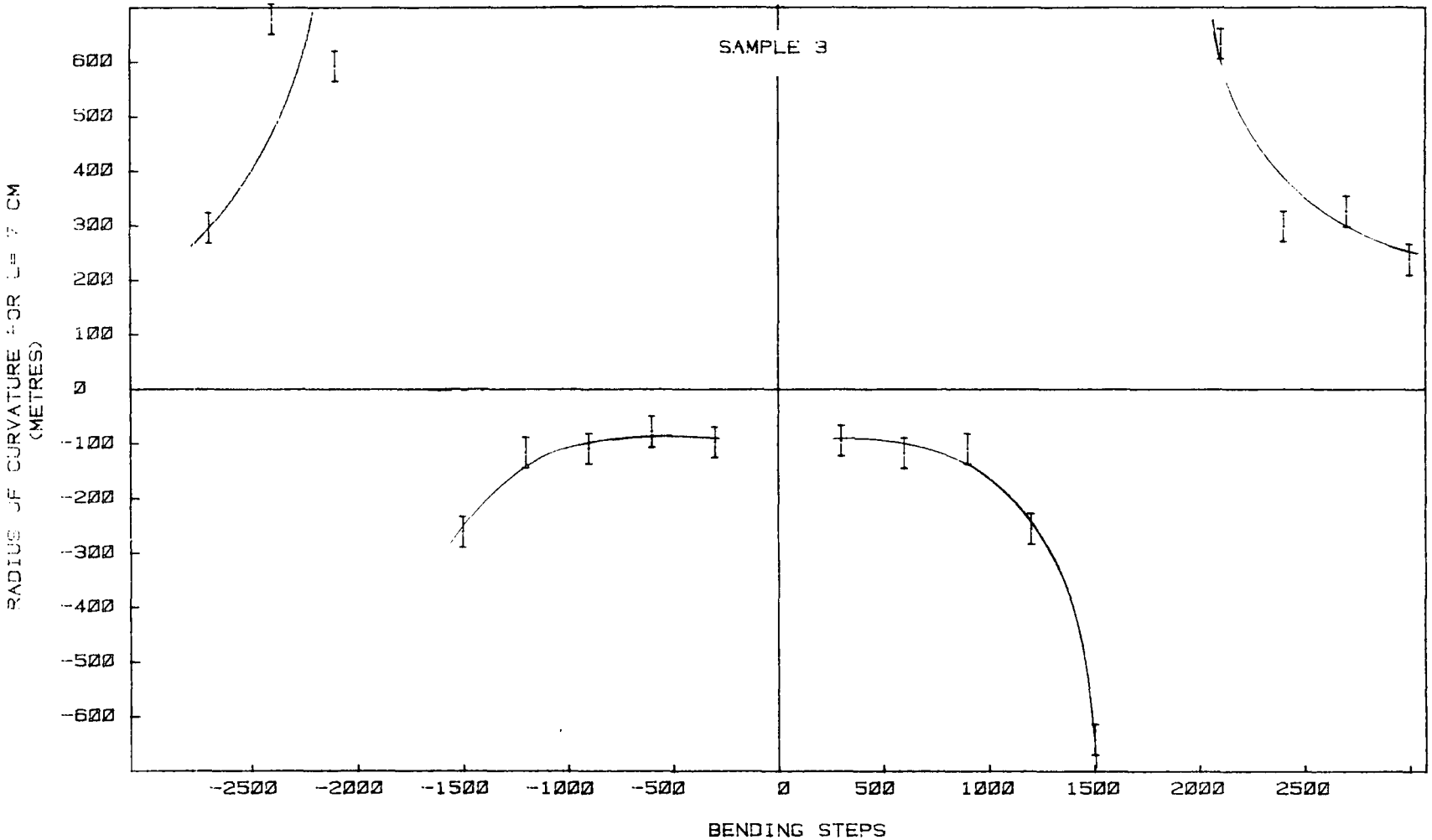

Fig. 7.20 (c) Variation of the radius of curvature as Sample 3 was bent.

CHAPTER 8

PILOT EXPERIMENTS ON THE DOUBLE CRYSTAL DIFFRACTOMETER AT THE INTERFEROMETRY STATION AT DARESBURY LABORATORY

8.1 Introduction

Pilot experiments were carried out using the double crystal diffractometer at the Interferometry Station and the synchrotron radiation source at Daresbury. The effect of applied magnetic field on hematite crystals and the dislocations present in indium phosphide and gallium arsenide crystals were studied.

8.2 Double Crystal Rocking Curve Analysis of Hematite Crystal Under an Applied Magnetic Fields.

The magnetic structure of hematite (α-Fe_2O_3) has been investigated by neutron diffraction (Shull, Strauser and Wollan 1951). It exhibits antiferromagnetic ordering along the trigonal axis where the spins are almost in a plane perpendicular to the axis. The small rotation of the spin about the trigonal axis results in a weak magnetic moment parallel to the two fold axis in the basal plane thus giving rise to a weak ferromagnetic behaviour. Domain structure in α-Fe_2O_3 have been observed indirectly by neutron diffraction (Nathans et al. 1964) and directly by X-ray topography (Labushkin et al. 1978 and Clark et al. 1982) in single crystal experiments. Clark et al. (1982) observed large area basal plane walls in thin flux grown platelets of

α-Fe_2O_3. The ratio of the uniaxial anisotropy field to the magnetization is favourable for the formation of in-plane Bloch walls. An X-ray sensitive imaging system was used to observe domain wall movement under the application of a weak field perpendicular to the two fold axis. The existence of the in-plane wall was confirmed by applying a field parallel to the two fold axis and a gradual change in diffracted intensity was observed which is reversible. The present experiments were aimed at detecting any magnetostrictive distortion between these domains and examining any changes in rocking curve structure under application of an in-plane magnetic field.

8.2.1 Experimental Procedure

The hematite crystals were grown at the Clarendon Laboratory, Oxford some years ago from a PbO/PbF_2 flux. The crystals are about 100 μm thick and a few square centimeters in area and are basal plane platelets. The crystals used by Clark et al. (1982) are from the same source.

A decent double crystal topograph was not successfully obtained as the background intensity was too high. The effect of magnetic field on the double crystal rocking curve was investigated using both the synchrotron radiation and a conventional X-ray source. The hematite crystal was orientated for the $30\bar{3}0$ reflection in the transmission geometry and the reference crystal was the 422 reflection from a LOPEX silicon. Fields up to 185 Gauss were applied to the hematite crystal parallel to the crystal surface that is

parallel to the two fold axis.

An absorption experiment was also carried out using a device grade silicon crystal orientated for the 111 reflection as the reference crystal. The beam reflected from the silicon crystal reached the hematite platelets placed on the second diffractometer axis perpendicular to the reflected beam. The intensity transmitted through it was recorded on a 25 μm Nuclear Emulsion plate placed behind and very close to the crystal. The experiment was repeated for X-ray wavelengths approaching and beyond that of the Fe absorption edge which is 1.743Å by varying the 2θ angle of the diffractometer turntable. Typical exposure times were about 30 minutes at 1.9 GeV 100 mA before the absorption edge wavelength and about 10 minutes when beyond the absorption edge.

8.2.2 Discussion of Results

Figure 8.1a is a zero field double crystal rocking curve for a hematite crystal at a wavelength of about 1.8Å, that is beyond the absorption edge of Fe and taken using the synchrotron radiation source. As a variable magnetic field was not available at this stage of the experiment a permanent bar magnet whose field was measured to be about 100 Gauss, was applied parallel to the two fold axis. A splitting of the rocking curve was obtained (Figure 8.1b) which corresponds to two domains in the crystal separated by about 76 arc seconds. This result prompted the experiment of applying variable magnetic fields on the sample to be carried out. A pair of coils which have a maximum field of up to 250 Gauss was built for the purpose. Using the same

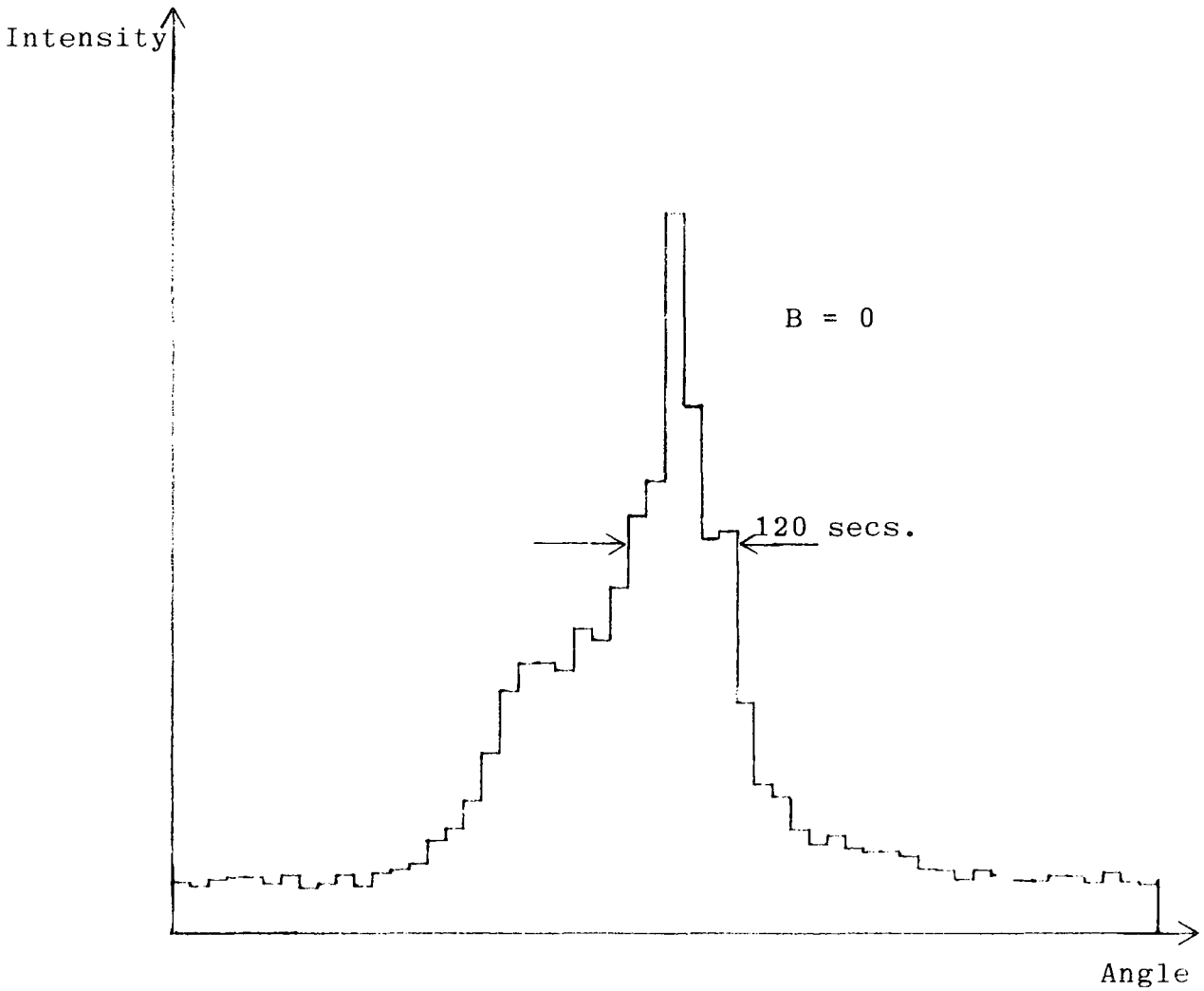

Fig. 8.1 (a)

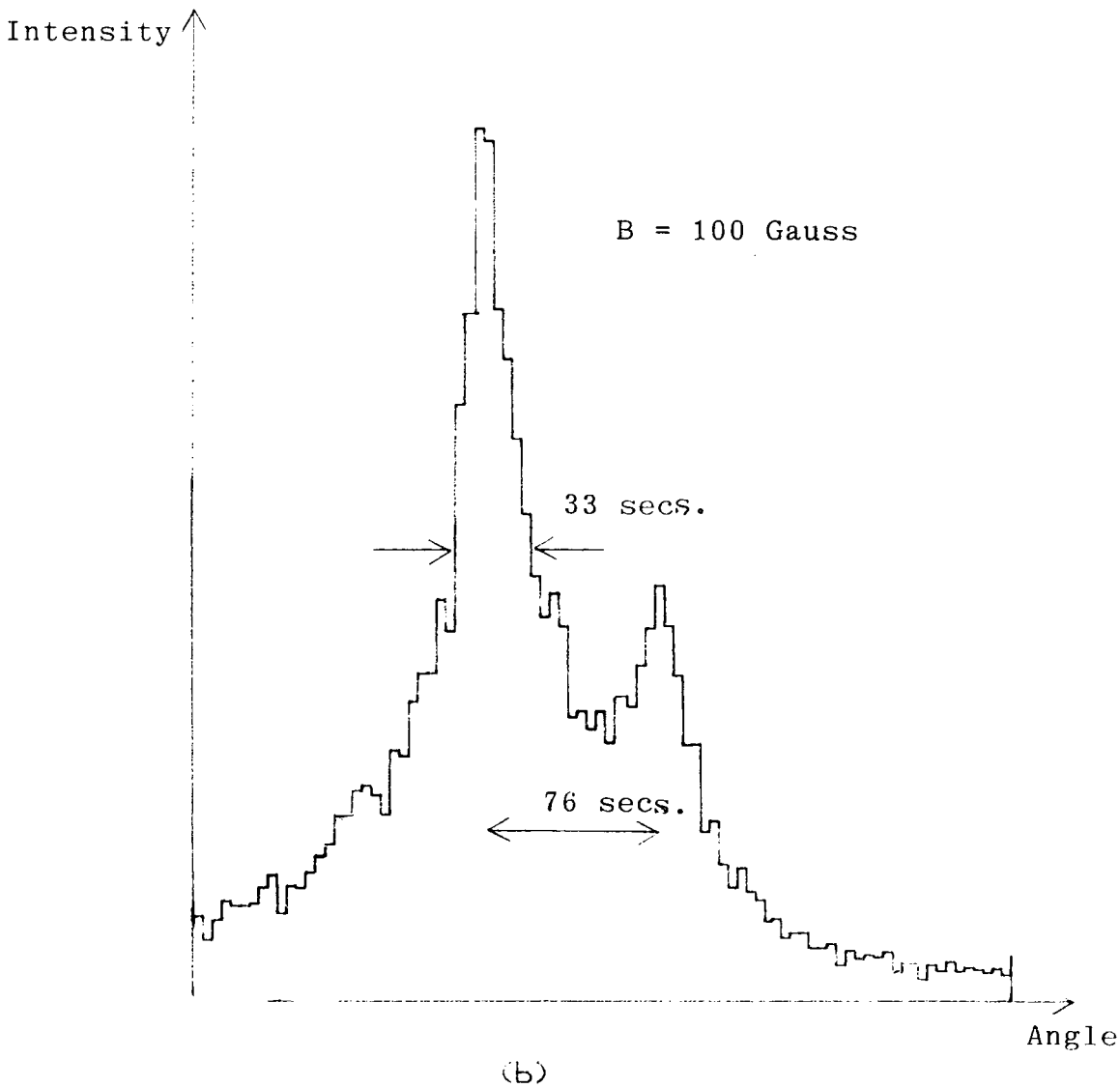

Fig. 8.1 Double crystal rocking curves of a hematite crystal at
(a) B=0
(b) B=100 Gauss

hematite crystal as the one above, a series of rocking curves (Figures 8.2 a-h) was obtained using the EGG and a conventional source for fields up to 60 Gauss only as the crystal was accidentally broken. The zero field rocking curve (Figure 8.2a) shows that only one domain exists with a FWHM of about 47 arc seconds. No significant changes occur up to a field of about 42 Gauss when splitting occurs (Figure 8.2e). Rocking curves obtained at a field of 50 Gauss show three domains present separated by about 25 arc seconds (Figure 8.2f). The plot was repeated but the field fluctuates by about ± 2 Gauss due to the coil heating up. The rocking curve (Figure 8.2g) shows quite a number of peaks (about 8) which suggests that the domains structure are extremely unstable. To confirm that splitting does not exist at zero field, the zero field curve (Figure 8.2a) was compared to the curve at 60 Gauss plotted with the same step size (Figure 8.2h) and the zero field curve was replotted at a higher sensitivity. Figure 8.2h shows that the splitting was obvious even at a lower sensitivity step size and the zero field plot at higher sensitivity shows that only one domain exists at zero field.

The experiment was repeated several times with different hematite crystals using the conventional X-ray source as well as synchrotron radiation. In some cases including the one carried out at Daresbury, no splitting was obtained. In two cases, results similar to the one discussed above were obtained that is multiple domains were formed which were extremely unstable. In the first case the crystal was part of the crystal used previously. The zero field rocking curve

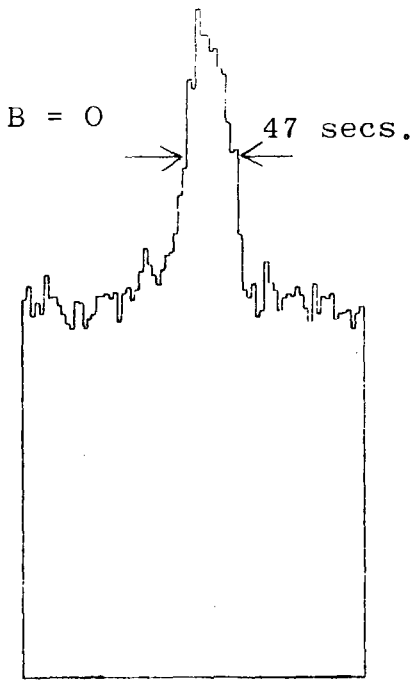

Fig. 8.2 (a)

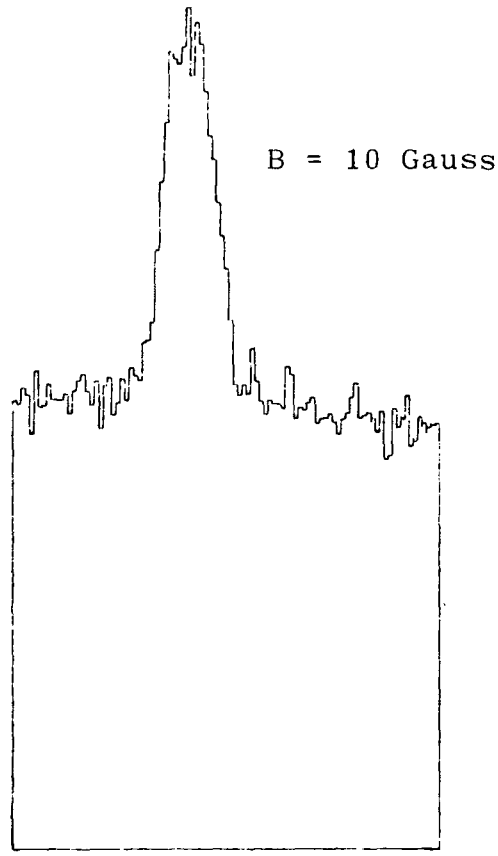

Fig. 8.2 (b)

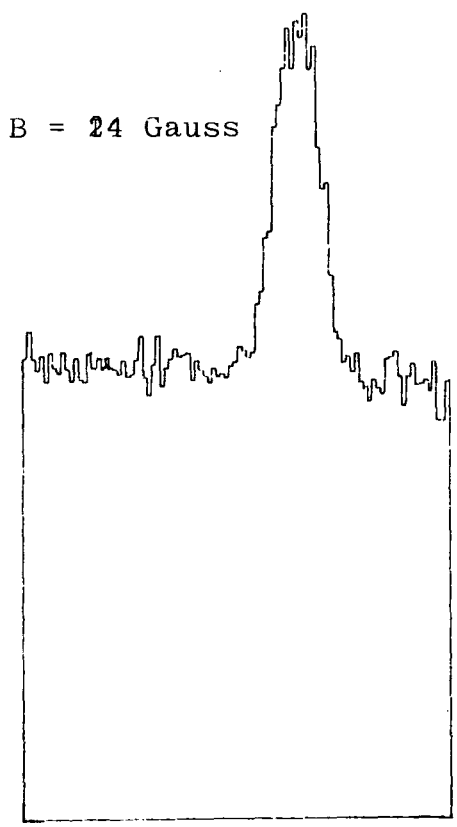

Fig. 8.2 (c)

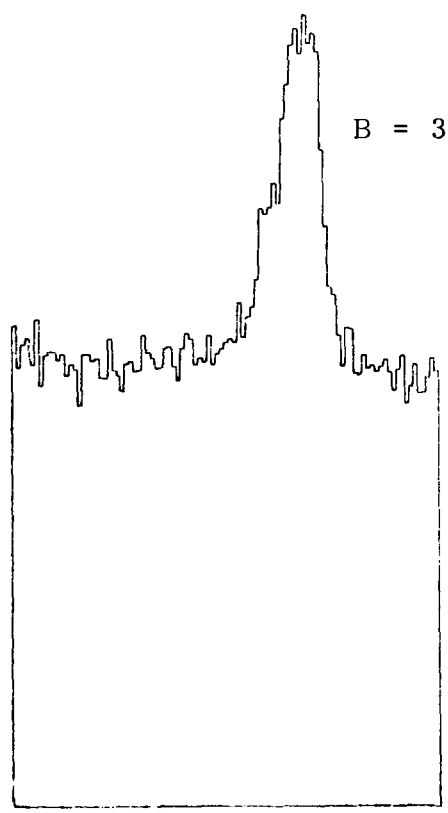

Fig. 8.2 (d)

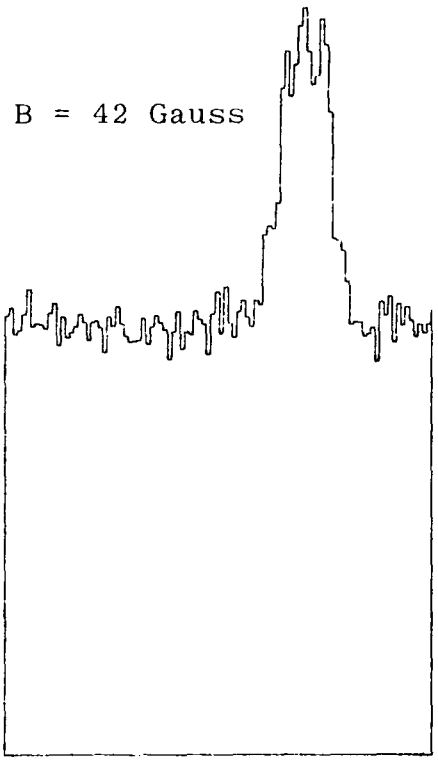

Fig. 8.2 (e)

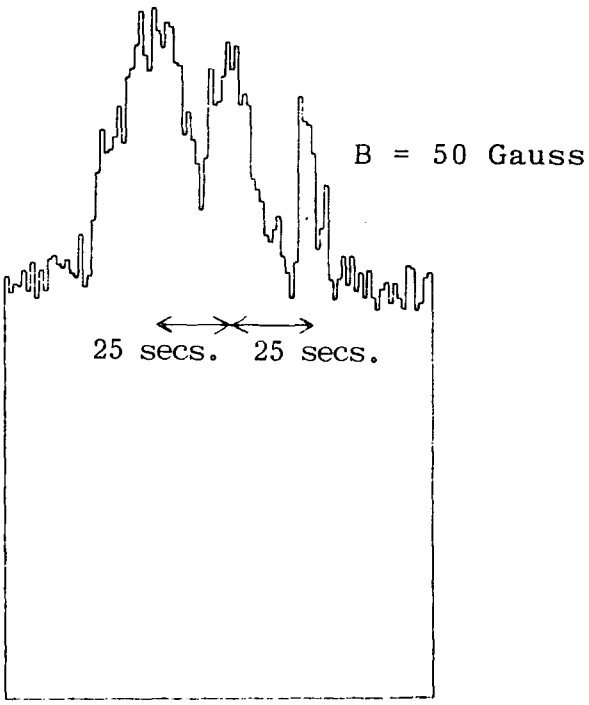

Fig. 8.2 (f)

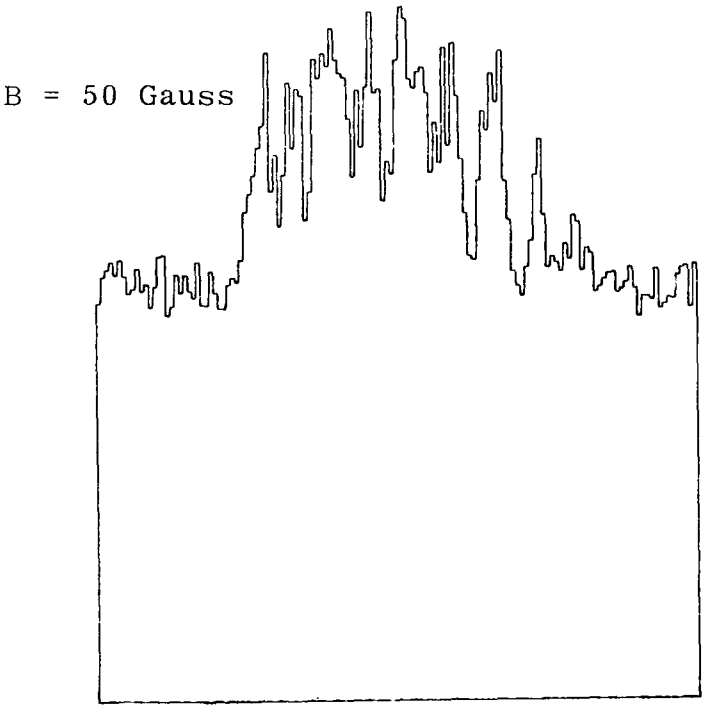

Fig. 8.2 (g)

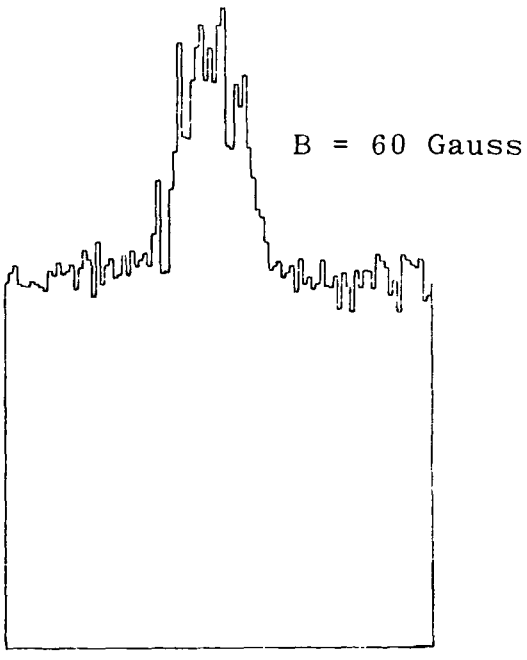

Fig. 8.2 (h)

Fig. 8.2 Double crystal rocking curves of a hematite crystal at different magnetic fields.

(Figure 8.3a) is about 90 arc seconds at FWHM with a kink at the peak which suggests that a domain boundary may exist. The domain boundary becomes dominant as the field was increased up to 21 Gauss (Figures 8.3b and c). As the field was increased further to 30 Gauss and up to the maximum of about 57 Gauss for this particular coil, multiple splitting again takes place which was non-reproducible for the same field setting. The curve identical to Figure 8.6a was obtained when the field was reduced back to zero.

In the second case two well defined domains separated by about 140 arc seconds were obtained at zero field for a different hematite crystal (Figure 8.4a). This suggests that there are two well defined magnetostrictive distortions in the two domains. At a field of 150 Gauss three well defined domains were obtained separated by about 100 and 110 arc seconds respectively (Figure 8.4c). The three peaks were not reproducible (Figure 8.4d). The splitting obtained as the field was increased up to 185 Gauss does not follow a systematic change (Figures 8.4 c-f). No splitting of the rocking curves was obtained when the experiment was repeated by first increasing the field quickly up to a maximum and then obtain rocking curves as the field was decreased to zero. In both cases where splitting occurs and does not occur the integrated intensity increased with field and was reversible, which confirms the existence of in-plane wall.

Single crystal X-ray diffractometry on very high magnetostriction rare earth element terbium (Clark, Tanner, Farrant and Jones 1982) also show well resolved splitting associated with the magnetic domains when the sample was

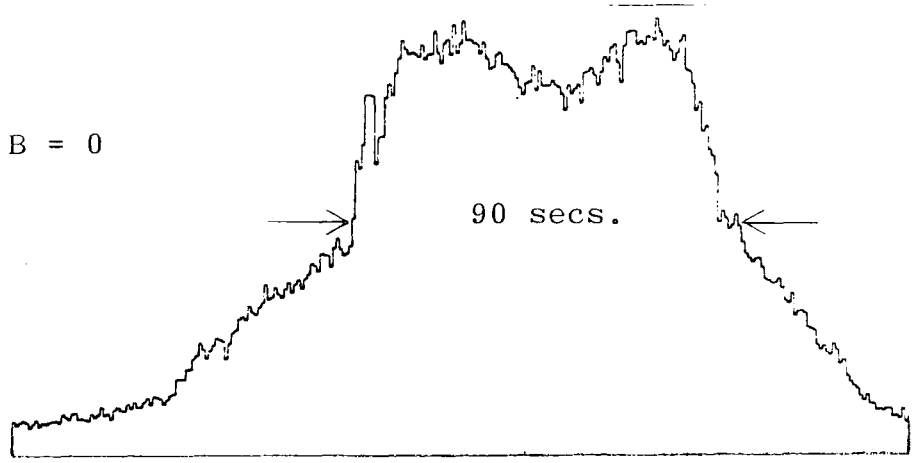

Fig. 8.3 (a)

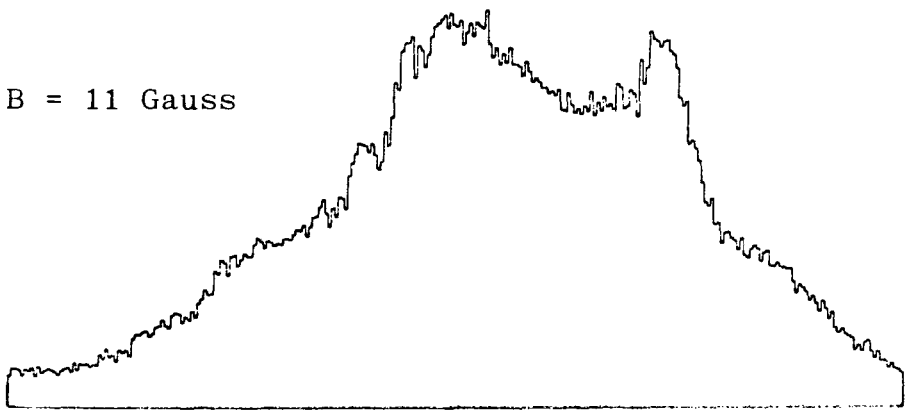

Fig. 8.3 (b)

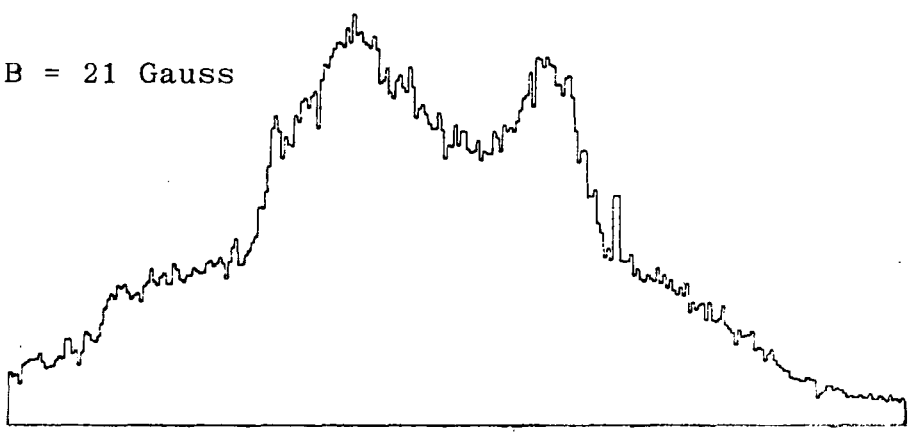

Fig. 8.3 (c)

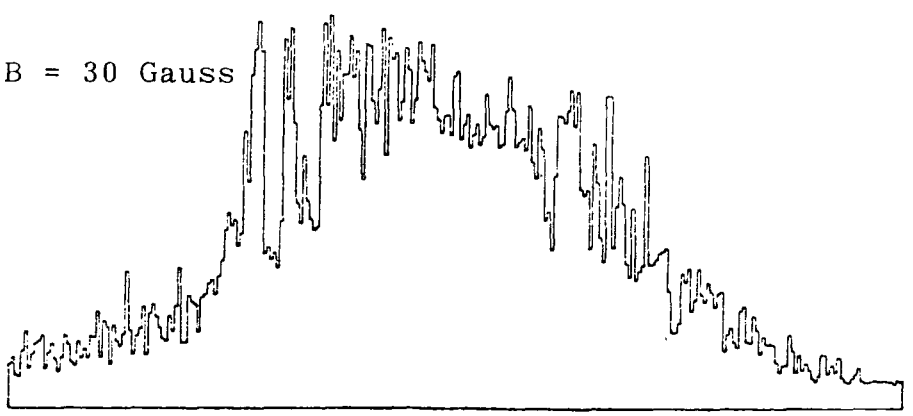

Fig. 8.3 (d)

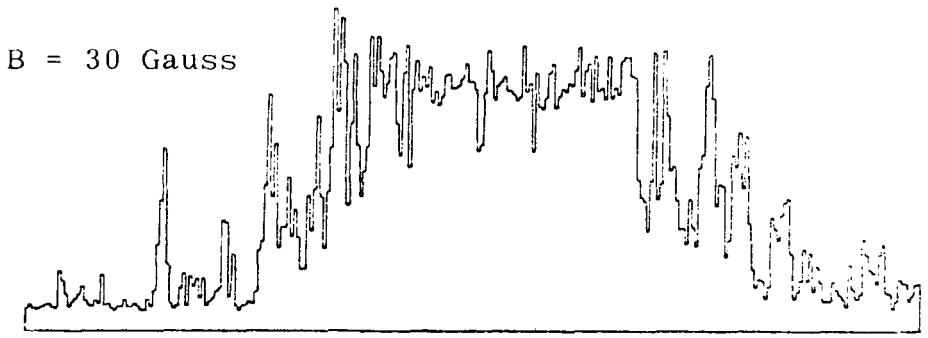

Fig. 8.3 (e)

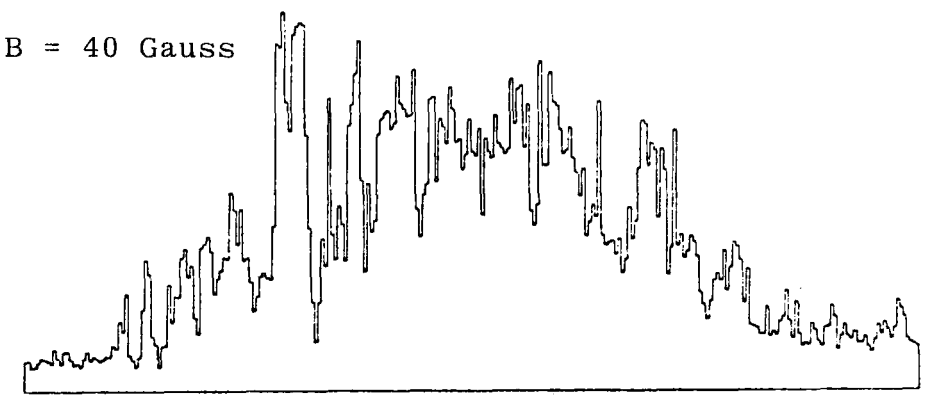

Fig. 8.3 (f)

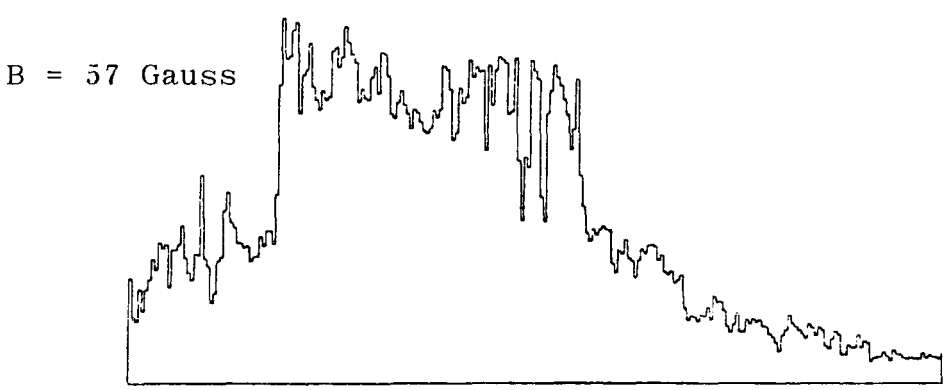

Fig. 8.3 (g)

Fig. 8.3 Double crystal rocking curves of a hematite crystal at different magnetic fields.

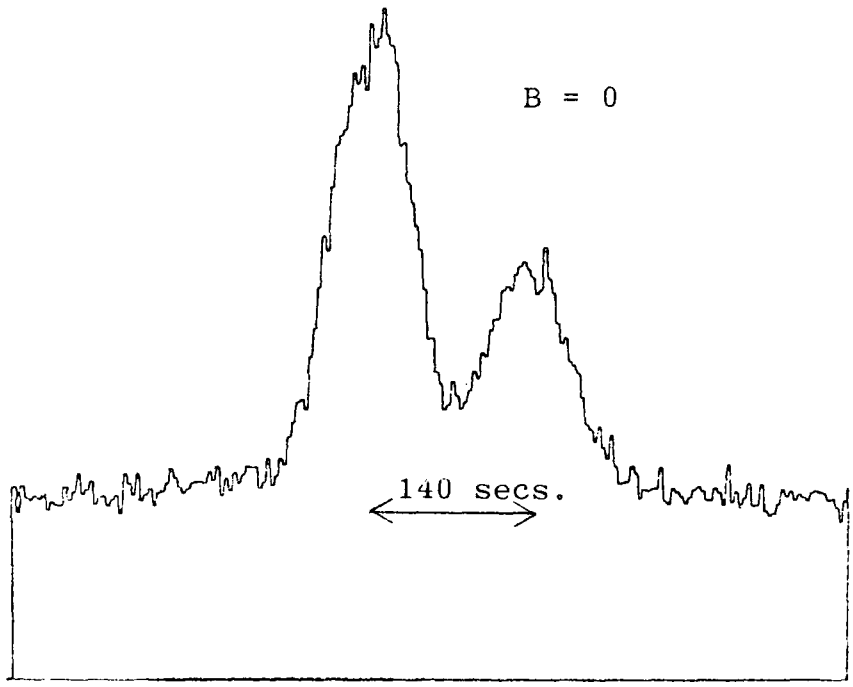

Fig. 8.4(a)

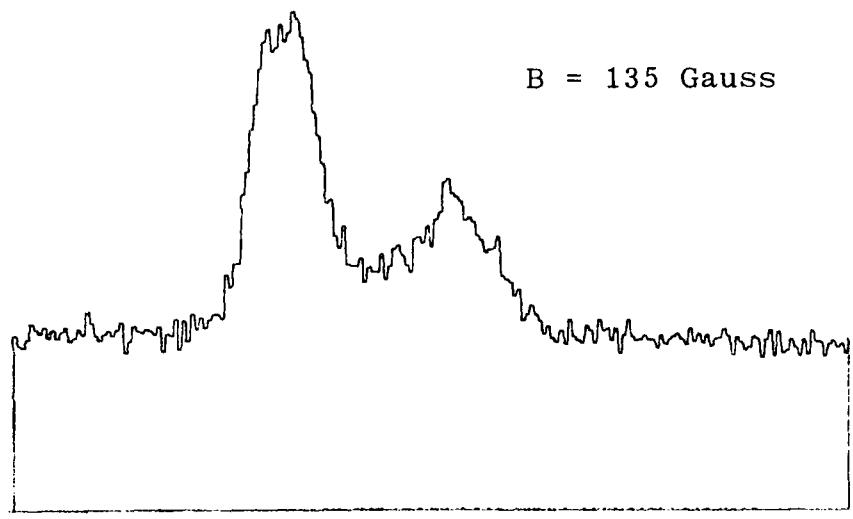

Fig. 8.4(b)

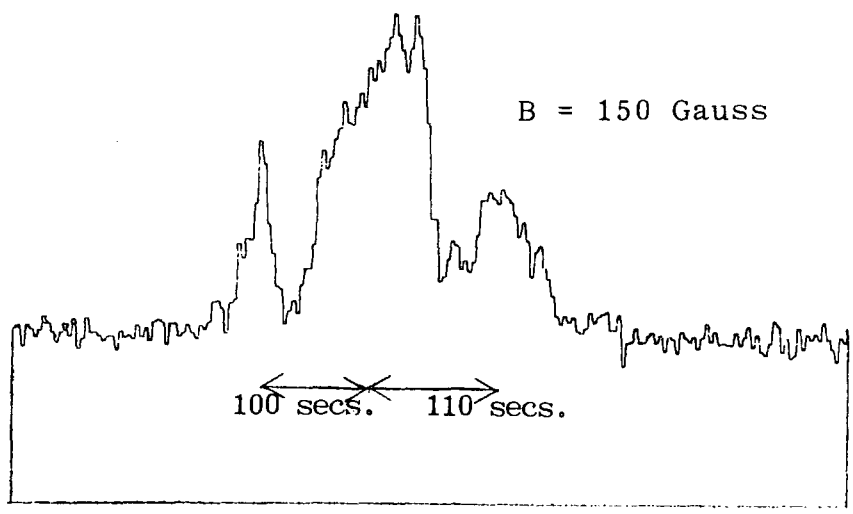

Fig. 8.4(c)

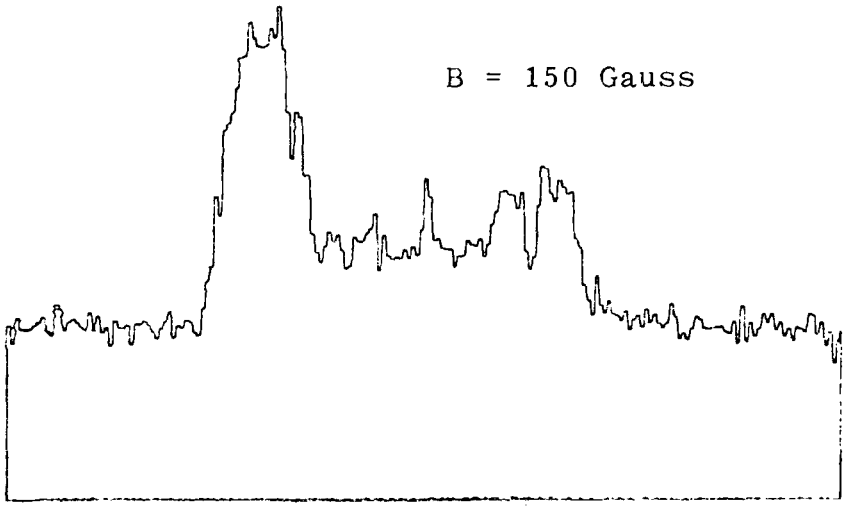

Fig. 8.4(d)

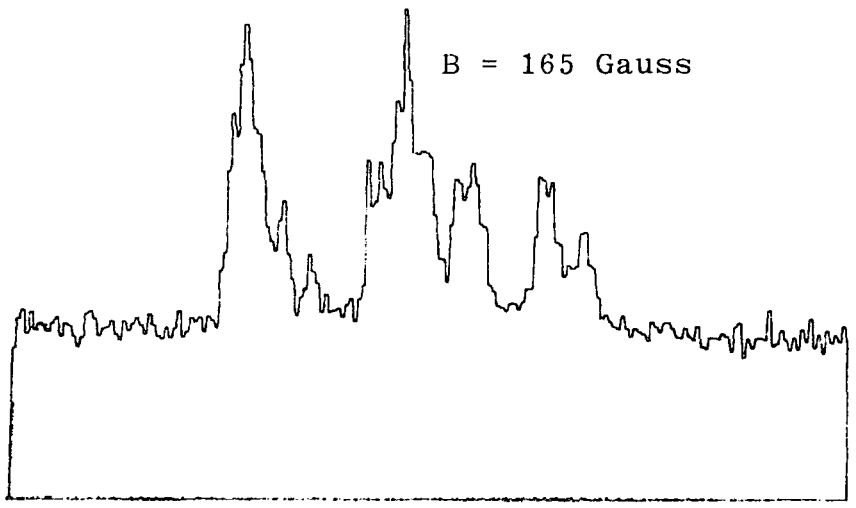

Fig. 8.4(e)

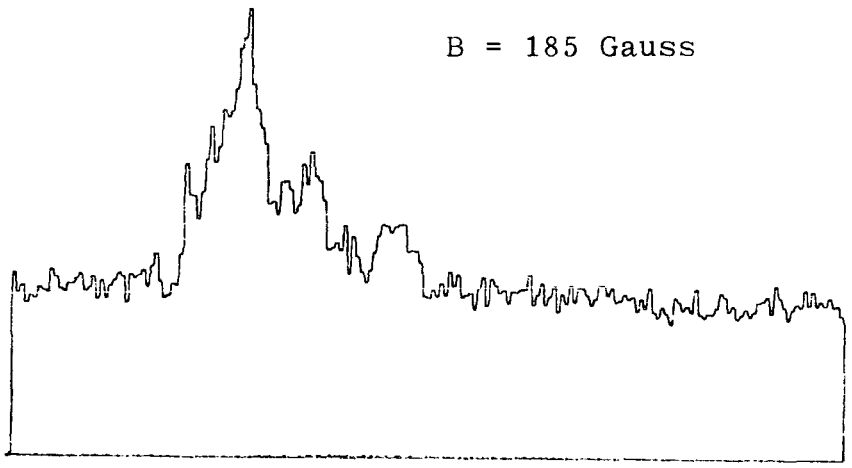

Fig. 8.4(f)

Fig. 8.4 Double crystal rocking curves of a hematite crystal at different magnetic fields.

cooled rapidly through the Curie temperature. However, slow cooling through the Curie temperature only produced broadening of the rocking curve but no individual domain peaks obtained. The above results on hematite crystals in applied field is not well understood. The zero field domains exhibits a complex and non-systematic behaviour at a field when the splitting occurs and were extremely unstable.

Figures 8.5a and b are the absorption photographs of a hematite crystal taken at X-ray wavelengths approaching and beyond the absorption edge of Fe (λ = 1.743Å). In both photographs the twin boundary A is dominant. As we pass across the absorption edge the lines B get fainter and almost disappear (Figure 8.5b). White spots appear along the twin boundary and regions C corresponding to total absorption of the Fe atoms which suggest that the twin boundary is iron rich. Absorption radiography can be done at 1 μm resolution with a large increase in sensitivity above the absorption edge.

8.3 Double Crystal Topographs of Indium Phosphide and Gallium Arsenide Single Crystals

Double crystal topography have been used to image defects in the surface of crystals (Bonse 1962) and to image very low levels of strains (Kohra et al. 1977). Due to its non-destructive nature, the technique is very useful in defect studies of materials such as indium phosphide and gallium arsenide which are extensively used as substrate materials for composite layer devices, for example, transferred electron oscillators, field effect transistors and hetero-

structural lasers. The evaluation of surface finish prior to epitaxy (Jones et al. 1980) and the correlation between features produced by chemical etching and the dislocation lines in X-ray double crystal topographs (Brown et al. 1981) are useful means of assessment of the nature and distribution of defects.

8.3.1 Experimental Procedure

Double crystal topographs of InP and GaAs substrate wafers were obtained using the (+,-) setting. The InP was grown by the Czochralski liquid encapsulation method. Both crystals were grown at the Royal Signals and Radar Establishment, Malvern. The reference crystal was a perfect silicon crystal with zero dislocation density and low in carbon and oxygen and was grown by the float zone technique. It is in the form of a cylinder 10 mm thick and 25 mm in diameter. The (111) surface was syton polished and etched chemically to provide a strain damage free surface (Jones et al. 1980). An asymmetric 422 reflection whose plane is at an angle of 19.5 degrees to the surface was used as the exploring beam where a wider area of the sample could be imaged ($b<1$). Topographs of 422 and 440 reflections of indium phosphide doped with germanium (Sample 886 InP, Ge doped) and the 440 reflection of gallium arsenide (Sample 280R) were taken. Both samples had a (111) surface. The 422 reflection topographs of InP were taken at four different positions on the flank of the rocking curve (Figure 8.6). The 440 reflection topograph of InP and GaAs were taken for the three

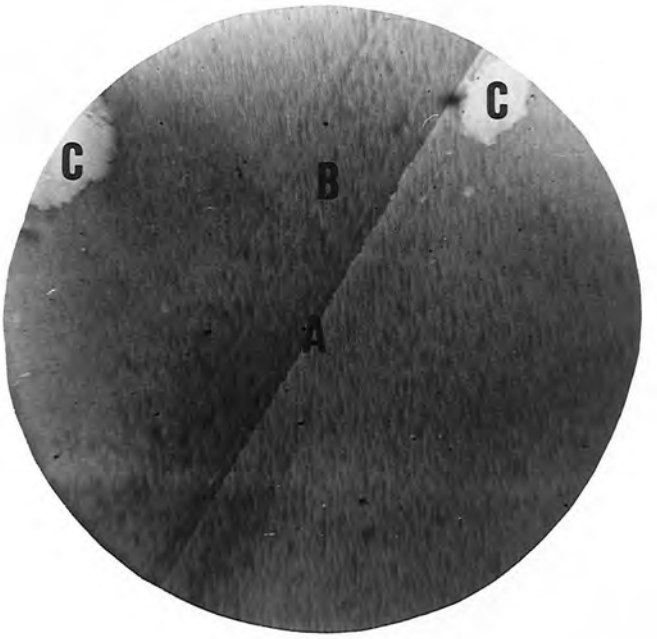

(a)

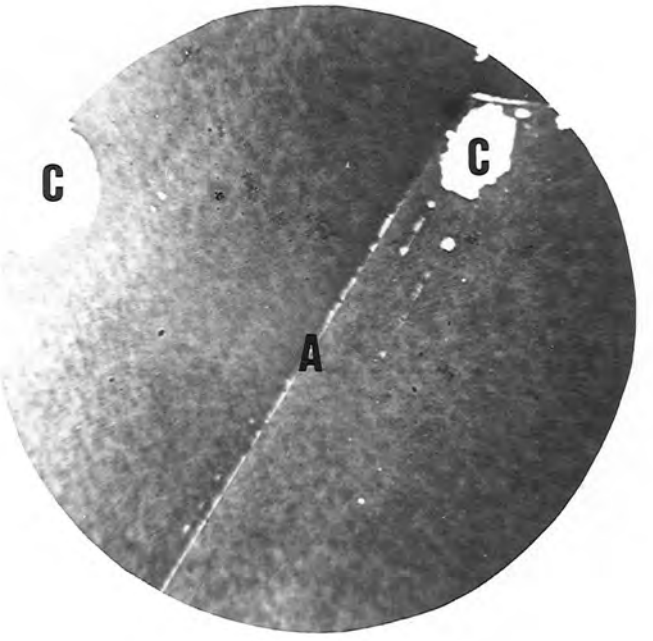

90 µm

(b)

Fig. 8.5 Absorption photographs of a hematite crystal (a) approaching and (b) beyond the absorption edge of Fe (λ=1.743Å).

{440} planes by rotating the crystal by 120° about the normal to the (111) surface. Typical exposure times were about 20-30 minutes at 1.9 GeV 90 mA using a 25 μm Nuclear Emulsion plate.

The wavelength used was 1.5Å and is fixed by the $2\theta_B$ angle of the diffractometer turntable. In setting up for the double reflection, transmission Laue photographs were taken by placing Polaroid films behind the second crystal to ensure that the diffracted beam from the first crystal was reaching the second crystal. An image intensifier placed at an angular distance of $2\theta_B$ from the direct beam was used to detect the doubly diffracted beam and a TV monitor was used to observe the image as the second crystal was rotated through the Bragg peak. A scintillation detector was used in the latter part of the experiment as the image intensifier was not available. The image intensifier has the advantage that the doubly diffracted beam can be found much quicker as the second crystal can be scanned at the fastest possible speed allowed by the software and the TV monitor observed for the image to appear. If using a scintillation detector the step count mode must be used.

8.3.2 Discussion of Results

Figure 8.7 is the double crystal topograph of the 422 reflection from InP taken at position S on the flank of the rocking curve (Fiugre 8.6). The difference in contrast suggests that the crystal is bent. The topographs of Figures 8.8 a-d are a magnification of region X of Figure 8.7

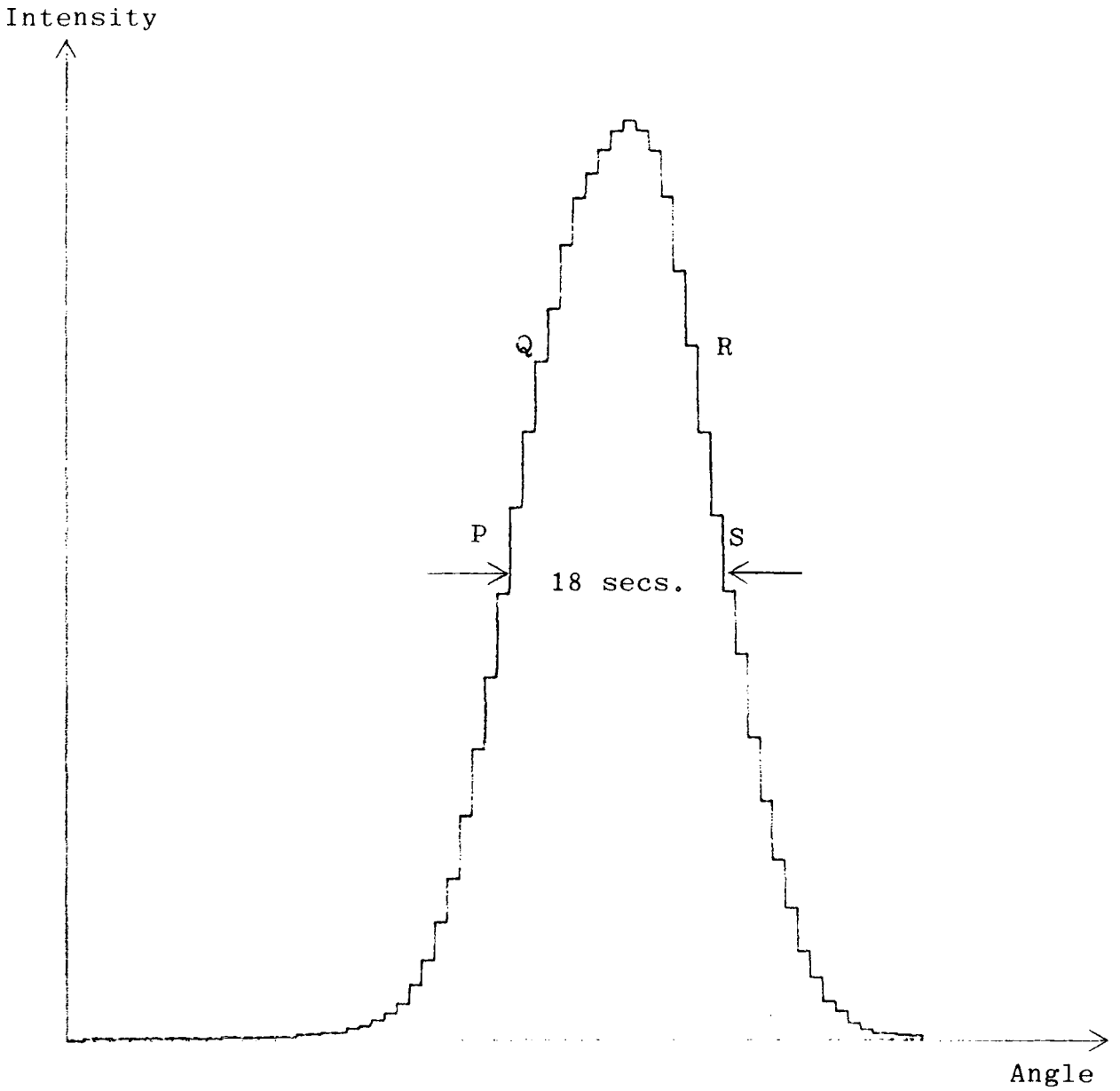

Fig 8.6 422 double crystal rocking curve of an indium phosphide crystal.

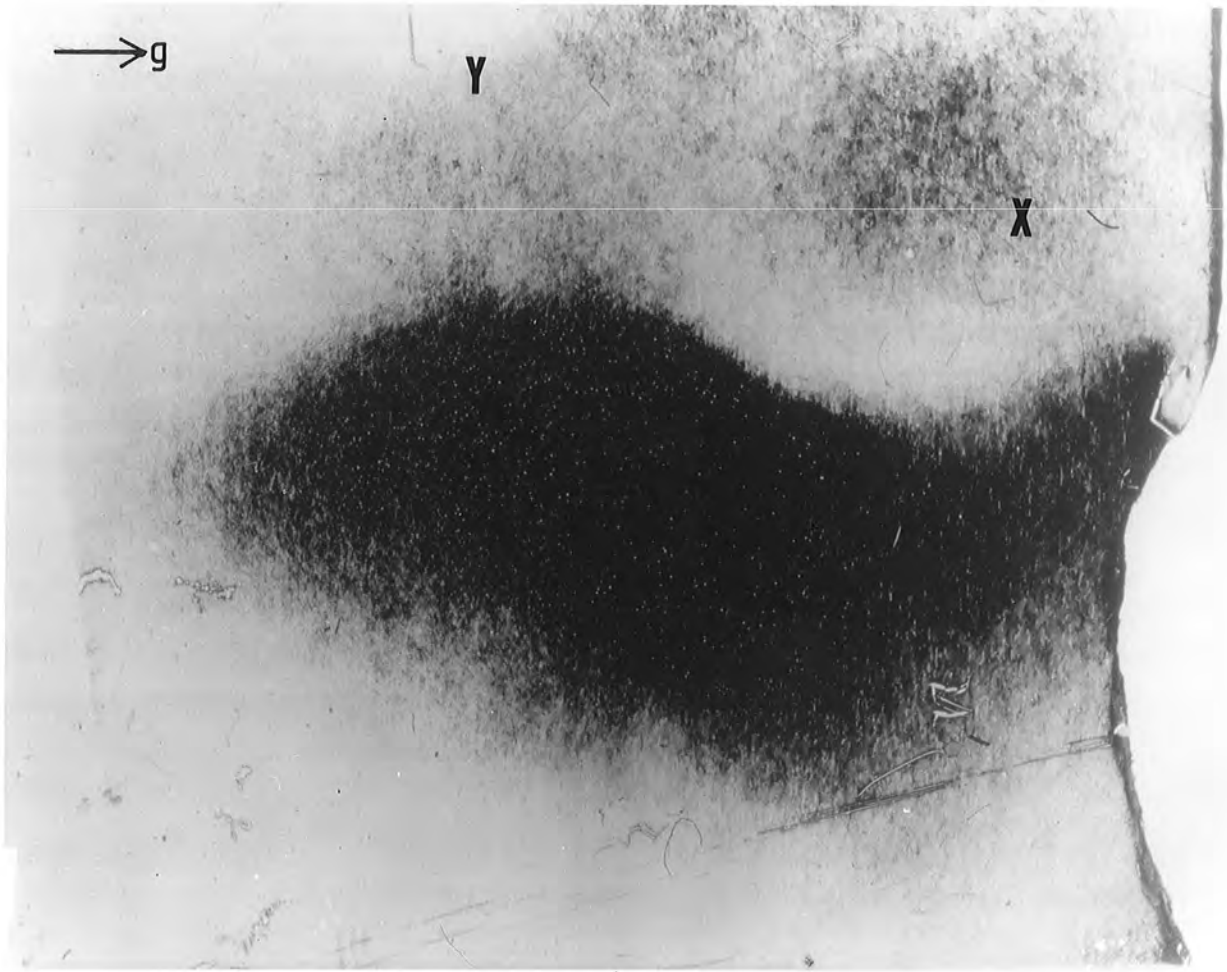

Fig. 8.7 422 reflection topograph of an InP crystal taken at position S on the rocking curve.

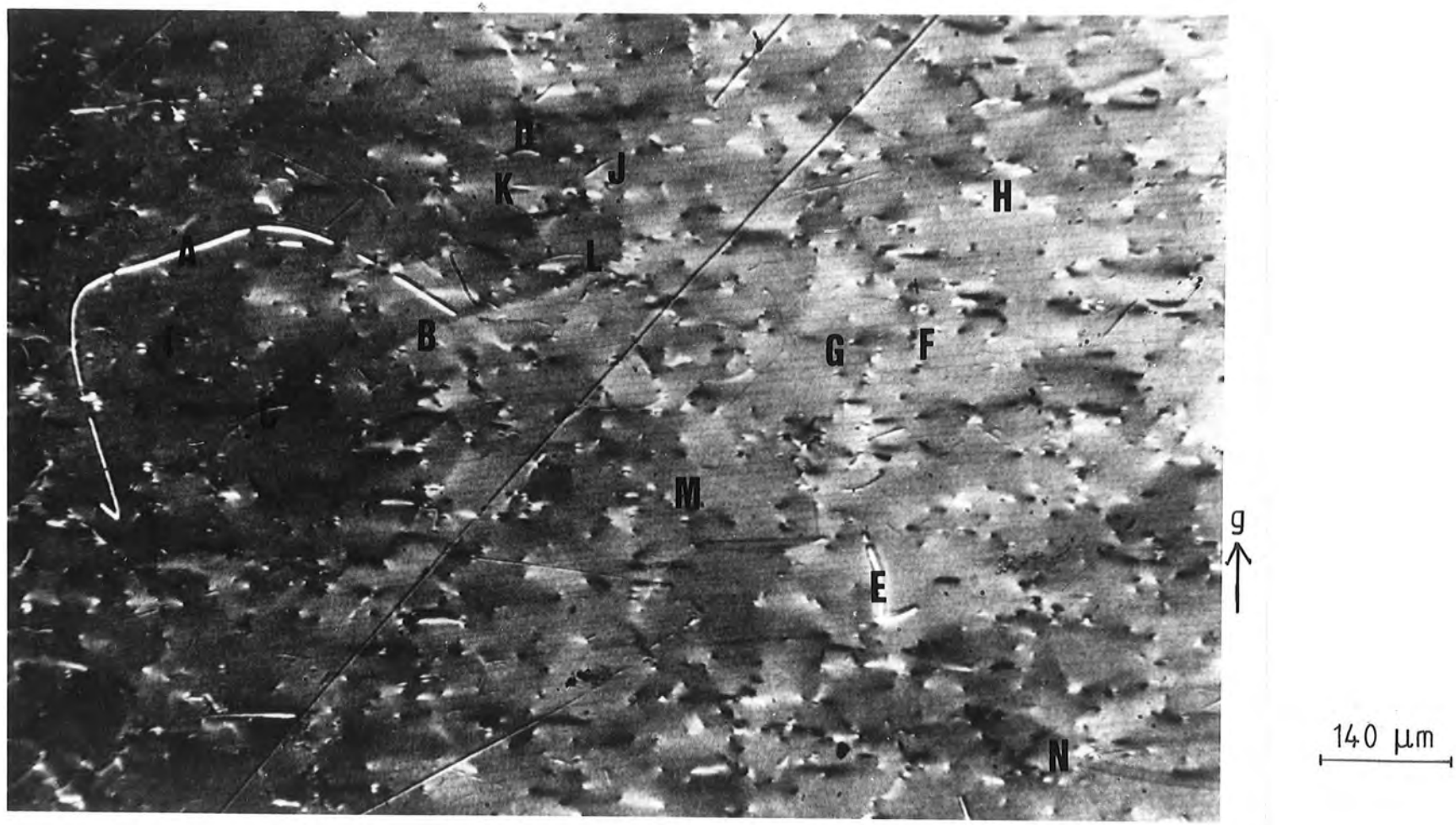

Fig. 8.8 a

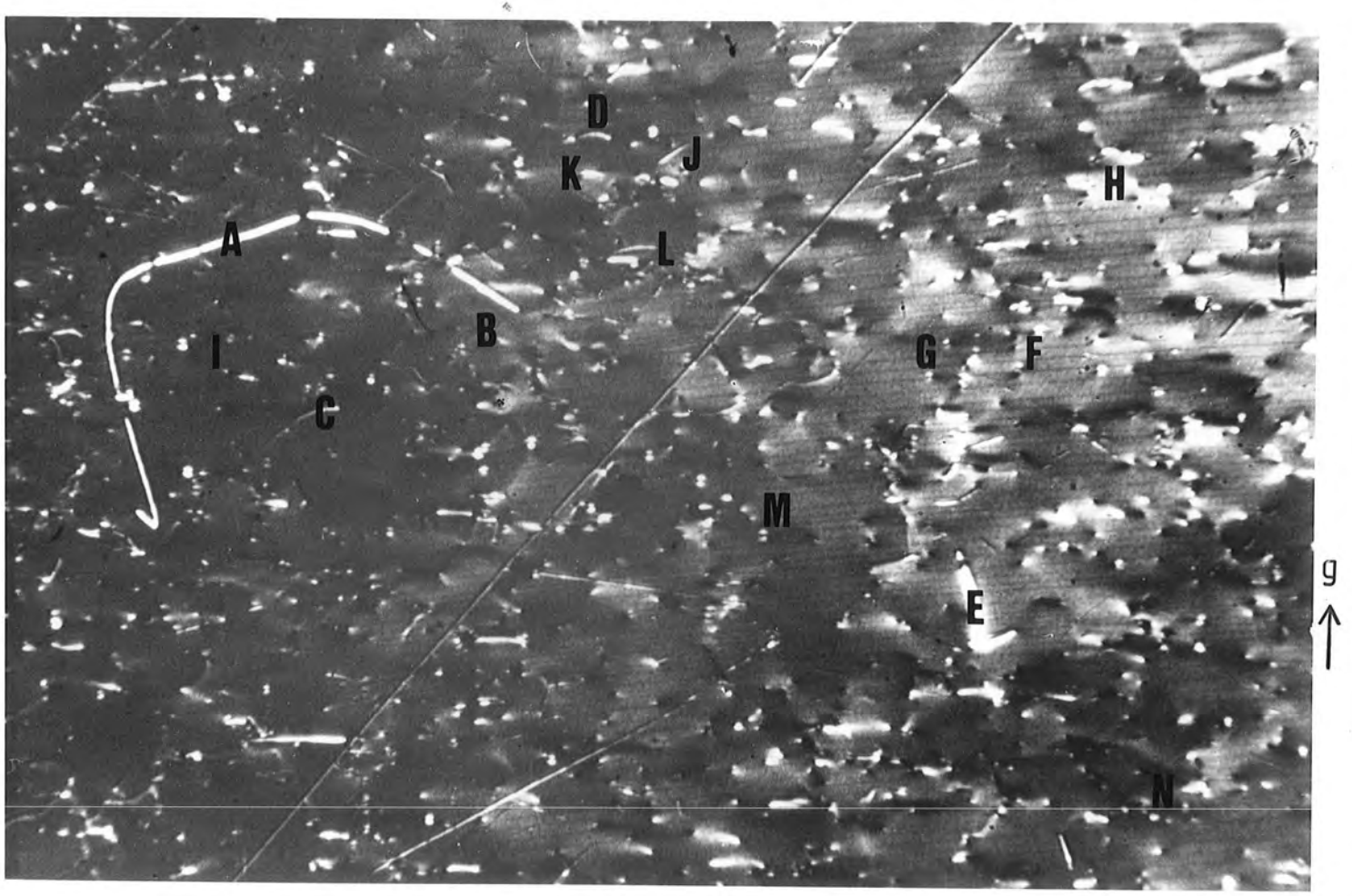

Fig. 8.8 b

Fig. 8.8 c

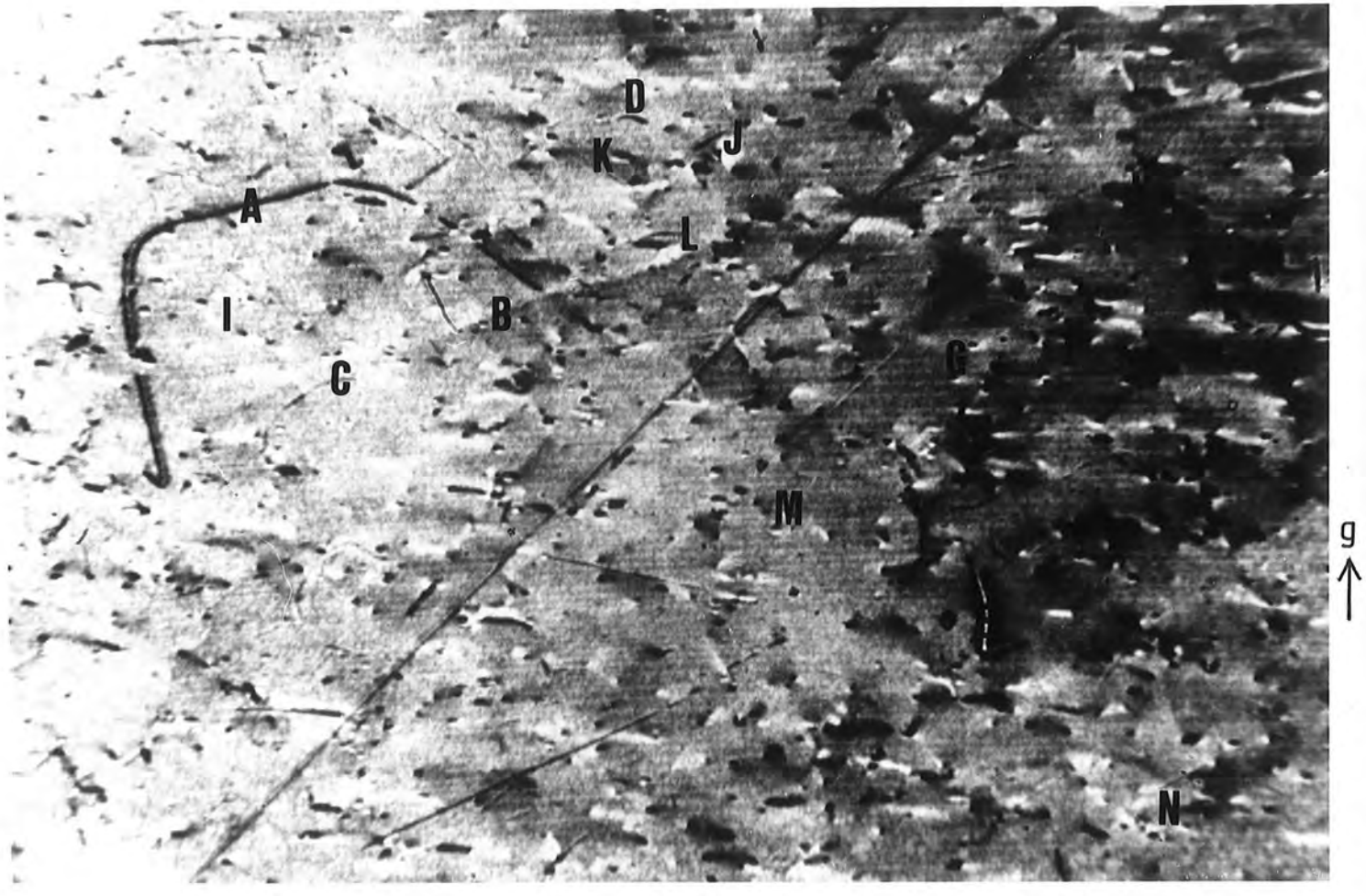

Fig. 8.8 d

Fig. 8.8 422 double crystal reflection topographs of InP corresponding to positions P, Q, R and S of the rocking curve.

corresponding to positions P, Q, R and S on the flank of the rocking curve (Figure 8.6). Observe the change in contrast as the crystal was rotated through its reflecting range. The change in contrast is obvious in Figures8.8 a and d as the topographs were taken on the linear part of the left and right flank of the rocking curve. Specific examples are features A, B, C, D and E (Figures 8.8 a and d).

The topographs display a large number of point-like profiles such as F, G, H and I (Figures 8.8 a and d) which are probably due to dislocations coming up from the deeper part of the crystal and piercing the surface rather steeply. These dislocations have complementary contrast which suggests that the Burger's vector are in opposite directions. The dash-like profiles D, J, K and L indicate that the dislocations run over a certain distance parallel to the surface.

Some of the point like profiles are arranged in the form of an arc of a circle. M in Figure 8.8 a, b and c have the same contrast and is opposite to that of Figure 8.8d. Other examples are F and N. Catholuminescense experiments in GaAs (Brown 1982) suggest that dislocations do not lie exactly in the (111) slip plane but go up and down the plane. They can be correlated to the arc of dots F, M and N.

Another interesting feature are the two semicircular images of the same contrast forming a circle but sandwiched by an image of opposite contrast. These features are marked in Figures8.9 a and b (A, B, C, D, E) which corresponds to region Y of Figure 8.7 and on opposite flank P and S of the rocking curve (Figure 8.6). They are probably due to Grappes

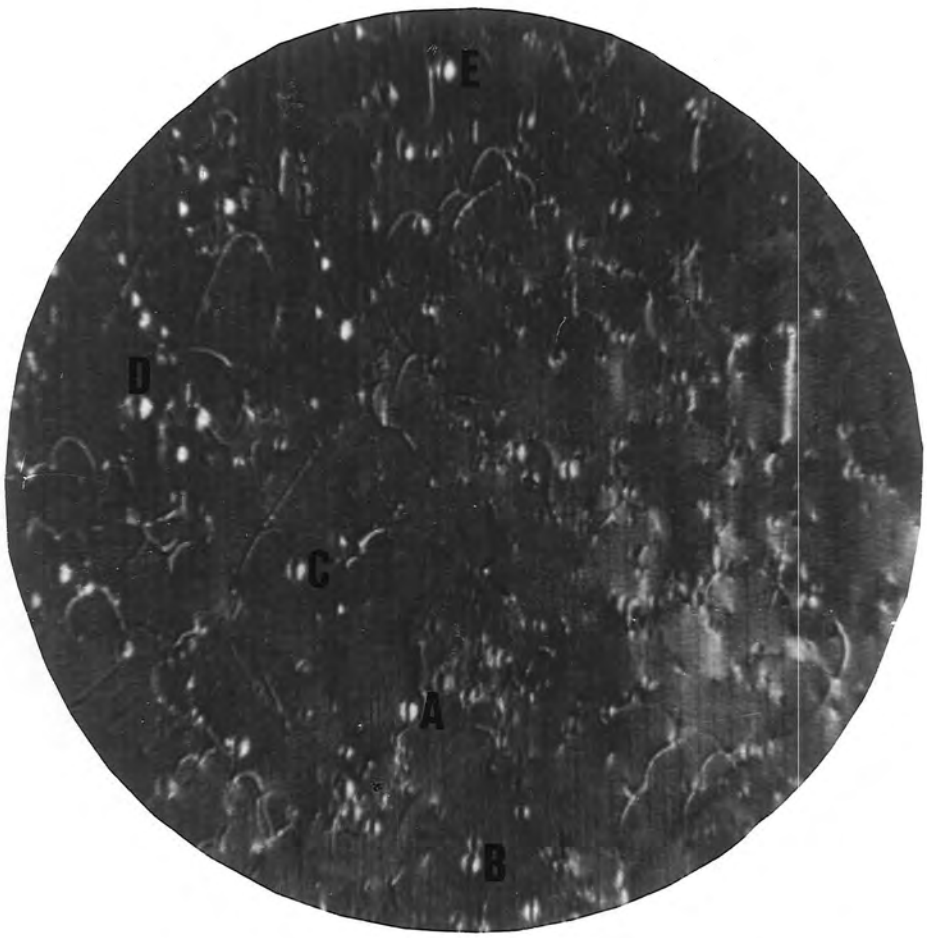

Fig. 8.9 a

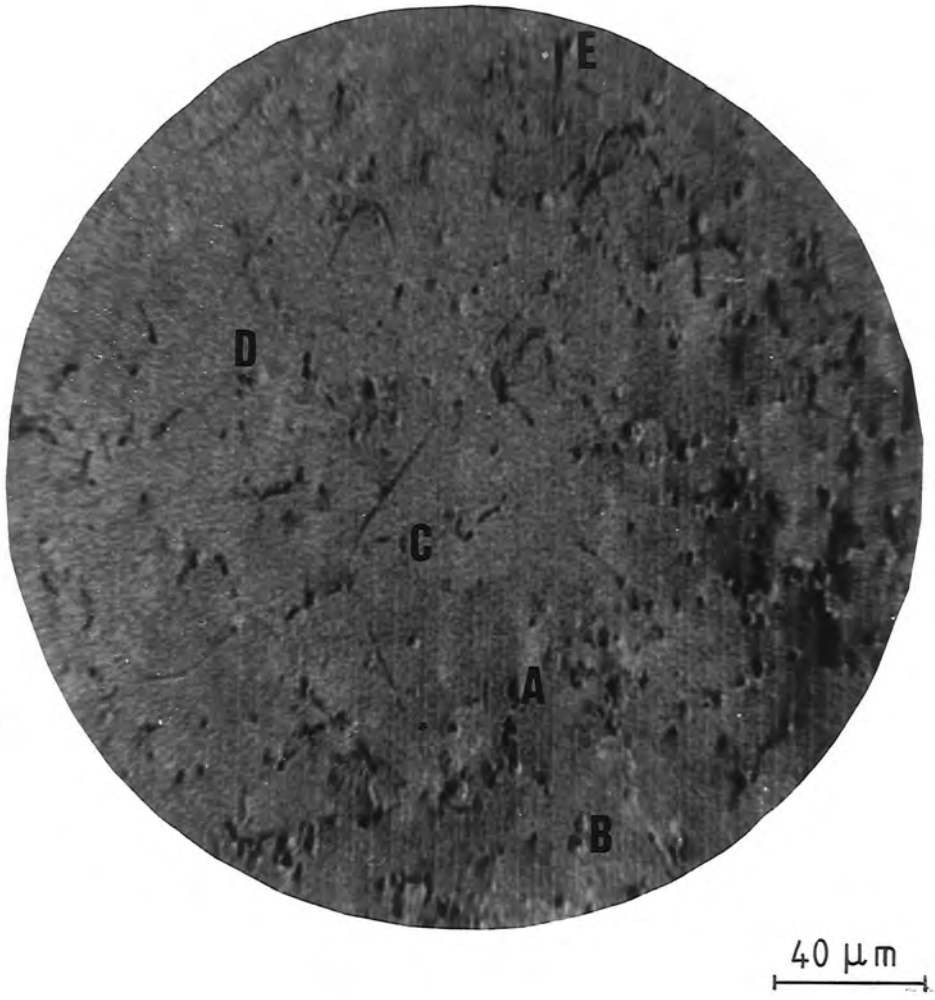

Fig. 8.9 b

Fig. 8.9 422 double crystal reflection topographs of InP corresponding to positions P and S of the rocking curve.

defects commonly found in impurity - associated inclusions.

Burgers vector analysis can be done on the three 440 reflection topographs of InP and GaAs. Figures 8.10a and b are the corresponding topographs of InP. The dislocation lines B, C, D, E and F are visible in Figure 8.10a but they are not completely invisible in Figure 8.10b. This suggests that they are 60^{o} type dislocations where the Burgers vector is neither parallel or perpendicular to the dislocation. The dislocation lines of GaAs (Figures 8.11 and 8.12) show a dendritic like pattern where the dislocations branch to other dislocations. Similarly a 60^{o} type dislocation can be identified at point A (Figures 8.11 a, b and c) and points A, B and C (Figures 8.12 a, b and c).

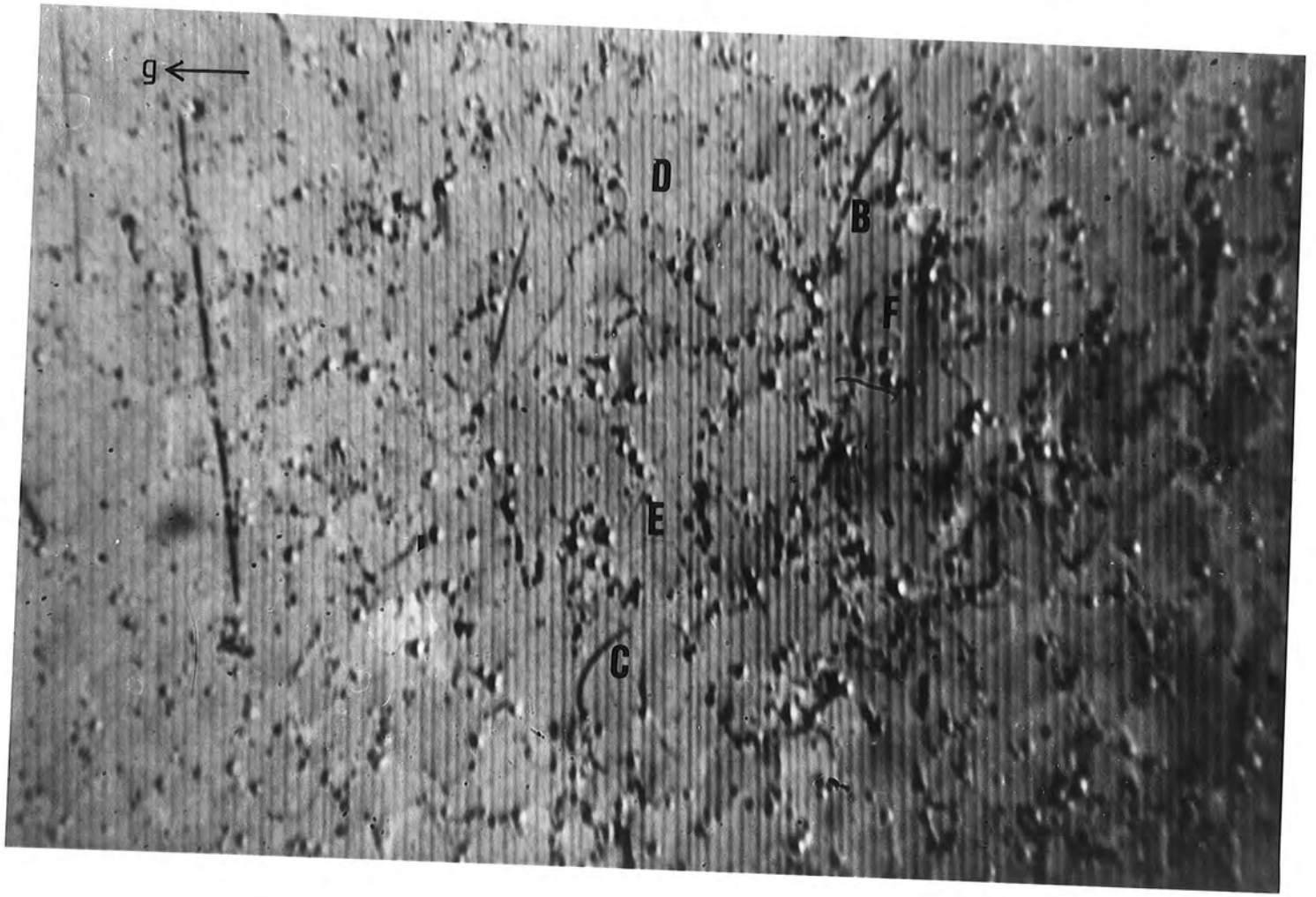

Fig. 8.10 a

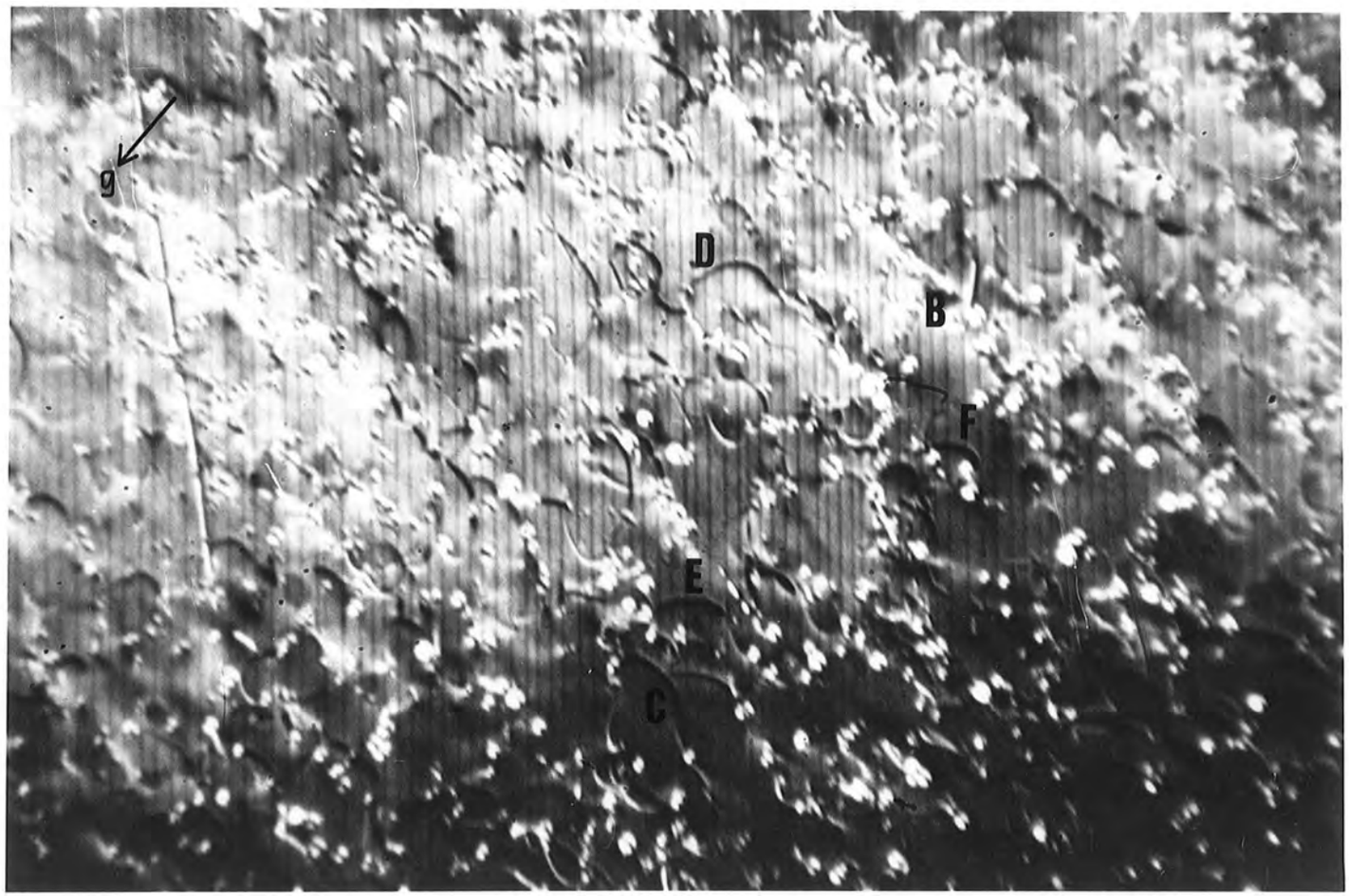

Fig. 8.10 b

Fig. 8.10 440 double crystal reflection topographs of an InP crystal.

Fig. 8.11 a

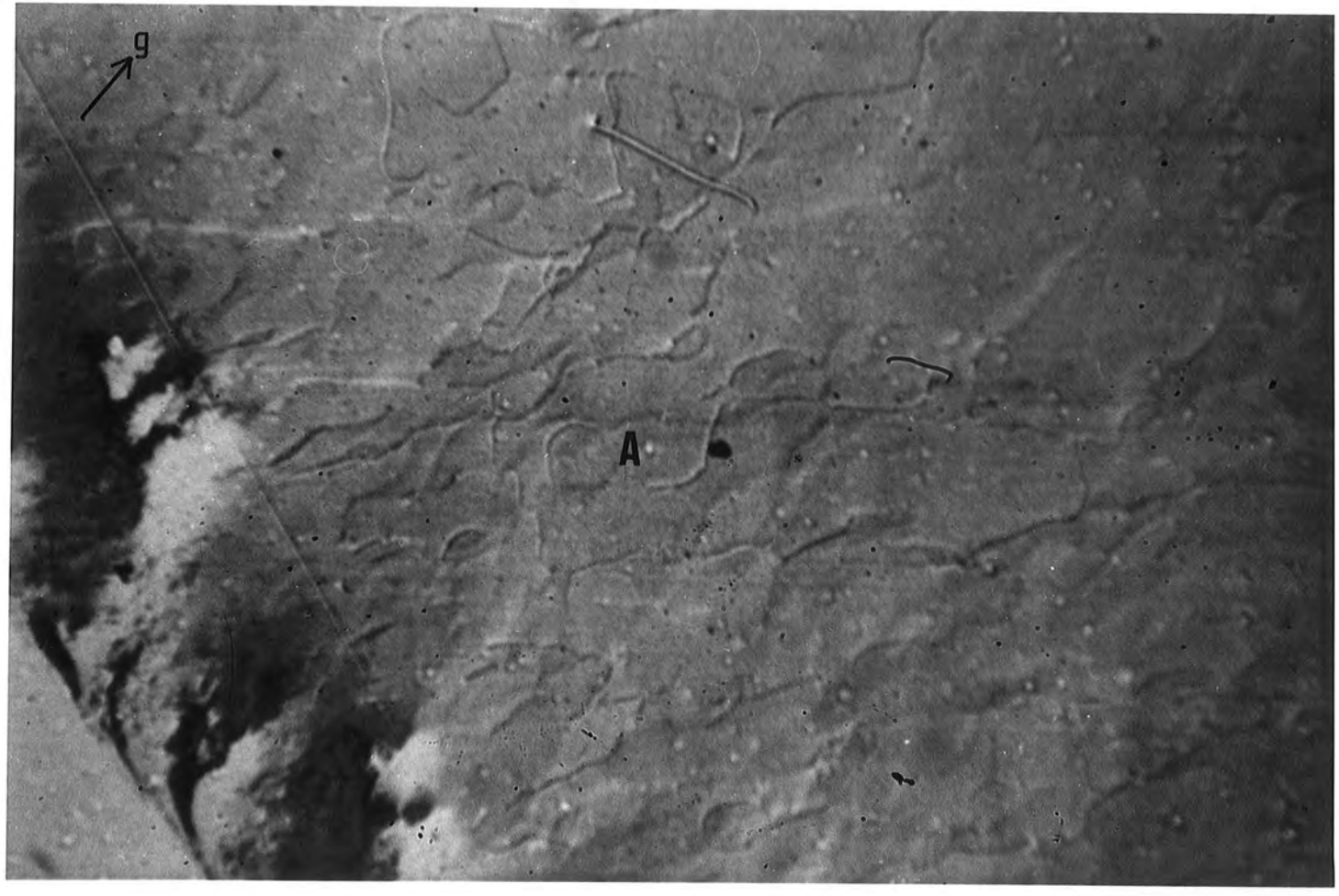

Fig. 8.11 b

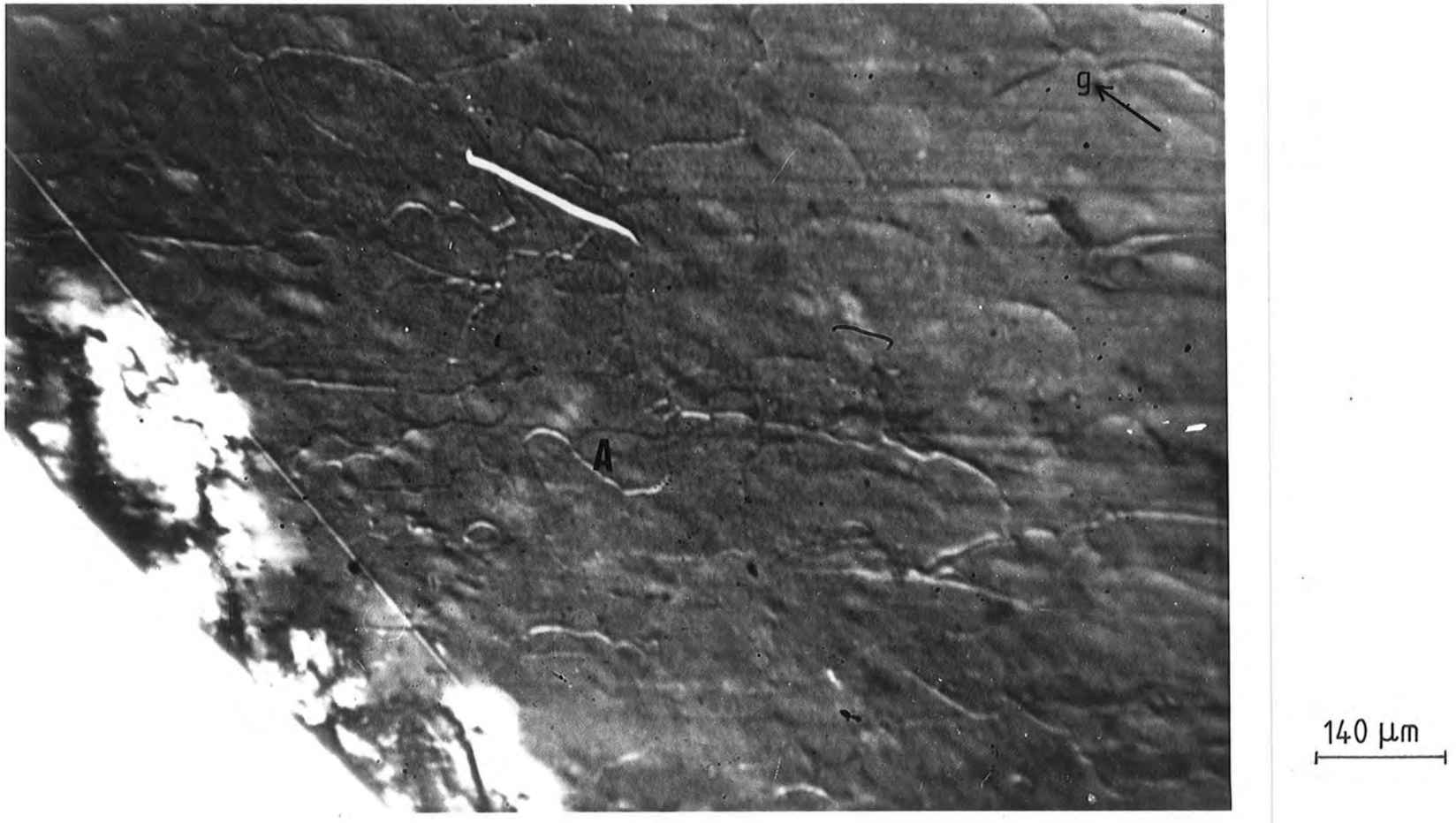

Fig. 8.11 c

Fig. 8.11 440 double crystal reflection topographs of GaAs crystal.

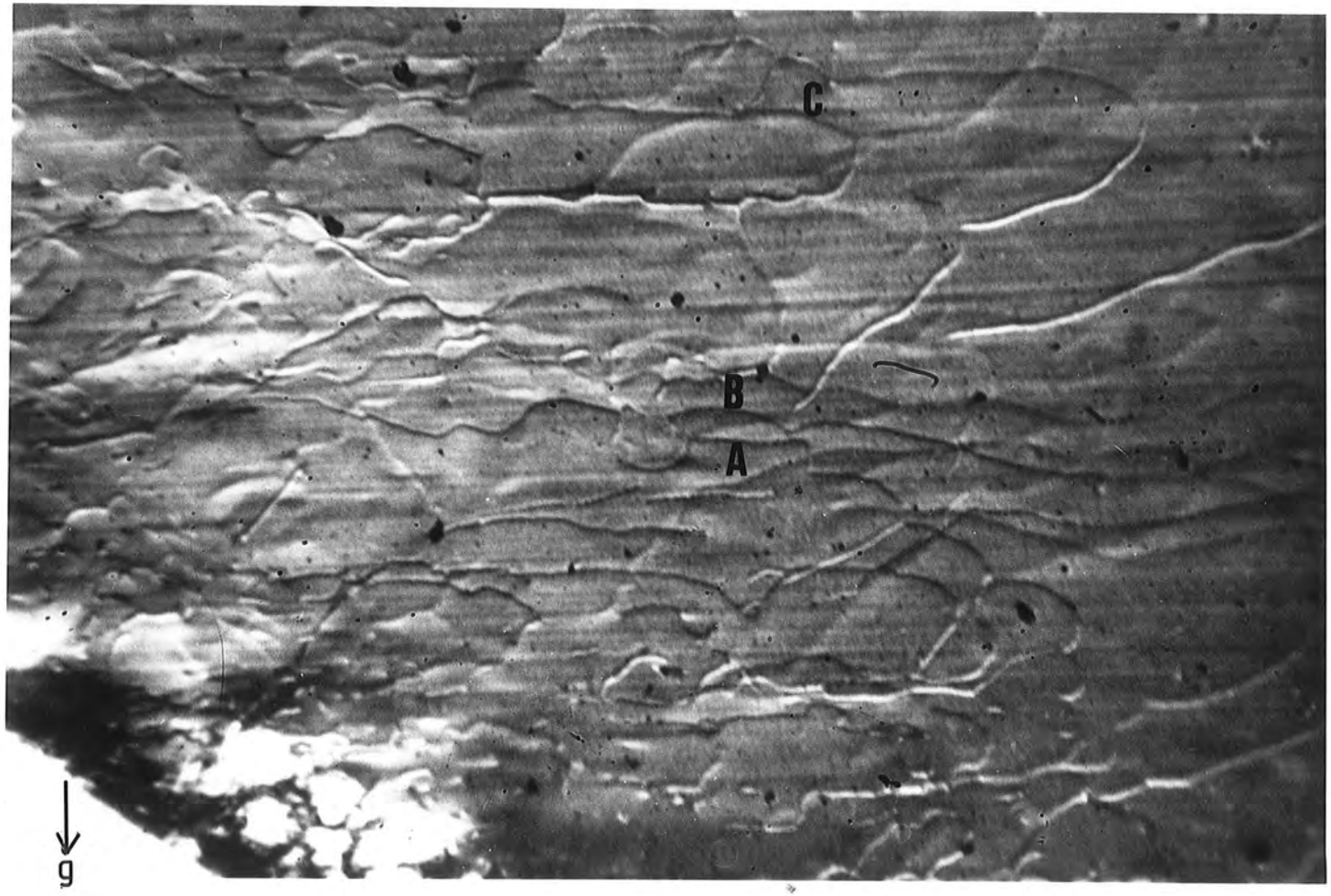

Fig. 8.12 a

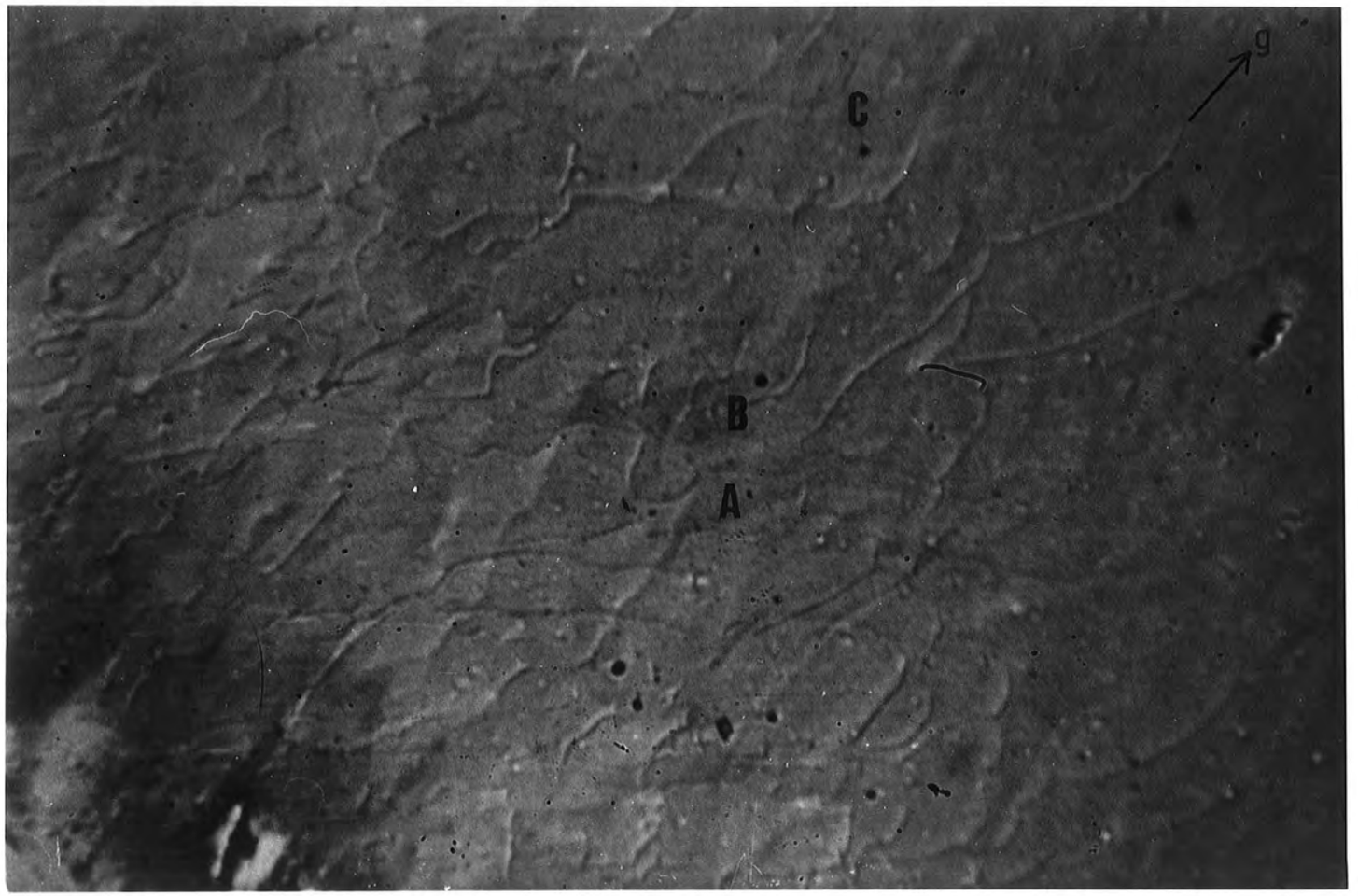

Fig. 8.12 b

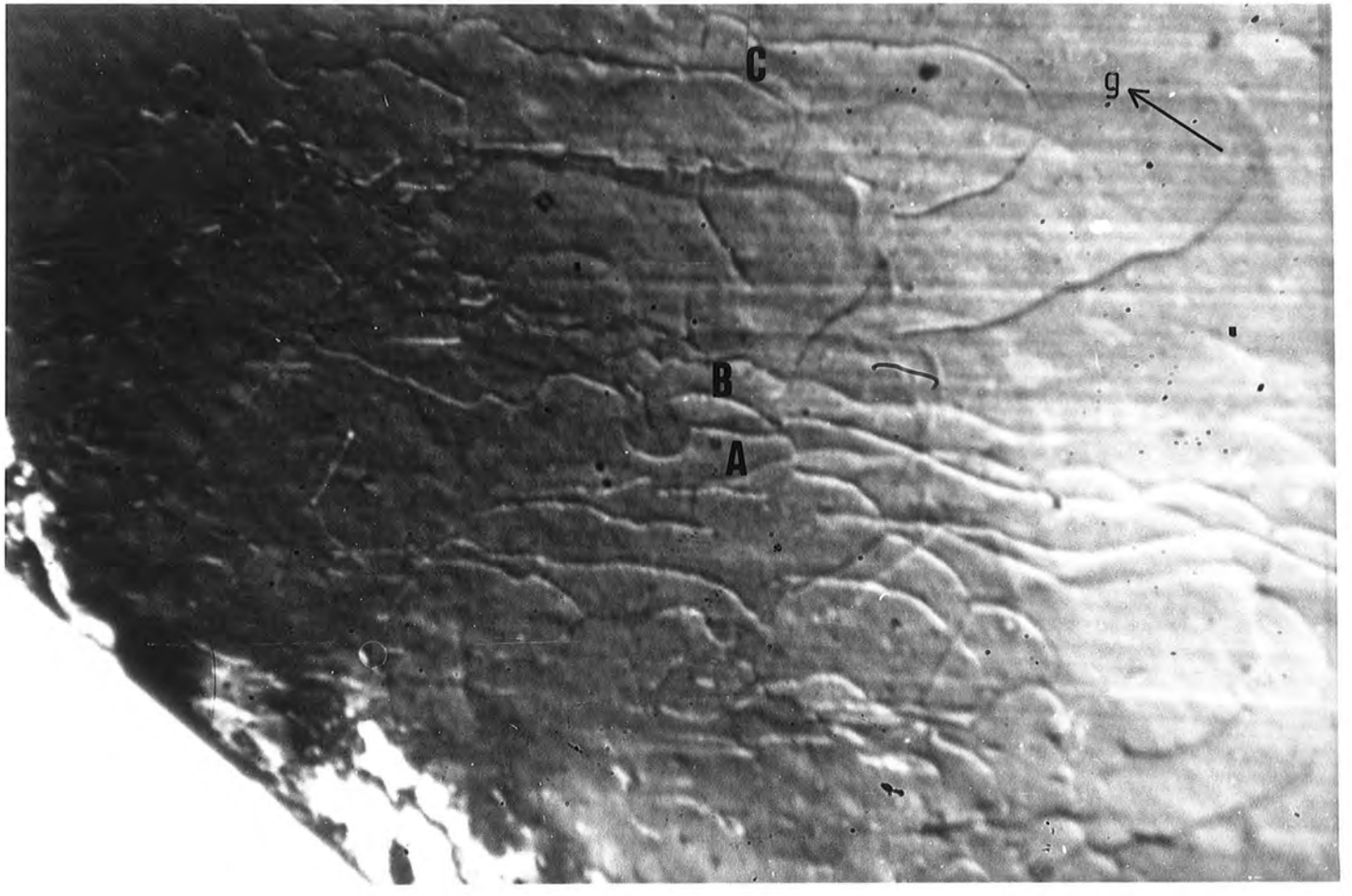

Fig. 8.12 c

Fig. 8.12 440 double crystal reflection topographs of GaAs crystal.

BIBLIOGRAPHY

Authier A.: (1970), Advances in Structure Research by Diffraction Method, 3, ed. Brill and Mason.

Baker T.W., George J.D., Bellamy B.A. and Causer R. : (1966), Nature, Lond. 210, 720.

Baker T.W., George J.D., Bellamy B.A. and Causer R. : (1967), Adv. X-ray Analysis 11, 359.

Baker J.A., Tucker T.N., Moyer N.E. and Buschert R.C. : (1968), J. Appl. Phys. 39, 4365.

Baker J.F.C. and Hart M. : (1975), Acta. Cryst. A31, 364.

Baker J.F.C., Hart M., Halliwell M.A.G. and Heckingbottom R.(1976), Solid State Electronics 19, 331.

Barrett C.S. : (1945), Trans. AIME, 161, 15.

Bastie P., Bornarel J., Lajzerowicz J., Vallade M. and Schneider J.R. : (1975), Phys. Rev. 1312, 5112.

Bastie P., Bornarel J., Lajzerowicz J. and Schneider J.R. : (1976), Ferroelectrics 14, 587.

Bastie P., Vallade M., Vettier C. and Zeyen C.M.E. : (1978), Phys. Rev. Lett. 40, 337.

Bastie P.M. and Bornarel J. : (1979), J. Phys. C. Solid State Phys. 12, 1785.

Batterman B.W. : (1962), Phys. Rev. 126, 1461.

Batterman B.W. and Cole B. : (1964), Rev. Mod. Phys. 36, 681.

Batterman B.W. and Hilderbrandt G. : (1968), Acta. Cryst. A24, 150.

Bearden J.A., Henins A., Marzolf J.G., Sauder W.C. and Thomsen J.S. : (1964), Phys. Rev. 135, A899.

Bearden J.A. and Henins A. : (1965), Rev. Sci. Inst. 36(3), 334.

Beckman O., Bergvall P. and Axelsson B. : (1958), Ark. Fysik. 14, 419.

Benjamin R.J. : (1978), Opt. Eng. 17(6), 574.

Berg W.F. : (1931), Naturwissenschaften 19, 391.

Bond W.L. and Andrus J. : (1952), Am. Mineralogist 37, 622.

Bond W.L. : (1960), Acta. Cryst. 13, 814.

Bonse U., and Kappler E. : (1958), Zeits. f. Naturforschg. 13a(4), 348.

Bonse U. : (1962), Direct Observation of Imperfections in Crystals ed. Newkirk and Wernick (Wiley, New York).

Bonse U., and Hartmann I. : (1981), Zeits. f. Kristallographie 156, 265.

Borchert G.L., Scheck W. and Schult O.W.B. : (1975), Nucl. Inst. and Meth. 124, 107.

Bormann G. : (1941), Z. Phys. 42, 157.

Bormann G. : (1950), Z. Phys. 127, 297.

Bormann G., Hartwig W. and Irmler H. : (1958), Z. Naturforschung 13a, 423.

Bormann G. and Hilderbrandt G. : (1959), Z. Phys. 156, 189.

Borner H., Gottel P., Koch H.R., Pinston J. and Roussille R. Proc. Second Inst. Symp. on Neutron capture gamma-ray spectroscopy and related topics. Petten 1974(1975), pp 691.

Bowen D.K., Clark G.F., Davies S.T., Nicholson J.R.S., Roberts K.J., Sherwood J.N. and Tanner B.K. : (1982), Nuc. Instr. and Meth. 195, 277.

Bradler J. and Polcarova M. : (1972), Phys. Stat. Sol(a) 9, 179.

Brown G.T., Cockayne B. and MacEwan W.R. : (1981), Inst. Phys. Conf. Ser. No. 60 : Section 7, Presented at Micros. Semicond. Mater. Conf., Oxford.

Brown G.T. : (1982), private communication.

Cauchois Y. : (1932), J. de Physique 3, 320.

Clark G.F., Goddard P.A., Nicholson J.R.S., Tanner B.K. and Wanklyn B.M. : (1982), Phil. Mag. - In press.

Clark G.F., Tanner B.K., Farrant S. and Jones D.W. : (1982), J. Magn. Mag. Mater - In press.

Compton A.H., and Allison S.K. : (1934), X-Rays in Theory and Experiment (Macmillan).

Darwin C.G. : (1914), Phil. Mag. 27, 315.

Darwin C.G. : (1914), Phil. Mag. 27, 675.

Dederichs P.H. : (1970), Phys. Rev. B1, 1306.

Du Mond J.W.M. : (1937), Phys. Rev. 52, 872.

Du Mond J.W.M. : (1947), Rev. Sci. Inst. 18, 626.

Du Mond J.W.M. : (1965), Alpha-, beta- and gamma-ray spectroscopy, 1st edition ed. Siegbahn K. (North-Holland Publ. Co., Amsterdam), Chapter 4.

Estop E., Izrael A. and Sauvage M. : (1976), Acta. Cryst. A32, 627.

Ewald P.P. : (1916), Ann. Physik. 49, 1.

Ewald P.P. : (1916), Ann. Physik. 49, 117.

Ewald P.P. : (1917), Ann. Physik 54, 519.

Ewald P.P. : (1958), Acta. Cryst. 11, 888.

Frank A.M., Bryan J.B. and Clouser R.W. : (1976), Appl. Optics 17, 671.

Frank A.M. : (1977), Optical Fabrication and Testing Workshop, San Francisco.

Frilley M. : (1929), Ann. Phys. 11, 483.

Gerth H.L., Sladky R.E., Bezik M.J. and WAshingotn C.A. : (1978), Opt. Eng. 17(6), 588.

Gruber U. : (1964), Z. Physik. 178, 472.

Halliwell M.A.G. : (1981), Inst. Phys. Conf. Ser. No. 60 : Section 5, Presented at Microsc. Semicond. Mater. Conf., Oxford.

Hart M. : (1968), Sci. Prog. Oxf, 56, 429.

Hart M. : (1969), Proc. Roy. Soc. A309, 281.

Hart M. and Milne A.D. : (1969), Acta. Cryst. A25, 134.

Hart M. and Lloyd K.H. : (1975), J. Appl. Cryst. 8, 42.

Hart M. : (1980), Characterization of Crystal Growth Defects by X-ray Methods ed. Tanner B.K. and Bowen D.K.

Hashizume H., Iida A. and Kohra K. : (1975), Japanese J. of Appl. Phys. 14(10), 1433.

Hattori H., Kuriyama H., Katagawa T. and Kato N. : (1965), J. Phys. Soc. Japan 20, 988.

Halliwell J.R., Greenhough T.J., Carr P.D., Moore P.R., Thompson A.W., Hughes G., Przybylski M.M., Ridley P.A., Rule S.A., Sumner I. and Wogan J.S. : (1981), Paper presented at the XIIth Congress of Crystallography, Ottawa.

Hendrix J., Koch M.J., Bordas J. : (1978), J. Appl. Cryst. 12, 467.

Hullubei M.H., and Cauchois Y. : (1934), Compt. Rend. 199, 857.

Hullubei M.H. : (1952), Compt. Rend. 234, 1071.

Hunter L.P. : (1959), J. Appl. Phys. 30, 874.

James R.W. : (1948), The Optical Principles of the Diffraction of X-rays (G. Bell and Sons, London).

Johann H.H. : (1931), Zeitschr. f. Physik 69, 185.

Jones F.J., and Tanner B.K. : (1980), J. Phys. E. Sci. Inst. 13, 1183.

Jones, G.R., Young I.M., Cockayne B., and Brown G.T. : (1981), Inst. Phys. Conf. Ser. No. 60 : Section 5, Presented at Microsc. Semicond. Mater. Conf., Oxford.

Kahn R., Fourme R., Gadet A., Janin J., Dumas C., and Andre D. : (1981), J. Appl. Cryst. 15, 330.

Kato N., and Lang A.R. : (1959), Acta. Cryst. 12, 787.

Kato N. and Tanemura S. : (1967), Phys. Rev. Lett. 19, 22.

Kikuta S., and Kohra K. : (1966), Japanese J. of Appl. Phys. 5(11), 1047.

Kikuta S. and Kohra K. : (1970), J. Phys. Soc. Japan 29(5), 1322.

Kikuta S. : (1971), J. Phys. Soc. Japan 30(1), 222.

King, A.G. and Wilks, J. : (1976), Int. J. Mach. Tool Des. Res. 16, 95.

Knowles, J.W. : (1957), Atomic Energy of Canada Limited, Chalk River report GP1-42.

Knowles J.W. : (1959), Can. J. Phys. 37, 203.

Knowles, J.W. : (1962), Can. J. Phys. 40, 237.

Kohra K. : (1962), J. Phys. Soc. Japan 17, 589.

Kohra K. and Kikuta S. : (1968), Acta Cryst. A24, 200.

Kohra K., Hashizume H. and Yoshimura J. : (1970), Japanese J. of Appl. Phys. 9(9), 1029.

Kohra K., and Matsushita T. : (1977), Semiconductor Silicon, ed. Huff H.R. and Sirtl E. (Princeton : Electrochemical Society) pp. 441.

Labushkin V.G., Seleznev V.W., Faleev N.W., and Figin V.A. : (1978), Sov. Phys. Solid State 20, 891

Lang A.R. : (1958), J. Appl. Phys. 29, 597.

Lang A.R. : (1959), Acta Cryst. 12, 249.

Larson B.C. : (1974), J. Appl. Phys. 45-2, 514.

Laue M. von. : (1931), Ergeb. Exakt. Naturw. 10, 133.

Laue M. von : (1952), Acta. Cryst. 5, 619.

Laue M. von : (1960), Rontgenstrahl-Interferenzen, Akademische Verlag, Frankfurt.

Lester R.S., and Saito T.T. : (1976), Appl. Optics 17, 671.

Mai Zhen-Hong, Mardix S., and Lang A.R. : (1980), J. Appl. Cryst. 13, 180.

Malgrange C., and Authier A. : (1965), C.R. Acad. Sci. Paris 261, 3774.

Matsushita T., Kikuta S. and Kohra K. : (1971), J. Phys. Soc. of Japan 30(4), 1136.

McKenney T.G. : (1981), Third Year Material Science Project Report, University of Warwick,

Merz K,M., : (1960), J. Appl. Phys. 31(1), 147.

Miyaka S. : (1949), Acta Cryst. 2, 192.

Nakayama K., Hashizume H., and Kohra K. : (1970), J. Phys. Soc. Japan 30, 893.

Nakayama K., Hashizume H., Miyoshi A., Kikuta S., and Kohra K. : (1973), Z. Naturforsch 28a, 632.

Nathans R., Pickart S.J., Alperin H.A., and Brown P.J. : (1964), Phys. Rev. 136, A1641.

North J.C., and Buschert R.C. : (1974), Phys. Rev. Letters 13, 609.

Nost B., Larson B.C., and Young F.W. Jr. : (1972), Phys. Stat. Sol. (a) 11, 263.

Ohama N., Sakashita H., and Okazaki A. : (1979), J. Appl. Cryst. 12, 455.

Okkersse B. : (1962), Phillips Res. Repts. 17, 464.

Patel J.R. : (1973), J. Appl. Phys. 44, 3903.

Penning P. : (1966), Proefschrift. Technishe Hogeschool te Delft.

Piller O., Beer W., Kern J. : (1973), Nucl. Inst. and Meth. 107, 61.

Pinsker Z.G. : (1978), Dynamical Scattering of X-rays in Crystals (Springer-Verlag Berlin Heidelberg, New York).

Ridou C., and Rousseau M. : (1980), Solid State Communications 35, 723.

Rodrigues A.R.D., and Siddons D.P. : (1979), J. Phys. E. Sci. Inst. 12, 403.

Rose D., Ostrander H. and Harmermesh B. : (1957), Rev. Sci. Inst. 28, 233.

Rutherford E., and Andrae E.N. da C. : (1914), Phil. Mag. 27, 854.

Rutherford E., and Andrae E.N. da C. : (1914), Phil. Mag. 28, 263.

Rutherford E., Chadwick , Ellis . : (1930), Radiation from radioactive substances (Cambridge University Press).

Ryde N., and Anderson B. : (1955), Proc. Phys. Soc. B68, 117.

Sauvage M. : (1978), Nuc. Inst. and Meth. 152, 313.

Schneider J.R. : (1974), J. Appl. Cryst. 7, 541.

Schneider J.R. : (1974), J. Appl. Cryst. 7, 547.

Schneider J.R. : (1975), J. Appl. Cryst. 8, 195.

Schneider J.R. : (1975), J. Appl. Cryst. 8, 530.

Schneider J.R. : (1978), Phil. Mag. B 38, 141.

Schneider J.R. : (1980), Characterization of Crystal Growth Defects by X-Ray Method ed. Tanner B.K. and Bowen D.K.

Schull G.B., Strauser W., and Wollan E.O. : (1951), Phys. Rev. 83, 333.

Schwarzschild M.M. : (1928), Phys. Rev. 32, 162.

Smith S.R.P., and Tanner B.K. : (1978), J. Phys. C11, L717.

Stacy W.T., Pistorius J.A. and Janssen M.M. : (1974), J. Cryst. Growth 22, 37.

Sumbaev O.I. : (1957), Zh. Eksp. Teor. Fiz. 32, 247.

Tanemura S and Kato N. : (1972), Acta. Cryst. A28, 69.

Tanner B.K. : (1976), X-Ray Diffraction Topography (Pergamon).

Thibaud T. : (1925), Thesis, Paris.

Wilks J. : (1980), Precision Eng. 2(2), 57.

Yeh T.H. and Joshi M.L. : (1969), J. Electrochem. Soc. 116, 73.

Yoshimura J. and Kohra K. : (1976), J. Cryst. Growth 33, 311.

Yoshimura J., Miyazaki T., Wada T. and Kohra K. : (1979), J. Cryst. Growth 46, 691.

Zachariasen W.H. : (1945), Theory of X-Ray Diffraction in Crystals (John Wiley and Sons, Inc., New York).

Appendix 1

The lay-out of the manual control system.

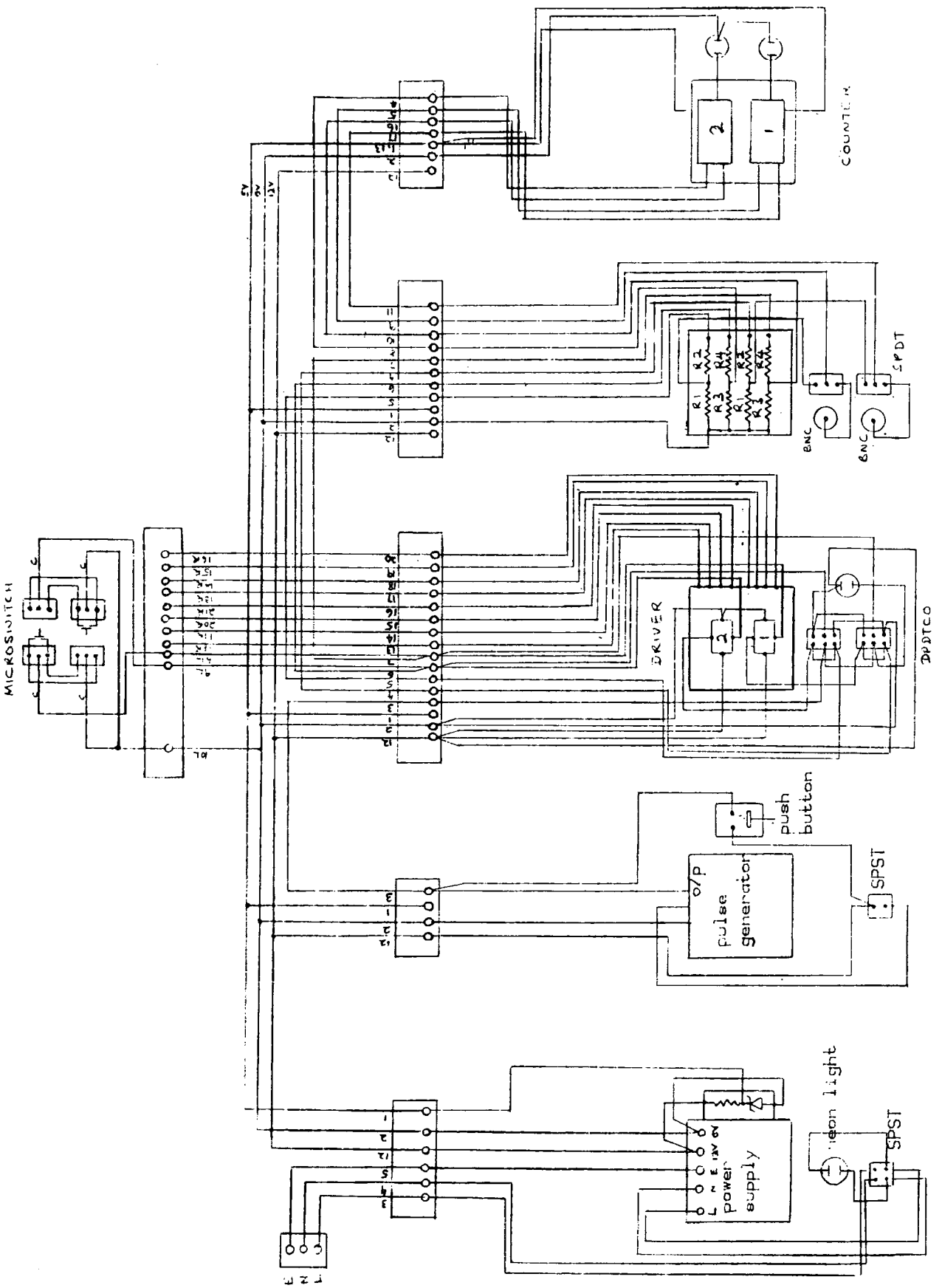

Appendix 2

The control program for the double crystal diffractometer.

```
10 poke1,0:poke2,148:a%=1:n%=1:t%=1
20 dima(500):dimp(50):dimhd(500)
30 ad=64:u1=36:d1=37:u2=40:d2=41
40 c1=32:a1=33:c2=44:a2=45:xi=16:yi=17
50 input"input axis 1 or 2";ax
60 input"angle per step";uu
70 print"********************"
110 print"counter add=";ad
120 print"axis 1 add=";u1;d1
130 print"axis 2 add=";u2;d2
140 print"goniometer 1 add=";c1;a1
150 print"goniometer 2 add=";c2;a2
160 print"d-a converter add=";xi;yi
170 print"********************"
180 print"rs:reset axis*co:count"
190 print"sc:scan*gn:tilt goniometer"
200 print"fi:find*pl:plot*fl:flank"
210 print"au:automatic tilting & plotting"
220 print"********************"
230 print"press any key to stop in co,sc,fi,pl&flroutine"
240 print"********************"
250 input"routine";r$
260 ifr$="rs"thengosub1000
270 ifr$="co"thengosub1500
280 ifr$="sc"thengosub2000
290 ifr$="gn"thengosub3000
300 ifr$="fi"thengosub3500
310 ifr$="pl"thengosub4000
320 ifr$="fl"thengosub4500
330 ifr$="au"thengosub5000
340 goto70
1000 rem resetting axis
1010 input"input axis:1 or 2";ax
1020 input"angle per step";uu
1030 return
1500 rem counting routine
1510 input"input counting time";s
1520 a%=ad:t%=s:printusr(2)
1530 getb$:ifb$=""then1520
1540 ifax=1thenprint"***position of axis 1***";s1:return
1550 ifax=2thenprint"***position of axis 2***";s2:return
2000 rem scanning routine
2010 print"axis=";ax
2020 ifax=1thenup=u1:dn=d1
2030 ifax=2thenup=u2:dn=d2
2040 input"input motor steps";ms
2050 input"input counting time";s
2060 print"********************"
2070 print"***positive no. of steps:clockwise***"
2080 print"*negative no. of steps:anticlockwise*"
```

```
2090 print"********************"
2100 input"input no. of cycles";no
2110 ifno=0then2230
2120 fori=1toabs(no)
2130 ifno>0thena%=up:n%=ms:t%=1:a=usr(1)
2140 ifno<0thena%=dn:n%=ms:t%=1:a=usr(1)
2150 a%=ad:t%=s:printusr(2)
2160 getb$:ifb$<>""then2190
2170 nexti
2180 i=abs(no)
2190 ifno>0thents=i*ms:a$="u"
2200 ifno<0thents=-(i*ms):a$="d"
2210 ifax=1thens1=s1+ts
2220 ifax=2thens2=s2+ts
2230 print"********************"
2240 ifax=1thenprint"***position of axis 1***";s1
2250 ifax=2thenprint"***position of axis 2***";s2
2260 print"***axis rotation=";a$:return
2500 rem d-a converter routine
2510 a%=xi:n%=x:b=usr(4)
2520 forz=1to50:nextz:a%=yi:n%=y:b=usr(4):forz=1to50:nextz
2530 return
3000 rem tilting goniometer routine
3010 input"input goniometer 1 or 2";gn
3020 ifgn=1thenup=c1:dn=a1
3030 ifgn=2thenup=c2:dn=a2
3040 print"********************"
3050 print"*positive no. of steps:stretch spring*"
3060 print"*negative no. of steps:compress spring*"
3070 input"input no. of steps";gs
3080 ifgs=0then3130
3090 ifgs>0thena%=up:n%=abs(gs):t%=1:a=usr(1)
3100 ifgs<0thena%=dn:n%=abs(gs):t%=1:a=usr(1)
3110 ifgn=1theng1=g1+gs
3120 ifgn=2theng2=g2+gs
3130 ifgn=1thenprint"***tilt position for gon 1***";g1
3140 ifgn=2thenprint"***tilt position for gon 2***";g2
3150 return
3244 print"***dn or d:anticlockwise rotation***"
3500 rem find routine
3502 print"*****up or u:clockwise rotation*****"
3504 print"***dn or d:anticlockwise rotation***"
3506 print"********************"
3510 print"axis=";ax
3520 ifax=1thenup=u1:dn=d1
3530 ifax=2thenup=u2:dn=d2
3540 input"input motor steps";ms
3550 input"input counting time";s
3560 input"input range in degrees";b
3570 print"range=";int(b*3600/uu);"steps"
3580 input"find in both directions?:y or n";c$
3590 input"input limit stop";ls
3600 input"input axis rotation:u or d";a$
3610 n=0
3620 gosub3800
```

```
3630 ifb$<>""ora>lsthen3740
3640 ifc$="y"then3660
3650 ifc$="n"then3740
3660 print"find in opposite direction"
3670 ifa$="u"thena%=dn
3680 ifa$="d"thena%=up
3690 n%=n*ms:t%=1:a=usr(1)
3700 n=-10
3710 ifa$="u"thena$="d":goto3730
3720 ifa$="d"thena$="u"
3730 gosub3800
3740 ifa$="d"thenn=-n
3750 ifax=1thens1=s1+n*ms
3760 ifax=2thens2=s2+n*ms
3770 ifax=1thenprint"***position of axis 1***";s1
3780 ifax=2thenprint"***position of axis 2***";s2
3790 print"***axis rotation=";a$:return
3800 ifn>abs(b*3600/uu/ms)thenreturn
3810 ifa$="u"thena%=up
3820 ifa$="d"thena%=dn
3830 n%=ms:t%=1:a=usr(1)
3840 a%=ad:t%=s:a=usr(2)
3850 n=n+1
3860 printa:ifa>lsthen3890
3870 getb$:ifb$<>""then3930
3880 goto3800
3890 a%=ad:t%=s:a=usr(2)
3900 printa:ifa>lsthen3930
3920 goto3800
3930 return
4000 rem plotting routine
4002 print"*plot routine is in clockwise rotation*"
4004 print"********************"
4010 print"axis=";ax
4020 ifax=1thenup=u1:dn=d1
4030 ifax=2thenup=u2:dn=d2
4040 input"input motor steps";ms
4050 input"input counting time";s
4060 input"input no of cycles";ra
4070 ifr$="au"thenprint"plotting"
4080 x=0:y=0:gosub2500
4090 pv=pp=0
4100 it=0
4102 print"cyclecountpeak valpeak pos"
4104 print"--------------------------"
4110 fori=1tora
4120 a%=up:n%=ms:t%=1:a=usr(1)
4130 a%=ad:t%=s:a(i)=usr(2)
4140 printi,a(i),pv,pp
4150 y=a(i):x=i:gosub2500
4160 ifa(i)>pvthenpv=a(i):pp=i
4170 it=it+a(i)
4180 getb$:ifb$<>""then4210
4190 nexti
```

```
4200 goto4220
4210 ra=i
4220 y=0:gosub2500
4230 forz=1to200:nextz
4240 x=0:gosub2500
4250 a%=dn:n%=(ra*ms)+100:t%=1:a=usr(1)
4260 a%=up:n%=100:t%=1:a=usr(1)
4270 ifr$="fl"thenreturn
4280 ifax=1thenprint"***position of axis 1***";s1
4290 ifax=2thenprint"***position of axis 2***";s2
4300 ifgn=1thenprint"***tilt position of gon 1***";g1
4310 ifgn=2thenprint"***tilt position of gon 2***";g2
4320 print"width of plot=";ra*ms*uu;"arc sec"
4330 print"motor steps=";ms;"or=";ms*uu;"arc sec"
4340 print"counting time=";s/10;"sec"
4350 print"integrated intensity=";it
4360 return
4500 rem sitting on flank of rocking curve
4502 print"*plotting is in clockwise rotation*"
4504 print"********************"
4510 print"axis=";ax
4520 ifax=1thenup=u1:dn=d1
4530 ifax=2thenup=u2:dn=d2
4540 input"input motor steps";ms
4550 input"input counting time";s
4560 input"input no of cycles";ra
4570 print"position on flank of curve is in the    form of"
4575 print"(c*peak value);0<c<1"
4580 input"input c";c
4590 input"which side of of curve:l or r";c$
4600 gosub4080
4610 n=0
4620 ifc$="r"then4690
4630 hd=abs(c*pv-a(1))
4640 fori=2topp
4650 hd(i)=abs(c*pv-a(i))
4660 ifhd(i)<hdthenhd=hd(i):hp=i:hh=a(i)
4670 nexti
4680 print"topograph is at position";hp;"on plot;count rate is"
4682 print"approx.";hh
4685 goto4750
4690 hd=abs(c*pv-a(pp))
4700 fori=(pp+1)tora
4710 hd(i)=abs(c*pv-a(i))
4720 ifhd(i)<hdthenhd=hd(i):hp=i :hh=a(i)
4730 nexti
4740 print"topograph is at position";hp;"on plot;count rate is"
4745 print"approx.";hh
4750 a%=up:n%=hp*ms:t%=1:a=usr(1)
4760 n=hp
4770 x=hp:y=hh:gosub2500
4780 ifc$="r"thengosub4850
4790 ifc$="l"thengosub4930
4800 ifax=1thens1=s1+(n*ms)
4810 ifax=2thens2=s2+(n*ms)
4820 ifax=1thenprint"***position of axis 1***";s1
```

```
4830 ifax=2thenprint"***position of axis 2***";s2
4840 return
4850 a%=ad:t%=s:b=usr(2)
4860 printb
4870 ifb<hh+(.1*hh)andb>hh-(.1*hh)theny=b:x=x:goto4900
4880 ifb=>hh+(.1*hh)thena%=up:n%=ms:t%=1:a=usr(1)
4885 ifb=>hh+(.1*hh)thenn=n+1:y=b:x=x+1:goto4900
4890 ifb=<hh-(.1*hh)thena%=dn:n%=ms:t%=1:a=usr(1)
4895 ifb=<hh-(.1*hh)thenn=n-1:y=b:x=x-1
4900 gosub2500
4910 getb$:ifb$<>""thenreturn
4920 goto4850
4930 a%=ad:t%=s:b=usr(2)
4940 printb
4950 ifb<hh+(.1*hh)andb>hh-(.1*hh)theny=b:x=x:goto4980
4960 ifb=>hh+(.1*hh)thena%=dn:n%=ms:t%=1:a=usr(1)
4965 ifb=>hh+(.1*hh)thenn=n-1:y=b:x=x-1:goto4980
4970 ifb=<hh-(.1*hh)thena%=up:n%=ms:t%=1:a=usr(1)
4975 ifb=<hh-(.1*hh)thenn=n+1:y=b:x=x+1
4980 gosub2500
4990 getb$:ifb$<>""thenreturn
4995 goto4930
5000 rem automatic tilting and plotting
5010 print"axis=";ax
5020 print""
5030 print"tilting goniometer routine"
5032 print"*****up or u:stretching spring******"
5034 print"*****dn or d:compressing spring*****"
5040 input"input goniometer 1 or 2";gn
5050 input"input goniometer motor steps";gs
5060 input "input tilt direction known:y or n";c$
5070 ifc$="y"theninput"input tilt direction:u or d";d$
5080 print""
5090 print"find routine"
5100 input"input motor steps";ml
5110 input"input counting time";ss
5120 input"input limit stop";ls
5130 print""
5140 print"fast scanning routine"
5150 input"input no of cycles";cy
5160 input"input motor steps";mf
5170 print""
5180 print"plot with the greatest peak value"
5190 input"input total number of plots";k
5200 print""
5210 print"plotting routine"
5220 input"input no of cycles";ra
5230 input"input motor steps";ms
5240 input"input counting time";s
5242 print"*****up or u:clockwise rotation*****"
5244 print"***dn or d:anticlockwise rotation***"
5250 input"input axis rotation:u or d";a$
5260 n=0
5270 ifax=1thenup=u1:dn=d1
5280 ifax=2thenup=u2:dn=d2
5290 ifa$="u"thena%=up:n%=ml:t%=1:a=usr(1)
5300 ifa$="d"thena%=dn:n%=ml:t%=1:a=usr(1)
```

```
5310 a%=ad:t%=ss:a=usr(2)
5320 n=n+1
5330 printa:ifa>1sthen5440
5340 getb$:ifb$=""then5270
5350 ifa$="d"thenn=-n
5360 ifax=1thens1=s1+(n*ml)
5370 ifax=2thens2=s2+(n*ml)
5380 ifax=1thenprint"***position of axis 1***";s1
5390 ifax=2thenprint"***position of axis 2***";s2
5400 print"axis rotation=";a$
5410 input"continue in au?:y or n";b$
5420 ifb$="y"thengoto5250
5430 ifb$="n"thenreturn
5440 a%=ad:t%=ss:a=usr(2)
5450 printa:ifa>1sthen5480
5460 getb$:ifb$=""then5270
5470 goto5350
5480 ifa$="u"thena%=dn
5490 ifa$="d"thena%=up
5500 n%=ml*5+100:t%=1:a=usr(1)
5510 ifa$="u"thena%=up
5520 ifa$="d"thena%=dn
5530 n%=100:t%=1:a=usr(1)
5540 n=n-5
5550 ifa$="d"thenn=-n
5560 ifax=1thens1=s1+(n*ml)
5570 ifax=2thens2=s2+(n*ml)
5580 ifc$="n"then5610
5590 ifd$="u"then5780
5600 ifd$="d"then6020
5610 ss=2*ss
5620 gosub8000
5630 p1=pv
5640 gosub6500
5650 gosub6500
5660 gosub7000
5670 gosub8000
5680 p2=pv
5690 gosub6500
5700 gosub6500
5710 gosub7000
5720 gosub8000
5730 p3=pv
5740 if(p1>p2)or(p2>p3)then5990
5750 ss=ss/2
5760 pv=int(pv/2)
5770 gosub7000
5780 gosub8000
5790 forr=1tok
5800 gosub6500
5810 gosub7000
5820 gosub8000
5830 p(r)=pv
5840 nextr
5850 gosub8500
5860 ift<>p(k)then5880
```

```
5870 gosub6800:goto5790
5880 print"tilting:compressing spring"
5890 ifgn=1thena%=a1:n%=(k-u)*gs:t%=1:a=usr(1):g1=g1-(k-u)*gs
5900 ifgn=1thenprint"tilt position of gon 1=";g1
5910 ifgn=2thena%=a2:n%=(k-u)*gs:t%=1:a=usr(1):g2=g2-(k-u)*gs
5920 ifgn=2thenprint"tilt position of gon 2=";g2
5930 pv=t
5940 gosub7000
5950 gosub8000
5960 gosub9000
5970 gosub4070
5980 return
5990 ss=ss/2
6000 pv=int(pv/2)
6010 gosub7000
6020 gosub8000
6030 forr=1tok
6040 gosub6800
6050 gosub7000
6060 gosub8000
6070 p(r)=pv
6080 nextr
6090 gosub8500
6100 ift<>p(k)then6120
6110 gosub6500:goto6030
6120 print"tilting:stretching spring"
6130 ifgn=1thena%=c1:n%=(k-u)*gs:t%=1:a=usr(1):g1=g1+(k-u)*gs
6140 ifgn=1thenprint"tilt position of gon 1=";g1
6150 ifgn=2thena%=c2:n%=(k-u)*gs:t%=1:a=usr(1):g2=g2+(k-u)*gs
6160 ifgn=2thenprint"tilt position of gon 2=";g2
6170 goto5930
6500 print"tilting:stretching spring"
6510 ifgn=1thena%=c1:n%=gs:t%=1:a=usr(1):g1=g1+gs
6520 ifgn=2thena%=c2:n%=gs:t%=1:a=usr(1):g2=g2+gs
6530 ifgn=1thenprint"***tilt position for gon 1***";g1
6540 ifgn=2thenprint"***tilt position for gon 2***";g2
6550 return
6800 print"tilting:compressing spring"
6810 ifgn=1thena%=a1:n%=gs:t%=1:a=usr(1):g1=g1-gs
6820 ifgn=2thena%=a2:n%=gs:t%=1:a=usr(1):g2=g2-gs
6830 ifgn=1thenprint"***tilt position for gon 1***";g1
6840 ifgn=2thenprint"***tilt position for gon 2***";g2
6850 return
7000 print"finding"
7010 ifa$="u"thenprint"axis rotation=d"
7020 ifa$="d"thenprint"axis rotation=u"
7030 n=0
7040 ifabs(n)=6*cythen7240
7050 ifax=1thenup=u1:dn=d1
7060 ifax=2thenup=u2:dn=d2
7070 ifa$="u"thena%=dn:n%=3*mf:t%=1:a=usr(1)
7080 ifa$="d"thena%=up:n%=3*mf:t%=1:a=usr(1)
7090 a%=ad:t%=ss:a=usr(2)
7100 printa
7110 n=n-3
7120 ifa<int(.6*pv)then7040
7130 ifa$="u"thena%=dn
```

```
7140 ifa$="d"thena%=up
7150 n%=int(cy*.6)*mf+100:t%=1:a=usr(1)
7160 ifa$="u"thena%=up
7170 ifa$="d"thena%=dn
7180 n%=100:t%=1:a=usr(1)
7190 n=n-int(cy*.6)
7200 ifa$="d"thenn=-n
7210 ifax=1thens1=s1+(n*mf)
7220 ifax=2thens2=s2+(n*mf)
7230 return
7240 print"axis rotation=";a$
7250 ifa$="u"thena%=up
7260 ifa$="d"thena%=dn
7270 n%=int(cy*1.8)*mf*3:t%=1:a=usr(1)
7280 n=n+int(cy*1.8*3)
7290 ifabs(n)>12*cythen7470
7300 ifa$="u"thena%=up:n%=3*mf:t%=1:a=usr(1)
7310 ifa$="d"thena%=dn:n%=3*mf:t%=1:a=usr(1)
7320 a%=ad:t%=ss:a=usr(2)
7330 printa
7340 n=n+3
7350 ifa<int(.6*pv)then7290
7360 ifa$="u"thena%=dn
7370 ifa$="d"thena%=up
7380 n%=mf*10+100:t%=1:a=usr(1)
7390 ifa$="u"thena%=up
7400 ifa$="d"thena%=dn
7410 n%=100:t%=1:a=usr(1)
7420 n=n-10
7430 ifa$="d"thenn=-n
7440 ifax=1thens1=s1+(n*mf)
7450 ifax=2thens2=s2+(n*mf)
7460 return
7470 ifa$="u"thenprint"axis rotation=d"
7480 ifa$="d"thenprint"axis rotation=u"
7490 ifa$="u"thena%=dn
7500 ifa$="d"thena%=up
7510 n%=int(cy*5.8)*mf*3:t%=1:a=usr(1)
7520 n=n-int(cy*5.8*3)
7530 ifabs(n)>12*cythenprint"lost peak":goto7670
7540 ifa$="u"thena%=dn:n%=mf*3:t%=1:a=usr(1)
7550 ifa$="d"thena%=up:n%=mf*3:t%=1:a=usr(1)
7560 a%=ad:t%=ss:a=usr(2)
7570 printa
7580 n=n-3
7590 ifa<int(.6*pv)then7530
7600 ifa$="u"thena%=dn
7610 ifa$="d"thena%=up
7620 n%=int(cy*.6)*mf+100:t%=1:a=usr(1)
7630 ifa$="u"thena%=up
7640 ifa$="d"thena%=d
7650 n%=100:t%=1:a=usr(1)
7660 n=n-int(cy*.6)
7670 ifa$="d"thenn=-n
7680 ifax=1thens1=s1+(n*mf)
7690 ifax=2thens2=s2+(n*mf)
7700 ifa$="u"thenprint"axis rotation=d"
```

```
7710 ifa$="d"thenprint"axis rotation=u"
7720 ifabs(n)>12*cyandax=1thenprint"**pos of axis 1**";s1:stop
7730 ifabs(n)>12*cyandax=2thenprint"**pos of axis 2**";s2:stop
7740 return
8000 print"scanning"
8010 pv=pp=0
8012 print"cyclecountpeak valpeak pos"
8014 print"-------------------------"
8020 fori=1tocy
8030 ifa$="u"thena%=up
8040 ifa$="d"thena%=dn
8050 ifa%=upthenn%=mf:t%=1:a=usr(1)
8060 ifa%=dnthenn%=mf:t%=1:a=usr(1)
8070 a%=ad:t%=ss:a(i)=usr(2)
8080 printi,a(i),pv,pp
8090 ifa(i)>pvthenpv=a(i):pp=i
8100 nexti
8210 ifa$="d"theni=-cy
8220 ifax=1thens1=s1+(i*mf)
8230 ifax=2thens2=s2+(i*mf)
8240 return
8500 print"plot with the greatest peak value"
8510 t=0:u=0
8520 forr=1tok
8530 ifp(r)<tthen8550
8540 t=p(r):u=r
8550 nextr
8560 print"peak count=";t
8570 print"plot no.=";u
8580 return
9000 print"positioning for plotting"
9010 n=0
9020 ifa$="u"thena%=dn
9030 ifa$="d"thena%=up
9040 ifa%=upthenn%=ms:t%=1:a=usr(1)
9050 ifa%=dnthenn%=ms:t%=1:a=usr(1)
9060 a%=ad:t%=ss:a=usr(2)
9070 printa
9080 n=n-1
9090 ifa<.75*pvthen9020
9100 ifa$="u"thena%=dn:n%=int(ra*3/5)*ms+100:t%=1:a=usr(1)
9105 ifa$="u"thenn=n-int(ra*3/5)
9110 ifa$="d"thena%=dn:n%=int(ra*2/5)*ms+100:t%=1:a=usr(1)
9115 ifa$="d"thenn=n+int(ra*2/5)
9120 ifa$="u"ora$="d"thena%=up:n%=100:t%=1:a=usr(1)
9130 ifa$="d"thenn=-n
9140 ifax=1thens1=s1+(n*ms)
9150 ifax=2thens2=s2+(n*ms)
9160 return
```

The control program for finding the separation of layer and substrate.

```
9500 rem plotting routine for two peaks
9510 print"*plot routine is in clockwise direction*"
9520 print"********************"
9530 print"axis=";ax
9540 ifax=1thenup=u1:dn=d1
9550 ifax=2thenup=u2:dn=d2
9560 input"input motor steps";ms
9570 input"input counting time";s
9580 input"input bragg angle in deg.";an
9590 input"input no of runs for averaging";l
9600 input"input total no of cycles";ra
9610 input"input no of cycles for first peak";r1
9620 ifr$="au"thenprint"plotting"
9630 x=0:y=0:gosub2500
9635 s12=0
9637 print"cyclecountpeak valpeak pos"
9639 print"--------------------------"
9640 forr=1tol
9650 v1(r)=p1(r)=0
9660 fori=1tor1
9670 a%=up:n%=ms:t%=1:a=usr(1)
9680 a%=ad:t%=s:a(i)=usr(2)
9690 printi,a(i),v1(r),p1(r)
9700 y=a(i):x=i:gosub2500
9710 ifa(i)>v1(r)thenv1(r)=a(i):p1(r)=i
9720 getb$:ifb$<>""then9750
9730 nexti
9740 goto9820
9750 ra=i
9760 y=0:gosub2500
9770 forz=1to200:nextz
9780 x=0:gosub2500
9790 a%=dn:n%=(r1*ms)+100:t%=1:a=usr(1)
9800 a%=up:n%=100:t%=1:a=usr(1)
9810 goto10100
9820 v2(r)=p2(r)=0
9830 fori=(r1+1)tora
9840 a%=up:n%=ms:t%=1:a=usr(1)
9850 a%=ad:t%=s:a(i)=usr(2)
9860 printi,a(i),v2(r),p2(r)
9870 y=a(i):x=i:gosub2500
9880 ifa(i)>v2(r)thenv2(r)=a(i):p2(r)=i
9890 getb$:ifb$<>""then9920
9900 nexti
9910 goto9930
9920 ra=i
9930 y=0:gosub2500
9940 forz=1to200:nextz
9950 x=0:gosub2500
```

```
9960 a%=dn:n%=ra*ms+100:t%=1:a=usr(1)
9970 a%=up:n%=100:t%=1:a=usr(1)
9980 ifra=ithengoto10100
9990 s12(r)=(p2(r)-p1(r))*ms
10000 s12=s12+s12(r)
10010 nextr
10020 forr=1tol
10030 printS12(r)
10040 nextr
10050 p12=s12/l*uu
10060 d=(p12/180/3600*)/tan(an/180*)
10070 print"av sep of film and substrate=";s12/l;"steps"
10080 print"ang sep of film & sub=";p12;"arc sec"
10090 print"delta d/d=";d
10100 print"width of plot=";ra*ms*uu;"arc sec"
10130 ifax=1thenprint"***position of axis 1***";s1
10140 ifax=2thenprint"***position of axis 2***";s2
10150 ifgn=1thenprint"***tilt position of gon 1***";g1
10160 ifgn=2thenprint"***tilt position of gon 2***";g2
10170 return
```